Feedback-assisted Sympathetic Cooling in a Hybrid Atomic-mechanical System

Dissertation

zur Erlangung des Doktorgrades
an der Fakultät für Mathematik, Informatik und Naturwissenschaften
Fachbereich Physik
der Universität Hamburg

vorgelegt von
Philipp Christoph

Hamburg
2018

Gutachter der Dissertation:	Prof. Dr. Klaus Sengstock Prof. Dr. Roland Wiesendanger
Zusammensetzung der Prüfungskommission:	Prof. Dr. Roman Schnabel Prof. Dr. Klaus Sengstock Prof. Dr. Roland Wiesendanger Prof. Dr. Michael Thorwart Prof. Dr. Andreas Hemmerich
Vorsitzender der Prüfungskommission:	Prof. Dr. Roman Schnabel
Vorsitzender des Promotionsausschusses:	Prof. Dr. Wolfgang Hansen
Leiter des Fachbereichs:	Prof. Dr. Michael Potthoff
Dekan der Fakultät für Mathematik, Informatik und Naturwissenschaften:	Prof. Dr. Heinrich Graener

Abstract

The last decades have seen a tremendous progress in the creation and control of novel quantum systems. As a part of this ongoing research, the field of hybrid quantum systems tries to combine different types of these quantum systems. The combination of their respective advantages offers exciting prospects for new quantum technologies ranging from quantum enhanced sensing to quantum information processing. Furthermore, hybrid quantum systems open the door for fundamental research on emergent phenomena or the universality of quantum mechanics. In sight of these research goals, we have realized a hybrid atomic-mechanical system consisting of a cryogenically cooled Si_3N_4 membrane oscillator coupled to a cloud of laser cooled ^{87}Rb atoms. The long-distance coupling is mediated by a light field and is enhanced by placing the mechanical oscillator inside an optical fiber cavity.

This thesis presents details on the experimental setup and the first experiments we have performed in our system. Specifically, the hybrid coupling enables sympathetic cooling of the mechanical oscillator to a minimum mode temperature $T_{\mathrm{min}} \approx 20\,\mathrm{mK}$ through laser cooling of the ^{87}Rb atoms. A maximum sympathetic cooling rate $\Gamma_{\mathrm{sym}} = 23.3(14)\,\mathrm{Hz}$ and a hybrid cooperativity $C_{\mathrm{hybrid}} = 151(9)$ could be determined. In addition to the sympathetic cooling, a setup for active feedback cooling of the oscillator was built up and characterized. The feedback is applied via the radiation pressure of a dedicated laser beam, which is modulated by the homodyne signal of the oscillator. In this way, we achieve a minimum mode temperature of $T_{\mathrm{min}} = 234(42)\,\mu\mathrm{K}$, which corresponds to a thermal mode occupation of $n_{\mathrm{m}} = 18.5(33)$ phonons.

In a further experiment we have demonstrated for the first time the combination of feedback cooling with sympathetic cooling. This proves the technical combinability of feedback cooling with the hybrid coupling mechanism. In the near future, this will enable us to couple a Bose-Einstein condensate to a feedback cooled mechanical oscillator near the quantum ground state. This will be the first realization of a true atomic-mechanical hybrid quantum system.

Zusammenfassung

In den letzten Jahrzehnten wurden enorme Fortschritte in der Entwicklung und Kontrollierbarkeit neuer Quantensysteme erzielt. Teil dieser Forschungsbemühungen ist das Feld der hybriden Quantensysteme, welches sich mit der Kombination verschiedener Quantensysteme beschäftigt. Die Kombination ihrer jeweiligen Vorteile eröffnet vielversprechende Aussichten für neue Quantentechnologien, welche von quantenbasierten Messverfahren bis zur Quanteninformationsverarbeitung reichen. Des Weiteren bieten sich zahlreiche neue Möglichkeiten der Grundlagenforschung in Bereichen wie Emergenz komplexer Systeme oder fundamentale Tests der Quantenmechanik. Mit Blick auf diese Forschungsziele haben wir ein hybrides System realisiert, bestehend aus einem kryogen gekühlten Si_3N_4 Membranoszillator und kalten ^{87}Rb Atomen. Die Wechselwirkung zwischen den räumlich getrennten Partnern des hybriden Systems wird über ein Lichtfeld vermittelt und durch eine optische Fasercavity verstärkt, in der sich der Oszillator befindet.

Diese Arbeit präsentiert die Ergebnisse erster hybrider Kopplungsexperimente in unserem System. Speziell wurde der mechanische Oszillator durch Laserkühlung der ^{87}Rb Atome sympathetisch bis zu einer minimalen Modentemperatur $T_{\mathrm{min}} \approx 20\,\mathrm{mK}$ heruntergekühlt. Eine maximale sympathetische Kühlrate $\Gamma_{\mathrm{sym}} = 23.3(14)\,\mathrm{Hz}$ und eine hybride Kooperativität $C_{\mathrm{hybrid}} = 151(9)$ konnten dabei ermittelt werden. Zusätzlich zum sympathetischen Kühlen wurde ein Aufbau zum aktiven Feedback-Kühlen des Oszillators fertiggestellt und charakterisiert. Das Feedback wird durch den Strahlungsdruck eines speziellen Laserstrahls ausgeübt, welcher mit dem Homodyne-Signal des Oszillators moduliert wird. Auf diese Weise erreichen wir eine minimale Modentemperatur von $T_{\mathrm{min}} = 234(42)\,\mu\mathrm{K}$, was einer thermischen Besetzung von $n_{\mathrm{m}} = 18.5(33)$ Phononen entspricht.

In einem weiterführenden Experiment haben wir zum ersten Mal erfolgreich Feedback-Kühlen mit sympathetischem Kühlen kombiniert. Dies zeigt die technische Kombinierbarkeit von Feedback-Kühlen und des hybriden Kopplungsmechanismus. In der nahen Zukunft werden wir so in der Lage sein, ein Bose-Einstein Kondensat an einen durch Feedback gekühlten mechanischen Oszillator nahe des Quantengrundzustandes zu koppeln. Dies wird die erste Realisierung eines wahren hybriden Quantensystems aus Atomen und einem mechanischen Oszillator darstellen.

Publikationen

Im Rahmen dieser Arbeit sind die folgenden Veröffentlichungen entstanden.

Publications

The following research articles have been published in the course of this thesis.

- A. Bick, C. Staarmann, P. Christoph, O. Hellmig, J. Heinze, K. Sengstock and C. Becker: "The role of mode match in fiber cavities", Review of Scientific Instruments **87**, 013102 (2016)
- H. Zhong, G. Fläschner, A. Schwarz, R. Wiesendanger, P. Christoph, T. Wagner, A. Bick, C. Staarmann, B. Abeln, K. Sengstock, C. Becker: "A millikelvin all-fiber cavity optomechanical apparatus for merging with ultra-cold atoms in a hybrid quantum system", Review of Scientific Instruments **88**, 023115 (2017)

Contents

1 Introduction **2**

2 The hybrid experiment **6**
2.1 Laboratory infrastructure . . . 9
2.2 The cold atom apparatus . . . 10
2.3 The cryogenic optomechanical device . . . 14
2.3.1 MiM setup . . . 15
2.3.2 Asymmetric fiber cavities . . . 16
2.3.3 MiM alignment . . . 25
2.4 The coupling laser system . . . 31
2.4.1 Coupling lattice setup . . . 34
2.4.2 Coupling lattice depth calibration . . . 38

3 Optomechanics in the MiM system **44**
3.1 Optomechanical coupling . . . 45
3.2 Mechanical systems in the quantum regime . . . 53
3.3 Homodyne detection of mechanical motion . . . 56
3.4 Optomechanical properties of the MiM device . . . 63

4 Feedback cooling **65**
4.1 Principles of feedback cooling . . . 66
4.1.1 Classical limits of feedback cooling . . . 70
4.1.2 Quantum limits of feedback cooling . . . 77
4.2 Quantum feedback control . . . 79
4.3 Experimental setup for feedback cooling . . . 82
4.3.1 Technical requirements . . . 84
4.3.2 Technical implementations . . . 85
4.4 Experimental realization of feedback cooling . . . 89
4.4.1 Feedback cooling in time domain . . . 89
4.4.2 Feedback phase adjustment . . . 91
4.4.3 Feedback cooling performance . . . 92
4.5 Further technical applications . . . 96

5 Sympathetic cooling **99**
5.1 Principles of sympathetic cooling . . . 100
5.1.1 Classical description of the hybrid coupling mechanism . . . 100
5.1.2 Quantum description and hybrid cooperativity . . . 105
5.1.3 Instability in the hybrid system . . . 107

5.1.4 Combined sympathetic and feedback cooling . . . 107
5.2 Experimental realization of sympathetic cooling . . . 109
5.2.1 Parameter optimization and experimental sequences . . . 109
5.2.2 Sympathetic cooling in time domain . . . 117
5.2.3 Resonant hybrid coupling . . . 119
5.2.4 Influence of the atom number . . . 126
5.2.5 Feedback-assisted sympathetic cooling . . . 128
5.3 Conclusion . . . 132

A Details of the coupling lattice **134**
A.1 Optical losses . . . 134
A.2 Theory of Kapitza-Dirac diffraction . . . 135

B Details of the feedback setup **137**
B.1 Experimental setup for feedback cooling . . . 137
B.2 Data sheet of homodyne photodetector . . . 138
B.3 Transfer function of electrical bandpass . . . 140
B.4 Data sheet of fiber EOM . . . 141

C Details of the sympathetic cooling measurements **142**
C.1 Measurement of the MOT temperature . . . 142
C.2 OD measurements of the atom number . . . 143
C.3 Parasitic heating in combined cooling . . . 148

Bibliography **150**

Chapter 1

Introduction

In the early 20th century, the discovery of quantum mechanics revolutionized our understanding of the world. Suddenly, unsolved puzzles like the stability of the atom or the spectrum of the black-body radiation could be explained consistently. Yet, the truly groundbreaking significance of quantum mechanics has been revealed in the following decades, when the fruitful interplay between theoretical and experimental research caused pioneering progress in physical science. Today, the quantum theory forms the foundation of all modern physics together with Einstein's theory of relativity. Closely tied to this scientific revolution, the quantum physical knowledge lead to breakthrough technologies like the laser or semiconductor chips, which are the basis of modern electronics.

In the beginning of the 21th century, quantum technology has reached a new level. Unlike lasers and semiconductors which can be described semi-classically, modern quantum technologies utilize physical systems that require a full quantum mechanical description. These systems range from single photons [1], atoms and ions [2, 3], spins [4] and semiconductor quantum dots [5] to superconducting [6] and nanomechanical devices [7, 8]. Complete control over these quantum objects enables the preparation, manipulation and detection of their individual quantum states and openes the door for fascinating new research fields. Some spectacular examples of quantum technological advances are the first realization of Bose-Einstein condensation in 1995 [9, 10] which opened up the field of ultra-cold quantum gases or the first detection of gravitational waves from a black hole merger in 2015 [11] which ushered in a new era of astronomy.

Besides the great importance of quantum technologies in fundamental research, a wide range of their practical applications are about to find their way into today's technology. This offers exciting prospects like quantum computation [12], quantum cryptography in secure communication [13] and quantum enhanced sensing [14]. The technological progress is, however, confronted with major difficulties, which complicates the miniaturization, performance and scalability of current quantum technologies. First of all, decoherence destroys pure quantum states which can only be prevented by perfectly isolating the quantum system from the environment. This requires elaborate techniques like ultra-high vacuum chambers or cryogenic cooling. Furthermore, none of the mentioned quantum systems is currently capable of combining reliable storage, processing and transmission of quantum states. The reason for that is that each of the systems is only suitable for one specific task, but no single system is universally suitable for

all desired applications. For example, photons are well suited for transmitting quantum information, spins may serve as long-lived quantum memories and superconducting devices could allow for rapid information processing. One very promising option to overcome these obstacles is the hybridization of different quantum systems, which forms a so-called *hybrid quantum system* [15–19]. These hybrid systems combine the advantages of different quantum systems at the price of a controllable interface between them. During the last decade, hybrid quantum systems have developed into a rapidly growing, interdisciplinary field of research. Within this context, a large amount of theoretical work has focused on hybrid systems and their prospects for quantum state preparation, quantum state transfer, enhanced probing and sensing, entanglement and ground state cooling [20–36].

One system that is particularly well suited for interfacing it with other systems is a mechanical oscillator. This is because mechanical objects can be designed to couple via all kinds of different interactions: capacitively, electrostatically, magnetically, via radiation pressure, via van der Waals forces, etc. Moreover, modern manufacturing techniques enable the construction of micro-mechanical devices with such a high quality, that individual mechanical modes can be cooled into the quantum ground state. Today, ground state cooling of mechanical motion has become state of the art [37–44]. Hence, mechanical oscillators are an ideal cadidate for hybrid quantum systems. A wide range of hybrid systems has been realized by coupling mechanical oscillators to spins [45–49], semiconductor quantum dots [50, 51], superconducting circuits [37, 44, 52, 53] and atomic ensembles [54–59].

Within this context, the *Nano-BEC experiment* aims at creating a hybrid quantum system by interfacing a mechanical oscillator with an ensemble of ultra-cold rubidium-87 atoms. For several reasons, cold atoms are particularly well suited as a constituent in a hybrid quantum system. Firstly, cold atoms can be perfectly isolated from the environment, which allows for very long coherence times on the order of seconds. This relaxes the experimental requirements on timing for the preparation and detection of quantum states. Secondly, bosonic rubidium-87 can be condensed into a Bose-Einstein condensate (BEC), which is the perfect realization of many-body system in its quantum ground state. This allows for high-purity quantum state preparation and offers exciting possibilities like entanglement and teleportation in the hybrid system [25]. Thirdly, the sophisticated toolset of quantum optics allows for full control over the internal and external states of the atoms [60]. This enables a wide variety of schemes for interfacing [61], state preparation and detection of the cold atoms.

Our experiment focuses on a light-mediated coupling between the two parts of the hybrid system, which has several advantages. Interfacing the mechanical oscillator via radiation pressure opens up the possibility to enhance the optomechanical coupling with an optical cavity and benefits from the sophisticated techniques of cavity optomechanics [8]. Like already mentioned, optical coupling is also an optimal way to couple different degrees of freedom on the atomic side of the hybrid system. Furthermore, optical coupling enables long-range interactions between the two systems, which allows for separating them by several meters. In this way, the setup can be kept modular and modifications on both sides of the hybrid system can be performed separately. Moreover, both parts can be housed in an environment that is specifically optimized for each individual system. Thus, the mechanical oscillator can be cryogenically cooled

with minimal optical access to prevent heating through black-body radiation, while the cold atoms can be trapped in a glass cell with maximal optical access to enable laser cooling, optical trapping, state preparation and detection.
For such a hybrid atomic-mechanical system with long-range mediated light interactions, several proposals for the coupling to internal [25, 35, 36, 62] and to external (motional) atomic states [27, 31, 34, 63] have been published. Recently, internal-state coupling has been realized in such a hybrid system and the coupling was utilized for quantum back-action evading measurements of the mechanical motion [59]. Likewise, this hybrid scheme was realized with external-state coupling [56] and it was used for sympathetic cooling of the mechanical oscillator by laser cooling the atoms [57].
In the first stage of the project we also couple a mechanical oscillator to the external degrees of freedom of an atomic ensemble, as depicted in Figure 1.1. The mechanical oscillator (a silicon nitride membrane [8, 64], widely used in optomechanics) is cryogenically pre-cooled and located inside a Fabry-Pérot cavity, which is called *membrane-in-the-middle* (MiM) configuration [65]. The cavity is formed by two glass fiber tips (called *fiber cavity* [66, 67]) and since light enters the cryostat only through these two fibers, the MiM system can be fully enclosed by cryogenic radiation shields. Furthermore, glass fibers have a low thermal conductivity, which minimizes the heat transfer into the cryogenic chamber. One of the cavity fibers guides the coupling light to a glass cell in which atoms can be trapped and laser cooled. This light forms an optical 1D lattice, which creates a bi-directional coupling of atomic and mechanical motion [31]. The lattice is formed by retro-reflected light from the cavity. The other cavity fiber is used for a feedback laser beam that cools the membrane motion far below the cryogenic equilibrium temperature via optical feedback cooling [68, 69]. For this, the membrane motion is measured via homodyne detection and the signal is fed back to the membrane through radiation pressure of the feedback beam. This creates an artificial damping force which removes kinetic energy from the membrane.

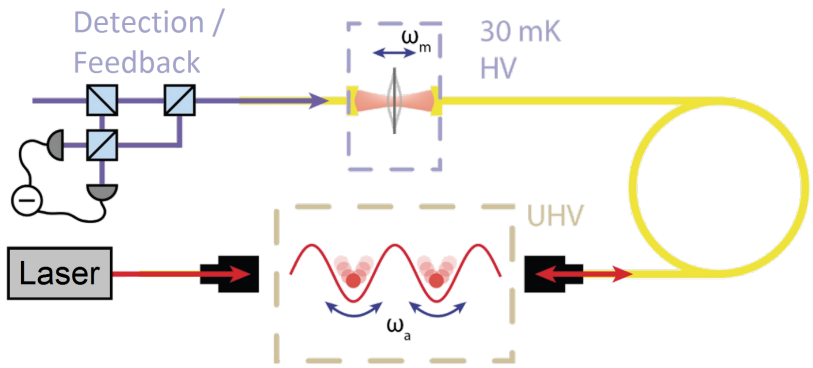

Figure 1.1: Sketch of the realized experimental setup. Experimental realization of a hybrid system consisting of a membrane oscillator inside a fiber cavity coupled to an ensemble of cold atoms trapped in an optical lattice. The membrane is housed in a cryogenic HV chamber (minimum achievable temperature 30 mK) and the cold rubidium-87 atoms are trapped in an optical 1D lattice inside a UHV chamber. The coupling is mediated by the optical lattice which is guided by a glass fiber (yellow line). Resonant coupling of mechanical motion and atomic motion is achieved if the oscillator frequency ω_m matches the atomic trapping frequency ω_at. Balanced homodyne detection is used for detection and optical feedback cooling of the membrane motion.

Our hybrid system consisting of a cryogenically cooled membrane oscillator coupled to the motion of cold rubidium-87 atoms is, to the best of our knowledge, the first realization of this scheme in combination with cryogenic cooling. In this setup, three major experiments were performed. Firstly, sympathetic cooling of the membrane to a minimum mode temperature of $T_{\mathrm{min}} \approx 20\,\mathrm{mK}$ was demonstrated. Both optical molasses cooling and magneto-optical trapping were used for laser cooling the atoms and their parameters for optimal sympathetic cooling of the membrane were optimized. Through these coupling experiments, a maximum hybrid system cooperativity of $C_{\mathrm{hybrid}} = 151 \pm 9$ was determined. Furthermore, the dependency of the hybrid coupling rate Γ_{sym} on the atom number and the atomic cooling rate were analyzed. In a second major experiment, feedback cooling of the membrane down to a minimum mode occupation of $n_{\mathrm{m}} = 18.5 \pm 3.3$ was achieved. Finally, feedback cooling could be combined successfully with sympathetic cooling. This demonstrates the coupling of a mechanical oscillator in the quantum regime to cold atoms in a lattice potential, which paves the way for quantum hybrid experiments with ultra-cold atoms and a quantum mechanical oscillator.
The present thesis is structured as follows:

Ch. 2 – The hybrid experiment

The second chapter deals with the experimental setup for a hybrid quantum system. After a brief description of the cold atom apparatus, the main focus will be on the design and alignment of the fiber cavity MiM system. In this context, an interferometric method will be presented which enables the alignment of the fiber cavity under cryogenic conditions. Finally, the optical coupling lattice will be characterized concerning technical implementations and calibration measurements on the lattice depth using matter wave diffraction of ultra-cold atoms.

Ch. 3 – Optomechanics in the MiM system

The third chapter covers the realized MiM system, beginning with measurements on the optomechanical coupling parameters. In the following, homodyne detection of the membrane motion will be discussed regarding the setup and detection limits. Furthermore, different thermometry calibrations will be presented and compared. Finally, the properties of the membrane oscillator will be characterized.

Ch. 4 – Feedback cooling of mechanical motion

In the course of this thesis, feedback cooling of a mechanical oscillator to a mode occupation of $n_{\mathrm{m}} = 18.5 \pm 3.3$ was realized using optical homodyne feedback. The fourth chapter focuses on the principles of feedback cooling and evaluates the experimental results in the context of fundamental limits and future enhancements.

Ch. 5 – Hybrid coupling experiments

The last chapter covers the experiments with cold atoms in an optical 1D lattice coupled to a mechanical oscillator. After introducing the principles of this coupling mechanism, the performed measurements on sympathetic cooling will be discussed. Finally, measurements on combined feedback cooling and sympathetic cooling will be presented. The chapter concludes with an outlook on future experiments with a hybrid quantum system using ultra-cold atoms.

Chapter 2

The hybrid experiment

This chapter outlines our setup for a hybrid quantum system with ultra-cold ^{87}Rb atoms coupled to a cryogenic optomechanical MiM device. Following the description of all individual parts of this setup, crucial alignment methods for the MiM device and for an optical lattice will be presented, which allows for coupling of the atomic motion to the optomechanical system.

Ultra-cold atoms and mechanical oscillators are particularly well suited for the creation of a hybrid quantum system. On the one hand, quantum optics offers a versatile toolset for trapping, laser cooling, quantum state preparation and detection of cold atoms. This allows for the preparation of quantum states with very long lifetimes of several seconds. Specifically, Bose-Einstein condensates (BECs) of ultra-cold atoms have found wide applications for quantum information storage [70], long-distance entanglement creation [71] and non-classical state preparation [72]. On the other hand, mechanical devices have the huge advantage of high scalabilty, small size and the potential for quantum operations at room temperature [73–75]. Besides these technical merits of mechanical oscillators, macroscopic solid state systems in the quantum regime are a fascinating subject for fundamental research. While the microscopic world is governed by the laws of quantum mechanics, macroscopic objects in the every day life experience behave classically. One century after the development of quantum mechanics, this contradiction is still in the focus of intensive research. Several studies propose general tests of quantum mechanics in the macroscopic regime including collapse models (non-standard decoherence) [76, 77], gravitational decoherence models [78, 79] or even tests of quantum gravity [80] using optomechanical devices.

The advantages of a long-range light interaction between the two parts of the hybrid system were already mentioned in chapter 1. In summary, long-range interactions allow for a modular setup with individually optimized subsystems, the possibility to couple different atomic degrees of freedom, as well as a cavity enhanced optomechanical coupling rate.

In the following, design considerations for the creation of an atomic-mechanical hybrid quantum system will be discussed. For this, both quantum systems should be housed in an optimal environment in terms of maximal coherence time, optimal detection and manipulation possibilities and a large coupling to the mediating light field. This light coupling can be quantified by the atom-light cooperativity C_a and the oscillator-light

cooperativity C_m. In the limit of negligible light losses, the cooperativity of the hybrid system C_hybrid is proportional to the product $C_\mathrm{a}C_\mathrm{m}$ [34]. Hence, in order to maximize C_hybrid, the two subsystem cooperativities should be maximized and light losses should be as small as possible.

Design considerations for a hybrid atomic-mechanical system

(i) **Cold atom apparatus**. First of all, the atomic species should allow for a robust creation of ultra-cold atoms using conventional laser cooling techniques. The science chamber for the cold atoms should have maximal optical access for preparation, detection and coupling of the atomic sample. UHV conditions are beneficial for long coherence times and the possibility to create BECs is desirable. It should also be possible to trap the atoms independent of their internal states, in order to enable all possible coupling schemes between the atoms and the oscillator. A variable spatial shape of the atomic ensemble can also be beneficial for an increased coupling to the light field of a laser beam.

(ii) **Mechanical oscillator**. In order to prepare a mechanical oscillator in the quantum regime, one specific mode of the oscillator must be isolated very well from the environment. That is, the coupling Γ_m of the mode to its supporting mechanical structure should be as small as possible and the mechanical noise (thermal or technical) in this supporting structure should be minimized. This can be achieved by large mechanical Q-factors $Q \sim 1/\Gamma_\mathrm{m}$ and a cryogenic environment with low technical noise (mechanical vibrations). Furthermore, the frequency ω_m of this mechanical mode should match an atomic frequency ω_a (internal or external) for resonant coupling of the hybrid system.

(iii) **Optical interface**. Placing the mechanical oscillator in a cavity enhances the optomechanical cooperativity C_m. For a maximal hybrid cooperativity C_hybrid, this cavity should have a large optical incoupling and large reflectivity on resonance, in order to minimize light losses in a bi-directional hybrid coupling scheme. Regarding the specific kind of coupling scheme, the coupling light beam should also be suitable in terms of wavelength, optical power and beam shape.

Cold atom apparatus. Regarding the considerations of item (i) we decided to implement a ^{87}Rb BEC machine in a 2D/3D MOT configuration [81], which can produce large samples of $N_\mathrm{MOT} \approx 1 \times 10^{10}$ cold atoms or $N_\mathrm{BEC} \approx 2 \times 10^6$ ultra-cold atoms in a robust manner. Furthermore, the modular configuration enables excellent optical access to the 3D MOT chamber. The setup is equipped with an optical crossed dipole trap for storing the atoms independently of the internal states. By changing the beam parameters, this enables the elongation of the atomic sample in order to increase the optical coupling along this dimension. Details on the cold atom apparatus will be described in section 2.2.

Mechanical oscillator. The mechanical oscillator which was used for the experiments presented in this thesis is a high-stress silicon nitride (Si_3N_4) square membrane from *Norcada*. The membrane is a thin film with a thickness of $d = 50\,\mathrm{nm}$, an area of $1.5\,\mathrm{mm} \times 1.5\,\mathrm{mm}$, whose fundamental mode has a large mechanical Q-factor of $Q \approx$

1×10^7 at low temperatures. High-stress Si_3N_4 membranes combine a very low optical absorption ($\mathrm{Im}(n) \lesssim 2 \times 10^{-5}$ at 780 nm [82]) with exceptionally high Q-factors which are among the largest in optomechanical devices [64, 73, 74, 83]. The Q-factor is so large due to the high stress of the membrane [73, 83], which minimizes the bending losses at the supporting frame. Regarding item (ii), Si_3N_4 membranes are also suitable for hybrid experiments with atoms, because their low fundamental mode frequencies of $f_\mathrm{m} \approx 300\,\mathrm{kHz}$ can be matched with external atomic trapping frequencies ω_a and Zeeman-splittings of the internal hyperfine states. A purely technical advantage of the low frequencies are the relaxed requirements on detection and processing of the measured signals from the oscillator.

As considered in item (ii), we use a customized ^{3}He/^{4}He dilution refrigerator from *Oxford Instruments* with a minimum base temperature of 30 mK in order to achieve the best cryogenic cooling of the mechanical oscillator. Dilution refrigerators have the advantage of large cooling powers at low temperatures, which is prevents heating of the cryogenic chamber due to the optical coupling beam of the hybrid system. Our cryostat has a cooling power of 560 µW at 100 mK. The cryogenic chamber is also UHV compatible in order to allow for coupling ultra-cold atoms directly to the mechanical oscillator in possible future experiments. Technical details on the cryogenic optomechanical system will be discussed in section 2.3. In order to minimize mechanical vibrations (technical noise), external pumps were placed in a neighboring room. Details on the laboratory infrastructure will be presented in section 2.1.

Optical interface. A beneficial way of interfacing micromechanical membranes is the so called $membrane - in - the - middle$ (MiM) configuration [65, 84], where the membrane is embedded in a Fabry-Pérot cavity. A MiM configuration enables a large optomechanical coupling, even though the reflectivity of Si_3N_4 membranes is typically rather low. A large on-resonance reflectivity of the cavity, as considered in item (iii), can be achieved by an asymmetric cavity with different mirror reflectivities. In order to minimize the mentioned light losses, the asymmetric cavity of our MiM device is a planar-concave fiber cavity [66], which enables perfect in-coupling mode match from the planar side [67]. As already mentioned in chapter 1, the fiber-based MiM device has also the huge advantage of being suitable for cryogenic operation (the thin fibers can be guided through tiny holes into the fully shielded cryogenic chamber). Since asymmetric fiber cavities require sub-micron alignment precision of the fibers with respect to each other [67], the cryogenic operation is problematic due to the thermal expansion of the used materials. Therefore, our fiber MiM device has piezo-driven alignment stages with five degrees of freedom for each fiber. The cryogenic MiM device as well as an alignment procedure at cryogenic temperatures is presented in section 2.3.

In our first hybrid coupling experiments, we couple the mechanical oscillator to the motion of the atoms in an optical lattice. Regarding the considerations in item (iii), the coupling lattice beam was optimized for the specific demands of the hybrid system. The atomic trapping frequency ω_a in the lattice has to match the oscillator frequency $\omega_\mathrm{m} \approx 300\,\mathrm{kHz}$. In order to achieve such a large ω_a with small laser powers on the order of $P_\mathrm{lat} \approx 1\,\mathrm{mW}$ (to prevent heating of the cryogenic MiM device), we employ a lattice beam which is very near-detuned (between 50 Mhz and 5000 Mhz) with respect to the atomic transition. Furthermore, the lattice beam waist at the position of the atoms has a small waist of $w_\mathrm{lat} = 78\,\mu\mathrm{m}$, which allows for large intensities and large

trapping frequencies at a small laser power. The setup of the coupling laser system, as well as lattice alignment methods and characterization measurements will be presented in section 2.4.

2.1 Laboratory infrastructure

The complexity of the hybrid experiment requires special arrangements for the different parts of the setup. Important parameters are spacial distances, temperature stability, air purity, mechanical vibrations and scientific convenience.
The laboratory is is divided into three rooms. The upper room contains the experimental control and the laser systems. This allows researchers the direct access to all parts of the experiments that need constant maintenance (lasers, phase locks, the cryostat, electrical drivers, experimental control, data acquisition etc.) without disturbing the experiments in the lower room, where the hybrid system is located. A third, separated room houses all noisy equipment like pumps for the cryostat or the water cooling of the cold atom apparatus. All pumps are mounted on rubber feet and soft bellows are used along all tube connections in order to reduce transmission of vibrations to the cryostat.

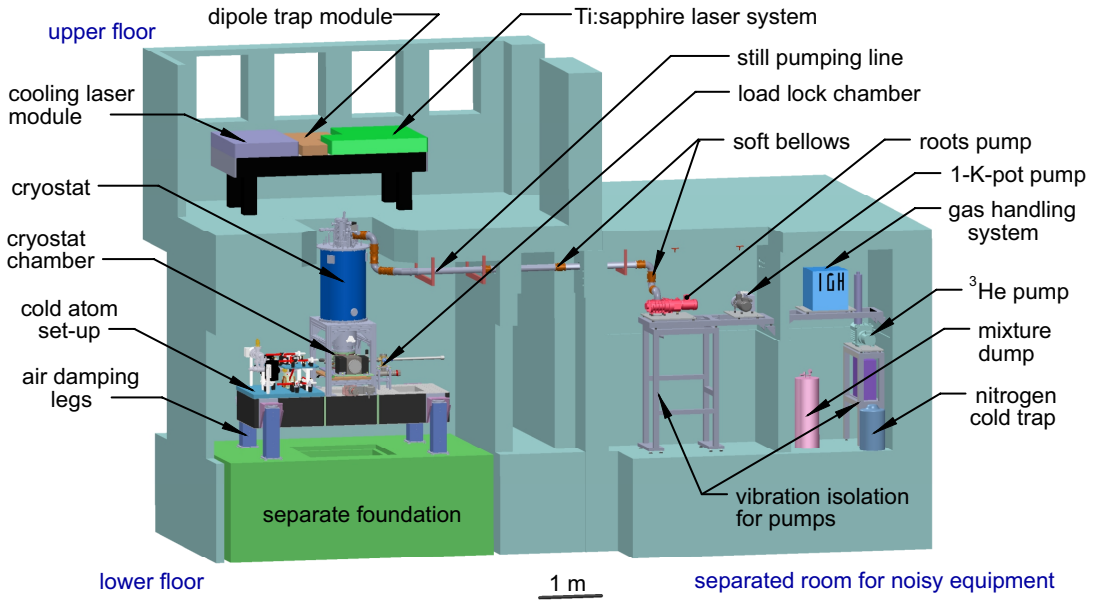

Figure 2.1: Sketch of the laboratory infrastructure. Overview of the laboratory with the experimental setup designed to realize an atomic-mechanical hybrid quantum system. The UHV dilution cryostat with the all-fiber MiM cavity inside (section 2.3), the cold atom apparatus (section 2.2) and the homodyne detection (section 3.3) are placed on an optical table in the lower floor, which stands on a separate foundation. The coupling and homodyne detection laser system (section 2.4), as well as the feedback cooling laser system (section 4.3) are assembled on a second optical table that is located in the upper floor, together with the experimental control and data acquisition. All mechanical pumps used to run the cryostat and the magnetic traps of the cold atom apparatus, as well as the gas handling system, the ^{3}He/^{4}He-mixture dump and the nitrogen cold trap of the cryostat are kept in a separate side room. Further details on the experimental setup were published in [85], where this figure was taken from.

The separation of the experiment into two rooms requires a well-conceived organisation of electrical and optical connections between these rooms. A large cable loom with patch fields in both rooms enables quick installations and changes of electrical connections, without the need of installing new cables trough the ceiling. Since the laser systems are located in the upper room, all laser beams are guided into the lower room by optical fibers which are shorter than 10m (high power transmission of $P \approx 10\,\mathrm{W}$ is possible). Both rooms have the same climate control which is regulated by an external temperature sensor, placed in the upper room.
In order to minimize the distance between the cryostat and the the cold atom apparatus, both systems were placed on the same optical table in the lower floor to minimize the optical phase noise in the coupling laser beam. A small phase noise is also beneficial for the homodyne detection of the mechanical oscillator, which is why the detector was also placed on the same table. This table is supported by air damping legs and for even better vibration isolation the table rests on a separate foundation. Above the area with the optical components, a temperature controlled flow box is installed. A hole in the ceiling provides access to the upper room from where the cryostat is supplied with liquid nitrogen and liquid helium.

2.2 The cold atom apparatus

The ^{87}Rb BEC machine was planned and set up by A. Bick and C. Staarmann and a detailed description can be found in their PhD theses [86, 87]. This sections outlines the key features of the machine.

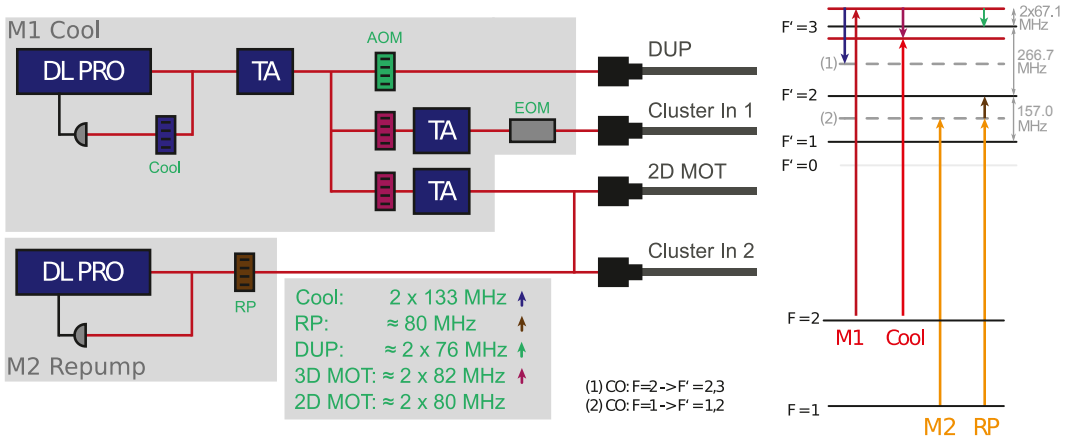

Figure 2.2: Sketch of the laser system for cooling and detection of ^{87}Rb. The laser system consists of two master lasers (DL Pro from *Toptica*), one cooling laser and a repumping laser. Both are locked by doppler free absorption spectroscopy to crossover transitions (dashed lines on the right). The cooling laser M1 seeds a tapered amplifier (TA), whose output beam is split for the detection, optical pumping and pushing light (DUP), and for the 3D MOT (Cluster Input 1) and 2D MOT. The 3D MOT can be switched on and off with a fast EOM. The repumping laser M2 is split and overlapped with the 2D MOT cooling beam and also coupled into a separate fiber for the 3D MOT (Cluster Input 2). The DUP fiber is depicted exemplary, even though in the experiment the three DUP beams are coupled into three individual fibers. Figure adapted from [86].

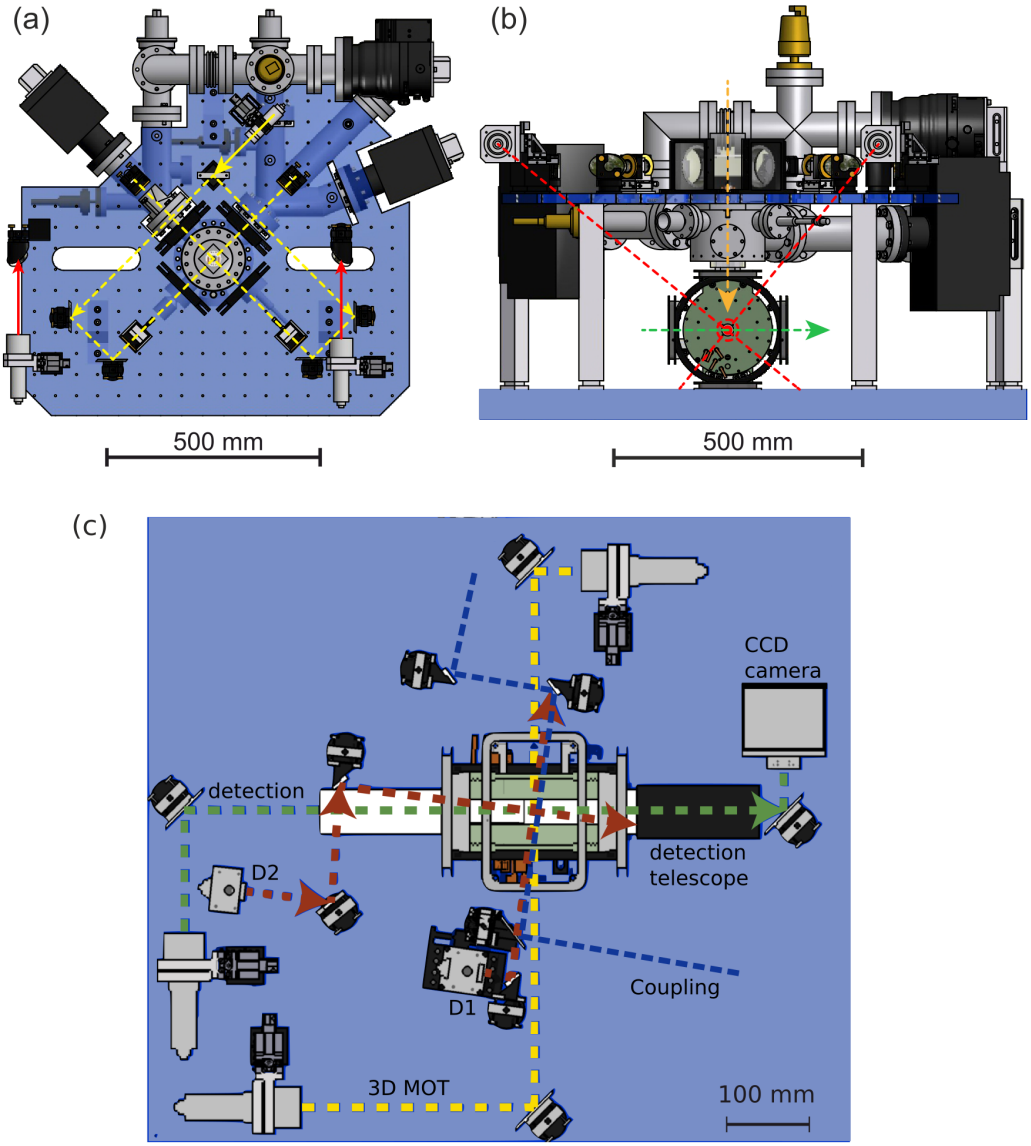

Figure 2.3: Drawing of the experimental apparatus to produce a ^{87}Rb BEC. (a) Top view showing upper breadboard and 2D-MOT setup. Shown are the beam paths for the 2D-MOT (yellow) and the 3D-MOT (red). The 2D-MOT beam is split using a polarizing beam splitter and expanded employing a cylindrical telescope to form elliptic beams as required for the 2D-MOT. **(b)** Side view showing upper and lower glass cell and the magnetic trap (green housing) in the magnetic field compensation coil cube. Two 3D-MOT telescopes are located on the upper breadboard. The corresponding beams (red) are reflected through elliptical holes in the breadboard onto the lower glass cell. Both beams are rotated by 8° with respect to the 45° axes which is reserved for a retro-reflected 2D lattice (not shown here). The pushing beam (orange) passes vertically through the differential pumping tube in the center of the vacuum chamber and transfers the atoms from the 2D-MOT into the 3D-MOT. Also shown is the detection beam (green). **(c)** Top view on the lower (3D MOT) breadboard showing the counter-propagating 3D MOT beams (yellow), the two perpendicular dipole trap beams D1 and D2 (red), the detection beam (green) and the coupling beam (blue). The glass cell is located in the center, where all beams cross each other. The D1 telescope is mounted on a translation stage in order to adjust the focus with respect to the atoms. Figure adapted from [86] and [87].

Rubidium is an ideal candidate for a reliable source of ultra-cold atoms, since it can be efficiently laser-cooled and the atomic transitions can be driven with standard commercial laser technology. The D2 line $|5^2S_{1/2}, F' = 2\rangle \rightarrow |5^2P_{3/2}, F' = 3\rangle$ serves as the cooling transition. Since this transition does not form a closed cycle, an additional repumping laser is used. The laser system is shown in Figure 2.2.

2D/3D MOT setup. The laser light is prepared in the upper part of the laboratory and propagates via optical fibers to the BEC system in the lower room, which is placed next to the cryostat on the same optical table. The setup is based on a scheme with two separated glass cells, as depicted in Figure 2.3. In the upper cell a two-dimensional magneto-optical trap (2D-MOT) catches atoms from a background gas and in the lower cell a 3D-MOT operates at pressures below 1×10^{-11} mbar. These two different vacuum glass cells are connected via a differential pumping stage, allowing for pressures that can differ by a factor of 10^3. The atoms are transferred from the upper to the lower glass cell by gravity or a near-resonant pushing beam. The advantage of this two-cell setup is the extremely good optical access to the lower 3D-MOT glass cell, which allows for different manipulation, coupling and detection schemes of the cold atoms.

Sequence for a BEC in the magnetic trap. A typical experimental sequence is depicted in Figure 2.4. We start by loading the 3D MOT for less than 10 s resulting in atom numbers of $N_{\mathrm{MOT}} \approx 1 \times 10^{10}$ at temperatures of $T \approx T_{\mathrm{D}}$, where $T_{\mathrm{D}} = 146\,\mu\mathrm{K}$ is the Doppler temperature of ^{87}Rb. Subsequently, the atoms can be further cooled in an optical molasses reducing the temperature to $T_{\mathrm{mol}} \approx 10\,\mu\mathrm{K}$, which is multiple times larger than the ^{87}Rb recoil temperature of $T_{\mathrm{rec}} \approx 362\,\mathrm{nK}$. In order to generate a BEC, we load our atoms in a magnetic trap (a hybrid cloverleaf 4D trap) and use forced evaporation cooling for less than 20 s. This magnetic trap loading is optimized by an optical pumping pulse in the molasses phase, which transfers the atoms into m_{F} states that can be captured by the magnetic trap. The BECs have a particle number of $N_{\mathrm{BEC}} \approx 2 \times 10^6$ without any discernible amount of thermal atoms.

Crossed dipole trap setup. For experiments aiming at coupling internal atomic degrees of freedom to the mechanical oscillator, it is necessary to trap the atoms in a potential that is independent of the particular internal state to avoid fast dephasing

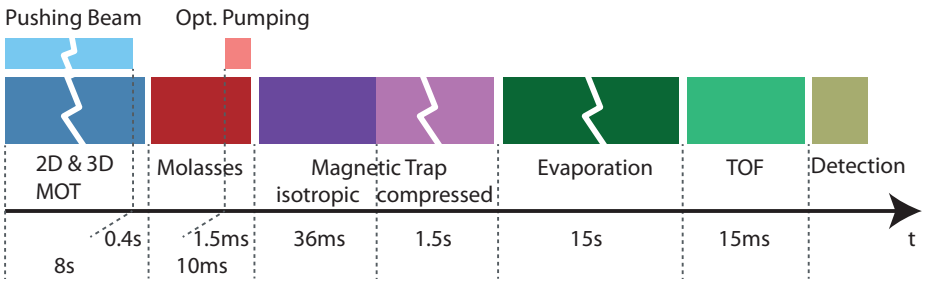

Figure 2.4: Experimental sequence for creating a ^{87}Rb BEC in the magnetic trap. The 3D MOT is loaded by a resonant pushing beam which transfers the atoms through the differential pumping stage (see Figure 2.3). After the molasses phase for Sub-Doppler cooling, the atoms are loaded into the isotropic magnetic trap which is subsequently compressed. This transfer is enhanced by an optical pumping pulse. The atoms are condensed into a BEC via radiofrequency evaporation and then released from the trap. Following a time-of-flight (TOF) phase, an absorption image is taken. The sequence takes less than 30 s. Figure taken from [87].

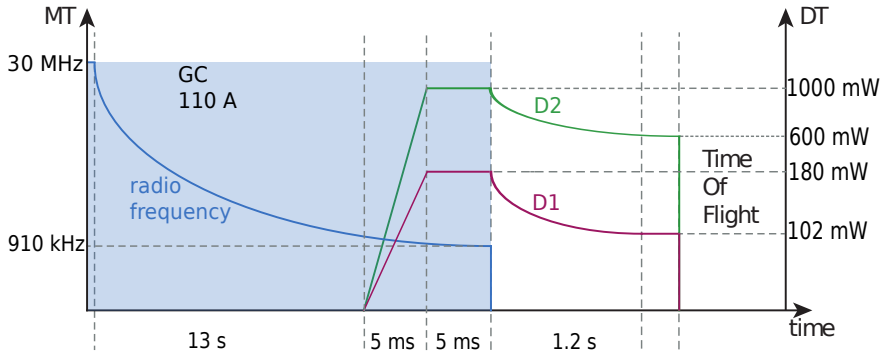

Figure 2.5: Experimental sequence for creating a ^{87}Rb BEC in the dipole trap. Initially, cold atoms are radio frequency evaporated in the magnetic trap (MT), depicted by the blue shaded area (see Figure 2.4). The final frequency of 910 kHz is slightly larger than the typical value for creating a BEC in the MT (typically 850 kHz). Shortly before switching off the gradient coils (GC) of the MT, the dipole trap (DT) beams D1 and D2 are ramped up to a power of $P_{\mathrm{D1}} = 180\,\mathrm{mW}$, $P_{\mathrm{D2}} = 1\,\mathrm{W}$. After the MT and the radio frequency are switched off, the power of the DT beams is ramped down exponentially, which causes a final evaporation in the DT. After the evaporation, the BEC can be held in the DT with a lifetime of $\tau_{1/\mathrm{e}} \approx 10\,\mathrm{s}$. After switching off the DT via the AOMs, the BEC is in freefall (time-of-flight) and can be detected via absorption imaging. This sequence was optimized for maximum particle number and optimal particle number stability in the DT BEC. Figure adapted from [87].

and to be able to trap all atomic hyperfine states. This is guaranteed by using a far detuned optical dipole potential. A dipole trap is also helpful for pure BEC experiments and characterization measurements like the calibration of the coupling lattice presented in section 2.4.2. For these purposes, our setup is equipped with a crossed optical dipole trap derived from a Nd:YAG laser operated at 1064 nm with circular beam waists of $w_{\mathrm{D1}} = 52\,\mu\mathrm{m}$ and $w_{\mathrm{D2}} = 242\,\mu\mathrm{m}$. The maximum available optical power at the experiment is 8 W per beam. A detailed description of the dipole trap setup and characterization measurements can be found in the PhD thesis of C. Staarmann [87].

Sequence for a BEC in the dipole trap. The experimental sequence for creating a BEC in the dipole trap starts with a normal BEC sequence in the magnetic trap (see Figure 2.4). During the evaporation phase in the magnetic trap, the BEC is loaded into the dipole trap, followed by a final evaporation phase where the atoms are trapped only by the dipole trap. Figure 2.5 shows the experimental sequence for creating a BEC in the dipole trap, which was optimized in terms of absolute value and stability of the particle number. The BECs have a particle number of $N_{\mathrm{BEC,DT}} \approx 4 \times 10^5$ without any discernible amount of thermal atoms.

Dipole trap frequencies. The BEC inside this dipole trap has an elongated cigar like shape and radial trapping frequencies $(\omega_y, \omega_z) = 2\pi \times (144, 105)\,\mathrm{Hz}$, where gravity points along the z-direction (for $P_{\mathrm{D1}} = 100\,\mathrm{mW}$, $P_{\mathrm{D2}} = 1\,\mathrm{W}$). The beam with the larger waist w_{D2} can be used to tune ω_x between $2\pi \times (1 \ldots 20)\,\mathrm{Hz}$ ($\omega_x \approx 12\,\mathrm{Hz}$ for $P_{\mathrm{D1}} = 90\,\mathrm{mW}$, $P_{\mathrm{D2}} = 1\,\mathrm{W}$). In this way, we can vary the elongation of the atomic cloud along the x-direction of the coupling beam in hybrid experiments. A BEC held in the crossed dipole trap has a lifetime of $\tau_{1/\mathrm{e}} \approx 10\,\mathrm{s}$.

Absorption imaging. In order to detect the properties of the cold atoms samples, a flexible absorption imaging system is used, which allows for different magnifications

ranging from 0.5 to 10 (telescope NA = 0.15, resolution ≈ 3 µm, focal length f = 137 mm, [86]). The detection beam used for imaging points in a direction perpendicular to the coupling beam, as depicted in Figure 2.3.

2.3 The cryogenic optomechanical device

The cryogenic membrane-in-the-middle (MiM) device is the central component of the optomechanical part of our experiment. The MiM cavity is an asymmetric fiber cavity with different reflectivities of the dielectric coatings at the fiber ends, respectively. Both fibers can be adjusted with five degrees of freedom for the alignment of the MiM system under cryogenic conditions. This is necessary, since asymmetric fiber cavities require an xy-alignment precision better than 200 nm [67] (see subsection 2.3.2), which can not be assured if the MiM structure is cooled down from room temperature. Furthermore, the full alignment control allows for exchanging the mechanical oscillator in the cavity, even without breaking the vacuum and also under cryogenic conditions.
This section deals with the design and the alignment of the MiM setup. Firstly, the structure of the MiM setup will be presented in subsection 2.3.1. Afterwards, subsection 2.3.2 gives a brief overview on the production and the properties of the asymmetric fiber cavities. Finally, the installation of the fiber cavity into the MiM structure and the alignment of the fiber cavity in the MiM configuration using a special white-light method will be presented in subsection 2.3.3.
The following people contributed to the experimental realization of the MiM setup: the fiber cavity was built by the author together with A. Bick, C. Staarmann and O.

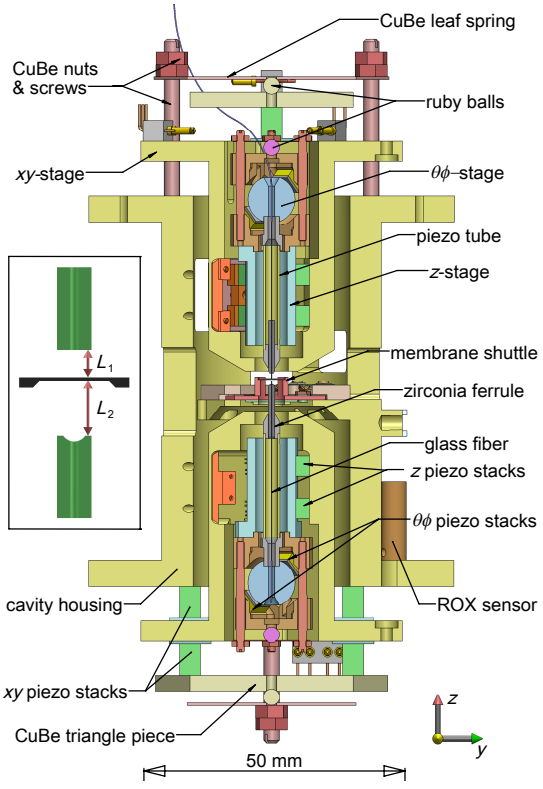

Figure 2.6: Section view of the MiM cavity setup. The inset on the left side of the figure is a sketch of the fiber cavity in the center of the MiM structure. The cavity housing encloses two identical piezo-driven positioning stages with a z-, xy-, and $\theta\phi$-stepper motor, which provide five degrees of freedom for each fiber. The membrane holder (see Figure 2.7) is located between them. Both fibers are glued into a piezo tube to fine-adjust their z-positions and to scan the cavity length L as well as the fiber-membrane spacings L_1 and L_1 (see inset). Details on the alignment can be found in subsection 2.3.3. The MiM cavity temperature T_{MiM} is measured with a ROX sensor as well as with a Cernox sensor. Both are attached next to each other to the cavity housing. A detailed description of the MiM setup and its implementation in the cryostat was published in [85], where this figure was taken from.

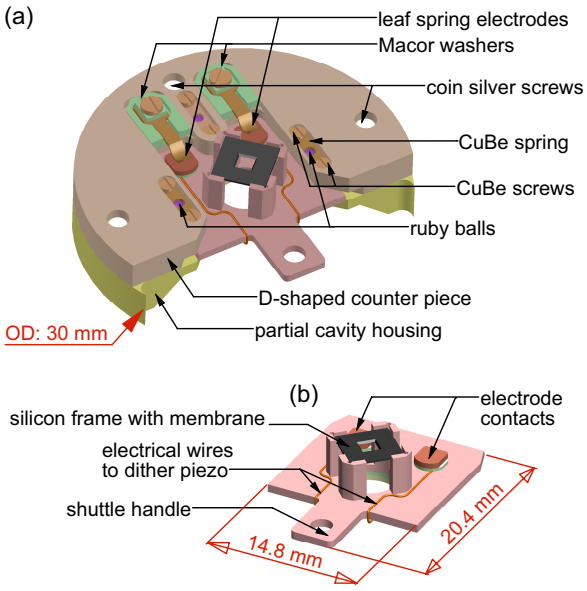

Figure 2.7: Membrane holder in the MiM device. The cavity housing of the MiM device (see Figure 2.6) has a slide-in slot **(a)** for an exchangeable shuttle **(b)** which carries the membrane. The experiments presented in this thesis were performed with is a high-stress Si_3N_4 square membrane from *Norcada* ($1.5\,\mathrm{mm} \times 1.5\,\mathrm{mm} \times 50\,\mathrm{nm}$, $\omega_m(0,0) = 2\pi \times 264\,\mathrm{kHz}$, $Q \approx 1 \times 10^7$ at $T_{\mathrm{MiM}} = 500\,\mathrm{mK}$). The membrane was glued to the shuttle with with *Torr Seal* epoxy. Electrical spring contacts allow for driving a dither piezo element underneath the shuttle. The shuttle can be inserted from outside the cryostat using a wobble stick. Details can be found in [85], where this figure was taken from.

Hellmig. The MiM structure was built by G. Fläschner and H. Zhong, who installed it into the cryostat together with the author. The interferometric white-light method for the alignment of the fiber cavity was developed and performed by the author.

2.3.1 MiM setup

Our all-fiber MiM cavity device (see Figure 2.6) is directly connected to the ^{3}He/^{4}He mixing chamber of the dilution refrigerator. It is made of gold-plated copper and has an outer diameter of 70 mm and a height of 135 mm. The two cavity fibers enter the UHV system via Swagelock fiber feedthroughs on the bottom of the UHV-cryostat chamber. They are guided through tiny holes in the cryogenic radiation shields to the MiM device. Further details on the cryogenic implementation of the MiM structure and all parts of the MiM device can be found in [85].

In the center of the MiM device, the two cavity fibers are glued into zirconia ferrules (see Figure 2.6). Each ferrule is glued into the free end of a piezo tube, which is used for fine-adjustments of the cavity length L in z-direction (tune the cavity resonance or fast scanning). This also changes the respective fiber-membrane spacing L_1 or L_2 (see inset of Figure 2.6). L_1 and L_2 can be scanned with the piezo tubes over approximately one free spectral range (FSR) $\Delta L \approx 1\,\mathrm{FSR} \approx 500\,\mathrm{nm}$ using high voltage. Basically all the rest of the MiM structure is used for the alignment of the fiber cavity with five degrees of freedom (x,y,z,θ and ϕ), which is described in subsection 2.3.3. For this purpose, piezo-driven slip-stick stepper motors [88] are used, which a translational and angular accuracy better than 1 nm and better than 0.1°, respectively. More details on the construction of the slip-stick positioning stages (design, electrical control, step size, calibration, etc.) was published in [89].

The MiM device is structured as follows: the supporting structure is the cavity housing, which is a copper tube (tube axis in z-direction) that can be mounted directly on the thermal link to the ^{3}He/^{4}He mixing chamber. The cavity housing has rectangular windows, in order to observe the fiber cavity using microscope cameras from outside

of the cryostat (for this, the radiation shields can be rotated [85]). Inside the cavity housing, the two xy-stages for the two fibers are located. They enable a transversal (xy) movement of the fibers in the cavity housing using slip-stick stepper piezos. Inside each xy-stage, a z-stage is installed, which allows for a z-movement of each fiber on the order of several millimeters. Each z-stage contains a rotatable $\theta\phi$-stage, based on a sapphire ball which is surrounded by piezos [89]. A slide-in slot in the center of the MiM structure allows for inserting a shuttle with a membrane oscillator, as shown in Figure 2.7. This can be done from outside of the cryostat using a wobble stick to transfer the shuttle from a separated load lock chamber to the shuttle slot in the MiM device [85]. In this way, different oscillators can be installed into the MiM device without breaking the vacuum and under cryogenic conditions. It should be noted that after inserting a membrane shuttle, the membrane position is fixed. Further alignment of the MiM cavity is done by moving the fibers with respect to the membrane. The membrane shuttle also has a piezo element attached to it. This can be used for resonant driving of the membrane or as a mechanical actuator for feedback cooling (see chapter 4).

2.3.2 Asymmetric fiber cavities

This subsection outlines the principles and the production of the asymmetric fiber cavities used in our experiment. We produce our cavities in-house using CO_2-laser ablation. Further details on the topic can be found in the Master's theses of the author [90] and J. Petermann [91], as well as in the PhD theses of A. Bick [86] and C. Staarmann [87]. These results were also published in [67].

The use of fiber cavities [66] for our cavity optomechanical system has several advantages: bending of the glass fibers allows flexible modifications of the MiM system or its surrounding cryogenic setup, without the need of adapting the optical coupling into the cryostat. Furthermore, no additional mode matching optics are needed in front of the cavity. The use of optical fibers also allows for perfect shielding the MiM setup with cryogenic radiation shields, without special coated windows in the shields to couple light into the cryostat. Fiber cavities have very small mode volume, which enables large optomechanical coupling to small mechanical devices like trampoline oscillators [73, 74], cantilevers or nano beams [7]. They are also typically very short ($L < 1\,\mathrm{mm}$), which results in a very large optomechanical coupling strength $g_\mathrm{m} = \partial\omega_\mathrm{cav}/\partial x_\mathrm{m} \sim 1/L_\mathrm{cav}$. This can be useful for reaching the so called *strong optomechanical coupling regime* in certain applications (for example a single atom in a cavity [66]).

Ideal fiber cavities. In order to enable a bi-directional light coupling in a hybrid quantum system, the cavity needs to be single-sided, which means that it has a finite reflectivity on resonance. This can be achieved by an asymmetric cavity with different reflectivities R_1 and R_2 of the two cavity mirrors. The combination of R_1 and R_2 can also be used to optimize the finesse $\mathcal{F}$ of the cavity for the specific application. To reduce light losses, the coupling efficiency into the cavity should be optimal, which requires a perfect mode match β between the optical mode in the fiber and the cavity mode on the incoupling mirror. This can be realized by using a planar-concave cavity, which has a planar mirror on the incoupling fiber.

Fiber cavities in practice. The practical realization of asymmetric fiber cavities is more complex than the simple considerations mentioned above may suggest. This is

because the fibers act as a mode filter for the reflected and transmitted light from the cavity. For this reason, the relative power σ_{ref} that gets reflected back into the incoupling fiber depends strongly and in a non-trivial manner on the mode match β [67]. Therefore, the concave cavity mirror needs to have an optimal radius of curvature around 50 µm and the fiber cavity needs to be aligned very precisely.

Production of fiber cavities. In order to meet the highly demanding requirements on the fiber cavity geometry, we produce our fiber cavities in-house using CO_2-laser ablation and an interferometric surface analysis of the machined concave fiber tips. The dielectric mirror coatings of the fibers were deposited with an in-house coating machine.

Ideal fiber cavities ($\beta = 1$)

The two most important properties of the fiber cavities for our experiment are the (relative) reflected power on resonance $\sigma_{\text{ref}} \in [0, 1]$ and the finesse $\mathcal{F}$. The finesse is defined by the total losses of the cavity: $\mathcal{F} = 2\pi/\mathcal{L}_{\text{tot}}$. If the only relevant loss mechanism is the light leakage through the cavity mirrors, the finesse only depends on the mirror (power) reflectivities R_1 and R_2:

$$\mathcal{F} = \frac{\pi (R_1 R_2)^{\frac{1}{4}}}{1 - \sqrt{R_1 R_2}}. \tag{2.1}$$

It is useful to introduce the (field) reflectivity on resonance $\bar{\rho}$ with $\bar{\rho}^2 = \rho$ [86]:

$$\bar{\rho} = \frac{\sqrt{R_1} - \sqrt{R_2}}{1 - \sqrt{R_1 R_2}}, \quad \bar{\rho} \in [-1, 1]. \tag{2.2}$$

If both mirrors have the same reflectivity, all light gets transmitted through the cavity and $\bar{\rho}$ is zero. If the cavity is asymmetric ($R_1 \neq R_2$), some of the light gets reflected by the resonant cavity. The fact that $\bar{\rho}$ is not symmetric in R_1 and R_2 gets important

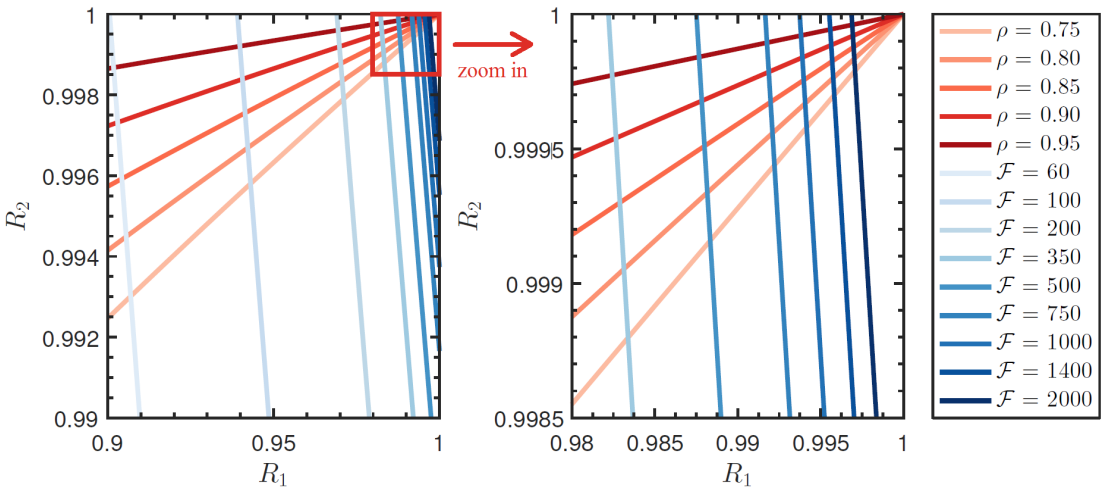

Figure 2.8: Combinations of cavity mirror reflectivities. Left panel: the plot shows lines of constant (power) reflectivity on resonance ρ (red) and constant finesse $\mathcal{F}$ (blue) in the parameter space spanned by R_1 and R_2. Right panel: zoom into the plot in the left panel into the high finesse region of large reflectivities.

for an imperfect mode match $\beta \neq 1$, which will be discussed in the following paragraph on practical realizations. However, for an ideal fiber mode match $\beta = 1$, the reflected power σ_{ref} (measured at the open end of the incoupling fiber) is equal to the reflected power ρ from the cavity.
By choosing a combination of R_1 and R_2, the cavity parameters ρ and $\mathcal{F}$ can be optimized for a specific application. For the hybrid experiment, a large reflectivity on resonance is beneficial. However, if $\rho \approx 1$, no light is transmitted through the cavity. Since the transmitted light is useful for many practical tasks (monitoring of cavity signals, etc.), the optimal ρ is around 0.85. The cavity reflection signal with a visible dip (for $\rho < 1$) is also useful for the alignment of the fiber cavity (see section 2.3.3). A large finesse is beneficial for the detection noise floor of the homodyning (see section 3.3) and for the cooperativity C_{hybrid} of the hybrid system. However, if the finesse is too large, the intra-cavity power gets so large that thermal heating becomes the dominant decoherence mechanism [31]. Hence, the reflectivities R_1 and R_2 of the fiber cavity must be carefully

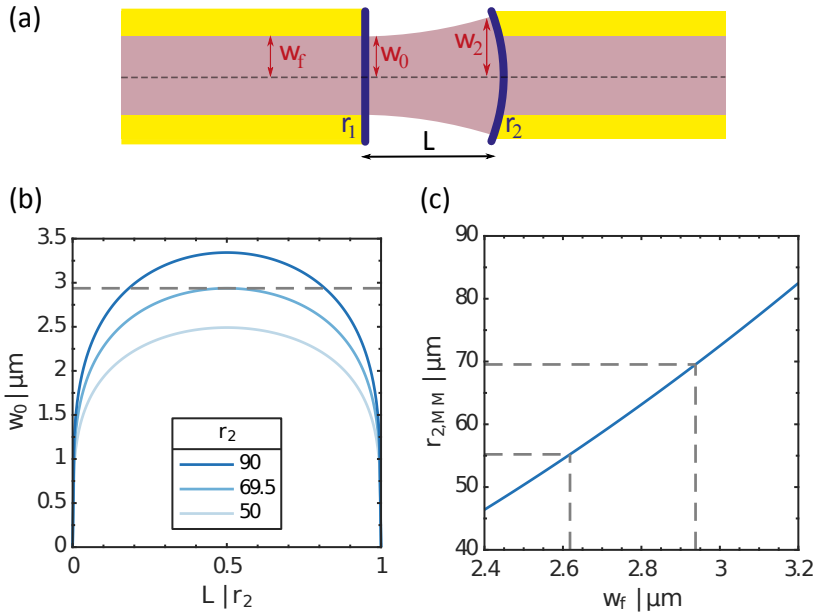

Figure 2.9: Mode match in planar-concave fiber cavities. (a) Sketch of a planar-concave fiber cavity (length L) with optimal mode match ($\beta = 1$, $w_0 = w_f$) on the planar side. The radius of curvature (ROC) of the cavity mirrors is denoted by r_1 and r_2. The waists w_{f}, w_0 and w_2 correspond to the fiber mode and the cavity mode on the mirrors, respectively. **(b)** Cavity waist on the planar mirror w_0 as a function of the cavity length L in units of r_2 for three different values of r_2 and $\lambda = 780\,\mathrm{nm}$ (see equation 2.3). The waist w_0 has a broad maximum at a cavity length of $L = 0.5\,r_2$. For an optimal ROC $r_{2,\mathrm{MM}}$ ($r_2 = 69.5\,\mu\mathrm{m}$ in this case), this maximum corresponds to the fiber waist w_{f} (indicated by the dashed line). For $r_2 < r_{2,\mathrm{MM}}$, perfect mode match is impossible. For $r_2 > r_{2,\mathrm{MM}}$, mode match is only possible at the two intersection points of w_0 and the dashed line. Note that the mode match on the curved side is always smaller than one, because even if $w_2 = w_{\mathrm{f}}$, the wave front curvature of the modes can not be matched [67]. **(c)** Optimal ROC $r_{2,\mathrm{MM}}$ as a function of the fiber waist w_{f}. The two dashed lines correspond to two different fibers that were used for the production of fiber cavities (HP780 from *Thorlabs* with measured $w_{\mathrm{f}} = 2.618(28)\,\mu\mathrm{m}$ and the Cu800 copper coated fiber with $w_{\mathrm{f}} = 2.938(17)\,\mu\mathrm{m}$ [91]). Figure (b,c) taken from [91].

balanced for an optimal performance and feasibility of the specific experiment. In order to visualize the dependency of ρ and $\mathcal{F}$ on the reflectivities, equations 2.1 and 2.2 were solved for R_1, as shown in Figure 2.8. This allows for plotting a specific ρ or $\mathcal{F}$ as a line in the parameter space spanned by R_1 and R_2. The combination of R_1 and R_2 for a given set of ρ and $\mathcal{F}$ can be read off at the intersection point of the two corresponding lines.

By choosing a planar-concave cavity geometry, at least the planar fiber can have a perfect mode match β with the cavity mode, as depicted in Figure 2.9 (a). In the experiment, the most critical beams can be coupled in from the mode matched planar side. Optimal mode match $\beta = 1$ is achieved if the cavity waist w_0 on the planar side is equal to the fiber mode waist w_f. In a planar-concave cavity the radius of curvature (ROC) of the planar mirror is $r_1 = \infty$ and the cavity waist w_0 only depends on the ROC on the curved side and the cavity length L [92]:

$$w_0(r_2, L) \;=\; \sqrt{\frac{r_2\lambda}{\pi}}\left(\frac{L}{r_2}\left(1-\frac{L}{r_2}\right)\right)^{\frac{1}{4}}. \tag{2.3}$$

This function has a broad maximum at $L = 0.5\,r_2$, as shown in Figure 2.9 (b). One can speak of *stable mode match* if (A) the cavity mode waist w_0 on the planar side can be matched with the fiber mode w_f and (B) this mode match does not depend on the cavity length L in a critical manner. This is only possible with the optimal ROC $r_{2,\mathrm{MM}}$ of the curved mirror, which depends on the specific fiber mode waist w_f. Solving the equation $w_0(r_2, L = 0.5\,r_2) = w_f$ for r_2 yields the optimal ROC $r_{2,\mathrm{MM}} = w_\mathrm{f}^2 \cdot 2\pi/\lambda$. The dependency of $r_{2,\mathrm{MM}}$ on the fiber waist w_f is shown in Figures 2.9 (b).

Fiber cavities in practice

In the previous paragraph, the reflectivity on resonance ρ was introduced as a key parameter for an asymmetric fiber cavity. However, for an imperfect mode match $\beta < 1$ the reflected intra-cavity power ρ can vary drastically from the observed reflected power σ_ref at the open end of the incoupling fiber. This effect is not only governed by light losses but also by a parasitic interference effect, which can fully cancel out the reflected power σ_ref. In practice, many technical reasons lead to an imperfect mode match. For example, our laser machining technique (see end of this subsection) creates Gaussian mirror profiles instead of perfectly spherical mirrors. Hence, the cavity modes differ from the ideal case of spherical mirrors, which changes the mode match in a complex manner. The above considerations about ideal fiber cavities also neglect the critical dependency of the mode match on the alignment of the fiber cavity. This paragraph gives a brief overview on the role of mode match in asymmetric fiber cavities and its great importance for their performance. A comprehensive study of the topic was published in [67] and [93].

In order to understand the critical role of mode match in asymmetric fiber cavities, one needs to calculate the propagation of an input field ψ_in, which is coupled into the open end of one fiber from the fiber cavity. The normalized input field ψ_in can be decomposed into a part ψ_m that is mode matched with the cavity ground mode and into a non-mode-matched part ψ_n [67]:

$$\psi_{\mathrm{in}} \;=\; \bar{\beta}_{\mathrm{n}}\psi_{\mathrm{n}} \;+\; \bar{\beta}_{\mathrm{m}}\psi_{\mathrm{m}}\,, \tag{2.4}$$

using $\beta = |\bar{\beta}_{\mathrm{m}}|^2 = 1 - |\bar{\beta}_{\mathrm{n}}|^2$. When the input field approaches the cavity, the mode matched part ψ_{m} enters the cavity and gets reflected with the on-resonance field reflectivity $\bar{\rho}$. The reflected light interferes with the non-mode-matched part ψ_{n} that is reflected directly by the incoupling cavity mirror with the off-resonance reflectivity $\bar{\rho}_{\mathrm{off}} \approx 1$. This is a good assumption for a sufficiently high finesse [67]. The reflected field is therefore:

$$\psi_{\mathrm{ref}} \;=\; \bar{\beta}_{\mathrm{n}}\psi_{\mathrm{n}} \;+\; \bar{\rho}\bar{\beta}_{\mathrm{m}}\psi_{\mathrm{m}}\,. \tag{2.5}$$

The interference of these two reflected fields is depicted in Figure 2.10 (a). The crucial point which leads to the non-trivial behavior of asymmetric fibers cavities is directly related to the field ψ_{ref}. It arises from the fact that ψ_{ref} needs to be mode matched with the fiber mode. Yet, for $\beta \neq 1$ the reflected field ψ_{ref} can have a circular shape far

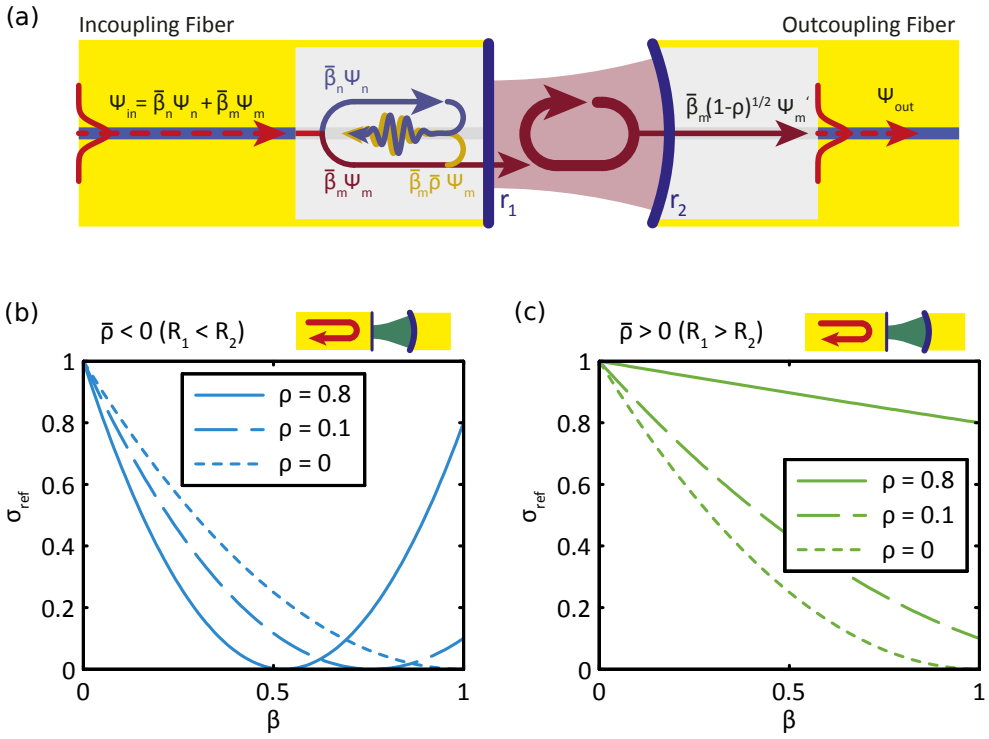

Figure 2.10: Interference effects in asymmetric fiber cavities. (a) The gray area indicates the virtual zone between the end of the fiber and the coating. The input field ψ_{in} is split into a mode-matched part ψ_{m} and a non-modematched part ψ_{n}. While the first enters the cavity and is subsequently reflected with the field reflectivity on resonance $\bar{\rho}$, the latter is non-resonant and gets directly reflected. These two fields interfere. The field transmitted through the cavity ψ'_{m} has to be matched with the mode of the outcoupling fiber ψ_{out}. **(b)** Reflected relative power σ_{ref} as a function of the mode match β for three different values of the reflectivity on resonance ρ, when coupling into the cavity from the lower reflecting side (see equation 2.6). For $\rho > 0$, the power σ_{ref} has a zero crossing for some specific mode match $\beta < 1$. **(c)** The same as (b) but for coupling into the higher reflecting side of the cavity. Figures taken from [67].

from Gaussian and a minimum in the region of the fiber core [67]. In this case, no light is coupled back into the incoupling fiber and the measured reflectivity on resonance σ_{ref} at the end of this fiber is zero, even though the reflectivity ρ of the cavity mirrors might be non-zero. For $\rho \approx 0.8$ this happens for a mode match $\beta \approx 0.5$, which can easily happen for imperfect cavity mirrors, the wrong cavity length of slight misalignment of the fiber cavity. The dependency of σ_{ref} on the mode match is shown in Figure 2.10 (b,c). The critical behavior of σ_{ref} only occurs if the light is coupled in from the lower reflecting side of the cavity. If the light is coupled into the higher reflecting side, σ_{ref} gets larger for decreasing β. However, also in this case the light has interacted less with the cavity than for $\beta = 1$. In most applications this is also not desirable.
The dependency of σ_{ref} can be directly calculated from the expressions ψ_{ref} and ψ_{in}:

$$\sigma_{\mathrm{ref}} \;=\; \int \psi_{\mathrm{ref}} \psi_{\mathrm{in}}^{*}\, \mathrm{d}A \;=\; |1 - \beta + \bar{\rho}\beta|^2 \,. \tag{2.6}$$

Since $\bar{\rho}$ can have a positive or negative sign depending on the incoupling side of the asymmetric cavity, σ_{ref} behaves differently for coupling into the higher or lower reflecting side.
Figure 2.10 shows the dependency of the reflected power σ_{ref} on the mode match. As mentioned before, the mode match itself depends on many other parameters like the cavity length L, the mirror shape or the cavity alignment. Therefore, σ_{ref} can also be plotted as a function of these parameters. Figure 2.11 shows the measurable reflected and transmitted power of the cavity as a function of the cavity length. Only for the optimal ROC $r_{2,\mathrm{MM}}$ the reflected signal σ_{ref} has a broad maximum. However, the plot also shows that the transmitted power σ_{trans} is not optimal for this ROC. Details on this calculation can be found in [67] and [86].

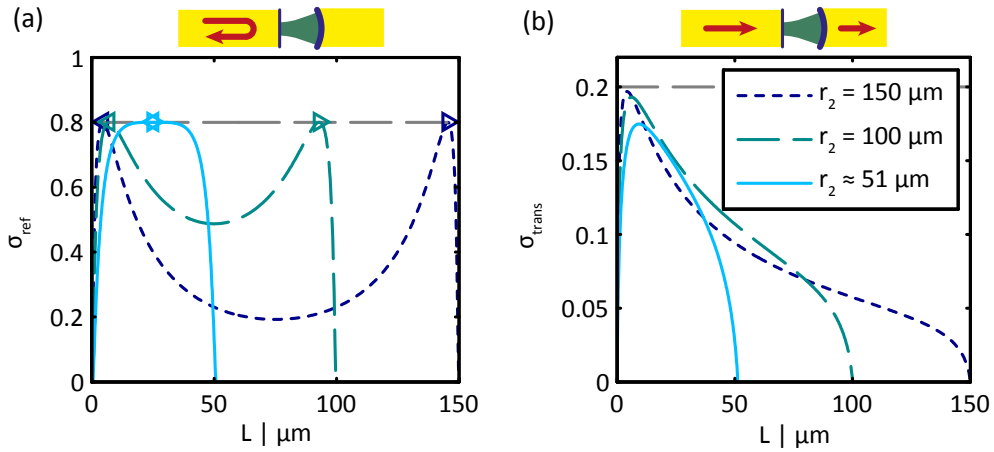

Figure 2.11: Cavity signals from asymmetric fiber cavities. (a) Reflected power σ_{ref} as a function of cavity length L for three different ROC r_2 of a planar-concave asymmetric fiber cavity. Simulation according to equation 2.6, for coupling into the lower reflecting, planar side. The dashed line indicates a maximum cavity reflectivity on resonance $\rho = 0.8$. The triangles indicate the points of perfect mode match β. In the case of stable mode match, these two points overlap. **(b)** Transmitted power σ_{trans} as a function of cavity length, calculated in a similar manner as (a). The dashed line is at the theroretical maximum of $\sigma_{\mathrm{trans}} = 0.2 = 1 - \rho$. The simulation assumes a fiber NA $= 0.12$ and $\lambda = 780\,\mathrm{nm}$. Figures taken from [67].

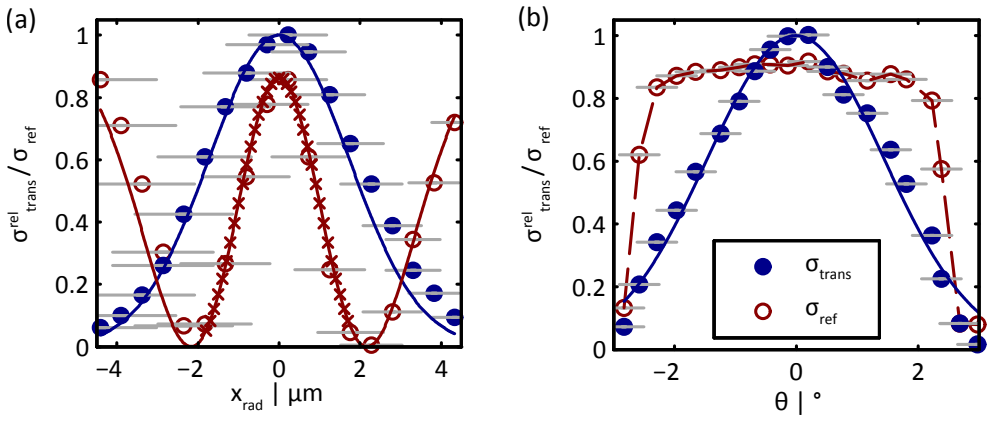

Figure 2.12: Alignment sensitivity of asymmetric fiber cavities. (a) Measured transmission and reflection signal from an asymmetric fiber cavity with $L = 25\,\mu m$ as a function radial (xy) displacement of the fibers. The error bars correspond to the error of the micrometer drive calibration. The solid lines are the expected behavior according to equation 2.6. The transmission data and model have been normalized. **(b)** Angular dependence of the transmission and reflection signal. The error bars correspond to the error of the angle determination using an optical microscope. The solid blue line is a Gaussian fit to the transmission signal. The transmission data and model have been normalized. The dashed red line is a guide to the eye. Figures taken from [67].

Using equation 2.6 one can also calculate the dependency of the cavity reflection signal σ_{ref} on the radial (xy) misalignment of the cavity fibers (and also in a similar manner the transmission signal σ_{trans} [67]). The behavior was also measured for an asymmetric fiber cavity with length $L = 25\,\mu m$ (not the one which was installed into the MiM device). For this, the cavity length was scanned around the resonance and the scan traces were acquired using an oscilloscope. In this way, the shape of the resonance (height of transmission peak σ_{trans} and reflection dip σ_{ref}) could be analyzed for different radial offsets of the two fibers using a micrometer screw. As shown in Figure 2.12, the data is in good agreement with the analytic model. For a radial misalignment of $x_{\text{rad}} = 200\,nm$ the reflection signal σ_{ref} drops already significantly and it goes to zero for $x_{\text{rad}} = 2\,\mu m$. The same measurement was done for different angular misalignments. We found that σ_{ref} is relatively insensitive on the tilt of the fiber axes, while an optimal transmission through the fiber cavity requires sub-degree alignment precision.

As mentioned before, our fiber processing using CO_2-laser ablation produces fiber tips with Gaussian profiles instead of spherical mirrors. The effect of this imperfect mirror shape was simulated using the numerical Matlab FFT-code *OSCAR*[1], which can calculate the steady-state circulating fields in Fabry-Pérot cavities. It turns out that the Gaussian shape leads to higher order modes in the cavity which creates unexpected dips in the reflection signal σ_{ref} for certain cavity lengths. Furthermore, the finite size of the mirrors (the area where the profile can be approximated by a sphere) limits the area of stable mode match to lengths $L < 0.5\,r_2$. For longer cavities the reflection and transmission signal start to behave very unpredictable. However, the optimal ROC $r_{2,\text{MM}}$ can be achieved with different depth and widths of the Gaussian profile. Hence, these two

[1] by Jerome Degallaix, v3.14, http://www.mathworks.com/matlabcentral/fileexchange/20607-oscar

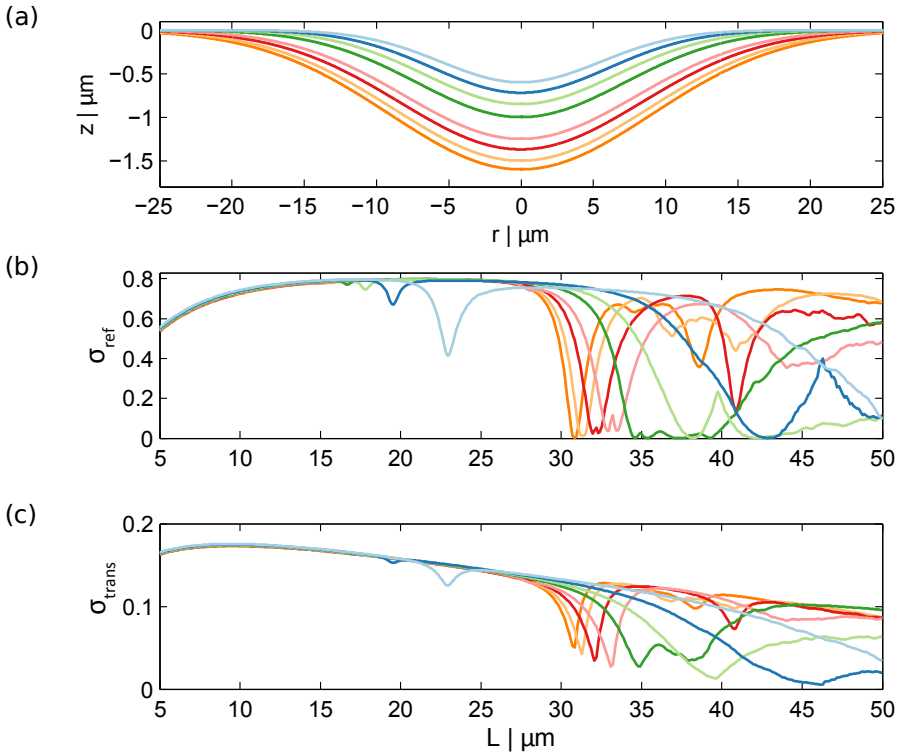

Figure 2.13: Fiber cavity signals for Gaussian mirror profiles. (a) Different Gaussian mirror profiles with ROC $r_2 = 51\,\mu\text{m}$, which are in the typical range of the used fiber profiles. **(b)** Simulations of planar-concave fiber cavities: reflectivity on resonance σ_{ref} as a function of cavity length L for the different profiles in (a) according to equation 2.6 using the numerical FFT-code *OSCAR* to calculate the intra-cavity field and the mode match. The maximum reflection is $\sigma_{\text{ref}} = 0.8$. **(c)** Transmitted power on resonance σ_{trans}. Figures taken from [87].

parameters can be optimized for a stable mode match around the wanted cavity length. Figure 2.13 shows that deeper and wider Gaussian profiles behave very predictable for $L < 0.5\,r_2$, but reflection and transmission quickly break down for $L > 0.5\,r_2$. Shallower and smaller Gaussian profiles can be used for cavities that must be longer than $0.5\,r_2$ at the cost of unwanted dips of the cavity signals for $L \approx 0.5\,r_2$.

Production of fiber cavities

In order to produce concave mirror structures on glass fiber tips, we employ CO_2-laser ablation as first described in [66] and [94]. For this, a single laser pulse with duration $\tau \approx 5 - 10\,\text{ms}$, a power of $P \approx 0.5\,\text{W}$ and a wavelength of $\lambda = 10.6\,\mu\text{m}$ is focused on the fiber surface using a parabolic mirror. The beam with a typical spot radius of $w = 50\,\mu\text{m}$ evaporates material from the surface which results in a concave Gaussian profile on the fiber tip. A thin melt layer on the surface of the structure results in an ultra-low roughness glass surface which can later be deposited with a dielectric mirror coating. After a pulse was fired on the fiber, a flip mirror enables the direct 3D analysis of the resulting structure using a home-built interferometric profilometer. The fiber cavity for the MiM device was deposited with an in-house coating machine. Further details on the fiber processing setup can be found in the Master's thesis of the author

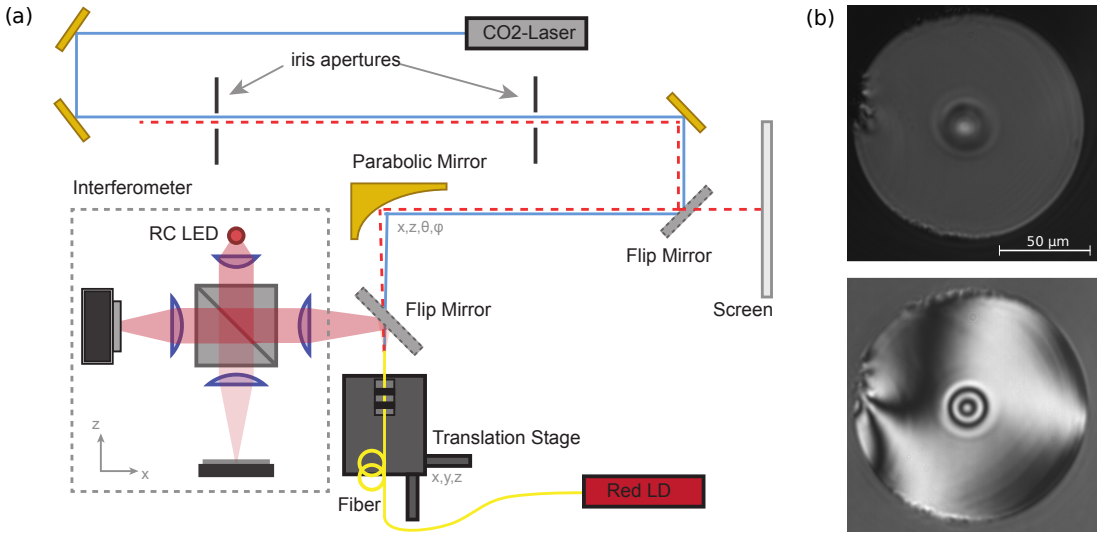

Figure 2.14: CO_2-laser setup for the production of fiber cavities. (a) A CO_2-laser ($P_{max} = 28\,W$, $\lambda = 10.6\,\mu m$, $w_0 = 1.8\,mm$) is focused onto a fiber on a translation stage using a parabolic gold mirror (RFL = 25.4 mm). The optimal focusing of the mirror (minimal aberrations) as well as the positioning of the fiber in the CO_2-laser focus is achieved by superimposing the CO_2-laser beam with an alignment beam from a red laser diode, which is coupled into the fiber. If the parabolic mirror collimates this alignment beam without aberrations (we use a removable flip mirror to observe the beam on a screen at a distance $> 5\,m$), the two beams can be superimposed using two iris apertures. Another flip mirror enables the direct interferometric analysis of the fiber surface using an imaging system (magnification $M \approx 20$, resolution $\approx 2\,\mu m$) with an integrated Michelson interferometer setup. The light source is a resonant cavity LED (PR65-F1P0T from *Optowell*, $\lambda = 650\,nm$, coherence length $l_c = 27\,\mu m$ [86]) and the image is taken with a CCD camera. An important feature is the use of similar lenses in the two arms (aspheric lenses with $f = 25\,mm$). A new version of the setup, which uses a ZnSe lens for focusing and a better CO_2-laser was described in [91]. Figure taken from [87]. **(b)** CCD image of a processed fiber. If the reference arm is blocked (top) a normal image of the fiber can be acquired. If the reference arm is unblocked (bottom) an interference image occurs. The circular fringes in the center correspond to a typical concave profile used for fiber cavities (depth $< 1\,\mu m$, ROC $\approx 50\,\mu m$) that was created by a laser pulse.

[90] and the PhD theses of A. Bick [86] and C. Staarmann [87]. The fiber cavity in the MiM device was produced with this setup. A new version of the setup was presented in the Master's thesis of J. Petermann [91], which uses a CO_2-laser with better stability and controlability. Furthermore, the new setup uses a ZnSe lens for focusing, instead of the parabolic mirror in the old setup.

Figure 2.14 shows a sketch of the CO_2-laser setup and the interferometric profilometer that was used for the production of the fiber cavity in the MiM device. Also shown is a typical interferometric image that can be acquired directly after the laser machining. By blocking the reference arm of the interferometer, a normal image can be acquired without interference. This additional reference image is used to remove the background of the interferometric image, which improves the fringe visiblity. We employ a method called *phase shifting interferometry* [95] for the three-dimensional reconstruction of the fiber profile. For this, different phase shifted interferometric images with an unknown, arbitrary phase relation are acquired, which can be done simply by applying mechanical

stress on the optical table. The images are then processed by a phase shifting algorithm which reconstructs the phase (the wrapped phase modulo 2π) of the interferometric images, which is proportional to the height profile of the fiber surface. A detailed comparison of the performance of different algorithms using images from our setup can be found in [87].

2.3.3 MiM alignment

The usage of asymmetric planar-concave fiber cavities requires a radial (xy) alignment precision of 200 nm, sub-degree angle ($\theta\phi$) alignment and cavity lengths $L < 30\,\mu$m (see section 2.3.2). Furthermore, in a MiM system based on a fiber cavity the membrane must be placed in the very short gap between the fibers. This alignment must be performed at cryogenic temperatures, since cooling down from room temperature while keeping the mentioned alignment precision would be technically very challenging. An additional factor that complicates the alignment is the fact that the silicon frame which supports the used membrane has a thickness of 200 µm and hides the view from the side on the lower fiber when it is close to the membrane (see inset of Figure 2.6). Therefore, we employ a special white-light method (similar to [96]) for measuring the distance between each fiber and the membrane with light coupled into the fibers. This method will be explained in the end of this subsection.
In the context of this subsection, the MiM system can be regarded as aligned if the fiber cavity is completely aligned and the membrane is located between the fibers, perpendicular to the fiber axis. This is achieved by a four-stage process including different techniques, which will be explained in the following. The procedure corresponds to the alignment of a new fiber cavity with a new membrane that is aligned for the first time. If an existing MiM system needs to be realigned (for example after a warm-up of the cryostat), some steps of the following procedure might be obsolete.
After the pre-alignment described in this subsection, the lengths L_1 and L_2 (see inset of Figure 2.6) must be fine-adjusted on the order of 10 nm to place the membrane in the right position of the intra-caviy standing wave. This fine-alignment will be presented later in section 3.1.

Step 1: Empty fiber cavity alignment

It is very helpful to align the empty fiber cavity first before inserting the membrane. This simplifies the later alignment of the fiber cavity with membrane in between. The fiber cavity alignment is done at a cryostat temperature $T_{\mathrm{MiM}} \approx 25\,$K. In this regime, the cryostat can be operated with open inspection apertures in the cryogenic radiation shields. This allows for observing the MiM system with microscope cameras from outside of the cryostat chamber (see also [85]). The two perpendicular visual axes enable the coarse alignment of the fiber cavity with respect to the angle ($\theta\phi$), the xy-displacement and the z-alignment ($L \approx 15\,\mu$m), as shown in Figure 2.15 (a). After this coarse alignment using the cameras, the xy fine-alignment on the order of 100 nm is done with the cavity signals. The three-step procedure to maximize the mode match of the fiber and the cavity ground mode using the reflection and transmission signals is described in Figure 2.15 (b). In the final alignment stage, the higher order mode next to the

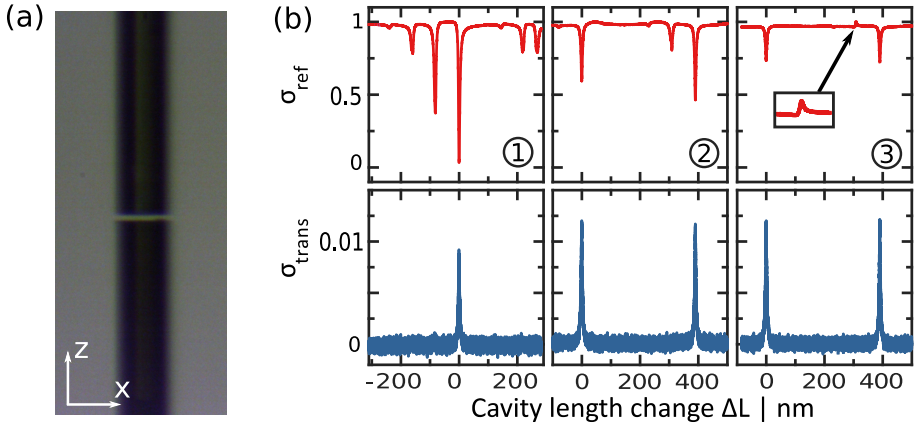

Figure 2.15: Alignment of the fiber cavity in the MiM device. (a) Image of the fiber cavity in the MiM device (see Figure 2.6) taken from outside of the cryostat chamber through the inspection apertures of the radiation shields using a microscope CCD camera (cryostat temperature $T_{\mathrm{MiM}} \approx 25\,\mathrm{K}$). The image was taken after a coarse alignment of the fibers using the five axis stepper motors of the MiM device. The cavity length $L \approx 15\,\mu\mathrm{m}$ was adjusted by using the fiber diameter $d = 125\,\mu\mathrm{m}$ as a reference. **(b)** Fine-alignment using the cavity reflection signal σ_{ref} and the transmission signal σ_{trans} of a beam coupled in from the lower reflecting side. For this, the cavity length is scanned with the piezo tubes (see section 2.3.1) over a range of $\Delta L \approx 500\,\mathrm{nm}$. Firstly, the xy-displacement is changed slightly on the order of $10\,\mu\mathrm{m}$ until cavity resonances like in panel ① occur with mode match $\beta \approx 0.5$ such that $\sigma_{\mathrm{ref}} = 0$ (see Figure 2.10). Then, the xy-displacement is changed slightly on the order of $1\,\mu\mathrm{m}$ to maximize the transmission like in panel ②. This also optimizes the mode match leading to $\sigma_{\mathrm{ref}} > 0$. Finally, very small xy-steps on the order of 100 nm are performed until the side dip next to the ground mode vanishes and turns into a peak, as indicated by the arrow in panel ③. The aligned cavity has a reflectivity on resonance $\sigma_{\mathrm{ref}} = 0.73$ and a finesse $\mathcal{F} = 60$.

ground mode turns from a dip into a peak. This has been found to be the the optimal xy-alignment of the fibers. The existence of this peak indicates that the off-resonance reflectivity is slightly smaller than expected (which would be ≈ 1). Further details on possible origins of such a peak in the reflection signal can be found in [93].

Step 2: Positioning of upper fiber close to membrane

After the empty fiber cavity was aligned in step 1, the fibers need to be fully retracted again with the z-stepper motors in order to insert the membrane. For this, the membrane shuttle (see Figure 2.7) is picked up from the load lock chamber using the wobble stick [85]. After the shuttle has been placed in the MiM device, the fibers can be moved back. Firstly, the upper planar fiber is brought near the membrane using the cameras, as can be seen in Figure 2.16. If the fiber is not centered in the middle of the membrane, it can be moved horizontally with the xy-stepper motors until the fiber is perfectly centered on the intersection point of the diagonals of the membrane. In this way, the optical coupling to the ground mode can be optimized, since its displacement is largest in the center. After the horizontal translation, an xy-alignment of the fiber cavity in step 1 is destroyed and needs to be repeated later. After centering the upper fiber, it can be approached to a distance of $L_1 \approx 5\,\mu\mathrm{m}$ using white-light that is coupled into the upper fiber (as described later). Distortions in the spectrum due to the lower

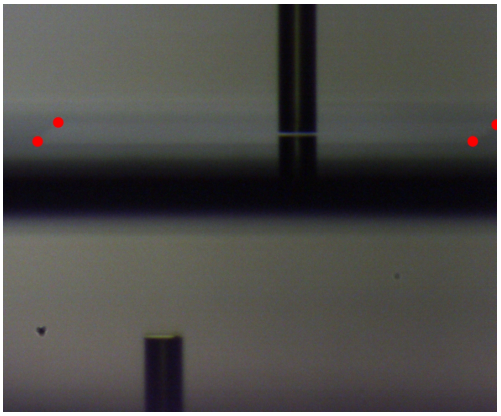

Figure 2.16: Fiber alignment around the membrane. Image taken from outside the cryostat with a microscope CCD camera. The upper fiber is very close to the membrane, visible by the small gap between the fiber and its mirror image on the membrane. The edges of the membrane in the silicon frame are indicated by red dots and can be used to define aid lines for centering the fiber in the middle of the membrane. The lower fiber is far below the membrane frame and needs to be further approached in a subsequent alignment step.

fiber can be avoided by axially misaligning the lower fiber. The distance L_1 is chosen to be shorter than L_2, since the waist of the intra-cavity field of the planar-concave cavity is located at the planar mirror of the upper fiber. Here, reflected light from the membrane is mode matched with the intra-cavity field.

Step 3: Positioning of lower fiber (creating a MiM system)

After the upper fiber has been positioned, the lower fiber can be approached. This can be done with the white-light method, by coupling into the lower fiber and measuring the spectrum of the reflected light. After a distance $L_2 \approx 15\,\mu\text{m}$ has been adjusted ($\Rightarrow L_1 + L_2 \approx 20\,\mu\text{m}$), the lower fiber can be moved horizontally until the fibers are axially aligned. Subsequently, the fine-adjustment of the fiber cavity xy-alignment (see Figure 2.15) can be repeated.

Step 4: Cooldown of MiM system to base temperature

After the alignment of the MiM system at $T_{\text{MiM}} \approx 25\,\text{K}$, the cryogenic radiation shields can be closed and the cryostat can be cooled down to base temperature. The expected thermal contraction of the fiber cavity is so small that this can be done safely. After the cooldown, the xy-alignment of the fiber cavity can be optimized again using the cavity signals (as in Figure 2.15) and the cavity lengths L_1 and L_2 can be measured again using white-light. After this final step the MiM system is aligned. This alignment has proven to be stable over months as long as T_{MiM} stays below 1 K.

White-light spectroscopy for distance measurements

In order to measure the length L of a Fabry-Pérot cavity, it is sufficient to know two wavelengths λ_i that fulfill the resonance condition $n_{\text{i,j}}\lambda_{\text{i,j}} = 2L$. Furthermore, they must be separated by a know index interval $\Delta n = n_\text{j} - n_\text{i}$. It follows:

$$L = \frac{\Delta n}{2}\left(\frac{\lambda_\text{i}\lambda_\text{j}}{\lambda_\text{i} - \lambda_\text{j}}\right). \tag{2.7}$$

For example, if the fiber cavity in the MiM system is aligned, the laser can be tuned from one resonant wavelength λ_i to the next resonance at $\lambda_{\text{i}+1}$, which can be measured

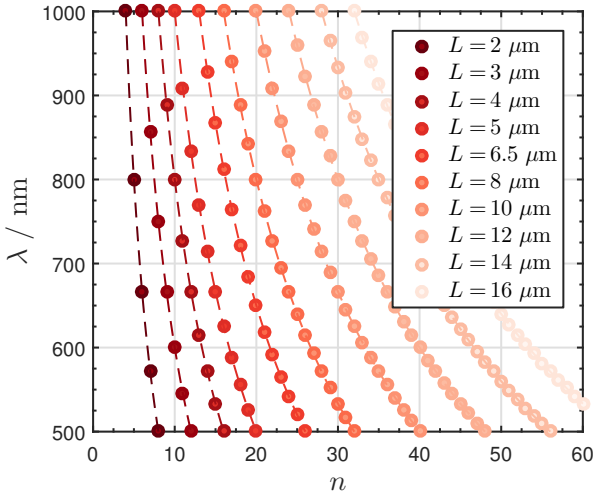

Figure 2.17: Resonant wavelengths in short Fabry-Pérot cavities. Shown are the resonant wavelengths in a Fabry-Pérot cavity for different lengths $L < 20\,\mu m$ plotted against their index n according to the resonance condition $n\lambda = 2L$. For cavities with $L \approx 5\,\mu m$ the spectral interval between two resonances is $\Delta\lambda \approx 60\,nm$ around 800 nm.

with a wavemeter. In this way, the cavity length L can be determined. Special care needs to be taken in the MiM system, since the membrane can significantly alter the FSR (λ_i - λ_{i+1}) and thus the measured L on the order of 30% (see section 3.1).
However, this method only works if the fiber cavity is already aligned, since the reflectivity of the mirrors is usually designed to be large for the wavelength of the used laser. Hence, no light can be coupled into the cavity if it is misaligned and not mode matched with the laser beam. This also means that the method is not suitable for measuring the distance of a fiber to the membrane, since its reflectivity is very small compared to the fiber mirrors. Hence, the fringe visibility of the fiber-membrane etalon would be extremely small. Furthermore, for very short cavities with $L < 15\,\mu m$ the spectral interval between two resonant wavelengths becomes larger than the usual wavelength range of a laser. This can be seen in Figure 2.17.
For two reasons, white-light can overcome the limitations mentioned above. Firstly, the spectral range of a white-light source can be much larger than the wavelength tuning

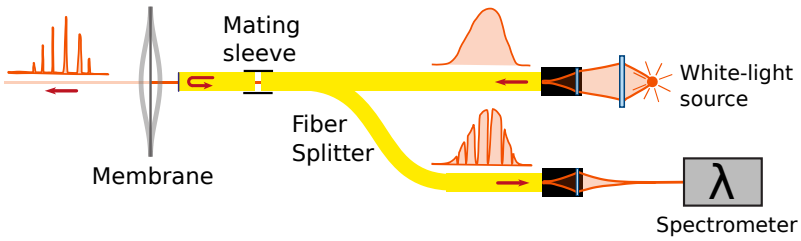

Figure 2.18: White-light spectroscopy setup for distance measurements. The light from a bright broadband LED light source (KL 1500 LED from *Schott*, $\lambda = 400 - 750\,nm$, spectrum in Figure 2.19) is focused by a lens ($f = 80\,mm$) into a fiber coupler at one port of a fiber splitter. The splitter is connected to one fiber of the MiM device, whose reflecting side is close to the membrane ($L_{1,2} < 150\,\mu m$). The dips in the reflected spectrum correspond to the resonant wavelengths of the fiber-membrane etalon. This light is free space coupled into a spectrometer (Qwave NIR from *rgb photonics*, resolution $< 0.5\,nm$) by focusing it with a fiber coupler into the spectrometer. If the other fiber of the MiM system is approached from the other side of the membrane (not shown), also the transmitted light can be analyzed and the reflected light will contain additional information about the total cavity length L.

range of a usual laser. It is also not necessary to tune the wavelength like described above, since all the wavelengths are present at the same time and can be analyzed simultaneously with a spectrometer. Secondly, the fiber coatings were designed to have the highest reflectivity around 780 nm. Thus, at wavelengths far away from 780 nm the reflectivity is much lower and the fiber-membrane etalon has a much larger fringe visibility.

The principle of our white-light method for measuring the fiber-membrane distance is to couple light with a very broad spectrum into the fibers and to measure the spectrum of the reflected light from the fiber-membrane etalon. The dips in the reflected spectrum correspond to resonances of this etalon, which can be used to determine its length by a fit with the function $\lambda = 2L/n$ (see Figure 2.17). A similar technique was published in [96]. Although the idea behind the method is rather simple, it is a technical challenge to couple enough white-light into a fiber and to couple the reflected light into a spectrometer. Furthermore, the analysis of the measured spectra is not trivial, since many parasitic effects lead to distortions of the original spectrum that need to be distinguished from the resonance features of interest.

Figure 2.18 shows a sketch of the optical setup for the white-light spectroscopy. We use a bright LED lamp to free space couple light into the fiber. This has been proven to be a suitable light source for our fibers and fiber coatings. Another possible choice would be a fiber coupled SLED. These are available on the market with wavelengths ranging from 400 nm to 1700 nm. However, the spectrum of the light source needs to include a broad interval of wavelengths $\Delta\lambda$ that is guided by the used fibers and that is reflected by the fiber coating in a suitable manner (broadband reflectivity $R_{\Delta\lambda} \approx R_{\mathrm{mem}}$). Hence, each mirror coating has its own optimal wavelength for the white-light method. Care should be taken when the materials in the dielectric coatings start to become absorptive at the used wavelengths, which might destroy the coating. In order to observe the reflected

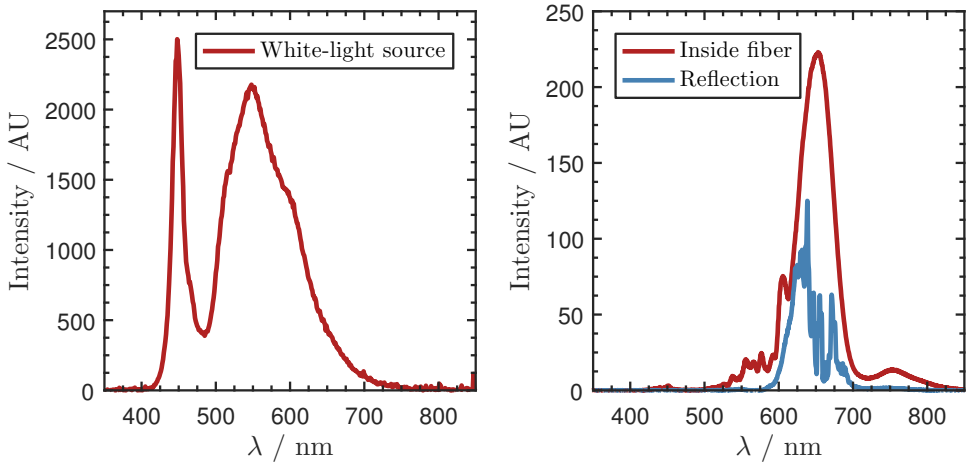

Figure 2.19: Light spectra of the white-light source. Left panel: spectrum of the broadband LED light source used for white-light spectroscopy. Right panel: spectrum of the light coupled into the fiber (780HP from *Thorlabs*) measured after the fiber splitter (see Figure 2.18) and the reflected spectrum from the lower reflecting, planar fiber in the MiM system. This spectrum can be used as a reference for the modulated spectra of the fiber-membrane etalon, since the membrane was far away from the fiber. The two spectra are not to scale.

light, we use a fiber splitter that is connected with a fiber optic mating sleeve with the fiber of the MiM system. Since the light power is very small, we free space couple the reflected light into the spectrometer, which has been proven to be more efficient than any fiber connection.
The spectrum that can be used in the white-light spectroscopy method is limited by the light that can be coupled into the fibers. Figure 2.19 shows that the usable spectrum in the fiber can be approximated by a Gaussian centered at $\lambda_0 = 650\,\mathrm{nm}$ with a width

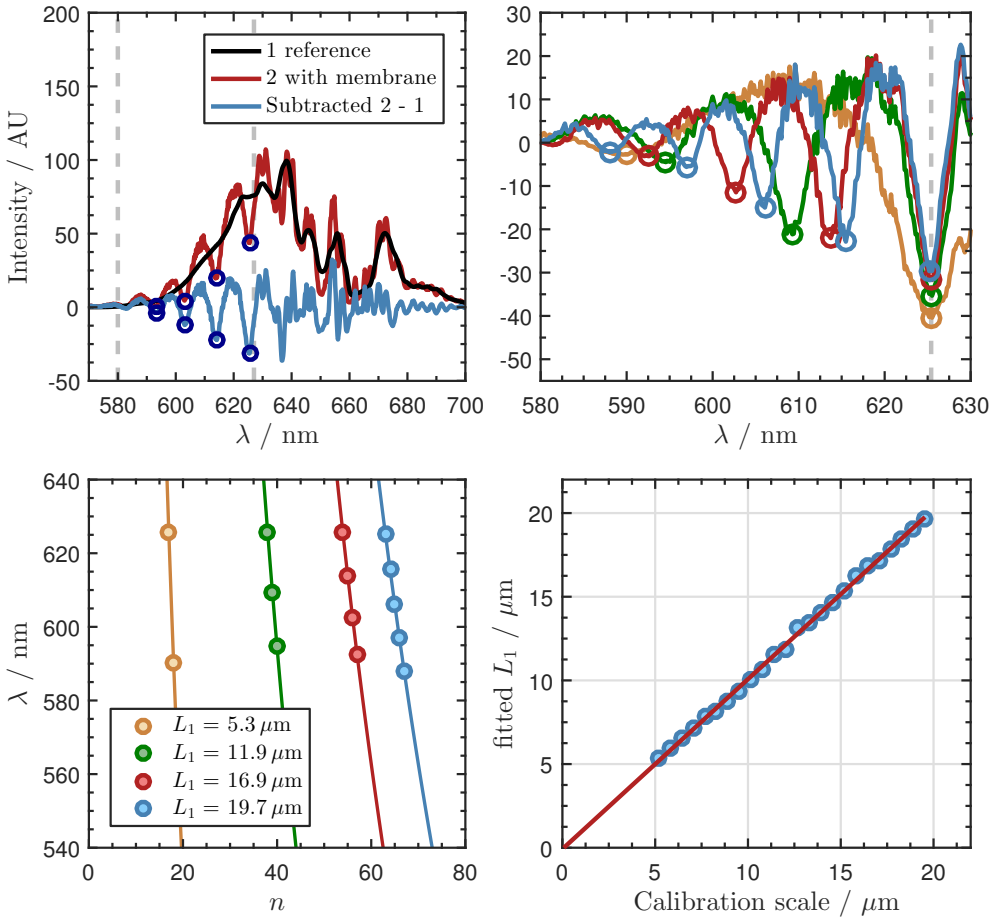

Figure 2.20: Validation of the white-light spectroscopy. (Top left) Spectra of the reflected light from the upper fiber (lower reflecting side) were acquired with a spectrometer in a setup similar to Figure 2.18 (0.7 s exposure time, two times averaging). From each spectrum a reference spectrum without membrane was subtracted (black curve). This spectrum is the one shown in Figure 2.19 after smoothing it with a moving average filter. In an interval $\Delta\lambda \in [580\,\mathrm{nm}, 630\,\mathrm{nm}]$ (dashed vertical lines), the resonances of the fiber-membrane etalon can be extracted from the subtracted signal using a peak finder routine (blue circles). **(Top right)** In the interval $\Delta\lambda$ the spectra were analyzed for different distances L_1 between fiber and membrane, which was altered by multiples of a calibration wavelength $\lambda_c = 625\,\mathrm{nm}$ (dashed vertical line). **(Bottom left)** Extracted resonant wavelengths λ (dots) and fits (function $\lambda_{\mathrm{fit}} = 2L/n$) to the data for the spectra shown in the top right panel. Each fits yields a length L_1 . **(Bottom right)** Fit results for L_1 versus the calibration scale defined by multiples of λ_c and a linear fit using slope and y-intercept as free parameters. Fit results: slope 1.015, y-intersect $-100\,\mathrm{nm}$, root-mean-square deviation $\Delta L \approx 150\,\mathrm{nm}$ from the data.

of $\Delta\lambda_{\mathrm{FWHM}} = 50\,\mathrm{nm}$. However, the reflected spectrum from the planar fiber mirror (lower reflecting side) is relatively smooth only below 650 nm, where it can be used for the distance measurement by fitting the resonances of the fiber-membrane etalon. This procedure is shown in Figure 2.20. In order to enhance the robustness of the fit routine, the reference spectrum without membrane (see Figure 2.19) is subtracted from the measured spectra. The number of dips (resonant wavelengths) in the resulting spectrum needs to be at least two in order to extract the fiber-membrane distance L_1 (L_1 defined in Figure 2.6). The corresponding wavelengths can be fitted with the function $\lambda = 2L_1/n$ using L_1 and n as two free fit parameters. After this, the resulting index n is rounded to the nearest integer and the fit is repeated with this fixed $n \in \mathbb{N}$ using L_1 as the only free fit parameter. Since n is known to be integer, this enhances the fit result for L_1.

Our white-light method (similar to [96]) enables the reliable determination of absolute distances $L_1 \in [5\,\mu\mathrm{m}, 150\,\mu\mathrm{m}]$ and has an accuracy of $\Delta L_1 \approx 150\,\mathrm{nm}$. This accuracy was determined by changing the distance L_1 between the upper fiber and the membrane by multiples of a calibration wavelength λ_c and comparing this calibration scale with the white-light fit results for L_1. Walking the distance λ_c can be performed simply by moving the z-stepper motor until a dip in the spectrum at λ_c reappears at the same position (see Figure 2.20).

White-light measurements of the distance of one fiber to the membrane if the other fiber is far away (as depicted in Figure 2.18) have proven to work for both the higher and the lower reflecting fiber. Furthermore, if the other fiber is approached from the other side of the membrane to build a MiM system, the lengths L_1 (first subcavity) and L (total length of the fiber cavity) can be measured simultaneously. For example, if the light is coupled in from the upper fiber, scanning the lower fiber position with the piezo tube washes out the resonances related to L and keeps only the resonances related to L_1. The same holds if the light is coupled into the lower fiber and the upper fiber is scanned, respectively (measuring L_2 and L). In these cases it is also possible to extract the total cavity length L from the transmitted light through the cavity. However, it should be noted that the measured L can deviate because of the optomechanical coupling of the membrane, which can change the effective FSR of the cavity on the order of 30% (see section 3.1). However, this effect is averaged out in the white light method since many resonances are taken into account.

2.4 The coupling laser system

In order to couple the two constituents of the atomic-mechanical hybrid system and to detect the motion of the mechanical oscillator, a dedicated laser system was implemented (see Figure 2.21). The laser system is located in the upper laboratory and all beams derived from this system are guided through optical fibers to the hybrid system apparatus in the lower room (see Figure 2.1). The system is based on a Ti:sapph, which has a wide wavelength tuning range including the D_2 line ($\lambda_{\mathrm{air}} = 780.0\,\mathrm{nm}$) and the D_1 line ($\lambda_{\mathrm{air}} = 794.8\,\mathrm{nm}$) [97] of the ^{87}Rb atoms, which makes it suitable for many different coupling and detection schemes of the cold atoms. Furthermore, this monolithic solid-state laser has a narrow linewidth resulting in a small phase noise for high-performance

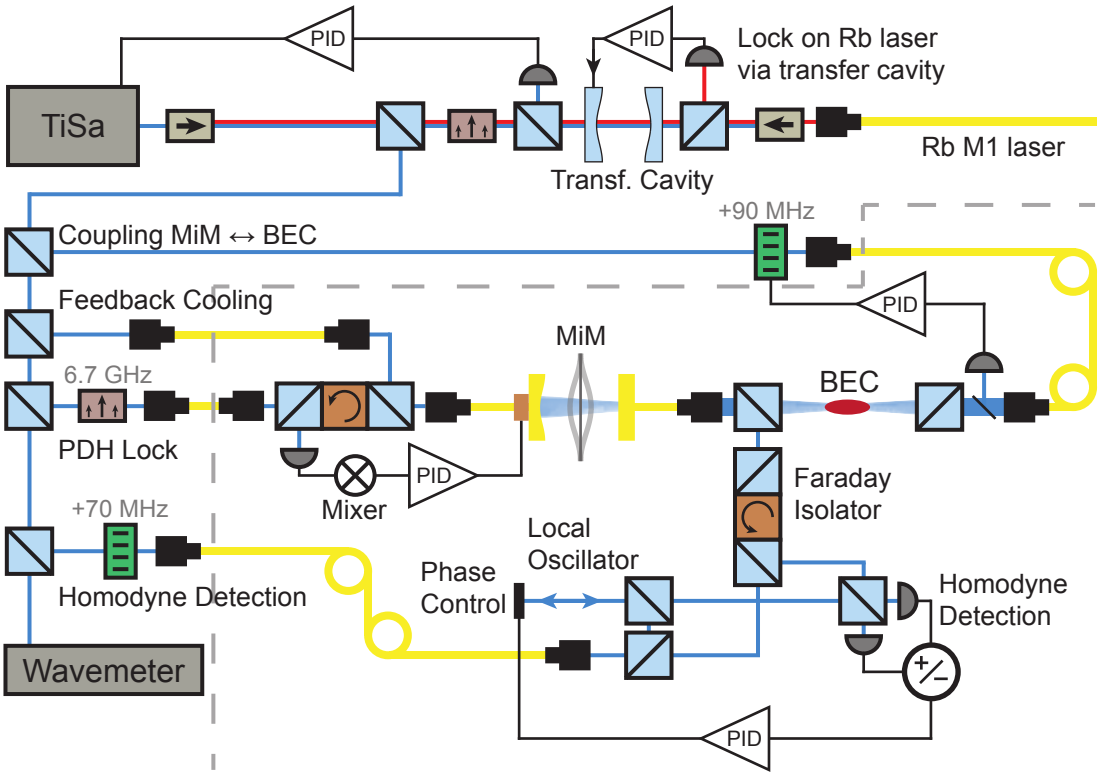

Figure 2.21: Laser system for coupling and detection of the MiM device. The Ti:sapph laser (MBR 110 from *Coherent*) can be locked relative to the ^{87}Rb D_2 line via a transfer cavity (FPI 100 from *Toptica*, FSR = 997.544(4) MHz [86]) which is locked to the M1 laser of the rubidium laser system (see Figure 2.2). Four branches are derived from the Ti:sapph laser: (1) the coupling beam for interfacing the oscillator in the MiM device with the Rb atoms, (2) a feedback cooling beam for cooling the oscillator, (3) A PDH locking beam for locking the fiber cavity in the MiM device and (4) a beam for homodyne detection of the oscillator. A wavemeter (WS6-600 from *HighFinesse*) allows for monitoring the wavelength of the Ti:sapph. The laser system is located in the upper room and guided via optical fibers to the MiM device and the BEC machine in the lower room, which is marked by the dashed line (see Figure 2.1). The coupling and homodyne beam are both blue detuned by 90 MHz and 70 MHz with AOMs, respectively. The AOMs are also used for the intensity control of these two beams. The PDH beam has sidebands at 6.72 GHz from a resonant phase modulator by *Newport*. Coupling and homodyne beam are coupled into the planar MiM fiber, which allows optimal mode match and minimal losses (see Figure 2.9). The realized setup for feedback and homodyning slightly differs from this sketch and is shown in appendix B.1. Figure adapted from [87].

homodyne detection without the need of additional filter cavities. The laser system is equipped with a transfer cavity which allows for locking the Ti:sapph relative to the atomic transitions by multiples of its FSR of appromimately 1 GHz. Four main beams are picked up from the Ti:sapph laser: (1) the coupling laser beam of the hybrid system, (2) a beam for feedback cooling of the oscillator, (3) a beam for Pound-Drever-Hall (PDH) locking of the fiber cavity in the MiM device and (4) a beam for balanced homodyne detection of the mechanical oscillator. After a brief description of the PDH locking scheme, the feedback cooling and the homodyne detection, the main focus of this section will be on the coupling laser beam.

Pound-Drever-Hall locking of the fiber cavity length

In order to be able to lock the fiber cavity length L to the coupling and detection laser system, a Pound-Drever-Hall (PDH) lock [98] has been implemented. For this, a resonant phase modulator is used to generate sidebands at 6.72 GHz on the PDH beam which is coupled through an optical isolator into the fiber cavity (see Figure 2.21). The reflected light from the cavity is then split off by the optical isolator and can be measured with a fast photodiode. The frequency for an optimal PDH signal would be around ten times larger than the linewidth of the fiber cavity. However, the fiber cavity with a length $L \approx 20\,\mu\text{m}$ and a finesse $\mathcal{F} \approx 100$ has a linewidth $\Delta\nu = \text{FSR}/\mathcal{F} = c/2L\mathcal{F} = 75\,\text{GHz}$ and frequencies on this order of magnitude or even larger are not suitable for electronic processing. Thus, sidebands at 6.72 GHz are a trade-off between electronic performance and the largest possible sideband frequency for the best PDH error signal. Furthermore, the electronics designed for generating and processing signals at 6.72 GHz will be compatible with a setup for driving the hyperfine ^{87}Rb ground state transition of 6.83 GHz [97] in possible future experiments.
The size of the PDH error signal depends on the ratio between sideband frequency and cavity linewidth, as well as the incoupling side of the asymmetric fiber cavity. We measured a ten times larger PDH error signal for coupling into the planar, lower reflecting side than for coupling into the curved, higher reflecting side of the fiber cavity. However, the planar side has the optimal mode match [67] and is reserved for the coupling and homodyne beam (see also Figure 2.9). Moreover, due to the small sideband frequency compared to the large cavity linewidth, the PDH error signal is very small and requires a large electronic amplification gain. For this, we employ two low noise amplifiers with a total gain of 90 dB to amplify the signal from the fast photodiode before mixing it down with the local oscillator that drives the phase modulator. When implementing an electric feedback loop for locking the cavity length with the piezo tubes of the MiM device (see Figure 2.6), special care needs to be taken. This is because any electric noise on the piezo tubes around the oscillator frequency can drive the mechanical oscillator.
The measurements presented in this thesis were performed without PDH locking the cavity length of the MiM device. This is possible because the passive stability of the used fiber cavity length is sufficiently high, caused by the extremely good thermal isolation of the MiM device in the cryostat and the low finesse. Further details on the passive stability of the cavity will be presented in section 3.1.

Homodyne detection and feedback cooling

The state of the mechanical oscillator in our hybrid experiment is measured with balanced homodyne detection [99, 100]. This quantum limited detection scheme allows for measuring the motion of the oscillator down to the single quantum level. Details on the principles of this optomechanical detection scheme, the experimental setup and a comprehensive characterization of the homodyne detection will be presented in section 3.3.
Furthermore, we use the homodyne measurement for active feedback cooling [68, 69] of the mechanical oscillator into the quantum regime. For this, the homodyne signal is fed back to the oscillator through radiation pressure of the feedback beam. This creates an

artificial damping force which removes kinetic energy from the oscillator. The feedback beam is coupled into the curved side of the fiber cavity and is intensity modulated by a fiber optic amplitude modulator. A comprehensive treatment of the principles of feedback cooling, as well as the experimental setup and realization is presented in chapter 4.

The coupling beam for hybrid experiments

In the first stage of the project, we couple the mechanical oscillator to the motion of the cold atoms in an optical 1D lattice, as depicted in Figure 1.1. The lattice is formed by the retro-reflected coupling beam from the cavity, which creates a bi-directional coupling of atomic and mechanical motion [31]. The setup of the coupling laser beam will be presented in the following subsection 2.4.1. Subsequently, lattice characterization measurements using matter wave diffraction in the lattice potential will be presented in subsection 2.4.2.

2.4.1 Coupling lattice setup

In order to generate a resonant coupling between the two parts of the hybrid system, the atomic trapping frequency ω_a along the 1D lattice has to match the oscillator frequency $\omega_\mathrm{m} \approx 250\,\mathrm{kHz}$ (further details on this hybrid coupling scheme will be given in chapter 5). In units of the atomic recoil energy $E_\mathrm{r}/h = 3.77\,\mathrm{kHz}$ [97] this corresponds to a 1D lattice potential depth of $V_0 = \frac{1}{2} m_\mathrm{a} \omega_\mathrm{a}^2/k^2 \approx 1100\,E_\mathrm{r}$ [101]. This is a relatively deep optical lattice potential, which is usually generated by very large laser powers on the order of 10 W. However, due to the cryogenic implementation and light absorption of the mechanical oscillator we are limited to a laser power of the coupling lattice beam on the order of $P_\mathrm{lat} \approx 1\,\mathrm{mW}$. Nevertheless, the lattice potential scales with $V_0 \sim I_0/\Delta$ [101] with the peak intensity I_0 of the laser beam and the detuning Δ from the atomic transition. Thus, we generate the required lattice depth using a very near-detuned laser beam with a detuning on the order of $\Delta \approx 1\,\mathrm{GHz}$ and a small waist of $w_\mathrm{lat} = 78\,\mu\mathrm{m}$ [87] to increase the intensity at the position of the atoms.

Frequency stabilization. Due to the near-resonant operation of the coupling beam, the wavelength of the coupling lattice needs to be monitored and precisely adjusted. For this, we monitor the wavelength of the Ti:sapph with a wavemeter, which allows for measuring relative frequency changes on the order of 5 MHz (digital quantization of the wavemeter). The absolute frequency of the Ti:sapph can be determined differently with an accuracy on the order of 3 MHz. This is done by locking the Ti:sapph to the transfer cavity (linewidth $\approx$ 3 MHz), which is locked to the rubidium M1 laser, as depicted in Figure 2.21. With this method we also calibrate the wavemeter on a daily basis. The frequency of the M1 laser corresponds to the frequency $\omega_{2,3}$ of the ^{87}Rb D_2 line ($|5^2\mathrm{S}_{1/2}, F = 2\rangle \rightarrow |5^2\mathrm{P}_{3/2}, F = 3\rangle$) [97] plus the frequency shift $2 \times 67.1\,\mathrm{MHz}$ of the double-pass AOM which tunes the M1 laser on resonance for the absorption imaging of the cold atoms (see Figure 2.2). Furthermore, the coupling lattice is 90 MHz blue detuned from the Ti:sapph laser. Hence, if the Ti:sapph is locked to the transfer cavity by multiples $n_\mathrm{FSR} \in \mathbb{N}$ of the cavity FSR, the lattice beam has a frequency of

$$\omega_\mathrm{lat}/2\pi \;=\; \omega_{2,3}/2\pi + 2 \times 67.1\,\mathrm{MHz} + 90\,\mathrm{MHz} + n_\mathrm{FSR} \times \mathrm{FSR}\,, \tag{2.8}$$

which is determined with an accuracy of 3 MHz (transfer cavity linewidth) and which is fixed by the lock with sub-megahertz precision over a time scale of hours [86]. However, in some of the hybrid experiments presented in this thesis the Ti:sapph was not locked to the transfer cavity, because the lattice frequency needed to be adjusted more precisely than the 1 GHz steps of the transfer cavity FSR. Nevertheless, we measured a stability of the internal lock of the Ti:sapph laser (an etalon dither lock and an internal reference cavity) on the order of 10 MHz on a time scale of 10 min [86], which was sufficient for the measurements presented in this thesis. Besides, if the Ti:sapph frequency drifts during a measurement, it can be readjusted manually in 20 MHz steps using the manual scan knob of the internal cavity.

Optical setup. The experimental setup of the coupling lattice is shown in Figure 2.22. The coupling beam is derived from the Ti:sapph in the upper room and is coupled through an AOM which is used for frequency shifting (90 MHz), fast switching ($\tau_{r,f} \approx 50$ ns) and intensity control. After the AOM the beam can be blocked with a mechanical shutter for total light extinction which is crucial for blocking the near-

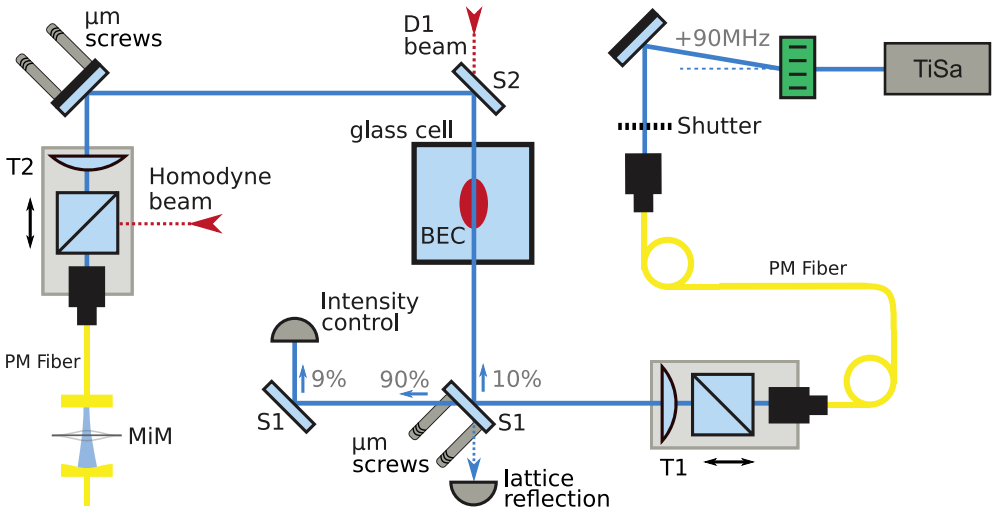

Figure 2.22: Setup of the optical coupling lattice. Sketch of the realized setup of the 1D lattice for coupling a BEC and a mechanical oscillator in a MiM system. Ti:sapph light is blue-shifted 90 MHz by an AOM and guided via a polarization maintaining (PM) fiber into the lower room (see Figure 2.1), where it is connected to the lattice telescope T1 (fiber collimator 60FC-L-4-M20L-02 with beam $\varnothing = 3.6$ mm and a focusing lens 13M-S500-05-S from *Schäfter+Kirchhoff*, in between a polarizer cube, specified working distance of 49.2 cm). T1 is mounted on a translation stage for fine-adjustment of the distance to the BEC. The beam is reflected into the glass cell using a beam splitter substrate S1 (home-built, reflectivity $R_{780} = 9.7\%$), mounted on a mirror holder with differential micrometer screws for fine-alignment of the beam onto the BEC. The transmitted light is reflected from an identical substrate (to compensate wavelength dependency) and used for the intensity control of the beam using the AOM. After the glass cell, a dichroic mirror substrate S2 reflects the lattice beam and allows for superimposing the dipole trap beam D1 at 1064 nm (compare also Figure 2.3). Subsequently, the beam is coupled into T2 (same components as T1) using another differential screw holder, used for superimposing the back reflected lattice beam with the incident beam. The cube in T2 superimposes the lattice with the homodyne beam (perpendicular polarizations). These beams are coupled into the planar fiber of the MiM device (PM fiber with AR-coated FC/APC connector). The fiber coupler in T2 is installed in a rotatable cage system mount (for PM coupling without wave plate).

resonant lattice during the BEC cycle (see Figure 2.4). Subsequently, the light is coupled into a polarization maintaining (PM) fiber for guiding the light into the lower room where the BEC machine is located. This fiber is connected to the first lattice telescope T1, which consists of a fiber collimator, a polarizer cube for optimizing the polarization purity and a focusing lens (see Figure 2.22). The telescope has a working distance of approximately 50 cm and is mounted on a translation stage in order to fine-adjust the beam focus z-position with respect to the BEC in the vacuum glass cell. The corresponding xy-alignment is done with differential micrometer screws in one of the mirror holders in front of the glass cell. The usage of differential screws is necessary due to the small lattice beam waist of $w_{\mathrm{lat}} = 78\,\mu\mathrm{m}$, which needs to be centered on the BEC. The mirror in this specific holder is a home-built substrate S1 with a reflectivity of $R_{780} = 9.7\%$ at 780 nm which is used to pick up light for the intensity control of the lattice beam. In order to control the lattice power P_{lat} at the position of the atoms, the control signal needs to be measured at a position where the power is proportional to P_{lat}. This is why we pick up the control light *after* purifying the polarization. Nevertheless, the reflectivity of the beam splitter substrate has a small wavelength dependency ($R_{780}/R_{783} = 1.02$) which would alter the control power in the glass cell if the wavelength of the lattice is changed. Therefore, we employ a second, identical substrate and pick up the reflected light for the intensity control (see Figure Figure 2.22). In this way, the parasitic effect of the wavelength dependency is suppressed by 99%. After the glass cell with the BEC, the beam is coupled into the telescope T2. This is done with a second mirror holder with differential screws, which is crucial for the fine-alignment of the back reflected beam with the incident beam in order to create an optical lattice. The PBS in telescope T2 is used for superimposing the homodyne detection beam with the lattice. Both beams are coupled into the planar (PM) fiber of the MiM device with perpendicular polarizations. In order to align the polarizations with the PM axes of the fiber, the components of telescope T2 are mounted in a cage system with a rotatable mount for the fiber coupler. In this way, additional optical losses of a wave plate to rotate the polarization can be avoided. The light gets reflected by the fiber cavity in the MiM device and after the reflected beam has passed the glass cell again it can be monitored on a photodiode behind the substrate S1 (see Figure 2.22). For example, this photodiode is very useful for monitoring the fiber coupling of the lattice into the cryostat, the cavity signals (cavity alignment, tuning on resonance, length determination, etc.) and the time evolution of the lattice power in experimental cycles.

Intensity control: stabilization, ramping and pulse generation. The intensity control for the lattice (bandwidth $\approx 50\,\mathrm{kHz}$) is based on a home-built analog control box. It stabilizes the signal from the intensity control photodiode (see Figure 2.22) to an analog reference signal by active feedback on the RF input of the lattice AOM. This is done by coupling the RF drive signal (90 MHz sine from a DDS) for the high-power AOM amplifier through a mixer and modulate the DC port of the mixer with the control signal from the intensity control box. In this way, the lattice power P_{lat} at the position of the atoms can be stabilized and ramped up and down with analog reference signals from the experimental control.

However, in some experimental protocols for the lattice it is necessary to generate arbitrary pulse strains of the lattice beam. For example, the characterization of deep lattices using Kapitza-Dirac diffraction of ultra-cold atoms is performed with short

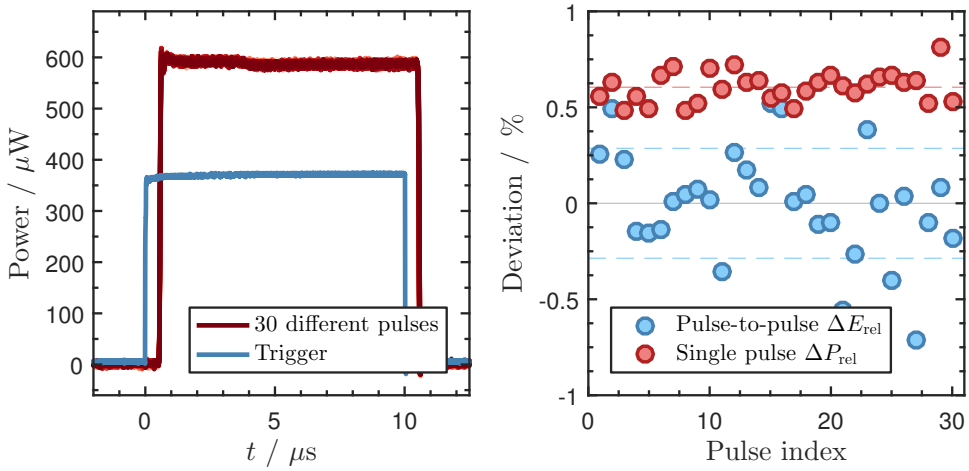

Figure 2.23: Performance of lattice pulse generation. For 30 experimental cycles (cycle time 26 s), a single lattice pulse of duration 10 µs was generated as described in the text (duration between sample-and-hold slot to the pulse ≈ 20 s). **Left:** 30 time traces of the pulses (red) and the pulse trigger (blue) from the experimental control. All 30 pulses perfectly overlap. Delay between pulses and trigger: 500 ns. The overshoot at the beginning of the pulses is an artifact of the used photodiode (intensity control photodiode, PDA36 from *Thorlabs*). **Right:** Analysis of the pulse fluctuations. Blue: shot-to-shot fluctuations ΔE of the integrated pulse energy from the mean value $\bar{E}$, normalized to $\bar{E}$. The root-mean-square (rms) deviation of 0.3% is indicated by the dashed blue lines. Red: rms deviation ΔP from the mean power $\bar{P}$ during a single pulse, normalized to $\bar{P}$. The average value of 0.6% is indicated by the dashed red line.

pulses of the lattice beam (see subsection 2.4.2). The duration of these pulses needs to be adjusted on the order of 100 ns. Furthermore, for loading a BEC into a near-resonant lattice, we perform an optimal control sequence for non-adiabatic state transfer into the ground state of the lattice. This procedure uses pulse strains of two or more pulses with a total duration of approximately 25 µs. Further details on the non-adiabatic loading of the lattice will be presented in the thesis of T. Wagner. We create these arbitrary pulse strains using a programmable function generator which is triggered and programmed by the experimental control via VISA commands. This function generator triggers a fast RF switch in the RF signal path of the AOM driver. In order to prevent interference with the intensity control (the RF switch is installed in the feedback control loop), we use the sample-and-hold function of the control box. In a typical experimental sequence, we regulate the lattice power to the desired value and use this sample-and-hold function to store the corresponding control signal in the control box. The light is then switched off and later switched on again for the pulse strain using the stored control signal for the AOM power. The power is then not regulated anymore, but set to the desired mean value by the hold function, whereas the time sequence of the pulse strain is generated by the function generator.
In this way, we are able to adjust pulse lengths on the order of 100 ns with a cycle-to-cycle pulse power stability of 0.3% in a normal BEC cycle of approximately 25 s (see Figure 2.23). For this technique it is particularly important to optimize the fiber coupling of the lattice in the upper room, because during the pulses the power fluctuations due to imperfect fiber couplings are not compensated by the intensity control.

Optical losses. In order to achieve a maximum cooperativity C_{hybrid} of the hybrid system, light losses in the coupling beam path should be as small as possible. Besides the linear decrease of C_{hybrid} with the optical losses [102], also more complex nonlinear effects can lead to a reduction of the hybrid coupling rate or even instabilities in the hybrid system [103, 104]. In section 5.1.3, these effects will be discussed in detail. Furthermore, the optical losses lead to a reduced lattice depth V_0 for a given incident beam power P_{lat}. This must be compensated by increasing the input power or by decreasing the detuning Δ from the atomic transition. The former leads to parasitic effects like heating of the cryogenic MiM device, heating of the mechanical oscillator or a potentially larger optical spring effect, which shifts the mechanical resonance frequency (see section 3.1). A small detuning Δ leads to an increased photon scattering of the atoms in the lattice and an effective loss of atoms which participate in the coupling through heating of the atoms out of the lattice potential.
For the above reasons, it is important to characterize the different optical loss mechanisms to optimize the optical setup and the system parameters. A detailed sketch and a listing of the measured losses of the optical elements is given in appendix A.1. The most relevant losses are the low reflectivity on resonance $\sigma_{\text{ref}} = 0.61$ of the aligned MiM system and the fiber coupling into the MiM cavity fiber, which also exhibits relatively large internal losses. All in all, only 35% of the light that passes the atoms in the lattice incident beam is reflected back to the atoms. This leads to a large power imbalance of the coupling lattice beams, which will be discussed later. In a future setup, a reflected power of 60% instead of 35% is a realistic prospect (see appendix A.1).

2.4.2 Coupling lattice depth calibration

In order to perform quantitative measurements with the coupling lattice, the lattice depth needs to be calibrated, which is discussed in this subsection. The presented measurements as well as the construction of the coupling lattice (see subsection 2.4.1) were performed by the author together with T. Wagner, who also programmed the Kapitza-Dirac fit routine which numerically solves the time dependent Schrödinger equation.
The depth of the lattice potential in the beam waist $V_0 \sim I_0/\Delta$ [101] depends on the lattice detuning Δ from the atomic transitions and the intensity I_0, which is given by the beam waist w_{lat} and the beam power P_{lat}. In principle, the quantities w_{lat}, P_{lat} and Δ can be measured precisely and the corresponding lattice depth V_0 can be calculated very accurately. However, the theoretically predicted V_0 usually deviates strongly from the experiment. The most critical factor is usually the alignment of the lattice beams with respect to each other (radial xy-alignment and z-position of the waists) and the alignment of the intensity maximum of the two beams with respect to the atoms. All these misalignments are difficult to measure. Further imperfections can be wave front errors in the beams, whose effect on the lattice depth may also be hard to predict. Moreover, pump asymmetries due to different waists or powers of the two beams (e.g. due to losses in the back reflected beam) can lead to a complex distortion of the lattice geometry through atomic back-action or dynamical instabilites of the atoms [103]. For these reasons, a calibration of the achieved lattice depth with respect to the theoretical value V_0 is necessary.

Since a direct measurement of the quality of the optical lattice is very difficult, optical lattices are usually calibrated indirectly by looking at an atomic sample in the lattice potential. For this, we use Kapitza-Dirac diffraction of ultra-cold atoms and validate the resulting lattice depths via parametric heating measurements of BECs in shallow lattices [105, 106]. The Kapitza-Dirac diffraction also generates an unambiguous signal which can be used to optimize the alignment of the lattice.

Principles of Kapitza-Dirac diffraction

The diffraction of matter waves from a standing light wave was originally predicted for electrons by Kapitza and Dirac in 1933 [107]. After the first observation of Kapitza-Dirac diffraction in a BEC in 1999 [108], it has become a standard tool in the field of ultra-cold atoms in optical lattices.
The effect can be understood as a coherent process of multi-photon scattering events. The atoms are located in a standing light wave, which can be regarded as two plane waves with the same intensity and frequency that travel in opposite directions. The lowest energy coherent process is the two-photon scattering event of absorption and stimulated emission into one of the two waves. While this process preserves the energy, the momentum change of the atoms is either zero (emission into the same wave) or $\pm 2\hbar k$ (emission into the opposite wave) along the direction of the traveling waves. During the interaction time with the optical lattice, the atoms experience coherent Rabi oscillations between these two momentum orders. Hence, if the lattice is switched off after a certain time Δt, the interaction has generated a certain population transfer from the initial order $p = 0$ to the first momentum order at $p = \pm 2\hbar k$. This momentum distribution can be measured via time-of-flight (TOF) images of the BEC. In a cycled experiment with different lattice pulse times Δt, the Rabi oscillations of the momentum orders can be visualized and its frequency is directly proportional to the lattice potential depth V_0. This is the basic principle of the lattice depth calibration using Kapitza-Dirac diffraction.
If the intensity of the light waves is increased (or the detuning Δ to the atomic transition is reduced), even higher order scattering processes ($p = \pm 4, 6, ... \hbar k$) start to become important. Since these processes have different Rabi frequencies, the resulting interference between all the coherent scattering processes leads to a more complicated time evolution of the momentum orders. For this, it is useful to turn away from the single particle picture above and describe the Kapitza-Dirac diffraction as the time evolution of waves in a periodic potential, similar to the formalism of electronic Bloch waves in an atomic crystal.
The eigenfunctions of a single particle in a periodic potential $V(x)$ are given by the Bloch wave functions

$$\psi_{n,q}(x) \;=\; e^{iqx/\hbar} \cdot u_{n,q}(x)\,, \tag{2.9}$$

where q is the quasi momentum of the wave function, n is the band index and $u_{n,q}(x)$ is a function with the same periodicity as $V(x)$, which in this case is the optical 1D-lattice[2] potential $V(x) = V_0 \cos^2(kx)$ with a periodicity of $\lambda/2 = \pi/k$. Neglecting mean-field

[2]This can be generalized to the 3D case, since the corresponding Hamiltonian is fully separable.

interactions, a BEC can be modeled as such a matter wave $\psi_{n,q}(x)$ in the optical lattice. If we use a BEC as a probe for the lattice potential, the information on the lattice depth V_0 is encoded in the function $u_{n,q}(x)$. However, since the BEC is measured in free space during TOF, we can only measure the Bloch state in the plane wave basis of the free space Hamiltonian. Therefore, it is useful to express the time evolution of the Bloch state in the basis of plane waves. In this basis, the Hamiltonian is non-diagonal and the wave function experiences a non-trivial time evolution, which can be directly measured with TOF images.
The Hamiltonian in the plane wave basis can be found by expressing the functions $u_{n,q}(x)$ with plane waves. Since $u_{n,q}(x)$ is a periodic function, the solution is simply given by the Fourier series $u_{n,q}(x) = \sum_{l=-\infty}^{\infty} c_{l,n,q} e^{i2klx}$, where the periodicity was set to be $\lambda/2$. With this ansatz the Bloch functions become

$$|n,q\rangle = \psi_{n,q}(x) = \sum_{l=-\infty}^{\infty} c_{l,n,q} \, |\phi_{2l\hbar k+q}\rangle \quad \text{with} \quad |\phi_{2l\hbar k+q}\rangle = e^{i(2lk+q/\hbar)x} \, . \tag{2.10}$$

Inserting this into the time independent Schrödinger equation yields [109]

$$\sum_{l=-\infty}^{\infty} H_{l,l'} \cdot c_{l,n,q} = E_{n,q} \, c_{l,n,q} \quad \text{with} \quad H_{l,l'} = \begin{cases} (2l + q/\hbar k)^2 + s/2 & \text{if } l = l' \\ -s/4 & \text{if } |l - l'| = 1 \\ 0 & \text{else} \end{cases} , \tag{2.11}$$

where $s = V_0/E_\mathrm{r}$ is the lattice potential depth in units of the recoil energy $E_\mathrm{r} = \hbar^2 k^2/2m$. For our analysis we assume that the lattice interaction takes place on a time scale that is much faster than the motion of the atoms. This so-called *Raman-Nath regime* [110] is a very good approximation, since we keep our BEC in the dipole trap during the lattice pulse ($q = 0$) and the lattice pulses are much shorter than the trapping frequency in the lattice. This means that the kinetic energy before and after the lattice interaction is zero, which is why we set $q = 0$ in the Hamiltonian above. It should be noted that for very deep lattices the trapping frequency becomes comparable to the time scale of the lattice pulses. However, in deep lattices the band structure becomes flat, which means that the Hamiltonian is also independent of q.
In order to fit the data from our TOF images, we numerically solve the time dependent Schrödinger equation $i\hbar \frac{\partial}{\partial t} |\psi(t)\rangle = H \, |\psi(t)\rangle$, where $|\psi(t)\rangle$ is a normalized vector with $2l + 1$ entries for the momentum orders ranging from $-l$ to l. We usually cut off the Hamiltonian at the maximal momentum order that can be detected in the absorption images. The entries of the parametric solution $|\psi(t)\rangle$ for each momentum order l can be fitted to the measured occupations N_l/N_tot in this specific order. Further mathematical details can be found in appendix A.2.

Validation of the Kapitza-Dirac calibration

In order to validate our Kapitza-Dirac calibration in a simple configuration, the back reflex of the lattice was generated by a mirror instead of the fiber cavity. In this way, possible parasitic effects like power fluctuations or phase noise of the back reflected

beam could be avoided. Furthermore, the Kapitza-Dirac measurements were compared with parametric heating measurements of a BEC loaded into the lattice [105, 106].

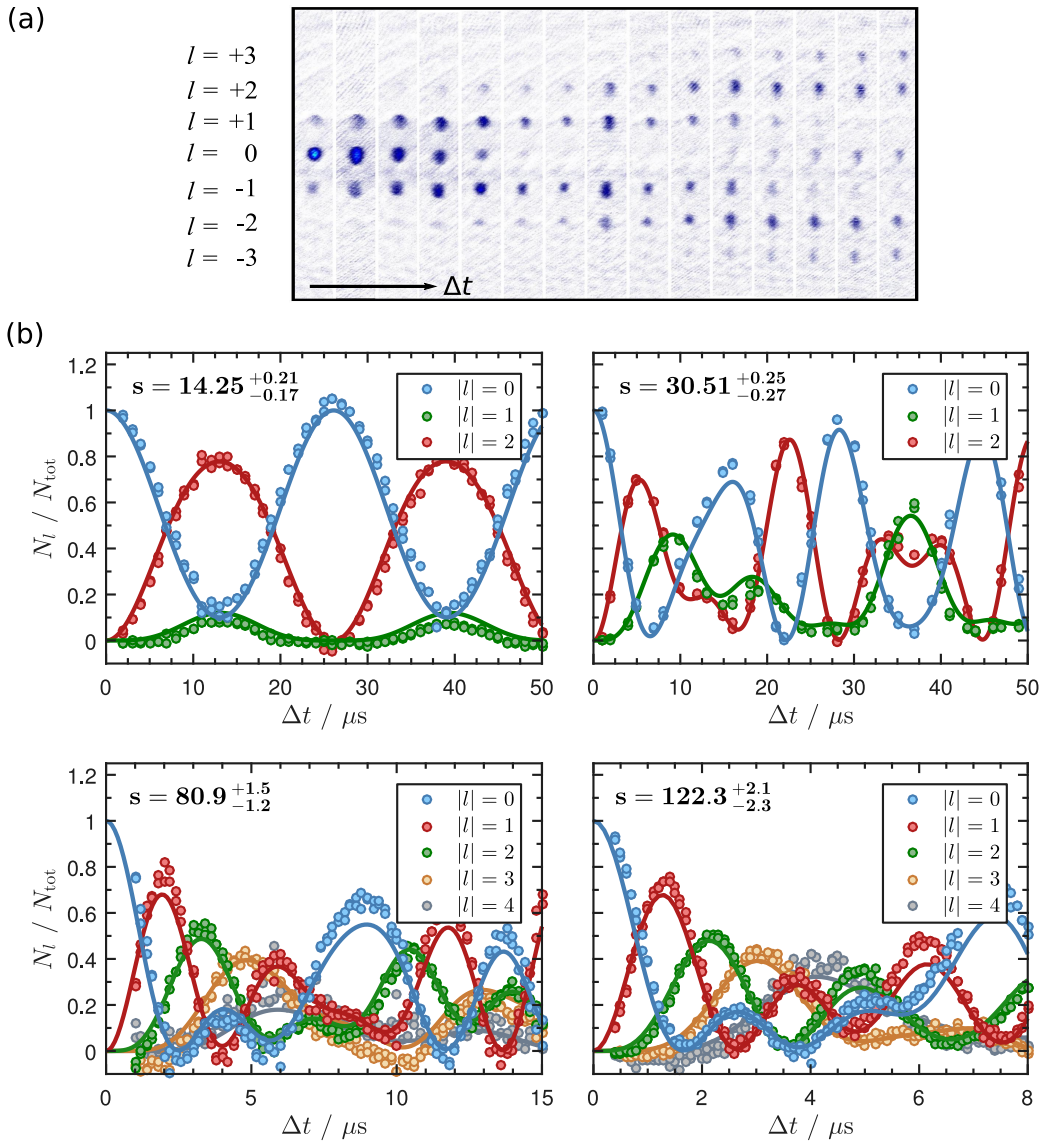

Figure 2.24: Time evolution during Kapitza-Dirac diffraction. (a) Images of a BEC in the dipole trap after a single lattice pulse during the hold time, acquired after 21.5 ms TOF for different lattice pulse duration Δt. The hold time in the dipole trap was 6 s to reduce the particle number and density effects like s-wave scattering. Each pulse leads to Kapitza-Dirac diffraction into different momentum orders l. The sequence was repeated once to obtain two samples for each Δt. The shown TOF images correspond to the fit in the lower left panel of (b) with $s \approx 80$. Lattice generated by a back reflex mirror. **(b)** Data from the TOF images and a fit to the data to obtain the lattice depth $s = V_0/E_\mathrm{r}$ for four different red lattice detunings Δ and constant lattice power $P_\mathrm{lat} = 1\,\mathrm{mW}$. The plots show the summed fractions N_l/N_tot of the atoms in the orders l and $-l$ and the fit functions multiplied by two, respectively. All momentum orders l were fitted together by minimizing the residual of all orders simultaneously which yields the value for s. The error bounds correspond to the lowest and largest boundaries of individual fits to the orders up to $|l| = 2$, which were performed separately.

Figure 2.24 (a) shows the TOF images of a typical Kapitza-Dirac measurement with a BEC in the dipole trap, which was illuminated by short lattice pulses of different duration Δt. The short pulses are generated with a dedicated function generator (see subsection 2.4.1). By fitting the parametric solution of the time dependent Schrödinger equation to the particle number in the different momentum orders, we can determine the lattice depth $s = V_0/E_\mathrm{r}$ with an accuracy of 1%, as shown in Figure 2.24 (b).
In this way, the lattice depth was determined for a constant power of $P_\mathrm{lat} = 1\,\mathrm{mW}$ and different detunings Δ between 60 GHz and 1700 GHz, as shown in Figure 2.25. The results were compared with parametric heating measurements [105, 106] of BECs which are loaded adiabatically into the lattice. For this, the lattice power is modulated at twice the atomic trapping frequency ω_a in the lattice and the excitation of atoms into higher bands is measured by counting the atom number in the momentum orders $l = \pm 1$ in the TOF images. The lattice modulation drives excitations at a frequency that corresponds to the energy between the lowest band and the third lowest band (according to $\Delta E = \hbar\omega_\mathrm{mod}$, $\Delta q = 0$ and parity conservation). We calculate the corresponding energy gap by solving the eigenvalues E_n of the Hamiltonian in equation 2.11 as a function of the lattice depth (assuming $q = 0$). Figure 2.25 shows the measured lattice depths s from the two different lattice calibration methods. Both methods agree very well for $s > 15\,E_\mathrm{r}$. For very large lattice depths only Kapitza-Dirac scattering can be used, since adiabatic lattice loading at small detunings $\Delta < 100\,\mathrm{GHz}$ is not possible for the parametric heating measurements.
A fit to the Kapitza-Dirac data of the test lattice with back reflex mirror yields a calibration of $c_\mathrm{cal} = s/s_\mathrm{theo} = 63.1\%$ between experimentally realized lattice depth s

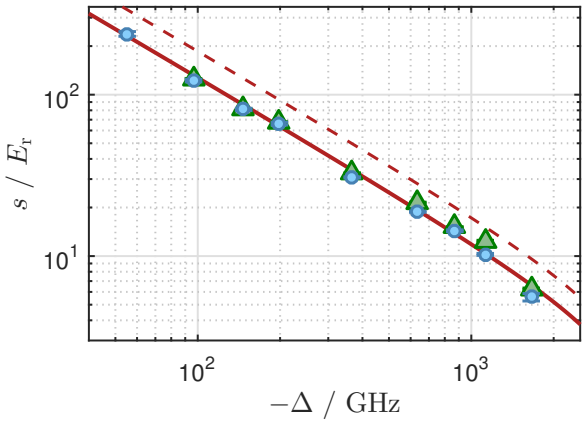

Figure 2.25: Validation of the Kapitza-Dirac lattice calibration. Kapitza-Dirac diffraction measurements (blue circles) of the lattice depth s compared to parametric heating measurements (green triangles) in a simple version of the lattice setup without fiber cavity (back reflex mirror instead of fiber coupler in telescope T2, see Figure 2.22). The different lattice depths were realized with a constant lattice power of $P_\mathrm{lat} = 1\,\mathrm{mW}$ and different red detunigs Δ between 60 GHz and 1700 GHz. The fit function (red solid line) to the Kapitza-Dirac data takes into account the D_1 line, as well as all involved hyperfine levels of the D_2 line. The fit yields a calibration of $c_\mathrm{cal} = s/s_\mathrm{theo} = 63.1\%$ of the theoretical lattice depth. Taking into account the optical losses of this setup (two times cube, lens, glass cell: $T_\mathrm{tot} = 0.845$, see appendix A.1), this realized lattice depth corresponds to $c_\mathrm{cal}/\sqrt{T_\mathrm{tot}} = 68.6\%$ of the theory value with losses (red dashed line). The measurements were performed over four days without realignment.

and the theoretical lattice depth s_{theo}. Here, s_{theo} follows from the incident beam power P_{lat}, the beam waist and the detuning (taking into account the D_1 line, as well as all involved hyperfine levels of the D_2 line). Including the known optical losses into the theoretical prediction s_{theo}, the resulting lattice depth is 68.6% of this value. Hence, the remaining lattice imperfections must originate from misalignment of the two lattice beams, deviations of the waists from the expected value or wave front distortions in the waist.

Lattice depth calibration

The optical coupling lattice in its final configuration ($T_{\text{MiM}} = 500\,\text{mK}$, setup as in Figure 2.22) was calibrated using the Kapitza-Dirac method described above. For this, the fiber cavity in the MiM device was tuned off-resonance with the piezo tubes, which creates a stable condition for the measurement. The resulting lattice depth $s = 19.0(2)E_{\text{r}}$ is 50.1% of the theoretical value ($P_{\text{lat}} = 500\,\mu\text{W}$, red detuning $\Delta_{\text{F=3}} = -264\,\text{GHz}$, taking into account the D_1 line and all involved hyperfine levels of the D_2 line, assuming no optical losses). If the optical losses of the back reflected beam are taken into account ($P_{\text{lat,2}} = T_{\text{tot}}P_{\text{lat}} = 0.576\,P_{\text{lat}}$, see appendix A.1), the realized lattice depth is $50.1/\sqrt{0.575} = 66.1\%$ of the theoretical value, as the lattice depth scales with $s \sim \sqrt{P_{\text{lat,2}}}\sqrt{P_{\text{lat}}}$.
In a further Kapitza-Dirac measurement, we validated that the lattice depth in a hybrid experiment (fiber cavity on resonance) is reduced by the expected factor $\sqrt{\sigma_{\text{ref}}} = 0.78$ due to the reduced power of the back reflected lattice beam: resulting lattice depths with fiber cavity on and off resonance $s_{\text{on}}/s_{\text{off}} = 0.79(3)$. Finally, the table below shows the realized lattice depth for a resonant (off-resonant) fiber cavity compared to the theoretical lattice depth including no losses (including the measured optical transmittance T_{tot}) in the back reflected beam, respectively (see appendix A.1). The fact that the resulting lattice depth is less than in the test lattice (with back reflex mirror) could be explained by a different waist size or waist z-position of the back reflected beam from the telescope T2. Also additional wave front distortions of this beam due to the fiber coupling could play a role.
Lattice alignment. For the final lattice alignment the incident beam was firstly aligned with respect to the atoms. For this, the near-resonant beam is first roughly aligned with respect to the MOT by looking at the resonant atom jet on a camera. Subsequently, the beam can be fine-aligned by maximizing the losses in the BEC. Afterwards, the back reflected beam is aligned by maximizing the Kapitza-Dirac diffraction into the first momentum order (see e.g. Figure 2.24 (a)). In this way, also the incident beam can be optimized again (using the differential screws in front of the glass cell). The alignment of the waist z-position of the back reflected beam using the BEC is very difficult and could not be performed. The fact that the z-position was only adjusted by measuring the distance of the telescope T2 to the glass cell might be the reason for the lower lattice depth compared to the test lattice.

Lattice depth calibration		
	cavity on resonance	cavity off-resonant
$c_{\text{cal}} = s/s_{\text{theo}}$	0.39 ± 0.01	0.50 ± 0.01
$c'_{\text{cal}} = s/(\sqrt{T_{\text{tot}}} \cdot s_{\text{theo}})$	0.52 ± 0.01	0.66 ± 0.01

Chapter 3

Optomechanics in the MiM system

To determine the optomechanical properties of the MiM device, a thorough characterization was performed. This enabled a precise optimization of the optomechanical coupling strength and a self-contained calibration method for homodyne thermometry of the mechanical mode temperature. The calibration was validated through temperature sweeps of the MiM device.

As discussed in the preface of chapter 2, the hybrid experiment benefits from a large optomechanical cooperativity between the coupling laser beam and the mechanical oscillator. In order to fine-align this optomechanical coupling, the optomechanical properties of the MiM device were characterized by measurements on the fiber cavity. This chapter covers the principles of cavity optomechanics in MiM systems, the performed characterization and alignment measurements on the MiM device and the homodyne detection of the mechanical oscillator.

The interdisciplinary field of cavity optomechanics [8] seeks control over mechanical quantum states by exploiting the powerful tools of quantum optics in optomechanical systems. The huge success of combining mechanical systems and quantum optics in the last two decades has lead to unprecedented engineering concepts for precision sensing, a wide variety of possible applications for novel quantum technologies and has opened the door for fundamental tests of quantum mechanics in a completely new parameter regime of macroscopic quantum objects. The transferability of techniques between quantum optics and optomechanics was facilitated by a strong analogy between the two fields: the optomechanical situation of an optical cavity mode interacting with a mechanical mode can be mapped onto the case of two-mode quantum optics where two optical modes interact via a non-linear medium [111]. The prototypical setup of this optomechanical paradigm is an optical cavity with a vibrating end mirror [112]. The motion of the end mirror changes the resonance frequency of the cavity and thus the intra-cavity pump power. This changes the amount of radiation pressure on the mirror which creates an optomechanical coupling between the mechanical motion and the cavity mode. Most of the optomechanical systems are modifications of this simple scheme.

A particularly well-studied optomechanical system is the so-called *membrane-in-the-middle* (MiM) configuration, where a thin dielectric membrane is placed between the

two mirrors of a Fabry-Pérot cavity [64, 65, 84, 113]. Recently, MiM systems were utilized for the observation of radiation pressure shot noise on mechanical motion [114], mechanical ground state cooling [40], as well as sympathetic cooling [57] and quantum back-action-evading measurements [59] in hybrid atomic-mechanical systems. The huge success of the MiM scheme is mainly based on the fact that the mechanical oscillator does not serve as an end mirror of the optical cavity, which would require a combination of exceptionally good mechanical and optical propoerties. In contrast, the MiM scheme combines the high mechanical Q-factors of membrane oscillators with the well-established production of optical high finesse cavities. Since the membranes are optically flat they scatter photons in a well-defined direction, which allows for stable high finesse cavity modes in the MiM scheme [112]. In this way, a purely dispersive (non-dissipative) optomechanical coupling can be created if the membrane is placed at the slope of the intra-cavity field. In this configuration of linear optomechanical coupling, the cavity detuning $\Delta\omega_{\mathrm{cav}}$ depends linearly on the membrane position x. Another interesting feature of the MiM scheme is the possibility to place the membrane at a node (or antinode) of the intra-cavity field. In this way, a quadratic dispersive coupling $\sim x^2$ is generated, which allows for quantum non-demolition (QND) measurements of the membrane's phonon number eigenstate [84]. The periodic change from linear to quadratic coupling (and even quartic coupling if the membrane is tilted) is another special feature of the MiM scheme [113].

3.1 Optomechanical coupling

In cavity optomechanical systems the mechanical displacement x_{m} changes the resonance frequency ω_{cav} of the cavity. For a simple Fabry-Pérot cavity of length L with a moving end mirror, this displacement-induced frequency shift is given by the optomechanical coupling G [112]:

$$G = \frac{\partial\omega_{\mathrm{cav}}}{\partial x_{\mathrm{m}}} = \frac{\omega_{\mathrm{cav}}}{L}\,. \tag{3.1}$$

However, in a MiM system the optomechanical coupling $g_{\mathrm{m}} = \partial\omega_{\mathrm{cav}}/\partial x_{\mathrm{m}}$ has a more complicated form and depends on many more parameters than just the total cavity length. For example, g_{m} is periodic in the membrane position x_{m}, as mentioned above. Hence, the membrane must be placed precisely at the right position of the intra-cavity field to obtain the maximal linear coupling. The best way to measure the behavior of g_{m} as a function of the membrane position in our system is to vary the distances L_1 and L_2 between the fibers and the membrane (see Figure 2.6), while measuring the transmission of the MiM system. In this way, the effective membrane position x_{m} in the cavity can be varied while the transmission signal provides information on the resonance condition, which yields the sought quantity $\omega_{\mathrm{cav}}(x_{\mathrm{m}})$.

In order to simulate this behavior of g_{m} in a MiM system for different subcavity lengths L_1 and L_2, the transmission $|t_{\mathrm{MiM}}|^2$ can be calculated using the transfer matrix formalism of a simple planar Fabry-Pérot cavity with a semitransparent film in the middle [115]. We use the explicit expression in [102] for $|t_{\mathrm{MiM}}(L_1, L_2)|^2$, which was calculated from the transfer matrices. Figure 3.1 (a) shows the calculated transmission $|t_{\mathrm{MiM}}|^2$ for

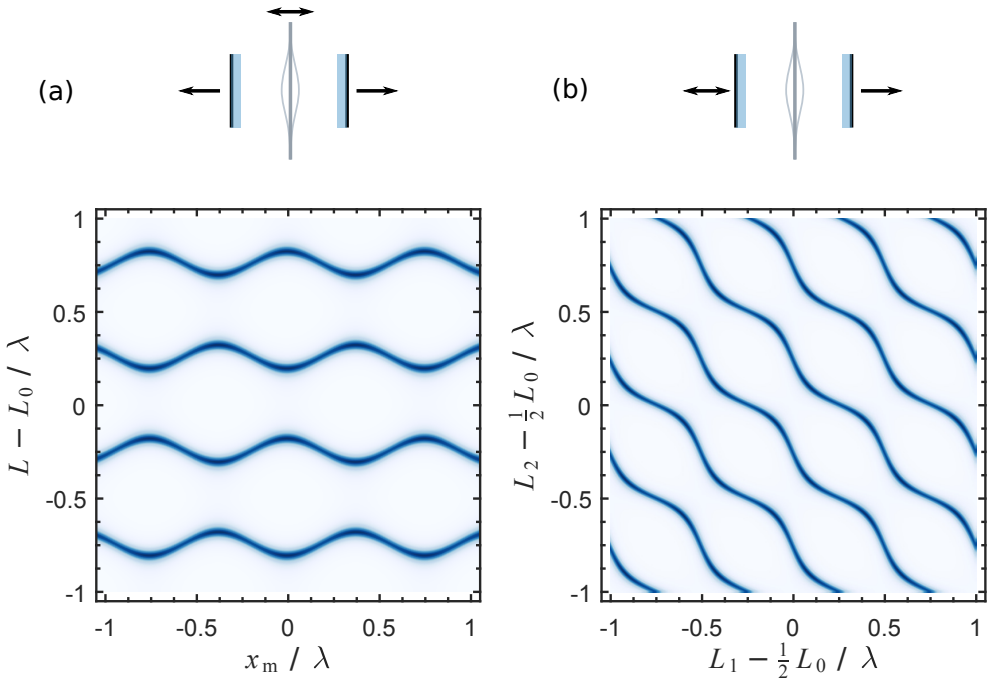

Figure 3.1: Modulation of the cavity resonant length by the membrane. Numerical simulation of the MiM transmission $|t_{\mathrm{MiM}}(L_1, L_2)|^2$ (eq. 1.69 in [102]) of a planar-planar Fabry-Pérot cavity for different subcavity lengths L_1 and L_2 (or the effective membrane position $x_m = (L_1 - L_2)/2$). Parameters used: mirror power reflectivities $R_1 = R_2 = 0.75$, membrane field reflectivity $r_m = 0.38$, total cavity length $L_0 = 2.34\,\mu\mathrm{m}$, $\lambda = 780\,\mathrm{nm}$, assuming no losses. **(a)** Four different resonant cavity lengths $L = L_1 + L_2$ for different membrane positions $x_m = (L_1 - L_2)/2$. L is altered by a symmetric change of the subcavity lengths L_1 and L_2 around the membrane. **(b)** $|t_{\mathrm{MiM}}|^2$ for an independent scan of the lengths L_1, L_2. The small sketches above indicate how the plots can be generated experimentally.

a planar Fabry-Pérot cavity as a function of the membrane position x_m and the total length $L = L_1 + L_2$. Here, L is varied by a symmetric change of L_1 and L_2 around the membrane. The sinusoidal lines correspond to the resonant lengths of the cavity, which are altered periodically by the position of the membrane. If the membrane is well centered in the MiM system ($L_1 = L_2$), this is also the expected plot for the resonant laser frequency as a function of the membrane position. The derivative of the sinusoidal resonance lines is related to the optomechanical coupling g_m in the MiM device. The plot shows that g_m changes its sign for each resonant length and is equal for every second cavity resonance.

Nevertheless, the technically more relevant case is depicted in Figure 3.1 (b). This is because it can be performed without any prior knowledge of the piezo constants of the cavity mirrors, since both mirrors are scanned individually and do not need to be synchronized as for the symmetric case in (a). In the end of this subsection it will be discussed how such an image can be measured and how it can be used for aligning the MiM system and extract the optomechanical coupling g_m.

Figure 3.1 shows that the resonant length of the cavity changes sinusoidally with the membrane position. However, the physically more relevant quantity is the change of the resonance frequency ω_{cav} as a function of the membrane position, which is more

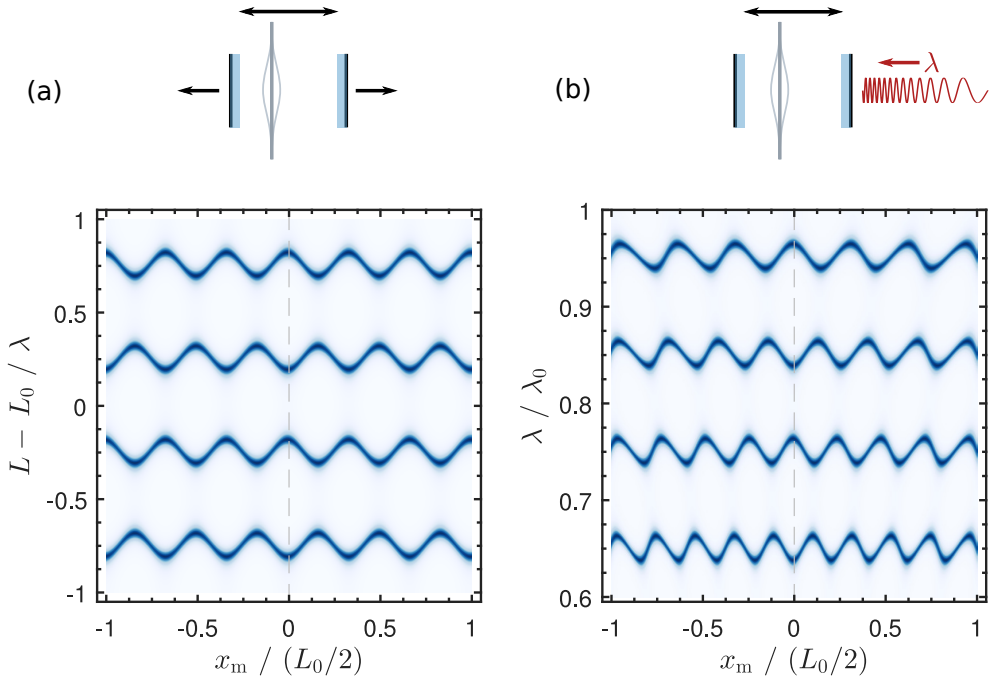

Figure 3.2: Modulation of the cavity resonance for off-centered membrane positions. Numerical simulation of the MiM transmission $|t_\mathrm{MiM}|^2$ (eq. 1.69 in [102]) of a short planar-planar Fabry-Pérot cavity for a sweep of the membrane position from one end mirror (at $x_\mathrm{m} = -L_0/2$) to the other end mirror of the cavity (at $x_\mathrm{m} = L_0/2$). Parameters as in Figure 3.1. **(a)** Four different resonant cavity lengths $L = L_1 + L_2$ for all possible membrane positions x_m in the cavity. L is altered by a symmetric change of the subcavity lengths L_1 and L_2 around the membrane. The sign of $|t_\mathrm{MiM}(x_\mathrm{m})|^2$ is equal for every second resonant length, which holds for all membrane positions. **(b)** $|t_\mathrm{MiM}|^2$ for four different resonant wavelengths λ and all possible membrane positions in the cavity. While $|t_\mathrm{MiM}(x_\mathrm{m} \approx 0)|^2$ is equal for every second resonance, the behavior for $|x_\mathrm{m}| = L_0/2$ is equal for every resonance, which yields an asymmetry of $\omega_\mathrm{cav}(x_\mathrm{m})$. The small sketches above indicate how the plots can be generated experimentally.

complicated, as it also depends on the macroscopic position of the membrane inside the cavity. This can be explained by a simple geometric argument. Consider a cavity with constant length L_0 with a membrane in the center ($L_1 = L_2$). If the driving laser is detuned by multiples of the FSR, the intra-cavity field at the membrane position will alternate between a node and an antinode, which yields the same g_m for every second FSR, similar to the symmetric length change as in Figure 3.1 (a). Now consider the case that the membrane is very close to one of the cavity mirrors. If the driving laser is detuned by multiples of the FSR, the intra-cavity field at the membrane position will look very similar from one FSR to the next. Hence, the optomechanical coupling must be periodic in one FSR, not in two FSR as if the membrane is centered. This behavior is depicted in Figure 3.2, which shows the change of the resonant length (a) and the resonant wavelength (b) if the membrane position is sweeped from one end mirror to the other.

Consequences of the asymmetry in $\omega_\mathrm{cav}(x_\mathrm{m})$. The fact that the behavior of $\omega_\mathrm{cav}(x_\mathrm{m})$ is altered if the membrane is off-centered was first described in [115] and has some important consequences. Firstly, the maximal optomechanical coupling $g_\mathrm{m}^\mathrm{max}$

is not equal for every slope of $\omega_{\mathrm{cav}}(x_{\mathrm{m}})$, which is relevant for the MiM fine-alignment presented later. Furthermore, $g_{\mathrm{m}}^{\mathrm{max}}$ can even become larger [115] than G for a moving end mirror (see equation 3.1). Hence, it can be beneficial to off-center the membrane in the cavity. This harmonizes well with the fact that the membrane in our planar-concave cavity is positioned close to the planar mirror, as mentioned in subsection 2.3.3 (Step 2 of MiM alignment). This is because close to the planar mirror the intra-cavity field has planar wave fronts, which means that reflected light from the membrane is reflected back into the cavity mode. This might be relevant especially for cavities with a larger finesse. Finally, the complicated behavior of g_{m} if the membrane is off-centered is the reason why measuring the total length of the MiM system by tuning the laser frequency (according to equation 2.7) is not reliable. This does not necessarily hold for measuring the total length of the MiM system with the white-light method described in subsection 2.3.3, because with much more resonances the membrane effects are averaged out.

Measurement of g_{m}

In order to measure the optomechanical coupling g_{m} of our fiber cavity MiM system, the theory plot in Figure 3.1 (b) was measured by acquiring the cavity transmission signal while the position of both cavity fibers were scanned at different frequencies

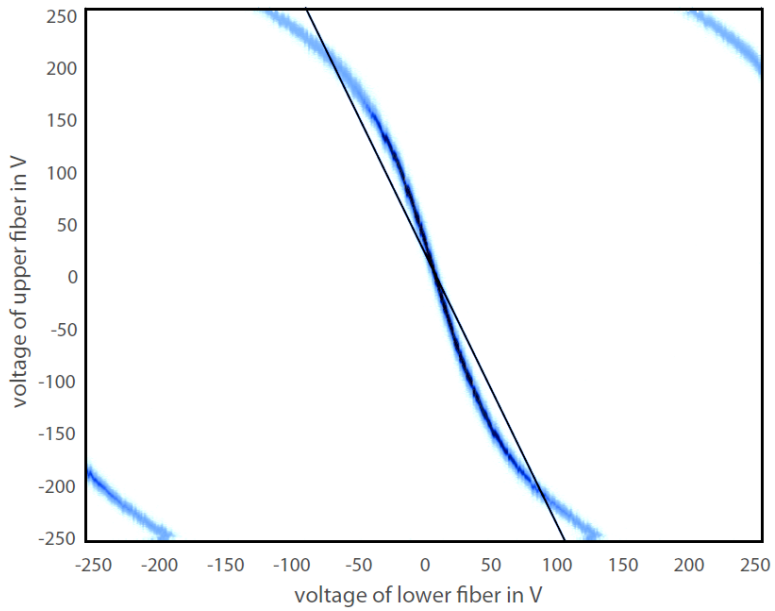

Figure 3.3: Transmission of the MiM system for different fiber positions. Measured transmission signal $|t_{\mathrm{MiM}}(L_1, L_2)|^2$ of the fiber MiM system for the maximum scan range of $\pm 250\,\mathrm{V}$ (of the used HV amplifier) applied to the piezo tubes of the MiM device (see Figure 2.6). The measurement corresponds to the simulation in Figure 3.1 (b). The solid line corresponds to a fit which indicates the line of constant cavity length $L_0 = L_1 + L_2$. Its slope (-2.43) is used to calibrate the piezo tubes with respect to each other, while the known distance $\lambda/2$ of the two resonances in the scan of the lower fiber gives an absolute calibration. Result: $c_{\mathrm{low}} = 1.24(1)\,\mathrm{nm/V}$, $c_{\mathrm{up}} = 0.51(1)\,\mathrm{nm/V}$. Parameters: cryostat temperature $T_{\mathrm{MiM}} = 500\,\mathrm{mK}$, $\lambda = 780\,\mathrm{nm}$, acquisition: upper fiber scanned with 10 Hz while lower fiber translated half a period with 10 mHz. Figure adapted from [116].

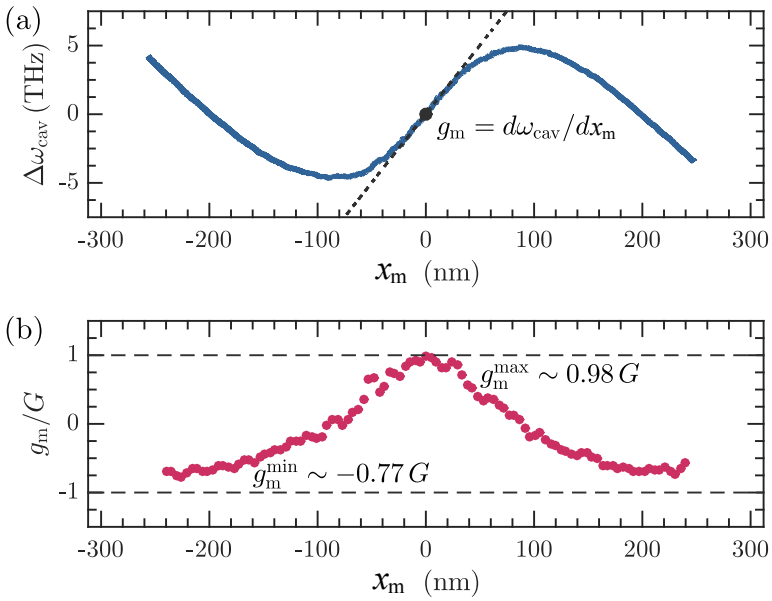

Figure 3.4: Change of resonance frequency through membrane displacement. (a) Measured change $\Delta\omega_{\mathrm{cav}}$ of the cavity resonance frequency as a function of membrane displacement x_{m} extracted from Figure 3.3 (see caption for parameters). The point of maximal linear optomechanical coupling g_{m} is indicated by the tangent (dashed line). **(b)** Numerical derivative of (a) in units of G (see equation 3.1). At $x_{\mathrm{m}} = 0$ the linear coupling g_{m} is maximal: $g_{\mathrm{m}}^{\mathrm{max}} = 0.98\,G$ with $G = 2\pi \times 16.2\,\mathrm{GHz/nm}$. At $|x_{\mathrm{m}}| = \lambda/4 = 195\,\mathrm{nm}$ the coupling is only $g_{\mathrm{m}}^{\mathrm{min}} = -0.77\,G$, caused by the asymmetry of $\Delta\omega_{\mathrm{cav}}(x_{\mathrm{m}})$ which is due to the off-centered membrane position ($L_1 \approx 6\,\mu\mathrm{m}, L_2 \approx 18\,\mu\mathrm{m}$). Figure taken from [85].

using high voltage at the piezo tubes (see Figure 2.6). In this way, $|t_{\mathrm{MiM}}(L_1, L_2)|^2$ can be measured in the whole parameter space of the maximum scan range of the piezo tubes. The measurement is shown in Figure 3.3. It shows that the maximum scan range of the used HV amplifier is not sufficient to scan the upper fiber over one FSR ($\lambda/2$). However, this is possible with the lower fiber which yields an absolute calibration of $c_{\mathrm{low}} = 1.24(1)\,\mathrm{nm/V}$ at the MiM temperature $T_{\mathrm{MiM}} = 500\,\mathrm{mK}$ [116]. The temperature is important since the piezo constants are strongly temperature dependent (for example, $c_{\mathrm{low}} = 1.70(1)\,\mathrm{nm/V}$ at $T_{\mathrm{MiM}} = 17\,\mathrm{K}$). The fit of the sinusoidal transmission signal $|t_{\mathrm{MiM}}|^2$ yields the line of constant cavity length (black line) which enables the relative calibration of the upper piezo tube: $c_{\mathrm{up}} = 0.51(1)\,\mathrm{nm/V}$ at $T_{\mathrm{MiM}} = 500\,\mathrm{mK}$ [116].
The calibration of the piezo tubes allows for converting the axes of Figure 3.3 in units of λ. In this way, the optomechanical coupling g_{m} can be extracted from the data. The result is shown in Figure 3.4, which shows that for our MiM configuration with $L_1 \approx 6\,\mu\mathrm{m}$ and $L_2 \approx 18\,\mu\mathrm{m}$ the maximal optomechanical coupling is $g_{\mathrm{m}}^{\mathrm{max}} = 0.98\,G = 2\pi \times 15.9\,\mathrm{GHz/nm}$ on the steeper slope of $\omega_{\mathrm{cav}}(x_{\mathrm{m}})$, while on the opposite slope it is $g_{\mathrm{m}}^{\mathrm{min}} = 0.77\,G = -2\pi \times 12.5\,\mathrm{GHz/nm}$. The data also allows for fitting the measured function $\omega_{\mathrm{cav}}(x_{\mathrm{m}})$ with the model [64, 65], which results in a membrane field reflectivity of $r_{\mathrm{m}} = 0.38$ [116]. This is close to the theoretical value of $r_{\mathrm{m}} = 0.4$ for our membrane. The fact that an oscillator with a very low power reflectivity of $R_{\mathrm{m}} = r_{\mathrm{m}}^2 \approx 0.15$ can reach the same optomechanical coupling ($g_{\mathrm{m}}^{\mathrm{max}} \approx G$) as a highly reflecting, moving end mirror confirms the surprising performance of MiM systems.

Alignment of g_m

As described above, the maximum linear optomechanical coupling $g_\mathrm{m}^\mathrm{max}$ is reached only if the membrane is placed precisely ($\Delta x_\mathrm{m} = \pm 10\,\mathrm{nm}$, see Figure 3.4 (b)) at the slope of the intra-cavity field. Furthermore, due to the off-centered membrane position in our MiM system, it must be ensured that the right slope is chosen, since for every second slope the coupling is only $g_\mathrm{m}^\mathrm{min}$.
The following alignment strategy holds for our current configuration of a planar-concave MiM system with the membrane close to the upper, planar fiber ($L_1 < L_2$, see Figure 2.6). The alignment goal is to reach a situation like in Figure 3.3, where the cavity is on resonance for very low voltages applied to the piezo tubes and the optomechanical coupling is maximal at the same time. To reach this point, we scan the lower fiber position with a triangular voltage at the piezo tube and observe the transmission signal like in Figure 3.3. By applying a DC voltage to the piezo tube of the upper fiber, the width of the transmission resonance can be minimized. This is achieved at the desired point of maximal optomechanical coupling (intersection point of transmission line and solid line in Figure 3.3). Similar to [65, 115], we also observe that the transmission is maximal at this point, which can be used as a further alignment signal. Subsequently, the z-stepper motor of the upper fiber can be used to compensate for the DC offset that was necessary to minimize the width of the transmission peak. Finally, the z-stepper motor of the lower fiber is used to shift the cavity resonance at approximately 6 V at the lower piezo tube, which is the optimal value for tuning the cavity on resonance with a 12 V battery, as described later.
We observe that this fine-alignment of the MiM device is stable over months, as long as the cryostat temperature is constant. This is indicated by the fact that the voltage that is needed to tune the cavity on resonance with the lower piezo tube is always the same (and symmetric drifts of L_1 and L_2 are rather unlikely).

Optical spring effect

In the above considerations, the shift of the cavity resonance frequency ω_cav due to the displacement of the membrane in the cavity was described by the optomechanical coupling $g_\mathrm{m} = \partial\omega_\mathrm{cav}/\partial x_\mathrm{m}$. Nevertheless, this interaction also works in the opposite direction: pumping the MiM system with a detuned laser leads to a shift $\Delta\omega_\mathrm{m}$ of the mechanical resonance frequency. To understand this effect, the oscillator position x_m must be treated as a dynamical quantity, not as a static quantity as in the previous considerations. The shift of ω_m by the so-called *optical spring effect* can be understood as a dynamical back-action of the radiation pressure on the oscillator [8, 112], which is modulated by the oscillator itself through the optomechanical coupling g_m (and a modulation of the intra-cavity power, correspondingly). This feedback effect can be treated mathematically in the same manner as the active feedback cooling formalism presented later in chapter 4. Here, the passive feedback loop generates a new effective susceptibility χ_eff of the mechanical oscillator with a new effective spring constant $k'_\mathrm{m} = m\omega'^2_\mathrm{m} = m(\omega_\mathrm{m}+\Delta\omega_\mathrm{m})^2$ and a new effective mechanical damping rate $\Gamma'_\mathrm{m} = \Gamma_\mathrm{m}+\Gamma_\mathrm{opt}$ [8]. This additional optomechanical damping rate Γ_opt can be positive or negative, which can lead to cooling or heating of the mechanical oscillator.
In the limit of weak radiation pressure the shift of the mechanical resonance frequency

$\Delta\omega_\mathrm{m}$ and the optomechanical damping rate Γ_opt are proportional to the intra-cavity photon number $\bar{n}_\mathrm{cav}$ and g_m^2 [8]:

$$\Delta\omega_\mathrm{m} = \bar{n}_\mathrm{cav}\, g_\mathrm{m}^2 x_\mathrm{zp}^2 \left[\frac{\Delta+\omega_\mathrm{m}}{(\Delta+\omega_\mathrm{m})^2+\kappa^2/4} + \frac{\Delta-\omega_\mathrm{m}}{(\Delta-\omega_\mathrm{m})^2+\kappa^2/4}\right] \tag{3.2}$$

$$\Gamma_\mathrm{opt} = \bar{n}_\mathrm{cav}\, g_\mathrm{m}^2 x_\mathrm{zp}^2 \left[\frac{\kappa}{(\Delta+\omega_\mathrm{m})^2+\kappa^2/4} - \frac{\kappa}{(\Delta-\omega_\mathrm{m})^2+\kappa^2/4}\right], \tag{3.3}$$

with the quantum zero-point motion $x_\mathrm{zp} = \sqrt{\hbar/(2m\omega_\mathrm{m})}$ of the oscillator, Δ the cavity detuning and $\kappa/2\pi = \mathrm{FSR}/\mathcal{F}$ the FWHM line width of the cavity resonance.
In order to measure the optical spring effect in our MiM system, the coupling beam ($P = 500\,\mu\mathrm{W}$) was coupled into the MiM device (see Figure 2.21) with the cavity on resonance. Subsequently, different Ti:sapph detunings were adjusted using the wave meter and the mechanical resonance frequency was measured with a spectrum analyzer connected to the homodyne detector (see section 3.3). The laser detuning leads to a cavity transmission signal which can be fitted very well with a Lorentzian, as shown in Figure 3.5. Hence, the intra-cavity power in this experiment is not constant as in equation 3.2 and we assume $\bar{n}_\mathrm{cav}$ to be a Lorentzian function of the cavity detuning. In this way, we can fit the optical spring shift $\Delta\omega_\mathrm{m}$ very accurately with equation 3.2, as shown in Figure 3.5. For the power of 500 µW the maximum frequency shift is $\Delta\omega_\mathrm{m}/2\pi \approx 30\,\mathrm{Hz}$ at a detuning $\Delta \approx 2\pi \times 2\,\mathrm{GHz}$ which corresponds to the point

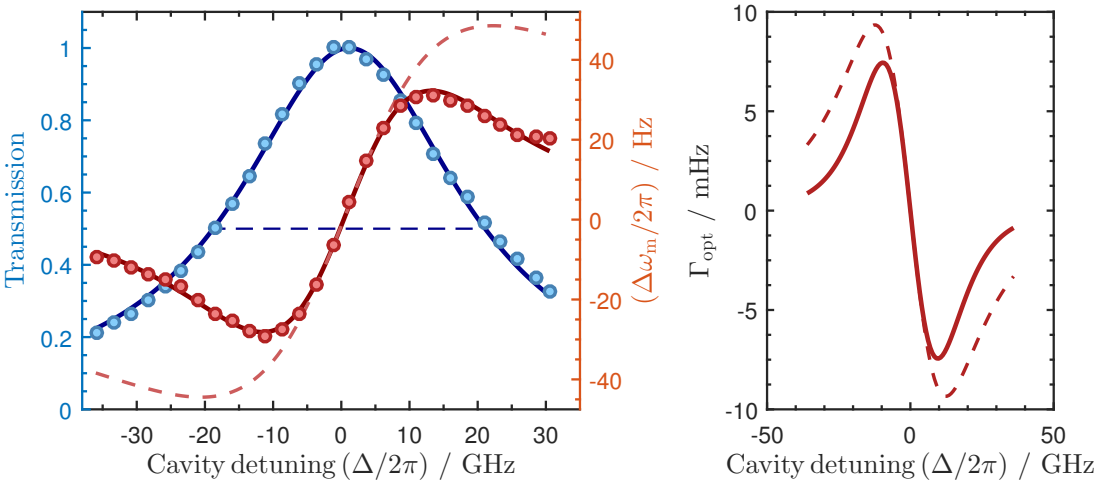

Figure 3.5: Optical spring effect in the MiM system. (Left) Measured cavity transmission (blue dots) with a Lorentzian fit (blue line) and measured mechanical frequency shift $\Delta\omega_\mathrm{m}$ (red dots) fitted with equation 3.2 modified by a Lorentzian intra-cavity photon number $\bar{n}_\mathrm{cav}(\Delta)$ for different Ti:sapph detunings Δ. The red dashed line indicates the fit result assuming constant $\bar{n}_\mathrm{cav}(\Delta = 0)$. The dashed blue line is the FWHM of the Lorentzian fit with $\kappa/2\pi = 40.0\,\mathrm{GHz}$, which deviates 7% from $\kappa/2\pi = 42.9\,\mathrm{GHz}$ which results from the fit to $\Delta\omega_\mathrm{m}$. Parameters: using coupling beam (see Figure 2.21/2.22) at 500 µW, deviation $\Delta\omega_\mathrm{m}$ from $\omega_\mathrm{m} = 2\pi \times 263.9\,\mathrm{kHz}$ (at $T_\mathrm{MiM} = 500\,\mathrm{mK}$) measured with a spectrum analyzer, fiber cavity passively stable (no lock). **(Right)** Optomechanical damping Γ_opt extracted from the fit of $\Delta\omega_\mathrm{m}$ (left) using equation 3.3 modified by a by a Lorentzian intra-cavity photon number $\bar{n}_\mathrm{cav}(\Delta)$. Γ_opt for constant $\bar{n}_\mathrm{cav}(\Delta = 0)$ indicated by the dashed line.

of approximately 70% cavity transmission. If the intra-cavity photon number would be constant at $\bar{n}_{\mathrm{cav}}(\Delta = 0)$ the maximum shift would be slightly larger ($\Delta\omega_{\mathrm{m}}/2\pi \approx 48\,\mathrm{Hz}$), which is indicated by the dashed red line.
Due to the same prefactor of the equations 3.2 and 3.3, the fit of $\Delta\omega_{\mathrm{m}}$ can also be used to extract the optomechanical damping Γ_{opt}, which is shown in the right panel of Figure 3.5. Similar to the fit of $\Delta\omega_{\mathrm{m}}$ we assume a Lorentzian function of $\bar{n}_{\mathrm{cav}}(\Delta)$ which yields a maximum optomechanical damping of $\Gamma_{\mathrm{opt}} \approx 7.5\,\mathrm{mHz}$ (again the function for a constant $\bar{n}_{\mathrm{cav}}$ is indicated by a dashed red line).
All in all, the optical spring effect in our current MiM system is almost negligible. This is caused by the small finesse of our cavity (small intra-cavity photon number $\bar{n}_{\mathrm{cav}}$) and the extremely large (empty cavity) linewidth $\kappa/2\pi \approx 75\,\mathrm{GHz}$ ($L \approx 20\,\mu\mathrm{m}$, $\mathcal{F} \approx 100$). Therefore, optomechanical cooling through dynamical back-action plays a minor role in our system, as the maximum cooling effect can be estimated to be a 10% reduction of the mechanical mode temperature using [57]

$$\frac{T_{\mathrm{opt}}}{T_{\mathrm{bath}}} = \frac{\Gamma_{\mathrm{m}}}{\Gamma_{\mathrm{m}} + \Gamma_{\mathrm{opt}}} \tag{3.4}$$

(assuming optimal detuning and $P = 1\,\mathrm{mW}$). Furthermore, small drifts of the cavity resonance during experiments will only cause very small drifts $\Delta\omega_{\mathrm{m}}$ of the mechanical oscillator frequency, which facilitates the time-resolved zero-span measurements of the oscillator temperature (as discussed later in section 4.4.1). This relaxes our demands on the cavity resonance condition and enables experiments without locking the cavity length, as discussed in the following.

Passive stability of the cavity length

In order to verify the passive stability of the fiber cavity length in our cryogenic MiM device, the cavity was tuned on resonance with a DC voltage from a stable power supply connected to one of the cavity piezo tubes. Subsequently, the transmission signal of the intensity controlled coupling beam was acquired over a period of 14 h. The measured fluctuations are on the order of 1% and include possible fluctuations of the fiber coupling into the MiM fiber and possible length changes of the cavity. Hence, this measurement

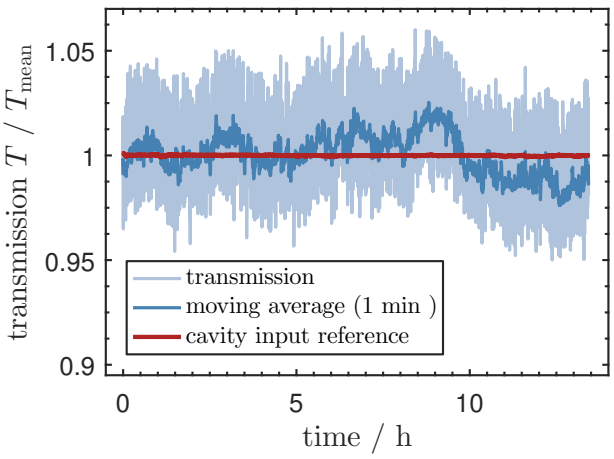

Figure 3.6: Transmission of the unlocked fiber cavity MiM device. Measured cavity transmission of an intensity controlled laser beam (red line: control signal) without locking the fiber cavity length, acquired over a time period of 14 h. The fluctuations include possible fluctuations of the fiber coupling into the MiM fiber and possible length drifts of the fiber cavity. Parameters: cryostat temperature stable at $T_{\mathrm{MiM}} = 500\,\mathrm{mK}$.

yields a lower boundary of the passive length stability of the cryogenic MiM system.
In the presented measurement in Figure 3.6 the passive stability of the fiber cavity length is so good that the optical spring effect (see Figure 3.5) (including the shift of the mechanical resonance frequency and the optomechanical damping Γ_{opt}) is completely negligible. However, in cycled experiments with beam powers on the order of 1 mW the thermal load of the laser can lead to a significant length change of the cavity and a potentially non-negligible optical spring effect. Therefore, we always monitor the cavity transmission signal (or the lattice reflection photodiode, see Figure 2.22) during cycled experiments to ensure that the thermal length drift is on an acceptable level. All measurements presented in this thesis were performed without using the Pound-Drever-Hall lock for the fiber cavity (see section 2.4).

3.2 Mechanical systems in the quantum regime

The previous section discussed how the motion of the mechanical oscillator in a cavity optomechanical system effects the optical mode of the cavity. However, the characteristic properties of this mechanical motion have not been discussed so far. It can be described in the framework of a thermally driven mechanical oscillator. This is important for understanding the characteristic displacement noise spectra of the oscillator, their relation to the mechanical mode temperature, the coupling to the environment, the timescales and sample size of the data acquisition and finally the quantum behavior near the quantum mechanical ground state. A comprehensive overview on the topic of nanomechanical systems in the quantum regime can be found in [7, 8, 115]. This section reviews the most important principles from these publications.
Assume a single, spectrally well isolated mechanical mode of vibration of frequency ω_{m}. The energy damping rate Γ_{m} describes the loss of mechanical energy of the mode and is related to the Q-factor: $Q = \omega_{\mathrm{m}}/\Gamma_{\mathrm{m}}$. The motion of the oscillator is generally described by some global mode displacement $x_{\mathrm{m}}(t)$, which can be defined very differently for different types of mechanical oscillators (consider cantilevers, doubly-clamped beams, membranes, microdiscs, etc.) or even for different modes of the same oscillator [7]. In order to describe the mode with the correct mechanical energy, the arbitrary definition of the mode function is accounted for by m_{eff}, the so-called *effective mass*. This is especially relevant for the measurement of the mechanical motion (see section 3.2). If the probe beam changes its size or the position on the mechanical mode function, the effective mass needs to be adapted in order to obtain the correct energy (or temperature) of the oscillator. For simplicity, the mechanical mode will in the following be regarded as being point-like with an effective mass $m_{\mathrm{eff}} = m$, which can easily be generalized to arbitrary mode functions with the corresponding $m_{\mathrm{eff}} \neq m$.
The temporal evolution $x_{\mathrm{m}}(t)$ of a thermally driven mechanical oscillator can be described by the equation of motion

$$m\frac{\mathrm{d}x_{\mathrm{m}}^2(t)}{\mathrm{d}t^2} + m\Gamma_{\mathrm{m}}\frac{\mathrm{d}x_{\mathrm{m}}(t)}{\mathrm{d}t} + m\omega_{\mathrm{m}}^2 x_{\mathrm{m}}(t) \;=\; F_{\mathrm{th}}(t)\,, \tag{3.5}$$

where $F_{\mathrm{th}}(t)$ denotes the random thermal Langevin force. Equation 3.5 can be solved in frequency space using the Fourier transform $x_{\mathrm{m}}(\omega) = \int_{-\infty}^{\infty} x_{\mathrm{m}}(t)e^{-i\omega t}\mathrm{d}t$:

$$-m\omega^2 x_\mathrm{m}(\omega) + im\omega\Gamma_\mathrm{m} x_\mathrm{m}(\omega) + m\omega_\mathrm{m}^2 x_\mathrm{m}(\omega) \;=\; F_\mathrm{th}(\omega)\,, \tag{3.6}$$

where $x_\mathrm{m}(\omega) = \chi_\mathrm{m}(\omega) F_\mathrm{th}(\omega)$ defines the mechanical susceptibility χ_m, which connects the external force to the response of the oscillator:

$$\chi_\mathrm{m}(\omega) \;=\; \frac{1}{m(\omega_\mathrm{m}^2 - \omega^2) - im\Gamma_\mathrm{m}\omega}\,. \tag{3.7}$$

Description in the frequency domain

The quantity $\langle |x_\mathrm{m}(\omega)^2| \rangle = S_\mathrm{x}(\omega)$ is called power spectral density (PSD) of the oscillator displacement. It is related to the force noise PSD $S_{\mathrm{F_{th}}}$ via the response function χ_m:

$$S_\mathrm{x}(\omega) \;=\; |\chi_\mathrm{m}(\omega)|^2\, S_{\mathrm{F_{th}}}(\omega)\,. \tag{3.8}$$

Assuming the force noise $S_{\mathrm{F_{th}}}$ is white around the oscillator bandwidth (and using expression 4.18 to integrate $|\chi_\mathrm{m}(\omega)|^2$), the (single-sided, $\omega > 0$) displacement PSD $S_\mathrm{x}(\omega)$ can be used to calculate the variance of the displacement:

$$\langle x_\mathrm{m}^2 \rangle \;=\; \frac{1}{2\pi}\int_0^\infty S_\mathrm{x}(\omega)\mathrm{d}\omega \;=\; \frac{1}{4}\frac{1}{m^2\Gamma_\mathrm{m}^2\omega^2}\, S_{\mathrm{F_{th}}}\,. \tag{3.9}$$

In thermal equilibrium the mode temperature of the oscillator equals the environmental temperature T_bath and the equipartition theorem relates the variance of the displacement to this temperature: $\frac{1}{2}m\omega_\mathrm{m}^2\langle x_\mathrm{m}^2\rangle = \frac{1}{2}k_\mathrm{B}T_\mathrm{bath}$. In this way, the relation between the single-sided force noise PSD $S_{\mathrm{F_{th}}}$ and the properties of the oscillator can be found:

$$S_{\mathrm{F_{th}}} \;=\; 4k_\mathrm{B}T_\mathrm{bath}\Gamma_\mathrm{m} m\,. \tag{3.10}$$

This Fluctuation-Dissipation Theorem shows that the force noise PSD can be obtained directly from the oscillator properties, without knowing its microscopic origin [7].
Out of equilibrium the force noise is no longer given by equation 3.10 and the oscillator temperature T_mode can be different from T_bath. However, the first equality in equation

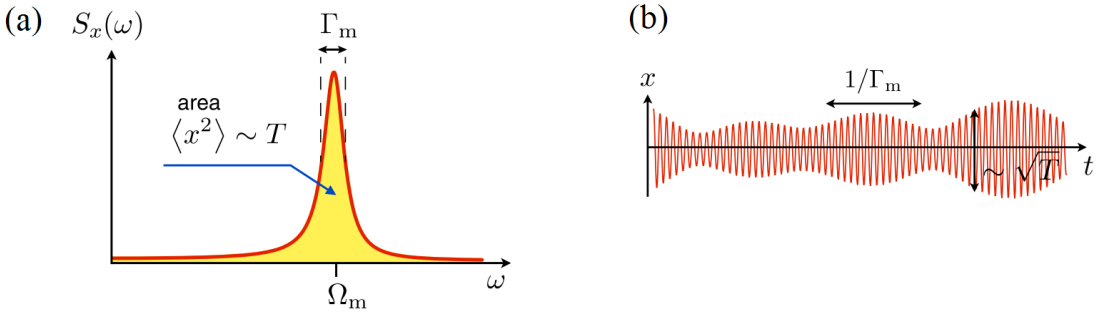

Figure 3.7: The oscillator in frequency and time domain. (a) Displacement noise PSD $S_\mathrm{x}(\omega)$ of a damped harmonic oscillator with natural damping rate Γ_m. The area under the curve is proportional to the mode temperature. **(b)** Brownian motion of the oscillator in time domain (schematic) with amplitude and phase fluctuations on a time scale set by Γ_m^{-1}. Figure taken from [8].

3.9 is always valid and one can define the general expression for the effective mode temperature of the oscillator:

$$T_{\mathrm{mode}} = \frac{m\omega_{\mathrm{m}}^2}{k_{\mathrm{B}}} \langle x_{\mathrm{m}}^2 \rangle = \frac{m\omega_{\mathrm{m}}^2}{k_{\mathrm{B}}} \cdot \frac{1}{2\pi} \int_0^\infty S_{\mathrm{x}}(\omega)\, \mathrm{d}\omega. \tag{3.11}$$

Hence, the mode temperature of the oscillator can be obtained by integrating the displacement PSD $S_{\mathrm{x}}(\omega)$, which yields the area under the PSD curve depicted in Figure 3.7 (a). For weak damping ($\Gamma_{\mathrm{m}} \ll \omega_{\mathrm{m}} \Leftrightarrow Q \gg 1$) this curve can be approximated by a Lorentzian of width Γ_{m}:

$$\begin{aligned} S_{\mathrm{x}}(\omega) &= |\chi_{\mathrm{m}}(\omega)|^2\, S_{\mathrm{F_{th}}}(\omega) = \frac{4k_{\mathrm{B}}T_{\mathrm{bath}}\Gamma_{\mathrm{m}}}{m} \frac{1}{(\omega_{\mathrm{m}}^2 - \omega^2)^2 - \Gamma_{\mathrm{m}}^2\omega^2} \\ \Rightarrow S_{\mathrm{x}}(\omega \approx \omega_{\mathrm{m}}) &\overset{Q\gg1}{\approx} \frac{k_{\mathrm{B}}T_{\mathrm{bath}}}{m\omega_{\mathrm{m}}^2} \frac{\Gamma_{\mathrm{m}}}{(\omega_{\mathrm{m}} - \omega)^2 + \frac{\Gamma_{\mathrm{m}}^2}{4}}. \end{aligned}$$

It should be noted that in the quantum regime ($k_{\mathrm{B}}T \approx \hbar\omega_{\mathrm{m}}$) the noise PSD becomes asymmetric around ω_{m} [117].

Description in the time domain

The time evolution of the thermally driven oscillator is of particular importance for the experimental determination of the mode temperature $T_{\mathrm{mode}} \sim \int_0^\infty S_{\mathrm{x}}(\omega)$. This is because the expectation value $\langle |x_{\mathrm{m}}(\omega)^2| \rangle = S_{\mathrm{x}}(\omega)$ of the displacement PSD can in principle only be measured over an infinite time or an infinite number of experimental runs. For this, the analysis of the theoretical time evolution $x_{\mathrm{m}}(t)$ of a thermally driven oscillator is necessary to estimate the principle limitations of experimental temperature determinations.

If a thermal noise force $F_{\mathrm{th}}(t)$ drives the oscillator with random kicks, the oscillator vibrates with its resonance frequency ω_{m} but its phase and amplitude vary on a much larger timescale, as depicted in Figure 3.7 (b). The auto-correlation functions of the displacement, amplitude and phase all fall off at time scales $\sim \Gamma_{\mathrm{m}}^{-1}$ [7].

Due to the Brownian motion of the oscillator the displacement PSD $S_{\mathrm{x}}(\omega)$ for temperature measurements must be acquired for a period $\tau \gg \Gamma_{\mathrm{m}}^{-1}$. However, this is experimentally not always possible, for example if a short interaction in the hybrid experiment is investigated. Therefore, the experiment must be performed many times N in order to obtain a meaningful temperature estimation. In [118] the Brownian motion was simulated numerically and the measurement error of the temperature T_{mode} of N averaged time traces of duration τ (with sufficient time separation $\gg \Gamma_{\mathrm{m}}^{-1}$) was quantified as:

$$\Delta T_{\mathrm{mode}} = \frac{T_{\mathrm{mode}}}{\sqrt{N(1 + \tau\Gamma_{\mathrm{m}}/2)}}. \tag{3.12}$$

Description in the quantum regime

For very low mode temperatures ($k_{\mathrm{B}}T_{\mathrm{mode}} \approx \hbar\omega_{\mathrm{m}}$), the classical description breaks down and the quantized energy-level structure of the mechanical oscillator becomes important. The quantum mechanical treatment yields the Hamiltonian $\hat{H} = \hbar\omega_{\mathrm{m}}(\hat{b}^\dagger\hat{b} +$

$\frac{1}{2}$) with the phonon creation ($\hat{b}^\dagger$) and annihilation ($\hat{b}$) operators. These are related to the position and momentum operators via $\hat{x} = x_{\mathrm{zp}}(\hat{b}^\dagger + \hat{b})$, $\hat{p} = im\omega_{\mathrm{m}} x_{\mathrm{zp}}(\hat{b}^\dagger - \hat{b})$, where

$$x_{\mathrm{zp}} = \sqrt{\frac{\hbar}{2m\omega_{\mathrm{m}}}} \tag{3.13}$$

is the zero-point fluctuation amplitude in the mechanical vacuum state $|0\rangle$. The quantity $\hat{b}^\dagger\hat{b}$ in the Hamiltonian is the phonon number operator, whose average yields the average phonon occupation $\bar{n}_{\mathrm{m}}$ of the quantum mechanical oscillator: $\bar{n}_{\mathrm{m}} = \langle\hat{b}^\dagger\hat{b}\rangle$.
The zero-point fluctuations lead to finite quantum thermal fluctuations at zero temperature which implies that in the quantum regime $T_{\mathrm{mode}} \neq T_{\mathrm{bath}}$ and at zero temperature the oscillator temperature saturates at the zero-point energy: $T^{\mathrm{zp}}_{\mathrm{mode}} = \frac{1}{2}\hbar\omega_{\mathrm{m}}/k_{\mathrm{B}}$. In the semi-classical approach (by replacing the force noise of equation 3.10 by the Callen and Welton equation [7, 117]) the average phonon occupation becomes:

$$\bar{n}_{\mathrm{m}} = \left[\exp\left(\frac{\hbar\omega_{\mathrm{m}}}{k_{\mathrm{B}}T_{\mathrm{bath}}}\right) - 1\right]^{-1} = \frac{k_{\mathrm{B}}T_{\mathrm{mode}}}{\hbar\omega_{\mathrm{m}}} - \frac{1}{2}\,. \tag{3.14}$$

At the temperature $T^{\bar{n}=1}_{\mathrm{bath}} = \ln(2)\,\hbar\omega_{\mathrm{m}}/k_{\mathrm{B}}$ the average phonon occupation is $\bar{n}_{\mathrm{m}} = 1$ and the probability of finding the oscillator in the ground state is 50%. In the context of optomechanics, cooling a mechanical oscillator into the ground state usually means a phonon occupation $\bar{n}_{\mathrm{m}} \leq 1$.
While classically the effect of mechanical dissipation is described by the decay of the amplitude at the damping rate Γ_{m}, the quantum mechanical description relies on the average phonon number. Assuming that the oscillator is initially in the ground state, $\bar{n}_{\mathrm{m}}(t = 0) = 0$, the average phonon number will evolve according to $\bar{n}_{\mathrm{m}}(t) = \bar{n}_{\mathrm{th}}(1 - e^{-\Gamma_{\mathrm{m}}t})$, where $\bar{n}_{\mathrm{th}}$ is the average phonon number of the environment. Hence, the rate at which the oscillator is heated out of the ground state is

$$\frac{\mathrm{d}}{\mathrm{d}t}\bar{n}(t = 0) = \bar{n}_{\mathrm{th}}\Gamma_{\mathrm{m}} \approx \frac{k_{\mathrm{B}}T_{\mathrm{bath}}}{\hbar Q}\,. \tag{3.15}$$

The quantity $\Gamma_{\mathrm{th}} = \bar{n}_{\mathrm{th}}\Gamma_{\mathrm{m}}$ is often referred to as the *thermal decoherence rate*. Another important quantity is the so-called *Qf product* [8, 73, 83], which is proportional to the ratio of the mechanical frequency ω_{m} and the thermal decoherence rate:

$$\frac{\omega_{\mathrm{m}}}{\Gamma_{\mathrm{th}}} = Qf_{\mathrm{m}} \times \left(\frac{h}{k_{\mathrm{B}}T_{\mathrm{bath}}}\right) \tag{3.16}$$

The Qf product gives the number of quantum coherent oscillations of an oscillator which is initially prepared in a quantum state and gets heated out of the quantum regime by the environment.

3.3 Homodyne detection of mechanical motion

The motion of the mechanical oscillator in the MiM device modulates the resonance frequency of the cavity, as discussed in section 3.1. This leads to a phase modulation of the reflected light from the cavity, which can be read out with a phase sensitive detector. Balanced homodyne detection [99, 100] is a standard detection scheme for phase sen-

sitive measurements of a laser beam, which is capable of being quantum noise limited. This section outlines the basic principles of homodyne measurements in cavity optomechanical devices, the realized experimental setup and characterization measurements on the performance of the detection. Finally, homodyne characterization measurements on the mechanical oscillator will be presented together with a comprehensive listing of the optomechanical properties of the MiM device.

Principles of continuous weak measurements

Homodyne detection is based on a signal beam which is brought into interference with a local oscillator beam that serves as a phase reference. This interference signal yields a measure of the signal phase. In contrast to heterodyne detection, the signal beam is derived from the local oscillator itself. Through a coherent subtraction of the two outputs of a beam splitter, all the noise contributions of the local oscillator can in principle be suppressed, while the difference signal scales with the amplitude of the local oscillator. This scheme is called *balanced homodyne detection* [99] and can be shot-noise-limited.

The optomechanical coupling of the mechanical oscillator in the cavity converts the displacement x of the oscillator to a phase shift $\phi \sim g_{\mathrm{m}} x_{\mathrm{m}}/\kappa$ [8, 117]. If N photons interact with the cavity, the uncertainty relation between photon number and phase yields a shot-noise-limited imprecision $\delta\phi = 1/2\sqrt{N}$ [8, 117]. This means that a very intense flash of light can produce an instantaneous phase (and position) detection with arbitrary precision. This leads to strong squeezing of the mechanical position quadrature, which will be discussed later in the context of pulsed optomechanics (see section 4.5). However, this intense pulse disturbs the oscillator through a large momentum kick, which can be seen as a measurement back-action on the oscillator. Usually the oscillator is continuously probed with a rather weak detection beam with an optimal power that corresponds to minimum shot-noise and minimum radiation pressure back-action.

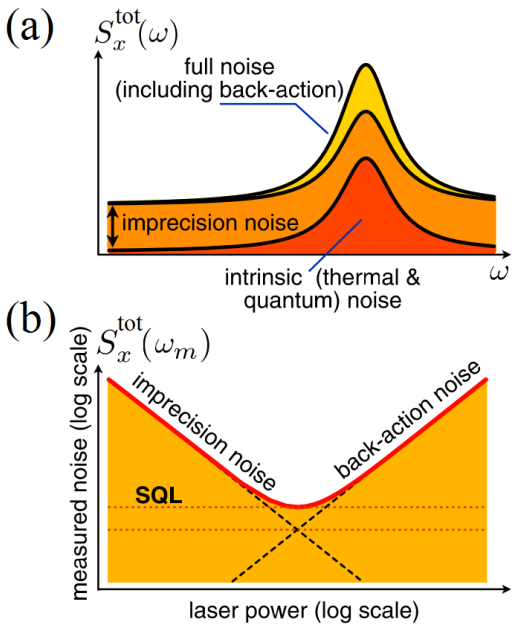

Figure 3.8: The standard quantum limit of displacement sensing. (a) Total measured noise PSD $S_{\mathrm{x}}^{\mathrm{tot}}(\omega)$ of a mechanical oscillator including its intrinsic displacement noise, the imprecision noise of the detector and the back-action noise from the radiation pressure of the detection beam. **(b)** PSD $S_{\mathrm{x}}^{\mathrm{tot}}(\omega)$ evaluated at the mechanical noise peak at ω_{m} as a function of the detection beam power. At low powers, imprecision noise dominates, while at larger powers the back-action noise dominates. Figure taken from [8].

This so-called *standard quantum limit* (SQL) [8, 117] represents a fundamental uncertainty principle. Nevertheless, through variational readout the sensitivity can become even better than the SQL, which was demonstrated in a MiM system similar to our configuration [119].
In summary, the optimal detection sensitivity is reached with a quantum-noise-limited detector which operates at an optical power which corresponds to the SQL of the cavity optomechanical device.

Experimental setup

The homodyne setup was built and characterized by T. Wagner during his Master's thesis [116]. This subsection very briefly outlines the most important technical features. We derive our homodyne detection beam from the Ti:sapph laser in the coupling laser system, as shown in Figure 2.21. Since many technical details are related to the realization of active feedback cooling, these will be discussed later in section 4.3.2. A detailed sketch of the balanced homodyne setup is shown in section 4.3 (see Figure 4.8 and B.1). Specifically, we use a digital AOM driver in the homodyne branch to reduce phase noise and control the detection beam power with a photodiode which is located directly at the PBS cube in the lattice beam telescope T2 (see Figure 2.22). Through this telescope, the homodyne detection beam is coupled into the planar fiber of the MiM system together with the coupling beam at orthogonal polarizations. The measurements presented in this thesis were performed with a detection beam power of approximately 150 µW (power in the fiber entering the MiM device).
An important issue is the generation of the error signal for the homodyne phase lock. Although the most simple solution is to use the DC part of the balanced homodyne signal as the error signal, this causes problems with electronic noise in the homodyne measurement of the oscillator. Therefore, we generate the phase lock signal with another photo detector using residual light from the PBS where the detection beam is superimposed with the local oscillator (LO) (see Figure 4.8). Another important feature is the optical isolator in the detection beam (see Figure B.1), which prevents that light which is amplitude modulated through interference with the LO gets reflected back into the MiM device. We observed that this light can potentially drive the mechanical oscillator. Particular care was also taken to optimize the common mode rejection of the balanced detection.

Characterization measurements

In order to estimate the frequency dependency of the detection noise floor of the homodyne setup, a broadband spectral measurement of the homodyne signal was acquired, as shown in Figure 3.9. The measured spectral noise PSD is denoted by $S_{\mathrm{y}}(\omega)$, which is the sum of the displacement noise PSD $S_{\mathrm{x}}(\omega)$ of the mechanical oscillator and the imprecision noise $S_{\mathrm{x_n}}(\omega)$ of the detector (note that this relation does not hold during active feedback cooling: $S_{\mathrm{y}}(\omega) \neq S_{\mathrm{x}}(\omega) + S_{\mathrm{x_n}}(\omega)$, as discussed later in section 4.1).
The measurement shows that the detection noise floor $S_{\mathrm{x_n}}(\omega)$ becomes flat for $\omega/2\pi > 50\,\mathrm{kHz}$ and is below the measured signal $S_{\mathrm{y}}(\omega)$ in a broad frequency interval. In a separate measurement, we verified that all the noise peaks for $\omega/2\pi > 100\,\mathrm{kHz}$ which are not related to the membrane modes do not come from vibrations in the MiM

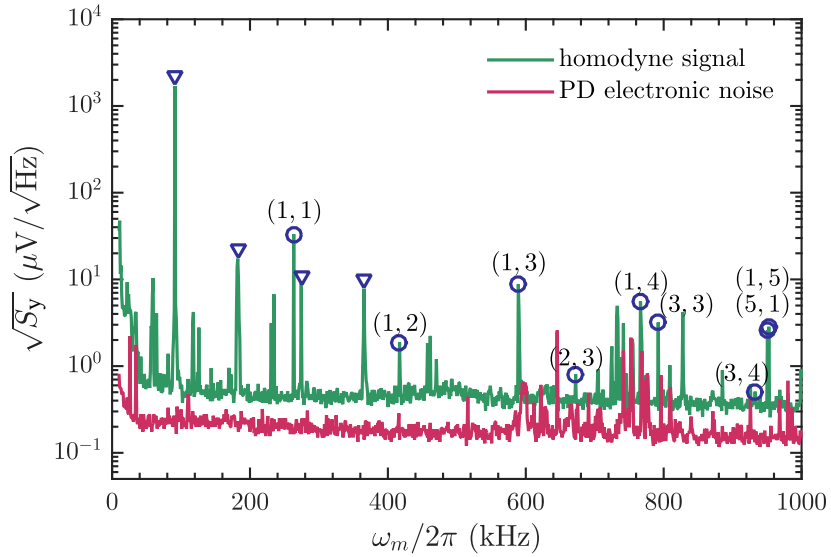

Figure 3.9: Broadband spectral measurement of homodyne signal. Measured electronic noise spectral density $\sqrt{S_y(\omega)}$ of the homodyne signal from the MiM device. The circles indicate the (m,n) eigenmodes of the membrane, while the triangles mark peaks originating from the intrinsic 91 kHz modulation of the Ti:sapph laser. The red noise signal corresponds to the electronic noise of the detector if the detection light is blocked. Parameters: $T_{\text{MiM}} = 480$ mK, light power 5 µW, acquisition with spectrum analyzer: span 10 kHz to 1 MHz and BW 30 Hz, properties of the optomechanical system summarized in table 3.1. Figure taken from [85].

system. This was proven by tuning the cavity far off-resonant. Hence, these peaks must originate from phase noise or intensity noise of the laser, which is not generated by the MiM cavity. It could also be proven that all of these noise peaks (except for the second Ti:sapph harmonic at 180 kHz) are mostly related to phase noise, because blocking the detection beam (measuring only the LO) could fully suppress these noise peaks. The fact that these peaks are mostly related to phase noise is also the reason why they are not fully suppressed by the common mode rejection of the balanced detection.
The fact that the (2,2) mode is not visible in the spectrum is caused by the centering of the fiber mode in the middle of the membrane, as described in section 2.3.3. The very small mode field diameter of the fiber cavity mode is thus very well centered on the node line of the even modes, where the displacement is zero.
In order to verify that our homodyne detector operates in the shot-noise-limited regime, the detection beam power was varied and the detection noise floor around 250 kHz was measured. As expected for a shot-noise-limited detection (see above), the noise floor spectral density $\sqrt{S_{\text{x,n}}}$ decreases with a square-root law if the detection beam power is increased.

Homodyne calibration for thermometry

This subsection describes how the mode temperature of the oscillator can be measured in practice using homodyne detection. As described in section 3.2, the mode temperature of the mechanical oscillator can be obtained directly from the displacement PSD $S_x(\omega)$. However, the signal from the homodyne detector is just a voltage signal which

is proportional to the oscillator displacement. Therefore, the homodyne signal needs to be calibrated in order to measure the oscillator displacement PSD.

Method 1: parameter estimation. The calibration factor between the homodyne voltage U and the oscillator displacement x_m is given by $\partial U/\partial x_\mathrm{m}$, which can be decomposed into three individual factors. Firstly, the optomechanical coupling $g_\mathrm{m} = \partial\omega_\mathrm{cav}/\partial x_\mathrm{m}$, which denotes the change of the resonance frequency in the cavity for a given oscillator displacement. Secondly, this change of the resonance frequency is related to a phase change of the reflected light from the cavity which is given by the quantity $\partial\phi/\partial\omega_\mathrm{cav}$. Finally, this phase change leads to a certain voltage signal of the homodyne detector, which is given by the quantity $\partial U/\partial\phi$. With these three quantities the homodyne calibration factor is given by:

$$\frac{\partial U}{\partial x_\mathrm{m}} = \frac{\partial\omega_\mathrm{cav}}{\partial x_\mathrm{m}}\frac{\partial\phi}{\partial\omega_\mathrm{cav}}\frac{\partial U}{\partial\phi}\,. \tag{3.17}$$

If this calibration factor and the effective mass (see section 3.2) are known, the displacement PSD $S_\mathrm{x}(\omega)$ can be measured[1] and the mode temperature can be calculated using equation 3.11.

In the Master's thesis of T. Wagner, three different ways to measure the factors in equation 3.17 for our MiM system were presented [116]. As shown there, one method yields the most promising result, which works as follows. Firstly, we measure the two factors $\frac{\partial\omega_\mathrm{cav}}{\partial x_\mathrm{m}}\frac{\partial\phi}{\partial\omega_\mathrm{cav}} = \frac{\partial\phi}{\partial x_\mathrm{m}}$ in one single step. For this, the membrane is displaced by a known distance $\pm\Delta x_\mathrm{m}$ which shifts the resonance frequency of the fiber cavity and reveals the line shape of the cavity resonance (this can be done by changing L_1 and L_2 at constant $L_0 = L_1 + L_2$ using the piezo tube calibration of the cavity fibers, see Figure 3.3). By measuring the line shape of the Lorentzian reflection dip, the phase change $\partial\phi/\partial x_\mathrm{m}$ can be estimated by a fit to the Lorentzian. This yields a phase change

$$\frac{\partial\phi}{\partial x_\mathrm{m}} = 0.93\,\frac{\mathrm{rad}}{\mathrm{nm}}\,. \tag{3.18}$$

Finally, we determine the homodyne voltage per phase change $\partial U/\partial\phi$ by scanning the phase of the local oscillator (LO) by multiples of 2π (using the phase lock piezo), which leads to a sinusoidal interference signal with a peak-to-peak voltage V_pp and a maximum slope of $\partial U/\partial\phi = V_\mathrm{pp}/2$. While $\partial\phi/\partial x_\mathrm{m}$ is a fixed quantity of our aligned MiM system (see subsection 3.1), the quantity $\partial U/\partial\phi$ depends on many critical parameters (fiber couplings, the spacial overlap between the LO beam and the detection beam, etc.). Therefore, we measure V_pp on a daily basis and obtain the homodyne calibration

$$\frac{\partial U}{\partial x_\mathrm{m}} = 0.93\,\frac{\mathrm{rad}}{\mathrm{nm}}\cdot\frac{V_\mathrm{pp}}{2}\,. \tag{3.19}$$

To calculate the mode temperature from the calibrated displacement spectra, we estimate the effective mass m_eff of the (1,1) mode ($\omega_\mathrm{m}/2\pi = 264\,\mathrm{kHz}$ at $T_\mathrm{MiM} = 500\,\mathrm{mK}$) of our membrane oscillator to be $m_\mathrm{eff} = \frac{1}{4}\,m_\mathrm{phys} = 76\,\mathrm{ng}$ (see section 3.4).

[1] If $S_\mathrm{x}(\omega_\mathrm{m}) \gg S_{\mathrm{x_n}}(\omega_\mathrm{m})$, the measured PSD $S_\mathrm{y}(\omega)$ is approximately equal to $S_\mathrm{x}(\omega)$ and the integrated, measured PSD $S_\mathrm{y}(\omega)$ is a very good estimate for the mode temperature. For very low mode temperatures, the real displacement PSD $S_\mathrm{x}(\omega)$ can be determined by a fit, as presented in section 4.4.3

Method 2: Direct calibration. Another possible way to calibrate the homodyne signal is to measure the homodyne noise spectrum at a known oscillator mode temperature (or a known temperature change). The advantage is that the result is the least prone to errors, because all factors in equation 3.17 and the effective mass are obtained simultaneously. The disadvantage is that the different factors in the product $T_{\mathrm{mode}} \sim m_{\mathrm{eff}}(\frac{\partial x_{\mathrm{m}}}{\partial U})^2 \int_0^\infty S_{\mathrm{x}}^{\mathrm{U}} \mathrm{d}\omega$ can not be determined individually (using the voltage PSD $S_{\mathrm{x}}^{\mathrm{U}} = \langle |U(\omega)^2| \rangle$ in equation 3.11). Furthermore, the measurement is very time consuming and can not be done on a daily basis. This is why we performed this method only once as a validation of the method 1 presented above. In this way, we combine the advantages of both methods to achieve on the one hand a reliable, very good estimate of the mode temperature, which on the other hand can be easily checked by measuring V_{pp} before and after each optomechanical experiment.
In order to adjust the mode temperature of the oscillator for the calibration, the temperature of the MiM device T_{MiM} was altered between 1.5 K and 37 K and the mode temperature of the oscillator was measured for each cryostat temperature. Special care needs to be taken since the fine-alignment of the optomechanical coupling g_{m} (see subsection 3.1) changes with T_{MiM} and needs to be readjusted for each cryostat temperature. Furthermore, we observe that the mode temperature very slowly approaches the steady state value after T_{MiM} was changed, which might be caused by a weak thermal link between the copper MiM structure and the membrane frame at low temperatures. Hence, one needs to wait approximately 1 h after T_{MiM} was adjusted until T_{mode} can be measured.
Figure 3.10 shows the measured mode temperatures T_{mode} as a function of the MiM temperature T_{MiM} and a linear fit to the data. It shows that the mode temperature is significantly larger than the cryostat temperature. This is consistent with the mode temperature of ≈ 3 K which we usually observe in experiments at the cryostat base temperature of 500 mK (see for example section 4.4) and which lies within the 95% confidence interval of the y-intercept of the linear fit curve. The reason for the larger mode temperature is unclear. However, it must be some kind of noise in the system which is not related to the temperature related thermal noise in the membrane frame.

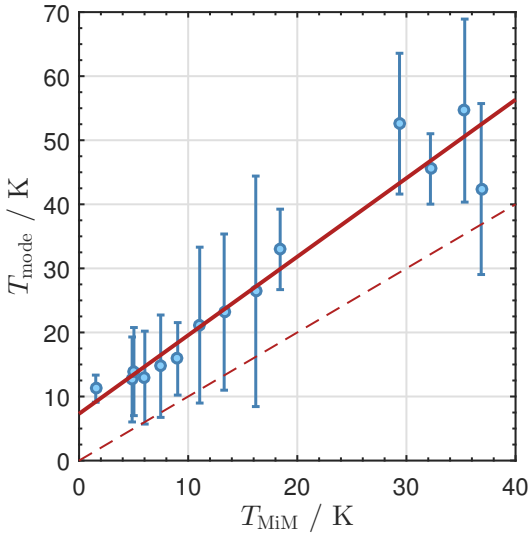

Figure 3.10: Mode temperature for different cryostat temperatures. Mode temperatures T_{mode} of the oscillator as a function of the MiM temperature T_{MiM}, calculated with the homodyne calibration from equation 3.19 with $m_{\mathrm{eff}} = 76$ ng. Fit result (red line): slope $s_{\mathrm{c}} = 1.23 \pm 0.22$, y-intercept 7.3 ± 4.3K. Acquisition: T_{MiM} measured with sensor in MiM device (see Figure 2.6), T_{mode} measured in zero-span mode of lock-in amplifier (as described in section 4.4.1): $N \approx 15$ sample traces of duration $\tau \approx 1$ min, demodulator BW 1 kHz. Each data point is the average of $N \approx 15$ temperature values obtained by time averaging each temperature time trace, the error bars correspond to their standard deviation.

For example, the dither piezo element on the membrane shuttle (see Figure 2.7) might act as a transducer between electric noise coupled in from outside of the cryostat and mechanical vibrations in the MiM system which drive the membrane. Most likely, the reason is not related to heating through the detection laser, because we observe no significant increase of the mode temperature if the laser power is increased.
Nevertheless, the actual result of the measurement is the slope of the fit curve. It must be exactly one and any deviation from this value must originate from a wrong temperature estimation of T_{mode} through the homodyne calibration in equation 3.19. This can be understood as follows. Assuming that the oscillator is in thermal equilibrium with the environment and the thermal Langevin force is the only force that acts on the oscillator, the mode temperature is equal to the temperature of the environment: $T_{\mathrm{mode}} = T_{\mathrm{bath}}$ (as long as $k_{\mathrm{B}}T_{\mathrm{mode}} \gg \hbar\omega_{\mathrm{m}}$). Hence, for an ideal homodyne calibration, the slope in Figure 3.10 must be one. If an additional, temperature independent force acts on the oscillator ($\Rightarrow T_{\mathrm{bath}} \neq T_{\mathrm{mode}}$ as in our case), this will lead to an increase of T_{mode} that is independent of T_{bath}. Hence, the slope of T_{mode} as a function of T_{bath} will also be equal to one.
Final calibration. We account for the deviation of the slope $s_{\mathrm{c}} = 1.23 \cdot (1 \pm 0.18)$ from one (see Figure 3.10) by adding $\sqrt{s_{\mathrm{c}}}$ as an additional correction factor into the homodyne calibration in equation 3.19:

$$\frac{\partial U}{\partial x_{\mathrm{m}}} = \sqrt{s_{\mathrm{c}}} \cdot 0.93 \,\frac{\mathrm{rad}}{\mathrm{nm}} \cdot \frac{V_{\mathrm{pp}}}{2} \,. \tag{3.20}$$

In this way, the calculated mode temperature $T_{\mathrm{mode}} \sim m_{\mathrm{eff}}(\frac{\partial x_{\mathrm{m}}}{\partial U})^2 \int_0^\infty S_{\mathrm{x}}^{\mathrm{U}} \mathrm{d}\omega$ (using the voltage PSD $S_{\mathrm{x}}^{\mathrm{U}} = \langle |U(\omega)^2| \rangle$ in equation 3.11) yields the correct value and the slope in Figure 3.10 is equal to one. By measuring the voltage V_{pp}[2] before every optomechanical experiment, we can perform mode temperature measurements of our oscillator with a systematic error of less than 20% (the relative error of s_{c}) using this calibration. All the measured mode temperatures shown in this thesis have this systematic error. However, this systematic temperature error will be omitted and only statistical errors from each measurement will be indicated (unless stated otherwise). The specified values for PSDs like for example the detection noise $S_{\mathrm{x_n}}$ have the same systematic error, assuming that the estimated effective mass is correct.
The calibration also allows for the determination of the homodyne displacement noise floor PSD $S_{\mathrm{x_n}}$ around the oscillator frequency ω_{m}. We perform our measurements with an LO power of 12 mW (the destruction threshold of the one single photodiode of the balanced detector is 10 mW, see appendix B.2) and a detection beam power of approximately 150 µW which yields $S_{\mathrm{x_n}} = 8.5 \cdot 10^{-33} \,\frac{\mathrm{m}^2}{\mathrm{Hz}} = 0.0085 \,\frac{\mathrm{fm}^2}{\mathrm{Hz}}$. This is the best detection noise floor which could be achieved in this setup, after implementing a digital AOM driver for the homodyne beam (with a significant enhancement) and after adjusting the beam powers mentioned above. It corresponds to the usual measurement configuration with the MiM cavity on resonance.

[2] In practice, we measure V_{pp} at a low detection beam power and scale the value according to the final measurement power, because at the final power the photodiode clipps at ±10 V. Furthermore, we scale V_{pp} by $\frac{0.95}{2}$, where 0.95 accounts for the losses of the bandpass (see Figure 4.8, appendix B.3) and the factor $\frac{1}{2}$ accounts for the fact that V_{pp} is measured at high-Z, while the oscillator is measured parallel to a 50 Ω resistor (see section 4.3.2).

3.4 Optomechanical properties of the MiM device

This section summarizes the optomechanical properties of the cryogenic MiM device. All measurements presented in this thesis were performed with this MiM setup.

Empty fiber cavity. Assuming a Finesse of $\mathcal{F}_0 = 60 \pm 2$ (see Figure 2.15) and a reflectivity on resonance $\rho = 0.76 \pm 0.013$ (see equation 2.2), one can use a plot similar to Figure 2.8 to give an estimate on the mirror power reflectivities R_1 and R_2 of the cavity fibers: $R_1 = 0.907 \pm 0.004$, $R_2 = 0.994 \pm 0.001$. For this, the lower error bound of ρ was estimated to be slightly larger than the reflectivity on resonance $\sigma_{\text{ref}} = 0.73$ of the empty fiber cavity.

MiM fiber cavity. The aligned MiM system has a reflectivity on resonance $\sigma_{\text{ref}} = 0.61$ (see appendix A.1) and a finesse $\mathcal{F}_{\text{m}}$ ranging from 45 to 160 [116], depending on the membrane position [115]. The optomechanical coupling also depends on the membrane position, as shown in Figure 3.3: $g_{\text{m}} = 2\pi \times -12.5 \cdots 15.9\,\text{GHz/nm}$. Compared to the optomechanical coupling for a moving end mirror (see equation 3.1), this corresponds to $g_{\text{m}} = g_{\text{m}}^{min} \cdots g_{\text{m}}^{max} = -0.77\,G \cdots 0.98\,G$ with $G = 2\pi \times 16.2\,\text{GHz/nm}$. At the point of highest optomechanical coupling $g_{\text{m}}^{\text{max}}$, the finesse is also maximal (corresponding to a minimal width of the transmission peak, see subsection 3.1). This behavior corresponds to an effective cavity linewidth $\kappa_{\text{m}} = \omega_{\text{FSR}}/\mathcal{F}_{\text{m}}$, which also depends on the membrane position: $\kappa_{\text{m}} = 2\pi \times 40 \cdots 140\,\text{GHz}$. The FSR of the MiM cavity is $\omega_{\text{FSR}} = 2\pi \times c/2L_{\text{cav}} = 2\pi \times 6.33\,\text{THz}$ for a cavity length $L_{\text{cav}} = 23.7\,\mu\text{m}$, which was measured with white-light spectroscopy (see section 2.3.3).

Mechanical oscillator. Our membrane oscillator is a commercially available high-stress Si_3N_4 square membrane from *Norcada* with the dimensions $1.5\,\text{mm} \times 1.5\,\text{mm} \times 50\,\text{nm}$ and a ground mode frequency of the (1,1) mode of $\omega_{\text{m}} = 2\pi \times 263.9\,\text{kHz}$ at $T_{\text{MiM}} = 500\,\text{mK}$. At this temperature we also determined a Q-factor of $Q = 1.07579(15) \cdot 10^7$ through a ringdown measurement [85]. This corresponds to a natural mechanical linewidth of $\Gamma_{\text{m}} = \omega_{\text{m}}/Q = 2\pi \times 24.5\,\text{mHz}$. This yields $\omega_{\text{m}}/\Gamma_{\text{th}} \approx 30$ at the cryogenic

Optomechanical MiM parameters			
ω_{m}	$2\pi \times 263.9\,\text{kHz}$	ω_{cav}	$2\pi \times 384\,\text{THz}$
Q	$1.07579(15) \cdot 10^7$	L_{cav}	$23.7\,\mu\text{m}$
Γ_{m}	$2\pi \times 24.5\,\text{mHz}$	κ_{m}	$2\pi \times 40 \cdots 140\,\text{GHz}$
m_{eff}	$76\,\text{ng}$	$\mathcal{F}_0$	60
x_{zp}	$6.47 \times 10^{-16}\,\text{m}$	$\mathcal{F}_{\text{m}}$	$45 \cdots 160$
$f_{1,1} \times Q$	2.8×10^{12}	g_{m}	$2\pi \times -12.5 \cdots 15.9\,\text{GHz/nm}$
$\omega_{\text{m}}/\Gamma_{\text{th}}$	30	g_0	$2\pi \times 10.3\,\text{kHz}$
S_{x_n}	$8.5(15) \cdot 10^{-33}\,\frac{\text{m}^2}{\text{Hz}}$	G	$2\pi \times 16.2\,\text{GHz/nm}$

Table 3.1: Proporties of the MiM device at a cryogenic temperature of $T_{\text{MiM}} = 500\,\text{mK}$, which was used for the measurements presented in this thesis. All the oscillator parameters correspond to the (1,1) mode of the membrane. We work at the point of maximal optomechanical coupling $g_{\text{m}}^{\text{max}} = 15.9\,\text{GHz/nm}$ and maximal finesse $\mathcal{F}_{\text{m}}^{\text{max}} = 160$, which corresponds to a minimal linewidth $\kappa_{\text{m}}^{\text{min}} = 2\pi \times 40\,\text{GHz}$. Fitting $g_{\text{m}}(x_{\text{m}})$ (see Figure 3.4) indicates a membrane field reflectivity $r_{\text{m}} = 0.38$. The detection noise floor S_{x_n} corresponds to a homodyne LO power of 12 mW and a detection beam power of about 150 µW (see end of section 3.3).

base temperature $T_{\mathrm{MiM}} = 500\,\mathrm{mK}$, which means that our system operates in the quantum coherent oscillation regime (see equation 3.16). The achieved optomechanical coupling in the MiM system indicates a membrane field reflectivity $r_{\mathrm{m}} = 0.38$ (see section 3.1). We estimate the effective mass m_{eff} of the (1,1) mode to be $m_{\mathrm{eff}} = \frac{1}{4}\, m_{\mathrm{phys}} = 76\,\mathrm{ng}$, assuming $\rho = 2700\,\frac{\mathrm{kg}}{\mathrm{m}^3}$ [115, 120] for high stress Si_3N_4 films. The factor 1/4 corresponds to a configuration with an infinitely small probe beam, which is exactly centered in the middle of the membrane [115]. Due to the very small mode field diameter of the fiber cavity mode and the precise centering of the fibers with respect to the membrane center (indicated by the absence of the peak of the (2,2) mode in Figure 3.9), this is a good approximation. For this effective mass, the zero-point fluctuation of the (1,1) mode is $x_{\mathrm{zp}} = \sqrt{\hbar/2m_{\mathrm{eff}}\omega_{\mathrm{m}}} = 6.47 \times 10^{-16}\,\mathrm{m}$ (see equation 3.13). This yields a maximum single photon optomechanical coupling strength of $g_0 = g_{\mathrm{m}}^{\mathrm{max}} \cdot x_{\mathrm{zp}} = 2\pi \times 10.3\,\mathrm{kHz}$.

Chapter 4

Feedback cooling

In the course of this thesis, feedback cooling of a mechanical oscillator to a mode occupation of $n_\mathrm{m} = 18.5 \pm 3.3$ was realized using optical homodyne feedback. This chapter focuses on the principles of feedback cooling and evaluates the experimental results in the context of fundamental limits and future enhancements.

It was shown in section 3.2 that the mechanical oscillator temperature is proportional to the mean square displacement $\langle x^2 \rangle$ of its random motion. If this quantity is reduced, the oscillator gets cooled. The easiest way of achieving this is to reduce the thermal noise force that drives the oscillator by placing it in a cryogenic environment. In the case of high frequency oscillators with resonance frequencies $\omega_\mathrm{m}/2\pi > 1\,\mathrm{GHz}$ the oscillator temperature of the quantum zero-point motion is $T_\mathrm{mode} > \frac{1}{2}\hbar\omega_\mathrm{m}/k_\mathrm{B} \approx 25\,\mathrm{mK}$ (see equation 3.14) which is accessible with cryogenic cooling. For low frequency oscillators this temperature is accordingly smaller and the only way of cooling below the thermal bath temperature of the oscillator environment is applying an additional force that reduces the motion of the oscillator. This force can be generated passively in cavity optomechanical systems that operate in the so-called *resolved sideband regime* and is often referred to as *self-cooling*. Several oscillators were cooled to the quantum ground state using optomechanical self-cooling [38–44]. Due to the experimental demands in building a hybrid quantum system, our optomechanical system is far away from the resolved sideband regime (see table 3.1) and operates in the so-called *bad cavity regime*. Nevertheless, even if passive self-cooling is not possible, the cooling force can also be applied actively. This procedure is called *active feedback cooling* or *cold damping* and it was shown theoretically that it also allows for ground state cooling [121, 122], even though it is technically very challenging and has not been realized to date.
The basic principle of feedback cooling is to obtain the position $x(t)$ of the oscillator (for example by a phase-sensitive detection of the cavity output) and generate a negative feedback force $F_\mathrm{fb}(t) = -m\Gamma_\mathrm{fb}\dot{x}(t)$ which is proportional to its velocity $\dot{x}(t)$. This increases the natural damping rate Γ_m of the oscillator to the new effective damping rate $\Gamma_\mathrm{eff} = \Gamma_\mathrm{m} + \Gamma_\mathrm{fb}$ without changing the coupling rate to the thermal bath of the environment. This *feedback damping* can be understood as cooling by coupling the oscillator to a bath of near zero temperature (for example the laser field in case of optical feedback). This reduction of entropy of the oscillator is finally limited by the

entropy due to the imperfect estimation of the position $x(t)$ of the oscillator [69].
The feedback cooling scheme was originally proposed in 1998 [123] and first realized in 1999 in Paris at LKB [68]. The mechanical oscillator was a compression mode of one end mirror of a high finesse cavity and the feedback was applied by a 500 mW AOM-modulated laser beam. This beam reduced the temperature of the mirror compression mode by a factor of 40. In 2006, Kleckner and Bouwmeester actively cooled a $f_\mathrm{m} = 12.5\,\mathrm{kHz}$ beam cantilever from room temperature to 135 mK [124]. A micro mirror attached to the cantilever served as the end mirror of a cavity and a second laser was used to apply a feedback force via radiation pressure. In the same year, Arcizet *et al.* feedback cooled a millimetre-scale oscillator in an optical cavity to 5 K by applying an electrostatic feedback force [125]. In 2007, Poggio *et al.* cooled a silicon cantilever with resonance frequency $\omega_\mathrm{m} \approx 2\pi \times 4\,\mathrm{kHz}$ from 2.2 K to 5 mK by applying a feedback force with a piezo element [126].
One main research goal of feedback cooling at that time was to cool the mirrors of gravitational wave detectors in order to reduce their thermal noise and improve the phase sensitivity of the measurements. In 2008, the ton-scale gravitational wave detector AURIGA was feedback cooled from 4.2 K to 170 mK [127]. One year later the kilogram-scale mirrors of the LIGO gravitational wave detector were cooled to a mode occupation of $n_\mathrm{m} \approx 200$ [128]. Since the effective resonance frequency of these mirrors is only $\omega_\mathrm{m} \approx 2\pi \times 150\,\mathrm{Hz}$, the corresponding temperature is only 1.4 µK which is the lowest mechanical oscillator temperature reported to date. Recent achievements in the context of feedback cooling are cooling of a microdisc whispering gallery mode oscillator to a mode occupation of $n_\mathrm{m} \approx 5$ in 2014 [69] and enhancement of feedback cooling by squeezed light in 2016 [129].
To date, feedback cooling of a mechanical oscillator to the quantum ground state has not been realized experimentally. However, a full quantum mechanical treatment reveals that feedback cooling to the quantum ground state is possible [122]. A brief discussion of the quantum mechanical description of feedback cooling and quantum noise contributions will be presented at the end of section 4.1.

4.1 Principles of feedback cooling

Feedback cooling aims at the reduction of the motion of an oscillator by active feedback control. This means that the motion is detected and the signal is fed back to the oscillator as a damping force in a closed feedback loop. This is a classical problem of control theory and has been intensively studied as a field of mathematics and engineering since the beginning of the industrial revolution. In 1867, James Clerk Maxwell studied the dynamical behavior of a centrifugal governor which controls the speed of a steam engine [130], which is an early example of a technical feedback system.
Feedback systems are generally described by a linear system representation in frequency space, as depicted in Figure 4.1. A thermal noise force $F_\mathrm{th}(\omega)$ acts on the system and is converted into oscillator displacement $x(\omega)$ by the intrinsic mechanical susceptibility $\chi_\mathrm{m}(\omega) = x(\omega)/F_\mathrm{th}(\omega)$. A detector adds noise $x_\mathrm{n}(\omega)$ to the displacement which adds up to a detection signal $y(\omega) = x(\omega) + x_\mathrm{n}(\omega)$. This signal is the so-called *in-loop detection signal* and it can be observed for example on a spectrum analyzer. This signal is fed

back to the oscillator to generate a feedback force

$$F_{\mathrm{fb}}(\omega) = -\chi_{\mathrm{fb}}^{-1}(\omega)\,[x(\omega) + x_n(\omega)] \equiv -\chi_{\mathrm{fb}}^{-1}(\omega)\,y(\omega) \tag{4.1}$$

which is linear in the measured displacement $y(\omega)$. The feedback force is the product of the detection signal and the feedback filter function $\chi_{\mathrm{fb}}^{-1}(\omega)$. Notably, stochastic fluctuations of the feedback actuator (a thermal component $F_{\mathrm{fb,th}}$) are neglected. This feedback force then adds up to the thermal Langevin force F_{th} that acts on the oscillator. The new effective susceptibility $\chi_{\mathrm{eff}}(\omega)$ of this closed loop system can be calculated using the equation for the subsystem of the input and output of the oscillator (see Figure 4.1):

$$x = \chi_{\mathrm{m}}\,[F_{\mathrm{th}} + F_{\mathrm{fb}}]\,. \tag{4.2}$$

If the feedback force in this equation[1] is expressed through the feedback filter function this yields

$$\chi_{\mathrm{m}}^{-1}\,x = F_{\mathrm{th}} - \chi_{\mathrm{fb}}^{-1}\,(x + x_{\mathrm{n}})$$

$$\Leftrightarrow \quad \left(\chi_{\mathrm{m}}^{-1} + \chi_{\mathrm{fb}}^{-1}\right) x \equiv \chi_{\mathrm{eff}}^{-1}\,x = F_{\mathrm{th}} - \chi_{\mathrm{fb}}^{-1}\,x_{\mathrm{n}} \tag{4.3}$$

$$\Leftrightarrow \quad \left(\chi_{\mathrm{m}}^{-1} + \chi_{\mathrm{fb}}^{-1}\right)(x + x_{\mathrm{n}}) \equiv \chi_{\mathrm{eff}}^{-1}\,y = F_{\mathrm{th}} + \chi_{\mathrm{m}}^{-1}\,x_{\mathrm{n}}. \tag{4.4}$$

Hence, the inverse effective susceptibility is $\chi_{\mathrm{eff}}^{-1} = \chi_{\mathrm{m}}^{-1} + \chi_{\mathrm{fb}}^{-1}$. Using the expression for the susceptibility of a mechanical oscillator (see equation 3.7) one can obtain the closed loop feedback transfer function

$$\chi_{\mathrm{eff}}(\omega) = \frac{1}{\chi_{\mathrm{m}}^{-1}(\omega) + \chi_{\mathrm{fb}}^{-1}(\omega)} = \frac{1}{m\,(\omega_{\mathrm{m}}^2 - \omega^2 - i\omega\Gamma_{\mathrm{m}}) + \chi_{\mathrm{fb}}^{-1}(\omega)}\,. \tag{4.5}$$

Compared to the susceptibility χ_{m} of an unperturbed oscillator with spring constant $k_{\mathrm{m}} = m\omega_{\mathrm{m}}^2$, the new effective spring constant is altered by the real part of the feedback filter function $\chi_{\mathrm{fb}}(\omega)$ to $k'_{\mathrm{m}} = k_{\mathrm{m}}\,(1 + \mathrm{Re}[\chi_{\mathrm{fb}}^{-1}]/k_{\mathrm{m}})$. This shifts the resonance frequency to $\omega'_{\mathrm{m}} = \omega_{\mathrm{m}}\sqrt{1 + \mathrm{Re}[\chi_{\mathrm{fb}}^{-1}]/k_{\mathrm{m}}}$. The real part of χ_{fb}^{-1} generates a feedback force that is purely proportional to the position $x(t)$ of the oscillator.

[1] Equation 4.27 yields a more precise calculation including back-action and thermal feedback noise.

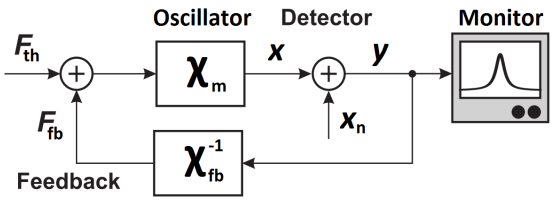

Figure 4.1: Linear system representation of the feedback cooling scheme. A thermal noise force F_{th} drives an oscillator and is translated into displacement x by its mechanical susceptibility χ_{m}. A detector adds noise to the signal that adds up to the detector output $y = x + x_{\mathrm{n}}$ which is monitored and also fed into the feedback cooling loop. The feedback filter function χ_{m}^{-1} converts y into a feedback force F_{fb} which adds up with the environmental, thermal force F_{th}. Figure adapted from [7].

Hence, one can define a displacement-proportional feedback gain g_d such that

$$k'_\mathrm{m} \;=\; k_\mathrm{m}\,(1+g_\mathrm{d}) \;\;,\;\; g_\mathrm{d} \equiv \mathrm{Re}[\chi_\mathrm{fb}^{-1}]/k_\mathrm{m}. \tag{4.6}$$

The effective susceptibility χ_eff (see equation 4.5) also shows that the imaginary part of $\chi_\mathrm{fb}(\omega)$ changes the oscillator damping to $\Gamma'_\mathrm{m} = \Gamma_\mathrm{m}(1 - \mathrm{Im}[\chi_\mathrm{fb}^{-1}]/m\omega\Gamma_\mathrm{m})$. It is proportional to the velocity $\dot{x}(t)$ of the oscillator. Therefore, we can define a velocity-proportional feedback gain g_v such that

$$\Gamma'_\mathrm{m} = \Gamma_\mathrm{m}\;(1+g_\mathrm{v}) \;\;,\;\; g_\mathrm{v} \equiv -\mathrm{Im}[\chi_\mathrm{fb}^{-1}]/m\omega\Gamma_\mathrm{m}. \tag{4.7}$$

Equivalently, the feedback filter function can be expressed through these feedback gains:

$$\chi_\mathrm{fb}^{-1} \;=\; \begin{pmatrix} g_\mathrm{d} & g_\mathrm{v} \end{pmatrix} \cdot \begin{pmatrix} k_\mathrm{m} \\ -\,i\,m\omega\Gamma_\mathrm{m} \end{pmatrix}. \tag{4.8}$$

Equations 4.3 and 4.4 define the real oscillator displacement $x(\omega)$ and the in-loop detected displacement $y(\omega)$ by its susceptibilities and the forces acting on the oscillator. Based on these results, the power spectral densities (PSDs) of these oscillator displacements in the feedback loop can be calculated. The single-sided PSD for the real, physical oscillator displacement $x(\omega)$ is

$$\begin{aligned} S_\mathrm{x}(\omega) \;&=\; \langle x(\omega)\,x^*(\omega)\rangle \\ &=\; |\chi_\mathrm{eff}|^2\,\langle F_\mathrm{th}(\omega)\,F_\mathrm{th}^*(\omega)\rangle \;+\; |\chi_\mathrm{eff}|^2\,|\chi_\mathrm{fb}|^{-2}\,\langle x_\mathrm{n}(\omega)\,x_\mathrm{n}^*(\omega)\rangle \\ &=\; |\chi_\mathrm{eff}|^2\,S_{\mathrm{F_{th}}}(\omega) \;+\; |\chi_\mathrm{eff}|^2\,|\chi_\mathrm{fb}|^{-2}\,S_{\mathrm{x_n}}(\omega) \\ \Leftrightarrow \qquad S_\mathrm{x}(\omega) \;&=\; |\chi_\mathrm{eff}|^2\,\Big[S_{\mathrm{F_{th}}}(\omega) \;+\; |\chi_\mathrm{fb}|^{-2}\,S_{\mathrm{x_n}}(\omega)\Big], \end{aligned} \tag{4.9}$$

where the frequency dependency of χ_eff and χ_fb was omitted for clarity. The cross terms including $F_\mathrm{th}(\omega)$ and $x_\mathrm{n}(\omega)$ drop out since the thermal noise and the detector noise are uncorrelated. This equation shows that the PSD of the real oscillator displacement still has its contribution from the thermal noise force but also contains a contribution from the imprecision noise that is fed back to the oscillator.
The PSD of the measured oscillator displacement $S_\mathrm{y}(\omega)$ can be calculated in the same manner:

$$S_\mathrm{y}(\omega) \;=\; |\chi_\mathrm{eff}|^2\,\Big[S_{\mathrm{F_{th}}}(\omega) \;+\; |\chi_\mathrm{m}|^{-2}\,S_{\mathrm{x_n}}(\omega)\Big]. \tag{4.10}$$

It becomes apparent that the measured PSD signal $S_\mathrm{y}(\omega)$ is not just the sum of the real oscillator displacement PSD $S_\mathrm{x}(\omega)$ and the imprecision noise PSD $S_{\mathrm{x_n}}(\omega)$. This is because the feedback loop creates correlations between the noise and the real oscillator displacement.

Ideal feedback cooling

Feedback cooling aims at minimizing the temperature of the mechanical oscillator and accordingly a minimization of the integrated PSD of the oscillator displacement (see section 3.2). This minimization problem is a classical example of optimal control theory

and the optimal filter function $\chi_{\mathrm{fb,opt}}$ for such problems can be found [7, 131]. The optimal control problem can be solved by the minimization of the cost function $\bar{S}_{\mathrm{xx}}(\omega)$, using the double sided PSD temporarily [69]:

$$\min_{\chi_{\mathrm{fb}}} \int_{-\infty}^{+\infty} \bar{S}_{\mathrm{xx}}(\omega)\, \frac{\mathrm{d}\omega}{2\pi}. \tag{4.11}$$

The solution of this variational problem can be found by solving

$$\frac{\mathcal{D}\,\bar{S}_{\mathrm{xx}}}{\mathcal{D}\,\chi_{\mathrm{fb}}} \;=\; 0, \tag{4.12}$$

where $\mathcal{D}$ stands for the variational (Gateaux) derivative [69]. This can be solved by separating magnitude $|\chi_{\mathrm{fb}}|$ and phase ϕ of the feedback filter function $\chi_{\mathrm{fb}} = |\chi_{\mathrm{fb}}|\, e^{i\phi}$. After a simple calculation, by taking the derivative of $\bar{S}_{\mathrm{xx}}$ with respect to the phase ($2\bar{S}_{\mathrm{xx}} = S_{\mathrm{x}}$, since S_{x} is real-valued), this yields [69]:

$$\begin{aligned} & \phi_{opt} \;\equiv\; \arg\left(\chi_{\mathrm{fb}}\right) \;=\; \arg\left(\chi_{\mathrm{m}}\right) \\ \Leftrightarrow \qquad & \phi_{opt} \;=\; \arctan\left(\frac{\omega\Gamma_{\mathrm{m}}}{\omega_{\mathrm{m}}^2 - \omega^2}\right) \;\approx\; \pm\frac{\pi}{2} \mp 2\frac{\omega - \omega_{\mathrm{m}}}{\Gamma_{\mathrm{m}}}. \end{aligned} \tag{4.13}$$

Hence, for this case of an ideal feedback loop the phase dependency of the feedback filter function should be equal to the phase of the unperturbed mechanical oscillator response function. The feedback phase $\arg\left(\chi_{\mathrm{m}}\right)$ is optimally $\pm\pi/2$ on resonance and drops quickly to zero on the order of the natural linewidth Γ_{m}. If the phase in equation 4.12 is replaced by this solution, the phase dependency drops out and the derivative with respect to the magnitude $|\chi_{\mathrm{fb}}|$ can be taken. An equally simple calculation yields

$$|\chi_{\mathrm{fb}}|_{\mathrm{opt}} \;=\; \chi_{\mathrm{m}}^{-1}\, \frac{S_{\mathrm{x_n}}}{S_{\mathrm{F_{th}}}}. \tag{4.14}$$

This shows that for the ideal feedback not only the phase but also the magnitude of the feedback filter function has a spectral shape related to the unperturbed mechanical oscillator. That means maximum gain should be applied only for a very small region around the peak of the mechanical resonance.

It is important to note that the above considerations are idealized in many respects. The oscillator is assumed to be classical and the feedback loop is a perfect, infinite band width position-to-feedback transducer without quantum uncertainties and back-action. If these effects are taken into account the optimal control problem gets more difficult but remains solvable. The optimal feedback filter function then becomes a rectangular bandpass filter centered at ω_{m} with a defined width and phase shift $\pi/2$ [132]. Notably, the optimal width of the feedback filter gets larger if the back-action is taken into account.

Practical feedback cooling

Due to technical limitations, the ideal feedback loop described above is hard to implement. Although an analog circuit could in principle realize the linear system of Figure

4.1, analog electronic devices are strongly limited by their bandwidth even for low frequency oscillators with resonance frequencies $\omega_m < 2\pi \times 1\,\mathrm{MHz}$. Furthermore, analog solutions are less versatile than digital implementations. On the other hand, digital processing that would just mimic analog circuits is also strongly limited by the computational speed. Hence, the most effective solution is either a very simple analog circuit that is just made out of analog filters and an adjustable delay [69, 127, 129, 133] or a digital feedback loop that mixes the signal down to frequencies that can be processed in real time [7, 133, 134].
As discussed above, most practical solutions of feedback cooling use a feedback filter χ_{fb} that is broad across the oscillator resonance frequency, both with respect to phase and magnitude. The phase ϕ is then adjusted by the feedback signal delay. Two characteristic cases can be distinguished: $\phi = \pi/2$ which creates a feedback force proportional to the velocity of oscillator, and $\phi = 0$ which creates a displacement-proportional feedback force.

4.1.1 Classical limits of feedback cooling

In order to calculate the effect of the feedback loop on the displacement PSD, the absolute values of the susceptibility χ_{eff} and the feedback filter function χ_{fb} can be expressed through the gains g_v and g_d (see equations 4.5 and 4.8):

$$\begin{aligned} |\chi_{fb}(\omega)|^{-2} &= (g_d k_m)^2 + (g_v m\omega\Gamma_m)^2 \\ |\chi_{eff}(\omega)|^{-2} &= m^2\left(\omega_m^2\,(1+g_d) - \omega^2\right)^2 + m^2\left(\omega\Gamma_m\,(1+g_v)\right)^2. \end{aligned} \tag{4.15}$$

Using these expressions the real PSD $S_x(\omega)$ and the measured PSD $S_y(\omega)$ in equation 4.9 and 4.10 can be plotted for different feedback gains. The result is shown in Figure 4.2 for pure velocity-dependent feedback ($g_d = 0$) and purely displacement-dependent feedback ($g_v = 0$).
In order to evaluate the feedback cooling efficiency in terms of optimal feedback gains g_v and g_d, the oscillator mode temperature T_{mode} can be calculated as a function of these feedback gains. According to the equipartition theorem the mode temperature is given by (see equation 3.11):

$$T_{mode} = \frac{m\omega_m^2}{k_B} \cdot \frac{1}{2\pi} \int_0^\infty S_x(\omega)\,\mathrm{d}\omega. \tag{4.16}$$

Using expressions 4.9 for $S_x(\omega)$ and expression 4.15 for the susceptibilities this becomes:

$$\begin{aligned} T_{mode} &= \frac{\omega_m^2}{2\pi m k_B} S_{F_{th}} \int_0^\infty \frac{1}{\left(\omega_m'^2 - \omega^2\right)^2 + \left(\omega\Gamma_m'\right)^2}\,\mathrm{d}\omega \\ &+ \frac{\omega_m^2}{2\pi m k_B} S_{x_n} \int_0^\infty \frac{g_d^2 k_m^2 + g_v^2\left(m\omega\Gamma_m\right)^2}{\left(\omega_m'^2 - \omega^2\right)^2 + \left(\omega\Gamma_m'\right)^2}\,\mathrm{d}\omega, \end{aligned} \tag{4.17}$$

where $S_{F_{th}}$ and S_{x_n} are assumed to be constant (a very good approximation for reasonable oscillator parameters) and $\omega_m' = \omega_m\sqrt{(1+g_d)}$ and $\Gamma_m' = \Gamma_m\,(1+g_v)$. With

$$\frac{\pi}{2\Gamma} = \int_0^\infty \frac{\omega^2 \, \mathrm{d}\omega}{\left(\omega_\mathrm{m}^2 - \omega^2\right)^2 + \left(\omega\Gamma\right)^2}, \quad \frac{\pi}{2\Gamma\omega_\mathrm{m}^2} = \int_0^\infty \frac{\mathrm{d}\omega}{\left(\omega_\mathrm{m}^2 - \omega^2\right)^2 + \left(\omega\Gamma\right)^2} \tag{4.18}$$

the mode temperature can be calculated as a function of the feedback gains g_v and g_d:

$$T_\mathrm{mode} = \underbrace{\frac{T_\mathrm{bath}}{(1+g_\mathrm{d})\,(1+g_\mathrm{v})}}_{\text{cold spring/damping}} + \underbrace{\left[\frac{k_\mathrm{m}\omega_\mathrm{m}Q}{4k_\mathrm{B}} \frac{g_\mathrm{d}^2}{(1+g_\mathrm{d})\,(1+g_\mathrm{v})}\right.}_{T \sim g_\mathrm{d}} + \underbrace{\left.\frac{k_\mathrm{m}\omega_\mathrm{m}}{4k_\mathrm{B}Q} \frac{g_\mathrm{v}^2}{1+g_\mathrm{v}}\right]}_{T \sim g_\mathrm{v}} S_{\mathrm{x_n}} \tag{4.19}$$

For pure velocity-proportional feedback gain ($g_\mathrm{d} = 0$) this expression is equal to the

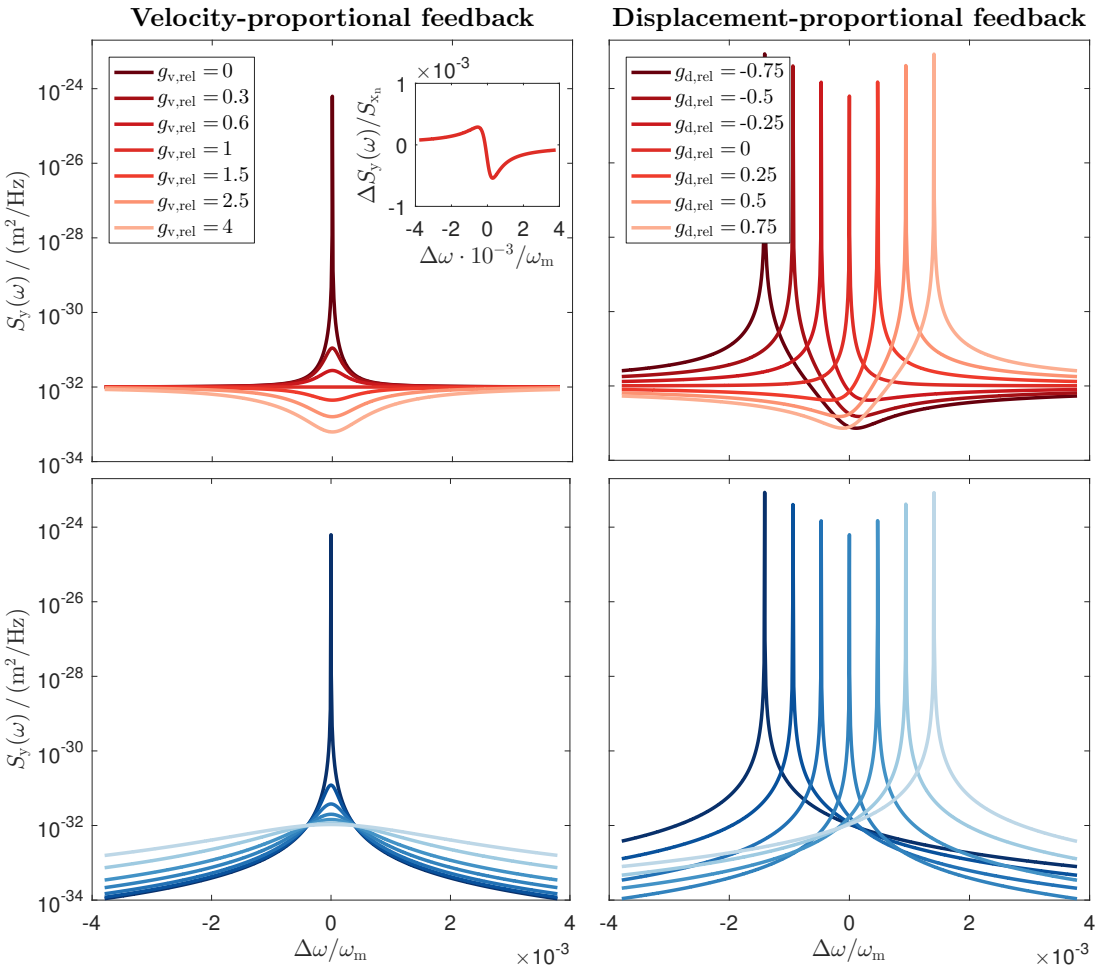

Figure 4.2: Feedback effects on the oscillator displacement PSD. Left column: Measured in-loop displacement PSD $S_\mathrm{y}(\omega)$ (top) and real PSD $S_\mathrm{x}(\omega)$ (bottom) for different velocity-proportional feedback gains g_v. Right column: $S_\mathrm{y}(\omega)$ (top) and $S_\mathrm{x}(\omega)$ (bottom) for different displacement-proportional gains g_d. Inset figure: zoom into the relative change of $S_\mathrm{y}(\omega)$ for the optimal gain $g_{\mathrm{v,rel}} = 1$. The gains are scaled to $g_{\mathrm{v,rel}} = g_\mathrm{v}/\sqrt{\mathrm{SNR}}$ (see equation 4.20, 4.21) and $g_{\mathrm{d,rel}} = g_\mathrm{d} \cdot k_\mathrm{m}$. Parameters used: $Q = 10^7$, $T_\mathrm{bath} = 0.5\,\mathrm{K}$, $m = 97\,\mathrm{ng}$, $S_{\mathrm{x_n}} = 1 \times 10^{-32}\,\mathrm{m^2\,Hz^{-1}} \Rightarrow \mathrm{SNR} = 6.3 \times 10^7$.

formula derived by Poggio *et al.* [126]. The first part of the expression shows that feedback cooling ($T_{\mathrm{mode}} < T_{\mathrm{bath}}$) with pure velocity-dependent feedback is only possible for $g_{\mathrm{v}} > 0$ and in case of pure displacement-dependent feedback with $g_{\mathrm{d}} > 0$, respectively. Hence, a stiffening of the spring constant k_{m} and increasing ω_{m} can cool the oscillator through displacement-proportional feedback. Velocity-dependent feedback cooling occurs if $\Gamma_{\mathrm{m}}^{'} > \Gamma_{\mathrm{m}}$. The first term of T_{mode} is therefore denoted with cold spring and cold damping. Even if this term goes to zero for large gains, the last two terms proportional to g_{d}^2 and g_{v}^2 will lead to an increase of the temperature due to detection noise that is fed back to the oscillator. Therefore, a global minimum of the temperature exists for $g_{\mathrm{d}}/g_{\mathrm{v}} \in (0, \infty)$. The minimum achievable temperature and the corresponding gain can be determined by taking the derivative of T_{mode} with respect to the gains. For this it is useful to introduce the signal-to-noise-ratio SNR, which denotes the ratio between the peak oscillator PSD $S_{\mathrm{x}}(\omega_{\mathrm{m}})$ and the detector noise level $S_{\mathrm{x_n}}(\omega_{\mathrm{m}})$. Using equation 3.10 for the thermal force noise PSD $S_{\mathrm{F_{th}}}$ the SNR is given by [7]

$$\mathrm{SNR} = \frac{S_{\mathrm{x}}(\omega_{\mathrm{m}})}{S_{\mathrm{x_n}}(\omega_{\mathrm{m}})} = \frac{Q^2}{k_{\mathrm{m}}^2}\frac{S_{\mathrm{F_{th}}}}{S_{\mathrm{x_n}}(\omega_{\mathrm{m}})} = \frac{4k_{\mathrm{B}}T_{\mathrm{bath}}}{k_{\mathrm{m}}\Gamma_{\mathrm{m}}S_{\mathrm{x_n}}}. \tag{4.20}$$

For pure velocity-dependent gain $g_{\mathrm{d}} = 0$ this yields:

$$\frac{\partial T_{\mathrm{mode}}}{\partial g_{\mathrm{v}}} = 0 \Rightarrow g_{\mathrm{v,opt}} = \sqrt{1 + \frac{4k_{\mathrm{B}}QT}{k_{\mathrm{m}}\omega_{\mathrm{m}}S_{\mathrm{x_n}}}} - 1 \equiv \sqrt{1+\mathrm{SNR}} - 1$$

$$\Rightarrow g_{\mathrm{v,opt}} \overset{\mathrm{SNR}\gg 1}{\approx} \sqrt{\mathrm{SNR}} \tag{4.21}$$

$$\Rightarrow T_{\mathrm{mode}}(g_{\mathrm{v,opt}}) \approx \frac{2\,T_{\mathrm{bath}}}{\sqrt{\mathrm{SNR}}} = \omega_{\mathrm{m}}\sqrt{m\Gamma_{\mathrm{m}}S_{\mathrm{x_n}}T_{\mathrm{bath}}/k_{\mathrm{B}}}. \tag{4.22}$$

It becomes apparent that the lowest temperatures with velocity-dependent feedback cooling can be achieved for a large SNR (at a given T_{bath}), which benefits from a large Q-factor, low mass and a low detection noise floor $S_{\mathrm{x_n}}$.

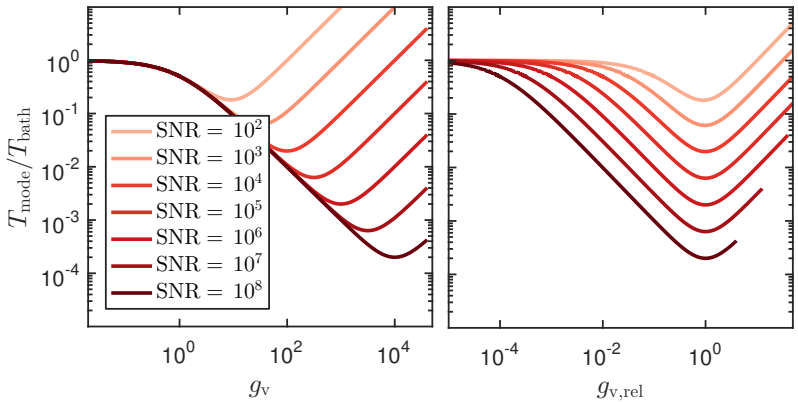

Figure 4.3: Mode temperature for pure velocity-dependent feedback. Left panel: relative mode temperature $T_{\mathrm{mode}}/T_{\mathrm{bath}}$ as a function of gain g_{v} for different SNRs. Right panel: plot with scaled gain $g_{\mathrm{v,rel}} = g_{\mathrm{v}}/\sqrt{\mathrm{SNR}}$. This shows that the optimal gain $g_{\mathrm{v,opt}}$ is very well approximated by $g_{\mathrm{v,rel}} = 1$ which corresponds to $g_{\mathrm{v}} = \sqrt{\mathrm{SNR}}$.

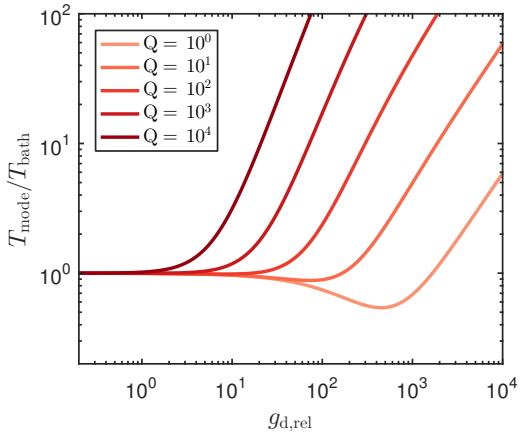

Figure 4.4: Mode temperature for pure displacement-dependent feedback. Relative mode temperature $T_{\mathrm{mode}}/T_{\mathrm{bath}}$ as a function of gain $g_{\mathrm{d,rel}} = g_{\mathrm{d}} \cdot k_{\mathrm{m}}$ for different Q-factors. Cooling only occurs for a very small Q-factor. For an oscillator with smaller ω_{m} the cooling would be much more efficient and possible for a larger Q. Parameters used: $T_{\mathrm{bath}} = 0.5\,\mathrm{K}$, $m = 97\,\mathrm{ng}$, $S_{\mathrm{x_n}} = 1 \times 10^{-32}\,\mathrm{m^2\,Hz^{-1}}$, $\omega_{\mathrm{m}} = 2\pi \cdot 265\,\mathrm{kHz}$.

The same calculation as in 4.22 can be made for displacement-dependent feedback. The main difference is that the gain for optimal cooling gets smaller for larger Q-factors: $g_{\mathrm{d,opt}} = \sqrt{1 + 4k_{\mathrm{B}}T/(k_{\mathrm{m}}\omega_{\mathrm{m}}QS_{\mathrm{x_n}})} - 1$. Hence, the temperature decrease due to $g_{\mathrm{d}} > 0$ is very small and only significant for very small Q-factors (or small m, small ω_{m}).
The mode temperature for velocity-dependent feedback cooling can be fully described by the SNR (see Figure 4.3). However, for displacement-proportional feedback the cooling occurs only for parameters that are very different from the parameters in our experiment. This is shown exemplary for different Q-factors in Figure 4.4. The plot shows that cooling occurs only for extremely small Q-factors for the parameters used and for large Q-factors the feedback only leads to heating. This is also visible in the PSD spectra of the right column in Figure 4.2, where the PSD only grows for $g_{\mathrm{d}} \neq 0$. The effect of heating for parasitic displacement-proportional gains in feedback cooling will be discussed in the following summary of the different types of feedback.

- **Velocity-proportional feedback**: For a purely imaginary feedback filter function χ_{fb} the displacement-proportional gain g_{d} is zero (see equation 4.8). The imaginary part of χ_{fb} is proportional to the velocity $\dot{x}(t)$ of the oscillator and can be expressed through the velocity-dependent gain g_{v} (see equation 4.7) which changes the damping of the oscillator to $\Gamma'_{\mathrm{m}} = \Gamma_{\mathrm{m}}\,(1 + g_{\mathrm{v}})$. The resulting measured displacement PSD of the oscillator S_{y} and the real PSD S_{x} are shown in the left column of Figure 4.2. For increasing g_{v} the oscillator is cold-damped and the PSD noise peak decreases. The optimal gain is very well approximated by the square root of the signal-to-noise-ratio SNR (see equation 4.21 and Figure 4.3).

  In the case of optimal gain and flat detection noise PSD $[S_{\mathrm{x_n}}(\omega \approx \omega_{\mathrm{m}}) = \mathrm{const}]$ the measured PSD $S_{\mathrm{y}}(\omega)$ is also flat: $S_{\mathrm{y}}(\omega) \approx S_{\mathrm{x_n}}(\omega_{\mathrm{m}})$. The relative deviation from a perfect flat line is very small and shown in the inset of Figure 4.2. If the gain g_{v} is further increased, the in-loop measured PSD signal $S_{\mathrm{y}}(\omega)$ can even become smaller than $S_{\mathrm{x_n}}(\omega)$ and a dip in the spectrum occurs. This phenomenon is known as *noise squashing* and it indicates that the detector noise and the displacement noise of the oscillator are correlated [8]. In this regime the corresponding real oscillator displacement $S_{\mathrm{x}}(\omega)$ only gets broader, which indicates that for $g_{\mathrm{v}} > g_{\mathrm{v,opt}}$ the oscillator temperature increases again. The minimal achievable temperature is very well approximated by $T_{\mathrm{mode}}^{\mathrm{min}} \approx 2T_{\mathrm{bath}}/\sqrt{\mathrm{SNR}}$. Hence, the minimum

achievable temperature with velocity-dependent feedback scales as

$$T_{\mathrm{mode}}^{\mathrm{min}} \sim \sqrt{Q^{-1}},\ \sqrt{m},\ \sqrt{S_{\mathrm{x_n}}},\ \sqrt{T_{\mathrm{bath}}}.$$

While the detection noise level $S_{\mathrm{x_n}}$ and the cryogenic bath temperature T_{bath} quickly run into fundamental and technical limitations, the oscillator mass m and the Q-factor are promising optimization parameters to reach the quantum ground state through velocity-dependent feedback cooling. The quantum limits of feedback cooling will be discussed on the following pages.

- **Displacement-proportional feedback**: If the imaginary part of χ_{fb} is zero, the feedback force is purely proportional to the displacement $x(t)$ of the oscillator (see equation 4.8). The real part of χ_{fb} is related to the displacement-dependent gain g_{d} (see equation 4.6) which changes the spring constant of the oscillator to $k'_{\mathrm{m}} = k_{\mathrm{m}}\,(1 + g_{\mathrm{d}})$. The resulting measured displacement PSD of the oscillator S_{y} and the real PSD S_{x} is shown in the right column of Figure 4.2. For $g_{\mathrm{d}} \neq 0$ the peak of the PSD is shifted to higher or lower frequencies. For the parameters used in the simulation no cooling is visible and the oscillator PSD S_{x} only increases. Contrary to velocity-dependent feedback, the PSD becomes asymmetric for $g_{\mathrm{d}} \neq 0$.

  As calculated above, the optimal gain $g_{\mathrm{d,opt}}$ for displacement-proportional feedback cooling gets smaller for larger Q-factors which leads to a negligible cooling effect unless the oscillator has an extremely small resonance frequency where large optimal gains are possible (since for large gain $g_{\mathrm{d,opt}} \sim \omega_{\mathrm{m}}^{-3/2}$). An example of displacement-proportional feedback cooling is the gravitational wave detector LIGO, where the resonance frequency of pendulum mirrors is shifted from subhertz to $\approx 150\,\mathrm{Hz}$. The stiffening of the oscillator spring constant k_{m} then leads to a reduction of thermal motion, which is referred to as "cold spring" [128].

- **Mixed feedback: Combinations of g_{d} and g_{v}**: If the feedback filter function χ_{fb} has both real and imaginary parts, velocity-dependent and displacement-dependent feedback is applied at the same time. This was done for example at the LIGO gravitational wave detector [128]. However, for our parameters a displacement-proportional gain can only lead to heating and it can be regarded as a parasitic effect that should be minimized. Figure 4.5 shows how the measured PSD signal $S_{\mathrm{y}}(\omega)$ transforms for small parasitic contributions of g_{d} near the optimal gain g_{v}. The most relevant configuration is for optimal gain $g_{\mathrm{v,opt}}$ where the coldest temperature is reached and the measured PSD S_{y} becomes flat (see Figure 4.5 at top right). For finite gain $g_{\mathrm{d}} \neq 0$ this flat PSD is transformed into an dispersive curve which has a shifted zero crossing at some $\Delta\omega_{\mathrm{cross}}$ that increases with larger g_{d}. The new minimum of the PSD occurs at some $\Delta\omega_{\mathrm{min}}$ which is largest for small g_{d}. The larger the velocity-dependent gain g_{v} the smaller the parasitic effects related to finite g_{d}. This can be explained by the fact that the displacement-dependent temperature increase is also suppressed by g_{v} (see equation 4.19 for the mode temperature).

  The relative increase of mode temperature for different gains g_{v} as a function of small parasitic gain g_{d} is shown in the lower left panel of 4.5. Especially for

the optimal gain $g_{\mathrm{v,opt}} = \mathrm{SNR}$ the relative temperature increase is small even for a parasitic g_{d} where the dispersive feature in the PSD is already quite significant. Notably, this result becomes important for the temperature evaluation of experimental data that will be presented at the end of this chapter.

In the previous description of feedback cooling quantum effects were omitted. Nevertheless, in order to evaluate the possibilities of ground state cooling by feedback control these effects need to be taken into account.

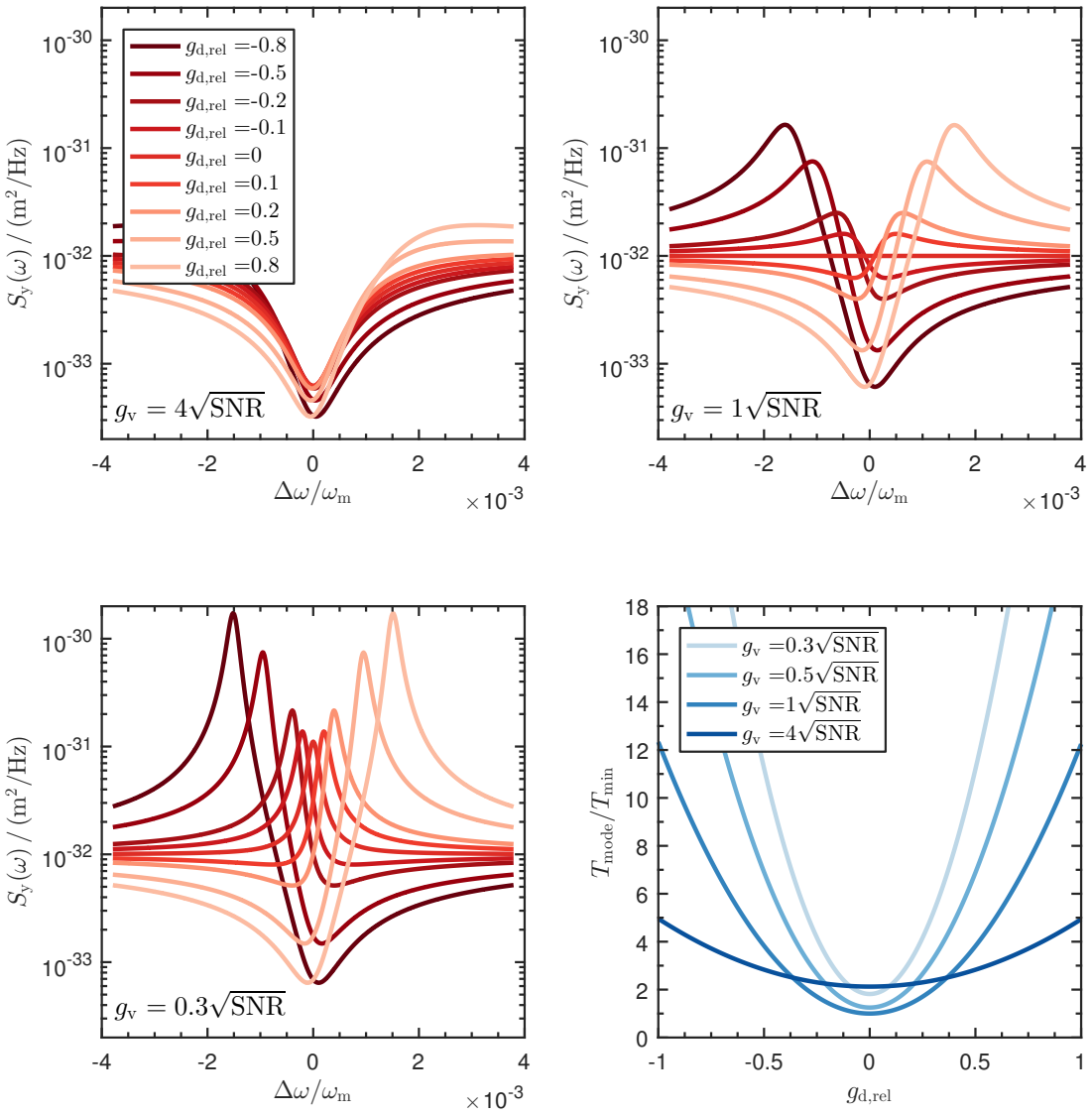

Figure 4.5: Effects of parasitic displacement-proportional gain. Measured displacement PSD $S_{\mathrm{y}}(\omega)$ for large velocity-dependent gains $g_{\mathrm{v}} = 0.3,\ 1,\ 4 \cdot g_{\mathrm{v,opt}}$ and different displacement-proportional gains g_{d}, respectively (upper panels and lower left panel). Lower right panel: Corresponding relative change in mode temperature for these values of g_{v} as a function of g_{d}. The displacement-gain is scaled to $g_{\mathrm{d,rel}} = g_{\mathrm{d}} \cdot k_{\mathrm{m}}$. Parameters as in Figure 4.2.

Time evolution during feedback cooling

So far, the steady state behavior of a feedback cooled mechanical oscillator was covered. Analytically, this state is reached after an infinite feedback cooling time with fixed parameters. However, in the experiment an effectively stable temperature is reached rather quickly. Nevertheless, it is interesting to regard the transient behavior of the oscillator during the cooldown process.
Suppose pure velocity-dependent feedback cooling is applied sharply at time $t = 0$. Then the equation of motion for $t > 0$ is given by [135]

$$\ddot{x}(t) + \Gamma_\mathrm{m}\,\dot{x}(t) + \omega_m^2\,x(t) \;=\; m^{-1}\,F_\mathrm{th}(t) - \Gamma_\mathrm{m}\,g_\mathrm{v}\,\dot{x}(t). \tag{4.23}$$

where $F_\mathrm{th}(t)$ is the time dependent, stochastic thermal Langevin force. It should be noted that in this equation the detector noise $x_\mathrm{n}(t)$ that is fed back to the oscillator is neglected (compare equation 4.3). The equation of motion can be solved for $\langle x^2\rangle(t)$ which is proportional to the mode temperature. This yields [135]

$$T_\mathrm{mode}(t) \;=\; \frac{T_\mathrm{bath}}{1+g_\mathrm{v}}\left(1 + g_\mathrm{v}\,e^{-\Gamma_\mathrm{m}(1+g_\mathrm{v})\,t}\right). \tag{4.24}$$

It becomes apparent that for $t \to \infty$ the mode temperature reaches $T_\mathrm{mode} = T_\mathrm{bath}/(1+g_\mathrm{v})$ which corresponds to equation 4.19 for $g_\mathrm{d} = 0$ and $g_\mathrm{v} \ll \mathrm{SNR}$ (see also Figure 4.3). Notably, the time scale in which the final temperature is reached is proportional to the natural linewidth Γ_m of the oscillator.
The rethermalization of the cooled oscillator after the feedback is switched off can be calculated in the same manner [135]

$$T_\mathrm{mode}(t) \;=\; T_\mathrm{bath}\left(1 - \frac{g_\mathrm{v}}{1+g_\mathrm{v}}\,e^{-\Gamma_\mathrm{m}\,t}\right). \tag{4.25}$$

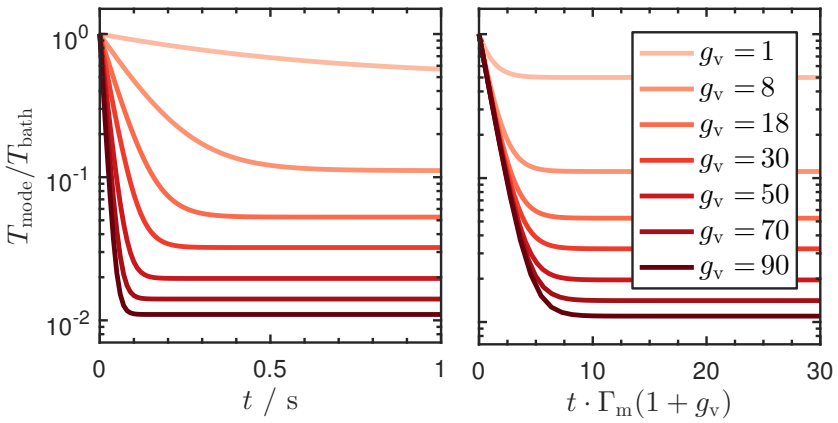

Figure 4.6: Mode temperature for pure velocity-dependent feedback as a function of time. The relative mode temperature $T_\mathrm{mode}/T_\mathrm{bath}$ is plotted as a function of time for different feedback gains g_v. At $t = 0$ the feedback cooling is started. For $t > 0$ the temperature drops and asymptotically reaches a steady state after a characteristic time $\tau_\mathrm{fb} = \Gamma_\mathrm{m}^{\prime -1}$ with $\Gamma_\mathrm{m}^\prime = \Gamma_\mathrm{m}(1+g_\mathrm{v})$. This time scale depends linearly on g_v (for $g_\mathrm{v} \gg 1$) and the natural linewidth Γ_m of the oscillator, which can be seen in the right panel, where the x axis is given by the dimensionless time $t \cdot \Gamma_\mathrm{m}(1+g_\mathrm{v})$. The steady state is reached after $t_\mathrm{cool} \approx 10 \cdot (\Gamma_\mathrm{m} g_\mathrm{v})^{-1}$.

4.1.2 Quantum limits of feedback cooling

In 1999, the group of M. Pinard first realized feedback cooling and shortly afterwards also evaluated the quantum limits of cold damping showing that ground state cooling is in principle possible [121]. In the light of the fact that all optomechanical cooling schemes can be classified into passive self-cooling mechanisms like resolved sideband cooling and active feedback cooling, much theory work has been done on comparing these two cooling approaches in terms of fundamental limits and potential advantages of one method over the other. In [122] it was shown that sideband cooling is superior in the good cavity regime while feedback cooling is superior in the bad cavity regime. A quantitative comparison of both methods on equal footing revealed that generally sideband cooling is superior to feedback cooling due to the projection noise of the position measurement of the oscillator during feedback cooling [136] (the projection noise is the measurement error due to the uncertainty of the oscillator position).
In order to reach the quantum ground state using feedback cooling, the measurement precision and the complementary disturbance of the system in terms of back-action noise must be carefully balanced. By choosing the right trade-off between these two quantities the cooling performance can be further improved [137]. A comprehensible quantum mechanical treatment of feedback cooling was given in the supplementary material of [69] and will briefly be reviewed in the following.
In a fully quantum mechanical treatment the back-action of the cavity light field on the oscillator and the stochastic fluctuations of the feedback actuator need to be taken into account. As a very good approximation in the bad cavity regime, the dynamical component of the back-action force that leads to self-cooling (also called *dynamical back-action cooling*) is negligible [69]. Hence, the back-action force does not depend on the oscillator position and can be modeled as a random thermal force $F_{\mathrm{ba,th}}$. Since every physical actuator used to excite the oscillator will also contain small random fluctuations, the feedback force in equation 4.1 must also be extended by an effective thermal component $F_{\mathrm{fb,th}}$:

$$F_{\mathrm{fb}}(\omega) \;=\; -\,\chi_{\mathrm{fb}}^{-1}(\omega)\, y(\omega) \;+\; F_{\mathrm{fb,th}}. \tag{4.26}$$

This specification is widely neglected in most publications by assuming the feedback actuator is a field of zero temperature. Taking into account these additional thermal force terms, the oscillator environment now contains three different thermal forces: The mechanical noise of the oscillator environment F_{th}, the back-action force $F_{\mathrm{ba,th}}$ and the fluctuations of the feedback actuator $F_{\mathrm{fb,th}}$. Equation 4.2 now extends to:

$$\chi_{\mathrm{m}}^{-1}\, x \;=\; F_{\mathrm{th}} + F_{\mathrm{ba,th}} + F_{\mathrm{fb,th}} + F_{\mathrm{fb}}\,. \tag{4.27}$$

For a high-Q oscillator, each reservoir can be assigned a thermal noise equivalent occupation n_{th}, n_{ba}, n_{fb} with $n_{\mathrm{th}} = \frac{1}{2}\coth\left(\hbar\omega_{\mathrm{m}}/2k_{\mathrm{B}}T_{\mathrm{bath}}\right)$ [69]. Thus, the total effective thermal noise PSD can be expressed by these occupations:

$$S_{\mathrm{F_{th}}}^{\mathrm{tot}}(\omega) \;=\; \left(n_{\mathrm{th}} + n_{\mathrm{ba}} + n_{\mathrm{fb}} + \frac{1}{2}\right) \cdot |\chi_{\mathrm{m}}(\omega_{\mathrm{m}})|^{-2} \cdot 2S_{\mathrm{x}}^{\mathrm{zp}}(\omega_{\mathrm{m}}), \tag{4.28}$$

where the peak displacement PSD $S_{\mathrm{x}}^{\mathrm{zp}}(\omega_{\mathrm{m}})$ in the ground state is introduced. It can be

calculated using the semi-classically Callen and Welton equation for the thermal force noise PSD [7]:

$$S_{\mathrm{F_{th}}}(\omega) = \frac{4m\omega}{Q} \cdot \frac{\hbar\omega}{2} \coth\left(\frac{\hbar\omega}{2k_{\mathrm{B}}T_{\mathrm{bath}}}\right) \tag{4.29}$$

$$\Rightarrow\ S_{\mathrm{x}}^{\mathrm{zp}}(\omega_{\mathrm{m}}) = |\chi_{\mathrm{m}}(\omega_{\mathrm{m}})|^2\, S_{\mathrm{F_{th}}}(\omega_{\mathrm{m}}) \overset{T\to 0}{\longrightarrow} \frac{4x_{\mathrm{zp}}^2}{\Gamma_{\mathrm{m}}} \tag{4.30}$$

with the quantum zero-point fluctuation $x_{\mathrm{zp}}^2 = \hbar/(2m\omega_{\mathrm{m}})$ (see equation 3.13). The quantity $S_{\mathrm{x}}^{\mathrm{zp}}(\omega_{\mathrm{m}})$ also defines the number of imprecision quanta as the apparent thermal occupation associated with the measurement noise: $n_{\mathrm{x_n}} = S_{\mathrm{x_n}}/2S_{\mathrm{x}}^{\mathrm{zp}}(\omega_{\mathrm{m}})$.
The mean phonon occupation n_{m} of the oscillator can be expressed by the variance of the displacement $\langle x^2\rangle$ and the zero-point fluctuation:

$$2n_{\mathrm{m}} + 1 = \frac{\langle x^2\rangle}{x_{\mathrm{zp}}^2} = \frac{1}{2\pi}\int_0^\infty \frac{S_{\mathrm{x}}(\omega)}{x_{\mathrm{zp}}^2}\,\mathrm{d}\omega\,. \tag{4.31}$$

Assuming pure velocity-dependent feedback ($g_{\mathrm{d}} = 0$), this integral can be solved in the same manner as for the mode temperature (see equation 4.17) using the new total thermal noise PSD $S_{\mathrm{F_{th}}}^{\mathrm{tot}}(\omega)$ and the susceptibilities from equation 4.15 in expression 4.9 for $S_{\mathrm{x}}(\omega)$:

$$n_{\mathrm{m}} = \frac{\left(n_{\mathrm{th}} + n_{\mathrm{ba}} + n_{\mathrm{fb}} + \frac{1}{2}\right) + n_{\mathrm{x_n}} g_{\mathrm{v}}^2}{1 + g_{\mathrm{v}}} - \frac{1}{2}\,. \tag{4.32}$$

Minimizing this expression with respect to the feedback gain g_{v} yields the optimal gain and the minimum phonon occupation:

$$\frac{\partial n_{\mathrm{m}}}{\partial g_{\mathrm{v}}} = 0 \Rightarrow g_{\mathrm{v,opt}} \overset{n_{\mathrm{th}}\gg\frac{1}{2}}{\approx} \sqrt{1 + \frac{n_{\mathrm{th}} + n_{\mathrm{ba}} + n_{\mathrm{fb}}}{n_{\mathrm{x_n}}}} - 1 \tag{4.33}$$

$$\overset{n_{\mathrm{th}}\gg n_{\mathrm{x_n}}}{\approx} \sqrt{\frac{n_{\mathrm{th}} + n_{\mathrm{ba}} + n_{\mathrm{fb}}}{n_{\mathrm{x_n}}}} \tag{4.34}$$

$$\Rightarrow\ n_{\mathrm{m,min}} \overset{n_{\mathrm{th}}\gg n_{\mathrm{x_n}}}{\approx} 2\sqrt{(n_{\mathrm{th}} + n_{\mathrm{ba}} + n_{\mathrm{fb}})\, n_{\mathrm{x_n}}} - \frac{1}{2} \tag{4.35}$$

It becomes apparent that the approximation of a zero temperature feedback actuator stays valid even in the quantum regime, since in experimentally relevant situations $n_{\mathrm{th}} \gg n_{\mathrm{fb}}$. The condition for ground state cooling then transforms into

$$n_{\mathrm{m}} < 1 \Rightarrow n_{\mathrm{x_n}} < \frac{9}{16}\,(n_{\mathrm{th}} + n_{\mathrm{ba}})^{-1}\,. \tag{4.36}$$

In [69] it is also shown that stochastic, thermal back-action for cavity optomechanical position measurements is related to the detection noise level $S_{\mathrm{x_n}}$ by the imprecision-back-action product

$$\hbar^2 S_{\mathrm{x_n}} S_{\mathrm{ba,th}} = 16 n_{\mathrm{x_n}} n_{\mathrm{ba}} \geq 1\,. \tag{4.37}$$

This continuous-detector equivalent of the Heisenberg uncertainty principle can also be found as equation (62) in the review paper by Poot and van der Zandt [7]. It is valid for the case of vanishing dynamical back-action and is based on the work of Clerk *et al.* [117, 138]. Using this relation the necessary condition for ground state cooling is

$$n_{\mathrm{x_n}} < (2n_{\mathrm{th}})^{-1} \tag{4.38}$$

$$\Rightarrow S_{\mathrm{x_n}} < \frac{S_{\mathrm{x}}^{\mathrm{zp}}}{n_{\mathrm{th}}} = \frac{4x_{\mathrm{zp}}^2}{n_{\mathrm{th}}\Gamma_{\mathrm{m}}}\,. \tag{4.39}$$

4.2 Quantum feedback control

The feedback cooling mechanism presented in the previous section can be seen in the wider context of quantum feedback control. After a brief overview of the significance of feedback control in many fields of quantum physics, the applications in other optomechanical systems and experimental prospects for the optomechanical system presented in this thesis will be discussed.

The concept of feedback control was introduced into quantum mechanics in the 1980's and has intensively been studied since the 1990's. Important contributions to the theoretical framework were made by Milburn and Wiseman, of whom the latter published the text book "Quantum Measurement and Control" which is often referred to in this context [139]. Quantum control theory has contributed significantly to the understanding of fundamental aspects of quantum theory such as the quantum zeno effect or quantum nondemolition (QND) measurements. Driven by the advances of quantum optics where it first became possible to detect and manipulate quantum systems with the necessary precision, quantum feedback control has evolved into an important tool with many applications in modern quantum technology and is part of ongoing fundamental research. A comprehensive theoretical and experimental overview of this topic can be found in the review paper by Zhang *et al* (2014) [140].

Generally, the term "quantum feedback" refers to feedback loops that cannot be described by a classical model. As depicted in Figure 4.7, one can distinguish two different types of quantum feedback: measurement-based quantum feedback and coherent feedback [140]. Measurement-based quantum feedback works analog to classical feedback: the feedback loop itself processes information classically (for example as part of a measurement device) but the back-action of the measurement cannot be neglected. Hence, the measurement perturbs the quantum state of the controlled system and changes its temporal evolution. This is prevented in a coherent feedback loop where no classical information is extracted and the controller itself is a quantum system, just as the system to be controlled (proposed by Lloyd in 2000 [141]). In this case the feedback control is simply given by the interaction of the two quantum systems.

Coherent feedback

Hybrid quantum systems: Sympathetic cooling in a hybrid atomic-mechanical system, which will be described later in chapter 5, can be regarded as a coherent feedback process [34].

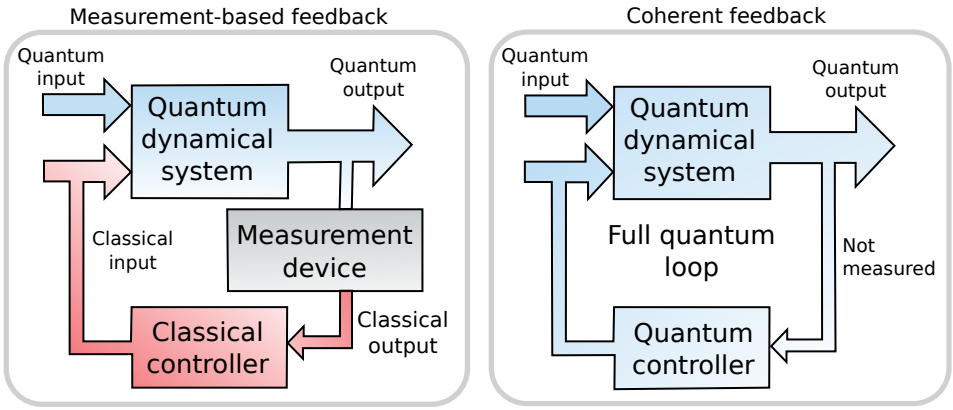

Figure 4.7: Comparison of measurement-based quantum feedback and coherent feedback. In measurement-based feedback (left) the system is controlled by a classical feedback loop, while in coherent feedback (right) the system is controlled coherently by a fully quantum mechanical feedback loop. Figure adapted from [140].

Self-Cooling: Another important example of coherent feedback control is optomechanical self-cooling in the resolved sideband regime [140, 142], where a cavity field coherently exchanges energy with a mechanical oscillator that gets cooled. The detuning of the cavity pump field then defines the sign and magnitude of the feedback gain. This technique was applied in optical and microwave cavities to cool the oscillator into the quantum ground state [38–43]. Since for the optomechanical system presented in this thesis the resolved sideband regime is far out of reach, this cooling technique will not be possible.
Noise reduction: The first realization of an all-optical coherent feedback loop in 2008 was performed by Mabuchi [143]. In this setup two coupled ring cavities formed the primary system and the controller, reducing the laser noise in the primary cavity.
Feedback cooling: Improvement of feedback cooling using coherent controllers was proposed by Hamerly and Mabuchi [144].
Squeezing enhancement: In 2012, Slida *et al* created a coherent feedback loop in order to enhance the squeezing of an optical beam. Squeezing was initially generated by a non-linear crystal and the coherent feedback was used to enhance its fidelity.
Squeezing of mechanical motion: Driving a cavity with two different lasers at frequencies $\omega_{\mathrm{cav}} \pm \omega_{\mathrm{m}}$, namely the mechanical sideband frequencies, can lead to arbitrarily large squeezing of the motional quadratures [145]. This technique also called *reservoir engineering* (the cavity acts as an engineered reservoir) can be seen as a coherent feedback process and it was successfully used to squeeze mechanical motion [42, 43, 146].
Coherent feedback was also proposed as a tool for ***Quantum error correction*** in quantum information processing [147, 148] and was sucessfully implemented for ***entanglement preservation*** in superconducting circuits [149].

Measurement-based feedback

Homodyne detection enhancement: An adaptive homodyne phase measurement based on quantum feedback was first realized in 2002 based on a proposal by Wiseman [150]. Homodyne detection is a powerful technique for quadrature measurements of a

laser beam if its phase is known roughly or can be locked with a classical feedback loop. However, if the phase of a laser pulse is completely unknown this task gets more difficult and the results become less accurate. Especially for quadrature measurements of low photon number pulses with unknown phase the adaptive phase method is superior to any other technique [151].

Quantum state preparation and stabilization: The first demonstration of quantum feedback in an atomic system was performed in a cavity interacting with a beam of atoms. A quantum feedback loop was used to freeze the Rabi oscillations of the cavity field [152]. In 2011, the preparation of Fock states of a microwave field in a superconducting cavity was demonstrated [153]. The field was measured by the internal state of Rydberg atoms flying through the cavity and fed back to the cavity field by changing the amplitude of the coherent cavity driving field. This quantum feedback loop narrows the photon distribution in the cavity towards a Fock state. Furthermore, measurement-based feedback was used in superconducting circuits for turning the entanglement of two qubits from probabilistic to full deterministic [154]. Also in the field of quantum gases proposals exist for quantum feedback. Using QND measurements of the spatial mode of a BEC the density distribution could be acitvely controlled, which could be used for narrowing the linewidth of atom lasers [155, 156]. An example of quantum feedback cooling is the cooling of the motional state of cold ions in a Paul trap to a mean phonon occupation of $n_{\mathrm{m}} = 12$ [157].

Measurement-based feedback in optomechanics

Feedback cooling: In order to feedback cool a mechanical oscillator into its quantum ground state, the back-action of the measurement must be taken into account [69, 137] (see equation 4.36). In this regime one can speak of feedback cooling by measurement-based quantum feedback, a regime that was recently reached by feedback cooling a SiO_2 microdisk whispering gallery mode resonantor to a mode occupation of $n_{\mathrm{m}} \approx 5$ [69]. For the optomechanical system presented in this thesis, the usage of trampoline oscillators would realistically enable feedback cooling into the quantum ground state, as discussed in section 4.4.3. Apart from feedback cooling, many other applications of quantum feedback control in optomechanics exist.

Squeezing of mechanical motion: Squeezing of mechanical fluctuations was first demonstrated far outside the quantum regime by parametrically modulating the spring constant of an oscillator [158] (parametric amplification). Although this method is limited to 3 dB of steady state squeezing, avoiding this limit using modified parametric techniques and feedback were proposed [159, 160] and experimentally realized [161]. A related technique uses back-action evading QND measurements for squeezing. This method was used in the context of sequeezing generation in many recent publications of optomechanical [42, 43, 146] and atomic spin systems [162]. It was proposed already decades ago by the pioneer work of Braginsky *et al* in the 1980's in the context of gravitaional wave detection [163]. The basic idea is a stroboscopic measurement of only one quadrature of the oscillator motion by synchronizing the measurement to the motion. Each short measurement pulse yields some information about the x quadrature and narrows the width of the density matrix in x-direction. Between the pulses the oscillator undergoes free evolution and the density matrix returns to the same state

one period later. In this way, many weak, imprecise measurements become equivalent to one precise measurement [159]. In 2005, Ruskov *et al* showed that this modulated measurement could in principle produce arbitrarily large squeezing for rectangular measurement pulses combined with a quantum feedback loop to cool the oscillator [159]. Also based on the work of Braginsky *et al*, Clerk *et al* [164] studied the mechanical squeezing in an optomechanical system driven by a laser modulated at the oscillator frequency ω_{m}, which creates two sidebands at $\pm\,\omega_{\mathrm{m}}$. This "two-tone-driving" leads to back-action evading measurements and squeezing. The authors show that the generated conditional squeezing can be turned into "real", unconditional squeezing of the mechanical oscillator by applying a sinusoidal feedback force. Similarly, feedback can also be used to generate unconditional entanglement in mechanical systems [165].

Although many of the squeezing schemes discussed above rely on the resolved sideband regime, the stroboscopic QND measurement combined with feedback cooling proposed by Ruskov *et al* is an interesting prospect for the system described in this thesis. As feedback cooling was already implemented, only the measurement beam would need to be modulated phase-synchronized. In order to distinguish noise squashing from real squeezing, an additional homodyne detector would also be helpful [164].

Enhancements by feedback: Recently it was demonstrated experimentally that sideband cooling of a mechanical oscillator can be improved significantly by adding a feedback loop that amplifies the amplitude fluctuations in the cavity. The feedback operates in the unusual "positive feedback" regime, improving the cooling even more than using squeezed light [166, 167]. Recently, the group of T. Kippenberg reported enhanced visibility of quantum correlations in their microdisc optomechanical system depending on the applied feedback cooling [168].

Summarizing the prospects of quantum feedback control for the optomechanical system presented in this thesis one can say that feedback cooling into the ground state is a realistic future prospect, as further discussed in section 4.4.3. If back-action plays a role in this regime, this could be avoided by stroboscopic, back-action evading measurements, which would also produce squeezing of mechanical motion. If the generation of non-classical states of motion would be possible in the future, feedback could be used to turn conditional states into "real" non-classical states of the oscillator.

4.3 Experimental setup for feedback cooling

In the beginning of this section, the technical demands on feedback cooling of mechanical motion will be discussed. Afterwards, the technical solutions implemented in the experimental setup described in this thesis will be presented.

As shown in section 4.1, the theoretical feedback cooling limit for a given optomechanical system is only defined by the detection noise level $S_{\mathrm{x_n}}$ (which might be back-action limited), see equation 4.39. Assuming this quantity is given by the detector specifications and the optomechanical system, the remaining part of the feedback loop is the feedback filter function χ_{fb}^{-1} and the feedback actuator that exerts the feedback force F_{fb} on the oscillator, as depicted in Figure 4.1. Notably, the demands on these parts of the feedback loop are purely of technical nature. Their theoretical performance assumed in the calculation of the cooling limit is technically challenging, yet achievable.

The following requirements need to be met in order to satisfy the theoretical "ideal" feedback loop consisting of a bandpass filter centered at ω_m, a feedback phase of $\phi = \frac{\pi}{2}$ and a zero temperature, arbitrary gain actuator field to exert F_{fb} on the oscillator.

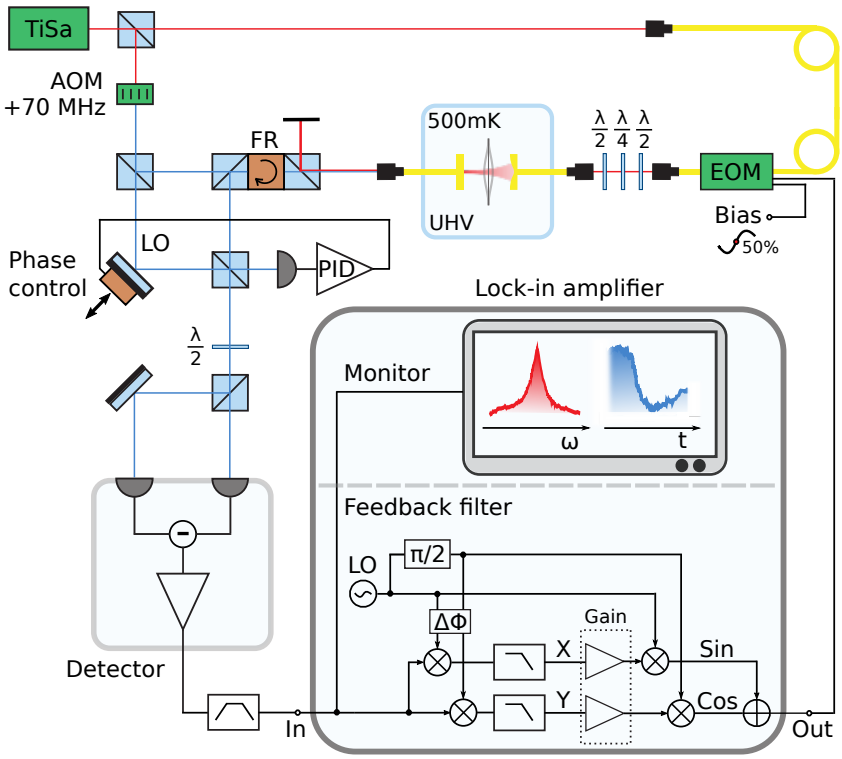

Figure 4.8: Experimental setup for feedback cooling. Light from a Ti:sapph (green box) is split into a feedback cooling beam (red) and a detection beam (blue), which is frequency-shifted +70 MHz by an AOM. One part of this beam serves a local oscillator (LO) and the other part is transmitted through a Faraday rotator (FR) and coupled through a glass fiber into a cryogenic UHV chamber where it gets reflected by an optomechanical MiM system (see chapter 2), now carrying phase information of the mechanical motion. This light is picked up on its way back through the FR and superimposed with the LO beam in a polarizing beam splitter cube (PBS). One of its outputs hits a photodiode, creating an interferometric error signal for a phase lock loop (interference occurs because of impure polarization). The other PBS output passes a wave plate creating interference between the two beams at another PBS that is part of a balanced homodyne detection. Its two outputs are subtracted and amplified by a customized photoreceiver from *Femto* (DC...1 MHz, gain 28.5 kV/W, NEP 1.1 pW/$\sqrt{\text{Hz}}$), generating a voltage signal proportional to the mechanical oscillator motion $x(\omega)$. This signal is filtered using an electrical bandpass (see appendix B.3) centered at ω_m to protect the input of a lock-in amplifier (HF2LI from *Zurich Instruments*) against possible DC voltages. It is then monitored and processed by the feedback filter that amplifies the quadratures X and Y with an adjustable gain after down-mixing with an LO at the mechanical oscillator frequency ω_m. The feedback phase is adjusted with a delay $\Delta\Phi$ with a phase-shifted LO for down-mixing. X and Y get mixed up again and the sum is fed out to a fiber EOM (AM785b from *Jenoptik*, data sheet in appedix B.4) that modulates the amplitude of the feedback light which is coupled into cryogenic MiM setup. Three wave plates in front of the cavity are used to separate the feedback light that is transmitted through the MiM system from the detection beam. The sketch schematically shows the planned setup using a FR in the detection beam, the realized setup is shown in appendix B.1. Most of the used wave plates, mirrors and PBS are omitted.

4.3.1 Technical requirements

- **Detector**: Homodyne detection is the quantum limited phase detection scheme mostly used for measuring the oscillator motion in optomechanical systems (see section 3). Phase fluctuations of the detection beam are translated into amplitude fluctuations that can be recorded with a photodetector. The detection should be shot noise limited, in order to enable quantum limited detection. The detector output is an electrical noise equivalent $S_{\mathrm{x_n}}^{\mathrm{el}}$ of the mechanical noise floor PSD $S_{\mathrm{x_n}}$, that should be well above the dark noise of the photodetector and possible parasitic electrical noise from the environment. The bandwidth of the detector should be much larger than the oscillator frequency ω_{m}.

- **Feedback filter**: The electrical signal from the detector is processed by the feedback filter function χ_{fb}^{-1}. In order to create a bandpass filter function that is centered at ω_{m} and has a finite width, the filter can be either a customized analog bandpass with sufficiently small and constant phase shift in the passband or a very fast digital real-time application with a bandwidth much larger than ω_{m}. The corresponding electrical noise added by the filter must be well below the noise equivalent displacement PSD $S_{\mathrm{x_n}}^{\mathrm{el}}$ of the detection noise level.

- **Feedback actuator**: The perfect feedback actuator is a field of zero temperature which exerts a force $F_{\mathrm{fb}}(\omega) = -\chi_{\mathrm{fb}}^{-1} y(\omega)$ on the oscillator that is purely linear in its measured displacement $y(\omega)$. This means that the random, thermal component $F_{\mathrm{fb,th}}$ of the feedback force in equation 4.26 can be neglected. As long as the corresponding thermal occupation n_{fb} of the "feedback field reservoir" is much smaller than the thermal occupation of the oscillator from the environment, this is a good approximation (see equation 4.28 for the total thermal noise force PSD). Furthermore, the coupling mechanism of the feedback force to the oscillator should allow for a sufficiently large regime of feedback gains (large $|\chi_{\mathrm{fb}}^{-1}|$) where these assumptions still hold.

- **Feedback-detection cross-talk**: Assuming all three technical requirements for ideal feedback cooling mentioned above can be met, a remaining vital condition for successful feedback cooling is a negligible cross-talk between all electrical and optical signals involved in the feedback loop and the measured in-loop oscillator signal $y(\omega)$. This cross-talk can be modeled as a detector noise $x_{\mathrm{n}}(\omega)$ that is not fully random, but correlated with the detection signal $y(\omega)$, the feedback filter $\chi_{\mathrm{fb}}^{-1}(\omega)$, the feedback force $F_{\mathrm{fb}}(\omega)$ or combinations of them. In this case the performance of the feedback cooling is reduced and the measured signal $y(\omega)$ can not be trusted. One possibility that is drastic but not far-fetched is a direct negative electrical feedback of the measured signal $y(\omega)$ on the detector, which cancels the measured signal. In this way, the detected oscillator signal is reduced without any real physical cooling of the oscillator. A large variety of other, more complex possible sources for cross-talk exists, which can never be fully prevented (electrically induced phase modulation of detection laser, feedback light entering the homodyne setup, etc.). Nevertheless, the sum of all cross-talk effects should be below a certain threshold. One can define this limit as follows:

(4.40)

Cross-talk limit. In the limit of negligible cross-talk, the following condition should be met: assuming the oscillator is kept at $x(\omega) = 0$ and an artificial "test feedback" signal is applied at a frequency ω_t, there should be no effect on the measured in-loop homodyne signal $y(\omega_t)$ - or more precisely $y(\omega_t) = S_{x_n}(\omega_t)$ - even if the test signal is stronger than feedback signals can become during feedback cooling.

The above technical requirements for an optimal feedback cooling were met in the course of this thesis and the implemented solutions will be presented in the following. Figure 4.8 shows a sketch of the electro-optical setup used for feedback cooling of a membrane oscillator in a cryogenic fiber cavity (the actual realization of the optical setup slightly differs and is shown in appendix B.1).

4.3.2 Technical implementations

- **Detector**: The mechanical oscillator motion is measured by balanced homodyne detection in the shot noise limited regime (see section 3). The detector is a low noise balanced silicon photoreceiver which was customized by *Femto* (data sheet in appendix B.2). It has a specified bandwidth of 1 MHz which is well above the ground mode frequency of $\omega_m/2\pi \approx 250\,\mathrm{kHz}$ of the used SiN membrane oscillators. The noise equivalent power spectral density (NEP) is specified as approximately $S^P_{Det} \approx 1\,\mathrm{pW}/\sqrt{\mathrm{Hz}}$ at 100 kHz. Also specified is a conversion gain of $c_P = 28.5\,\mathrm{kV/W}$, which yields in an electrical noise floor of $S^V_{Det} = S^P_{Det} \times c_P = 2.85 \times 10^{-8}\,\mathrm{V}/\sqrt{\mathrm{Hz}}$. Using the current experimental homodyne calibration $c_V \approx 1 \times 10^{10}\,\mathrm{V/m}$ (see section 3) this can be converted into a displacement NEP of the detector: $S^x_{Det} = S^V_{Det} \times c_V^{-1} = 2.85 \times 10^{-18}\,\mathrm{m}/\sqrt{\mathrm{Hz}}$. For the MiM setup described in this thesis the smallest achievable homodyning noise floor around the oscillator frequency is $S_{x_n} \approx 1 \times 10^{-16}\,\mathrm{m}/\sqrt{\mathrm{Hz}}$. Hence, in the relevant regime the electrical detector noise floor is more than 30 times smaller than the homodyne detection noise floor of the optomechanical system.

  The photodetector is electrically isolated from the optical table where it is located and connected via a low noise triaxial cable (G_02330_HT from *Huber+Suhner AG*) to the measurement and processing unit, where the outer shield of the triaxial cable is grounded. Notably, this is the only electrical connection between photodetector and measurement unit. The phase control of the homodyning is generated by another error signal (not the homodyne signal itself) in order to minimize the electrical noise in the homodyne signal path. This proved to be the best way of minimizing electrical noise in the signal path, superior to all other tested solutions.

- **Feedback filter**: The electrical signal from the photodetector that is proportional to the oscillator displacement $x(\omega)$ is first filtered by an electrical bandpass filter with a center frequency of $f_m = 245\,\mathrm{kHz}$ and a 3 dB width of 55 kHz (KR2994 from *KR Electronics*). Detailed information on the passband ripples, power loss

at the oscillator frequency and phase shift can be found in appendix B.3. All those effects are so small that the filter can still be regarded as ideal. Nevertheless, in case the bandpass causes problems at some point, it can also be omitted regarding the fact that its main purpose is to protect the input of the following lock-in amplifier from possible DC voltages that might destroy the input stage.[2]

The homodyne signal is then fed into a digital lock-in amplifier (HF2LI from *Zurich Instruments*, bandwidth 50 MHz, LabOne toolset) that is used for monitoring, data acquisition and processing of the homodyne signal for feedback cooling. In order to generate the ideal feedback force that is proportional to the velocity of the oscillator (see section 4.1) one needs to create an electrical output signal that is proportional to the input signal and phase-shifted such that finally the oscillator motion is phase-shifted $\pi/2$ against the feedback force (additional delays in the feedback loop need to be compensated). Since the oscillator frequency $\omega_\mathrm{m}/2\pi \approx 250\,\mathrm{kHz}$ is too large for common real-time applications, the signal is mixed down for processing. The schematic of the digital processing circuit is shown in Figure 4.8: the analog homodyne input signal is first digitized and then mixed down with a local oscillator (LO) well centered at the mechanical oscillator frequency ω_m with a demodulator bandwidth much larger than Γ_m (stable against small frequency drifts of ω_m). The resulting quadrature signals are then amplified by the same amount, which corresponds to the adjustable feedback gain g_v. After mixing the DC quadratures up again with the LO, the sine and cosine components of the signal are recovered and the sum generates the output of the feedback filter. The phase shift between input signal and output signal is generated by mixing down with a phase-shifted LO. This phase shift $\Delta\Phi$ was adjusted manually regarding optimal feedback cooling performance (see Figure 4.11). Finally, the signal is converted to an analog signal again and fed out to the fiber EOM that generates the feedback force acting on the oscillator.

- **Feedback actuator**: The choice of the right feedback actuator has proven to be a crucial component for successful feedback cooling and is closely related to the issue of feedback-detection cross-talk. Generating mechanical feedback through piezo elements that are positioned close to the oscillator is prone to electrical noise, even if great care of electrical shielding is taken. Therefore, the zero temperature condition of the actuator force is very difficult to realize using piezo elements.

  A feedback actuation force that meets all requirements of near zero temperature and negligible feedback-detection cross-talk was implemented by using optical feedback through radiation pressure. The force is generated by an amplitude-modulated laser beam that is coupled into the cavity of the MiM system (see Figure 4.8). Since the linewidth κ_cav of the fiber cavity is much larger than the oscillator frequency ω_m, the intracavity field adiabatically follows the modulation

[2] If the homodyne phase lock jumps out of lock, the homodyne signal can easily reach the maximum output of the photodetector. Therefore, the measurements presented in this thesis were performed with an additional $50\,\Omega$ resistor parallel to the input of the lock-in amplifier, which reduces the maximum output voltage of the photodetector by 50% to $\pm 5\,\mathrm{V}$ (it has $50\,\Omega$ output impedance) which is the damage threshold of the lock-in amplifier input. Hence, the bandpass could in principle be omitted if the $50\,\Omega$ resistor is always used or replaced by a slightly larger resistance.

of the feedback beam. Accordingly, the membrane oscillator located at the point of maximum optomechanical coupling experiences a radiation pressure force that is proportional to the modulated intracavity power (see section 3). The amplitude modulation is generated by a fiber coupled waveguide EOM (AM785b from *Jenoptik*, data sheet in appedix B.4). Its main characteristics are an extremely small half-wave voltage of $V_\pi < 3\,\mathrm{V}$ and an extremely large bandwidth in the gigahertz range ($\tau_{\mathrm{rise}} \approx 500\,\mathrm{ps}$). The small half-wave voltage is essential for small electrical feedback-detection cross-talk. Specifically, the electrical peak-to-peak output voltage of the lock-in amplifier must be smaller than $1\,\mathrm{V_{pp}}$, otherwise the output signal will couple into the input stage and will appear as a parasitic signal above the electrical noise floor that may distort the homodyne measurement. Anyhow, $1\,\mathrm{V_{pp}}$ is the largest voltage that one can apply for an approximately linear response of the fiber EOM. Hence, electrical cross-talk between output and input of the lock-in amplifier is not an issue in this setup.

The working point of the fiber EOM is adjusted manually with a small battery-driven bias voltage. After ramping up the bias voltage the output quickly stabilizes at the desired 50% working point with a small creep effect that vanishes on the time scale of one minute. The more severe creeping effects are thermal drifts due to the optical power inside the EOM. Therefore, optical input powers larger than $\approx 5\,\mathrm{mW}$ should be avoided and thermal drifts need to be taken into account for pulsed experiments. The EOM fibers are polarization maintaining fibers (PM) and the output fiber was connected with a mating sleeve to the fiber that guides the light to the experiment. The EOM transmission is strongly polarization dependent and the input polarization was adjusted such that the EOM transmission was maximized. The EOM including the bias voltage control were installed into a closed metal box in order to reduce electrical noise that could couple into the modulation input. The same triaxial low noise cable as in the photodetector circuit was used to connect the EOM with the lock-in amplifier.

- **Feedback-detection cross-talk**: As described above, electrical cross-talk between the detection signal and the feedback output could be strongly reduced by using a fiber EOM with a small half-wave voltage. The remaining cross-talk sources are mainly of optical nature. The largest contribution is given by feedback light with a wrong polarization that is transmitted through the MiM system and enters the homodyne detection branch. If the homodyne detection is not perfectly balanced (bad common-mode rejection), this amplitude modulated feedback light has a contribution in the homodyne signal. Therefore, the polarization of the feedback light needs to be adjusted correctly and the common-mode rejection of the homodyne setup should be optimized carefully (see section 3). This alignment should be done on a daily basis if feedback cooling experiments are performed. Figure 4.9 describes the procedure of reducing this optical cross-talk (including all other possible contributions) to a negligible amount.

  Although the condition for negligible feedback-detection cross-talk (see parenthesis 4.40) can be clearly specified, its test is technically non-trivial, since $x(\omega) \approx 0$ can not be realized (especially if a near resonant signal is acting on the oscillator). Even if the test frequency ω_{t} is detuned several kilohertz from the oscillator fre-

quency ω_m, the mechanical susceptiblity $\chi_m(\omega_t)$ is still large enough to allow for mechanical driving. This results in a peak in the measured homodyne signal at ω_t, which is actually no cross-talk but the natural, *wanted* form of optomechanical coupling between feedback signal and oscillator motion. One way of circumventing this problem is to block the homodyne light so that the oscillator can not be detected anymore. Then at least all remaining electronic and optical (feedback light related) cross-talk contributions can be tested. Figure 4.9 shows how the polarization of the feedback light can be adjusted in order to minimize the light that enters the homodyne detection branch. The total cross-talk including homodyne light (the real experimental condition of feedback cooling) can at least be checked for $\omega_t \gg \omega_m$, where χ_m is so small that mechanical driving of the oscillator is negligible. We observe that if the procedure described in Figure 4.9 is done properly, the total cross-talk for the real experimental condition (with homodyne light, checked at $\omega_t \gg \omega_m$) is also negligible. Notably, even if a small cross-talk effect would be visible in this test, this cross-talk would only have a small contribution in the beginning of the cooling process. Since the cross-talk signal will most likely be proportional to the feedback signal, it is also proportional to the decreasing PSD S_y of the cooled oscillator. Hence, for very low oscillator temperatures where the feedback cooling performance is most important, the cross-talk effect would still be negligible.

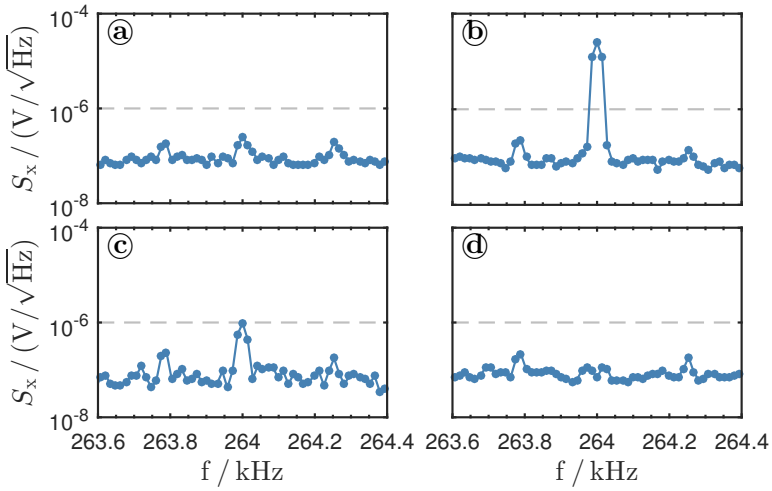

Figure 4.9: Alignment process of the feedback-detection cross-talk. Zoom-FFT spectra of the photodetector output for blocked homodyne light if feedback light modulated at $\omega_t/2\pi = 264.5\,\text{kHz}$ is sent into the MiM system with a resonant cavity (light power $P_{0.5} = 426\,\mu\text{W}$ in front of cavity fiber at 50% working point of EOM, modulation voltage $V_{pp} = 1\,\text{V}$, spectra averaged 20 times). (a) Before alignment. A small peak is visible at 264 kHz. (b) Blocked one photodiode of the balanced photodetector - the signal gets larger due to prevented common-mode rejection. (c) Adjusted polarization of feedback light using the wave plates in front of cavity fiber (see Figure 4.8). (d) Unblocked the photodiode - the common-mode rejection fully removes the cross-talk signal. The sidebands at $\omega_t/2\pi \pm 250\,\text{Hz}$ are an artifact of the demodulator operating at 264 kHz (in this particular measurement). This is also the reason why the signal at $\omega_t/2\pi = 264.5\,\text{kHz}$ occurs at 264 kHz. The dashed line indicates the noise floor if homodyne detection is switched on.

4.4 Experimental realization of feedback cooling

In this section, experimental results concerning feedback cooling of a SiN membrane oscillator will be presented. They can be regarded as characterization measurements of the feedback cooling setup described in section 4.3. Furthermore, the demonstration of feedback cooling to very low occupation numbers of the fundamental mode ω_m of a mechanical oscillator constitutes an important milestone towards a hybrid quantum system consisting of ultra-cold atoms and a quantum mechanical oscillator.
The following people contributed to these experimental results: the optical feedback setup and the fiber cavity were built by the author, who also installed it into the cryostat and aligned it together with H. Zhong. The homodyne setup was built and characterized by T. Wagner, who also participated in the implementation of the digital feedback loop together with H. Zhong. The feedback cooling measurements and data analysis were done by the author and T. Wagner.

4.4.1 Feedback cooling in time domain

Zero-span measurements allow for monitoring the time evolution of the integrated PSD in a certain frequency interval centered at f_0 through demodulation with a local oscillator at that frequency. This interval is given by the bandwidth B_d of the demodulator filter. Assume an electrical PSD signal $S_\mathrm{y}^\mathrm{el}(\omega)$ originating from the displacement PSD $S_\mathrm{x}(\omega)$ of a mechanical mode centered at ω_m is measured with zero-span. Then the demodulator output voltage $V_\mathrm{d}(t)$ is proportional to the integrated PSD $\langle x^2(t)\rangle$ and hence proportional to the mode temperature of the oscillator (see section 3). This holds as long as $B_\mathrm{d} \gg \Gamma_\mathrm{m}$ and $S_\mathrm{y}(\omega) \approx S_\mathrm{x}(\omega)$ (measured PSD corresponds to real displacement PSD, see for example Figure 4.2) which is a good approximation if the thermal noise peak $S_\mathrm{x}(\omega_\mathrm{m})$ is well above the noise floor $S_{\mathrm{x_n}}$.
Time domain acquisition of the mode temperature of the mechanical oscillator is helpful for monitoring, parameter optimization and the understanding of transient processes in the experiment. However, due to the constraints mentioned above, very small temperatures need to be measured in frequency domain, as discussed later.
The transient mode temperature during feedback cooling was measured in zero-span mode. As predicted by the model (see equation 4.24), the oscillator temperature exponentially decreases after the feedback is switched on using a mechanical shutter in the feedback beam. As shown in Figure 4.10, this model shows a very good agreement with the data. The maximum gain is $g_\mathrm{v} \approx 3500$ (with $T_\mathrm{min} \approx 1\,\mathrm{mK}$, respectively). Larger gains are possible but were not taken into account, since below 1 mK the in-loop signal $S_\mathrm{y}(\omega)$ starts to deviate significantly from the real oscillator displacement $S_\mathrm{x}(\omega)$ and the zero-span signal is not proportional to the mode temperature anymore. Furthermore, for larger gains the cooldown happens so fast that the acquisition is limited by the bandwidth B_d of the demodulator.
Due to the effectively broadened linewidth $\Gamma'_\mathrm{m} = \Gamma_\mathrm{m}(1 + g_\mathrm{v})$ during feedback cooling (see equation 4.7), the Brownian motion is less pronounced and the T_mode behaves very predictable. Thus, the temperature during the cooldown process can be fitted very well. However, if the feedback cooling is switched off the natural damping at rate Γ_m sets in again and Brownian motion occurs on a time scale τ_th that is larger by a factor $\Gamma'_\mathrm{m}/\Gamma_\mathrm{m}$.

Strictly speaking, the displacement autocorrelation function of the oscillator motion decays on the time scale $\tau_{\mathrm{th}} = 1/\Gamma$ [7]. Hence, the rethermalization process needs to be averaged more often and must be monitored on longer time scales. Therefore, all rethermalization temperature curves for $g_{\mathrm{v}} > 400$ ($T_{\mathrm{min}} \leq 10\,\mathrm{mK} \approx 0$ on a linear temperature scale) were averaged to get a better estimate.

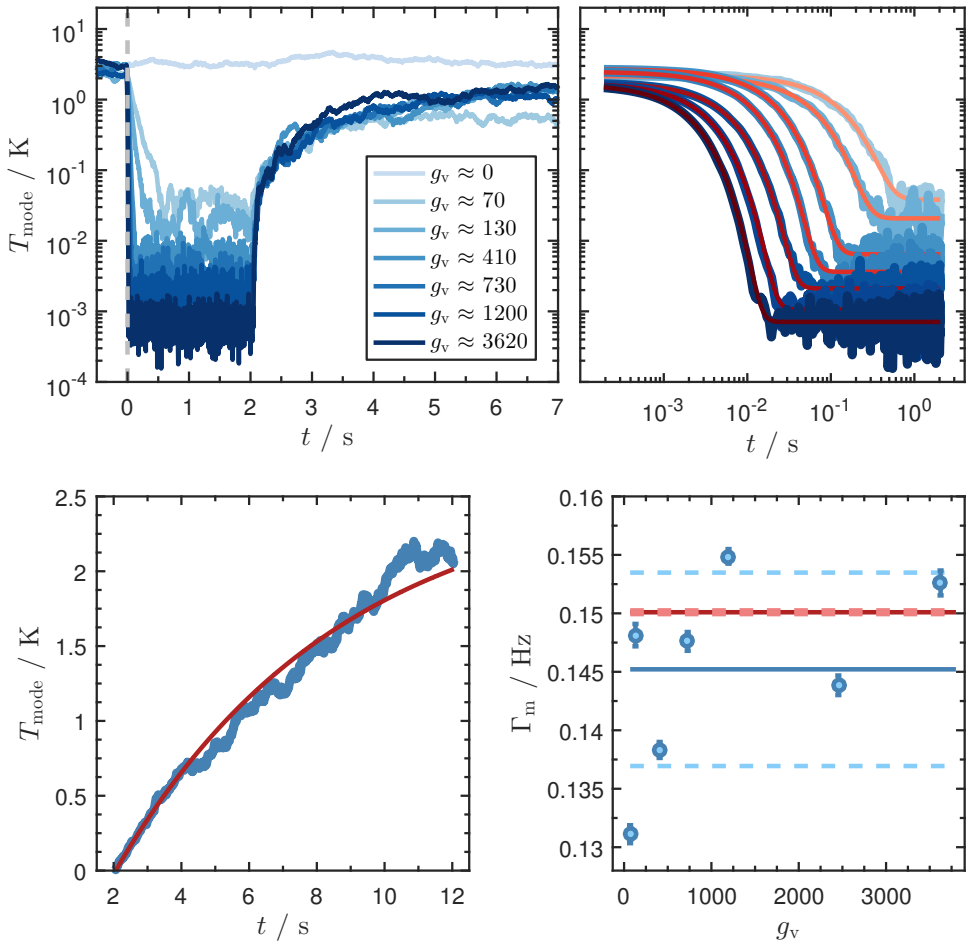

Figure 4.10: Time domain measurement of feedback cooling. Upper left panel: Mode temperature as a function of time for different feedback gains g_{v}. Feedback cooling starts at $t = 0$ and is switched off at $t = 2\,\mathrm{s}$. For $t > 2\,\mathrm{s}$ the oscillator rethermalizes and its mode temperature slowly approaches the bath temperature again. Feedback gains in the legend were determined by $g_{\mathrm{v}} \approx T_{\mathrm{bath}}/T_{\mathrm{min}} - 1$ where $T_{\mathrm{bath}} = 2.6(5)\,\mathrm{K}$ is the average of all time-averaged temperatures for $t < 0$. Data acquisition: zero-span traces from lock-in amplifier, demodulator bandwidth (3 dB) $B_{\mathrm{d}} = 200\,\mathrm{Hz}$, each trace averaged ten times, experiment cycle time 17 s. Parameters: feedback light power $P_{0.5} = 285\,\mu\mathrm{W}$ in front of cavity fiber at 50% working point of EOM, optomechanical system and detection parameters summarized in table 3.1. Upper right panel: log-log plot of the cooldown process and the fits according to equation 4.24 using Γ_{m}, g_{v}, t_0 as free fit parameters and T_{bath} as a fixed parameter. Lower left panel: rethermalization process of the oscillator for $t > 2\,\mathrm{s}$ and fit according to equation 4.25 using the same fit parameters. The single time trace is the average of 80 time traces (8×10 traces with gain $g_{\mathrm{v}} > 400$, $T_{\mathrm{min}} \leq 10\,\mathrm{mK}$). Lower right panel: fit results for the natural linewidth Γ_{m}. The blue dots are the results from the cooldown fits (blue solid line indicates mean value, $\Gamma_{\mathrm{m}}^{\mathrm{cool}} = 0.145(8)\,\mathrm{Hz}$). The red line indicates the result from the rethermalization fit: $\Gamma_{\mathrm{m}}^{\mathrm{heat}} = 0.1501(2)\,\mathrm{Hz}$.

The lower left panel of Figure 4.10 shows the average of 80 time traces of the temperature during rethermalization and a fit to the data. Even for this large number of averages the random walk of the temperature curve is still visible. Nevertheless, the curve can be fitted very well with a precise fit result $\Gamma_\mathrm{m} = 0.1501(2)\,\mathrm{Hz}$ for the natural linewidth of the oscillator. This yields a mechanical Q-factor $Q = \omega_\mathrm{m}/\Gamma_\mathrm{m} = 1.100(2) \times 10^7$, which is slightly larger than the value $Q = 1.0758(2) \times 10^7$ determined by the ringdown method (see table 3.1). Due to the fact that the whole cooldown process (from start until the steady state T_min is reached) happens on time scale that is much shorter than the rethermalization process ($t_\mathrm{cool} \approx 10 \cdot (\Gamma_\mathrm{m} g_\mathrm{v})^{-1}$, see Figure 4.6), the fit of the cooldown curves yields a larger error for Γ_m. However, the value of Γ_m determined by the rethermalization fit lies in the standard deviation of the values determined by the cooldown fits.

4.4.2 Feedback phase adjustment

As discussed in section 4.1, the optimal feedback phase is obtained for a purely imaginary feedback filter function with $\phi = \arg(\chi_\mathrm{fb}^{-1}) = \pi/2$, which corresponds to pure velocity-dependent feedback ($g_\mathrm{d} = 0$), see equation 4.8. Since many parts in the feedback loop cause an unknown delay, the total phase of the feedback loop can be adjusted by adding an additional known delay such that the total phase between oscillator and feedback force matches $\pi/2$. This known phase delay $\Delta\Phi$ is added in the digital feedback filter by mixing down with a phase-shifted local oscillator (see Figure 4.8).

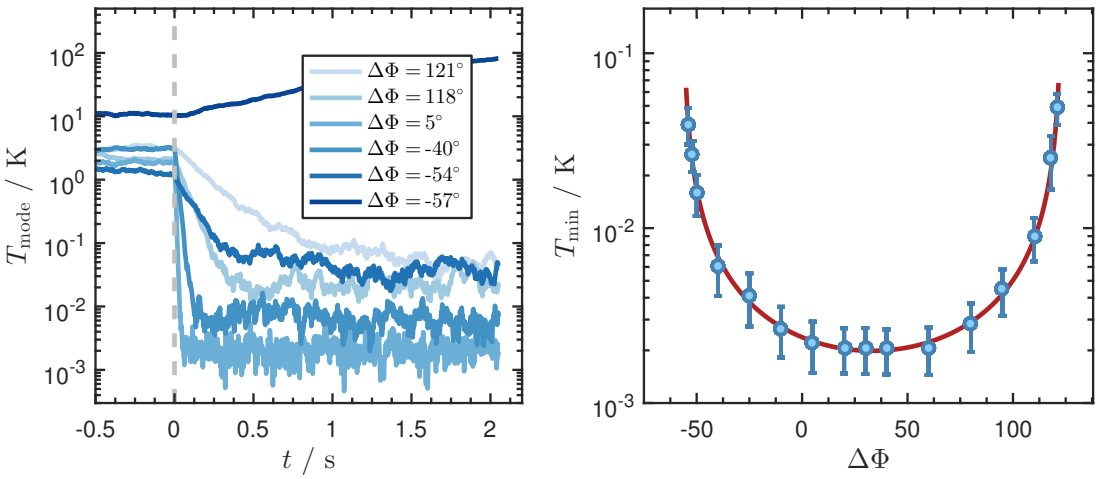

Figure 4.11: Adjustment of the feedback cooling delay $\Delta\Phi$. Left panel: Mode temperature as a function of time for different feedback delays $\Delta\Phi$ and a fixed absolute value $|\chi_\mathrm{fb}^{-1}|$ of the feedback filter function. Heating instead of cooling occurs if $\Delta\Phi$ exceeds a critical value (see trace for $\Delta\Phi = -57°$). Data acquisition: zero-span traces from lock-in amplifier, demodulator bandwidth (3 dB) $B_\mathrm{d} = 200\,\mathrm{Hz}$, each trace averaged ten times, experiment cycle time 17 s. Parameters: feedback light power $P_{0.5} = 285\,\mu\mathrm{W}$ in front of cavity fiber at 50% working point of EOM, optomechanical system and detection parameters summarized in table 3.1. Right panel: Minimum temperature obtained by time-averaging of traces on the left for $t > 1.4\,\mathrm{s}$ as a function of feedback delay $\Delta\Phi$. Fit function (red solid line) according to equation 4.41 yields a minimum temperature at $\Delta\Phi_\mathrm{opt} = 33.2(1)°$ and a gain $g_\mathrm{v} = 1375(50)$. The fixed parameter $T_\mathrm{bath} = 2.7(8)\,\mathrm{K}$ is the average of the time-averages of all traces for $t < 0$.

Figure 4.11 shows time traces of the oscillator temperature for a fixed absolute value $|\chi_{\mathrm{fb}}^{-1}|$ of the feedback filter function (set by a fixed amplification gain of the quadratures X and Y, see Figure 4.8) and different feedback delays $\Delta\Phi$. At time $t = 0$ the feedback cooling beam is switched on with a mechanical shutter, which leads to cooling of the oscillator. At time $t_{\mathrm{cool}} \approx 10 \cdot (\Gamma_{\mathrm{m}} g_{\mathrm{v}})^{-1}$ (see Figure 4.6) the oscillator has reached thermal equilibrium and the new steady state temperature T_{min} can be obtained from the traces by time-averaging the mode temperature for $t > t_{\mathrm{cool}}$.
The steady state temperature T_{min} for different phase delays $\Delta\Phi$ is shown in the right panel of Figure 4.11. Changing $\Delta\Phi$ and accordingly the feedback phase $\arg(\chi_{\mathrm{fb}}^{-1})$ for a fixed $|\chi_{\mathrm{fb}}^{-1}|$ corresponds to different combinations of velocity-proportional gain g_{v} and displacement-proportional gain g_{d} (see equation 4.8). Hence, the mode temperature in the steady state is given by equation 4.19. However, the measurement was performed with a rather small maximal velocity-proportional gain $g_{\mathrm{v}}^{\mathrm{max}} \approx 1400$ at $\arg(\chi_{\mathrm{fb}}^{-1}) = \pi/2$, which means that the maximal g_{d} can be $g_{\mathrm{d}}^{\mathrm{max}} = g_{\mathrm{v}}^{\mathrm{max}} m\omega_m \Gamma_{\mathrm{m}}/k_m = g_{\mathrm{v}}^{\mathrm{max}}/Q \approx 10^{-4}$. Therefore, the displacement gain g_{d} can be neglected in equation 4.19 and the minimum temperature is well approximated by

$$T_{\mathrm{min}}(\Delta\Phi) \;=\; \frac{T_{\mathrm{bath}}}{1 + g_{\mathrm{v}}^{\mathrm{max}} \sin(\phi_0 + \Delta\Phi)}\,, \tag{4.41}$$

where ϕ_0 denotes the sum of all unknown phase delays in the feedback loop. This model shows a very good agreement with the measured data, as can be seen in Figure 4.11. The fit yields an optimal feedback delay $\Delta\Phi_{\mathrm{opt}} = 33.2(1)°$, which was adjusted in all other feedback related measurements in this thesis. It should be noted that the plot has a logarithmic scale. On a linear scale the temperature has a very broad and flat minimum, which means that the feedback cooling performance is very insensitive to small drifts of $\Delta\Phi$.

4.4.3 Feedback cooling performance

The minimum feedback cooling temperature is achieved with a velocity-dependent gain $g_{\mathrm{v,opt}} \approx \sqrt{\mathrm{SNR}}$, $g_{\mathrm{v,rel}} = 1$ (see equation 4.21), where the in-loop PSD $S_{\mathrm{y}}(\omega)$ becomes flat. This is shown in the upper left panel of Figure 4.2. In this regime of large gains, zero-span temperature measurements as described in section 4.4.1 are unsuitable, since the measured PSD $S_{\mathrm{y}}(\omega)$ and the real PSD $S_{\mathrm{x}}(\omega)$ differ significantly. Hence, feedback cooling for large gains must be regarded in frequency domain.
In order to investigate the feedback cooling performance for a large span of feedback gains, spectra of the cooled oscillator PSD $S_{\mathrm{y}}(\omega)$ were acquired with the so-called *Zoom-FFT* function[3] of the used lock-in amplifier. The spectra were acquired for each gain after the steady state temperature was reached ($t \gg t_{\mathrm{cool}}$). Since the real displacement PSD $S_{\mathrm{x}}(\omega)$ can not be measured (a second out-of-loop homodyne detector would be

[3] In normal FFT, the frequency resolution of the resulting spectrum is determined by the acquisition time and a frequency span is determined by the sampling rate of the data acquisition. In Zoom-FFT, the signal is first mixed down and the Fourier transform is performed with the demodulated quadratures X and Y. This allows for using a much lower sampling rate and sample number to achieve the same frequency resolution as in the normal FFT case. Thus, a very high frequency resolution can be achieved with Zoom-FFT, with a resolution given by the sampling rate divided by the number of recorded samples. The span is twice the demodulator sampling rate.

necessary), it must be calculated from the measured in-loop PSD $S_y(\omega)$. This can be done by fitting the spectra with expression 4.10 for $S_y(\omega)$. Due to the fact that the spectral shape qualitatively changes from an extremely narrow peak for $g_v = 0$ to a flat line for $g_{v,opt} \approx \sqrt{SNR}$, this fitting is not a trivial task. For example, the PSD at $g_{v,opt}$ is always the same flat line for all kinds of initial bath temperatures. Hence, this quantity can not be determined by a fit in this case. However, using a two-step fitting routine the mode temperature can be determined for all different feedback gains in a robust manner. This procedure will be described in the following.

Step 1: Determination of the bath temperature

As presented in section 4.1.1, the mode temperature T_{mode} of the oscillator can be obtained by integrating the oscillator displacement PSD $S_x(\omega)$, which yields expression 4.19. In this equation, the relevant unknowns are the feedback gain g_v and the bath temperature T_{bath} (the displacement-proportional gain g_d is assumed to be zero, which will be discussed later). These quantities can be obtained by fitting the measured spectrum with expression 4.10 for $S_y(\omega)$ with g_v and T_{bath} as free fit parameters. The noise floor S_{x_n} and the oscillator frequency ω_m can be read off directly from the spectrum. It is not meaningful to include the Q-factor as an additional fit parameter, since Q mainly contributes to the spectrum through the product $g_v\Gamma_m = g_v\omega_m/Q$ in the effec-

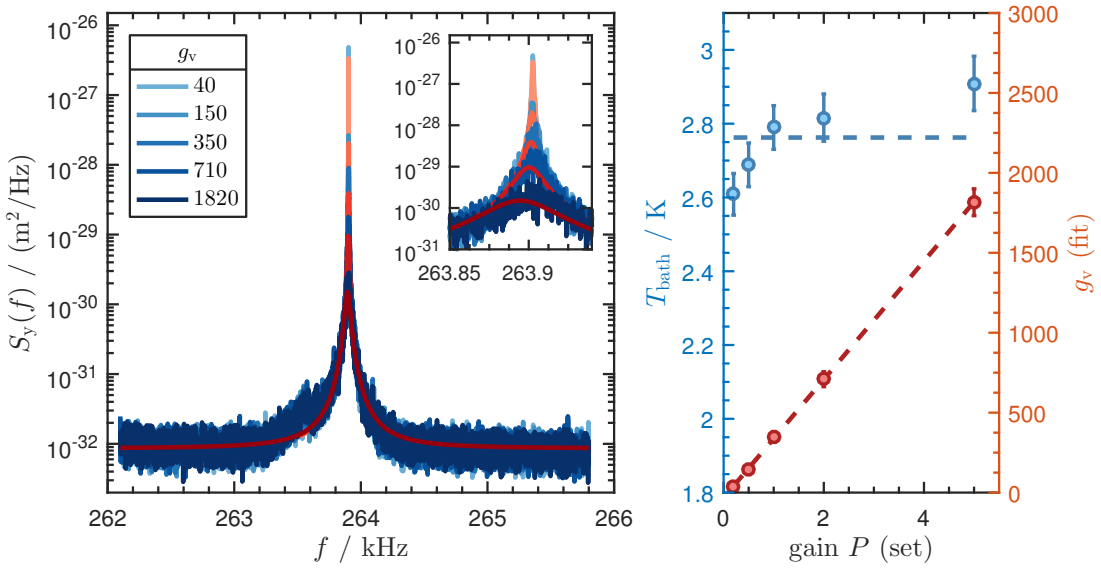

Figure 4.12: Spectral determination of the bath temperature T_{bath}. Left panel: In-loop displacement PSD $S_y(f)$ for different feedback gains g_v (blue) and fits to the spectra (red) using expression 4.10 with g_v and T_{bath} as free fit parameters. Inset figure: zoom into the peak area. Right panel: bath temperatures and feedback gains obtained by the fits in the left panel for the different amplification gains P used in the feedback loop (set by the amplification of the quadratures X and Y, see Figure 4.8). Mean of bath temperatures is $T_{bath} = 2.76(12)$ K (blue dashed line). Data acquisition: Zoom-FFT spectra from lock-in amplifier, resolution 220 mHz, each spectrum averaged ten times. Parameters: feedback light power $P_{0.5} = 462\,\mu W$ in front of cavity fiber at 50% working point of EOM, optomechanical system and detection parameters summarized in table 3.1.

tive susceptibility χ_{eff} (see equation 4.8) and through the product $T_{\mathrm{bath}}\Gamma_{\mathrm{m}} = T_{\mathrm{bath}}/Q$ in the thermal force noise PSD $S_{\mathrm{F_{th}}}$ (see equation 3.10). Hence, the Q-factor could be absorbed in the fit parameters g_{v} and T_{bath} and the fit would not be sensitive to Q. Nevertheless, the mechanical Q-factor (and the natural linewidth Γ_{m}, respectively) is a fixed quantity that does not change during feedback cooling. It can be determined by ringdown measurements or the rethermalization after feedback cooling is switched off (see Figure 4.10).
Figure 4.12 shows the measured spectra for feedback gains between $g_{\mathrm{v}} \approx 50$ and $g_{\mathrm{v}} \approx 2000$. In this regime, the spectra can be fitted very well with free fit parameters g_{v} and T_{bath}. The fits were performed using the logarithm of the spectral data, which yields a good fitting of the whole spectrum without the need of any additional weight functions. Nevertheless, for smaller and larger gains it is not possible to obtain accurate fit results. In the limit of very small gains this is caused by technical difficulties. On the one hand, the Brownian motion happens on a much larger time scale, which results in a larger scatter of the measured bath temperature for a given number of spectral averages (as already discussed in section 4.4.1). On the other hand, the peak for small gains is extremely narrow and requires extremely stable conditions, otherwise the measured peak can shift caused by various reasons and effectively gets broadened during the long acquisition time. However, for larger gains the SNR becomes smaller and the fits become less accurate, respectively (finally the spectrum becomes a flat line which makes the fit impossible, as mentioned in the beginning of this section). The right panel of Figure 4.12 shows the resulting bath temperatures for the intermediate gain regime where the fit works reliably. The resulting mean value $T_{\mathrm{bath}} = 2.82(12)\,\mathrm{K}$ is in good agreement with the bath temperatures determined by the zero-span measurements presented above (see Figure 4.10, 4.11). The fact that the scatter is larger than the confidence interval of the individual data points could be explained by the finite number of spectral averages or small drifts of the bath temperature due to heating of the feedback beam. The right panel also shows the fit results for the feedback gains g_{v} as a function of the set amplification gain P in the feedback loop. It shows that g_{v} is highly linear in P. Particularly, this shows that the fiber EOM operates well in the linear regime.

Step 2: Determination of the mode temperature

After the bath temperature was extracted from the spectra in the intermediate regime in step 1, the spectra can be fitted for all possible gains using T_{bath} as a fixed parameter and g_{v} as the only free fitting parameter. The left panel of Figure 4.13 shows the acquired spectra for feedback gains between $g_{\mathrm{v}} = 0$ and $g_{\mathrm{v}} \approx 10^5$ and the fits to the data. Similar to step 1, the fits were performed with the logarithm of the PSD $S_{\mathrm{y}}(f)$. In this way, all spectra can be fitted accurately with a usual least-square fitting and without any additional weight functions. For large gains the PSD peak turns into a dip, which is known as *noise-squashing* [8]. In this regime, the detector noise around the oscillator frequency ω_{m} gets canceled by the feedback loop. The right panel of the figure shows that even for very large amplification gains P of the feedback loop the resulting feedback gain g_{v} is linear in P. This curve is the main result of the spectral fitting and can be used to calculate the mode temperature of the oscillator.
It should be noted that the fits were performed in the approximation of negligible

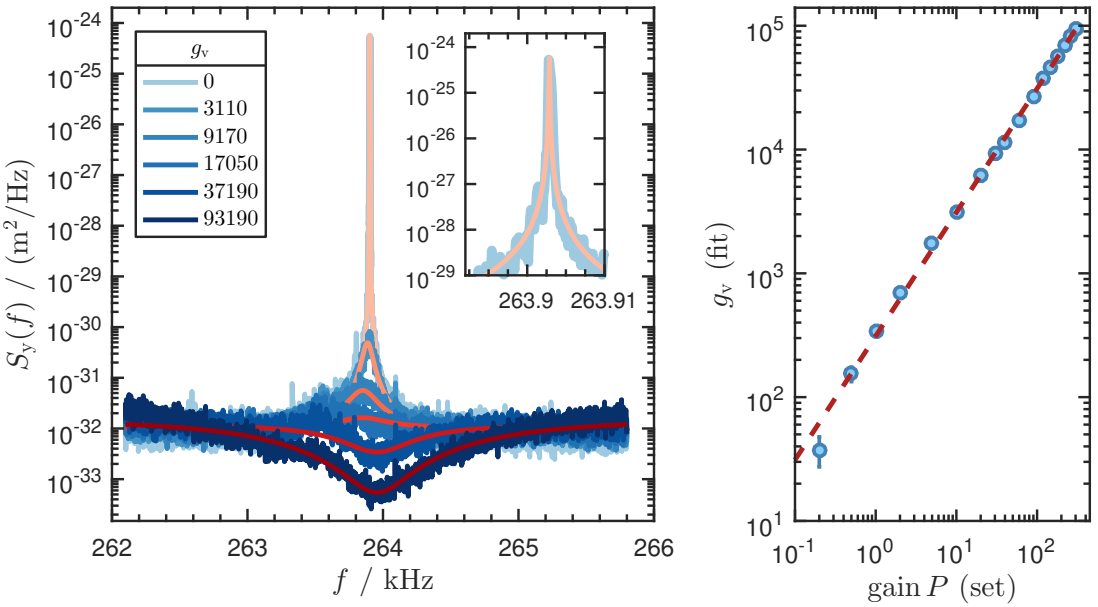

Figure 4.13: Spectral analysis of feedback cooling. Left panel: In-loop displacement PSD $S_y(f)$ for different feedback gains g_v (blue) and fits to the spectra (red) using expression 4.10 with g_v as the only free fit parameter. Inset figure: zoom into the peak area. Right panel: feedback gains obtained by the fits in the left panel for the different amplification gains P used in the feedback loop (set by the amplification of the quadratures X and Y, see Figure 4.8). T_{bath} determined previously by fits to the spectra with intermediate gain (see Figure 4.12). Data acquisition: Zoom-FFT spectra from lock-in amplifier, resolution between 100 mHz (small gains) and 440 mHz (large gains), each spectrum averaged ten times. Parameters: feedback light power $P_{0.5} = 462\,\mu W$ in front of cavity fiber at 50% working point of EOM, optomechanical system and detection parameters summarized in table 3.1.

---

displacement gain g_d. This is a good approximation, since even for a very pessimistic estimation of a feedback phase mismatch $\Delta\Phi - \Delta\Phi_{opt} = 10°$ the resulting relative gain would be $g_{d,rel} = g_d k_m \approx 0.1$ at the optimal velocity-gain $g_v \approx 2.5 \cdot 10^4$ (see equation 4.8). As shown in the lower right panel of Figure 4.5, this would only lead to a very small change in mode temperature. Furthermore, the effect of a non-negligible displacement gain would lead to a significant asymmetry in the measured spectra (see Figure 4.5). Although the noise-squashing dips in the spectra show a slight asymmetry, this could not be clearly related to the expected shape of the spectra for finite g_d. Therefore, it does not make sense to include g_d in the fitting. Probably the slight asymmetry originates from a noise floor S_{x_n} that is not perfectly flat round ω_m, which leads to a noise squashing dip that is not perfectly symmetric.

Using the fitted gains from Figure 4.13 the mode temperatures for the different spectra can be calculated using expression 4.19 for T_{mode}. The minimum temperature $T_{min} = 234(42)\,\mu K$ is achieved for a gain $g_v = 2.36 \cdot 10^4$. This is in good agreement with the theoretical value $g_{v,opt} = \sqrt{SNR} = 2.42 \cdot 10^4$ using expression 4.20 for the SNR and the same values for T_{bath}, S_{x_n} and Q as in the fit in Figure 4.13. The minimum mode occupation of the oscillator is $n_m = 18.5 \pm 3.3$ (see equation 3.14). The errors of T_{min} and n_m are mainly the systematic error of the homodyne calibration (equation 3.20).

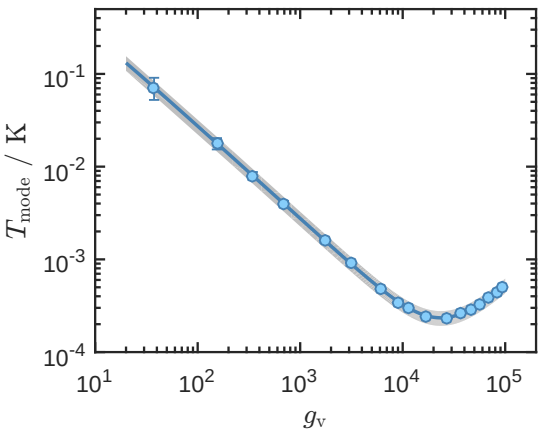

Figure 4.14: Observation of the feedback cooling limit. Mode temperatures of the oscillator as a function of the feedback gain g_{v} and a least-square fit to the data using expression 4.19. The mode temperatures were obtained by fits to the spectra in Figure 4.13. The error bars are mostly hidden by the data points (calculated using the confidence intervals of T_{bath}, g_{v} and $S_{\mathrm{x_n}}$). The minimum temperature of the fit curve is $T_{\mathrm{min}} = 234(42)\,\mu\mathrm{K}$ at a gain $g_{\mathrm{v}} = 2.36 \cdot 10^4$. The error comes from the systematic error of 18% of the homodyne calibration (see equation 3.20) and is indicated by the gray area.

Future enhancements

The presented measurements show that the experimental results for feedback cooling into the quantum regime of tens of phonons is in very good accordance with the theory. This suggests that improved feedback cooling into the quantum ground state is possible if condition 4.39 is met. In the current setup, $S_{\mathrm{x_n}} \approx 300 \times 4x_{\mathrm{sp}}^2/n_{\mathrm{th}}\Gamma_{\mathrm{m}}$. Assuming that the noise floor $S_{\mathrm{x_n}}$ can not be significantly improved, the factor $4x_{\mathrm{sp}}^2/n_{\mathrm{th}}\Gamma_{\mathrm{m}}$ would have to be reduced by a factor of 300 to enable ground state cooling. For example, this would be possible by reducing the thermal occupation n_{th} by a factor of 3 (through improvements of the cryogenic cooling), reducing the oscillator mass m by a factor of 10 and increasing the Q-factor by a factor of 10. A lower oscillator mass and a higher Q-factor could be achieved by using trampoline oscillators [73, 74].
Trampoline oscillators have been produced for our experiment and are currently tested. Implementing these oscillators will facilitate ground state cooling of the mechanical motion. Furthermore, larger Q-factors lead to longer mechanical coherence times, which relaxes the technical requirements for the preparation and detection of non-classical states of the oscillator (as discussed in the following section 4.5). This paves the way for the observation of macroscopic mechanical quantum states and exciting quantum dynamics in the hybrid quantum system.
Another possible upgrade of the setup is the improvement of the homodyne noise floor with squeezed light. This was first demonstrated in 2016 with a microtoroid oscillator using squeezed detection light and an electrical feedback actuator [129].

4.5 Further technical applications

The experimental setup presented in this section (see Figure 4.8) was built for efficient feedback cooling of a mechanical oscillator. Nevertheless, many other promising optomechanical applications apart from feedback cooling are conceivable. In the following paragraph, some of these possible experimental schemes related to the subject of so-called ***pulsed quantum optomechanics*** will be reviewed.
An exceptional property of the MiM system (see section 3) with an extremely large cavity linewidth κ in combination with an ultra-fast fiber EOM is the possibility to

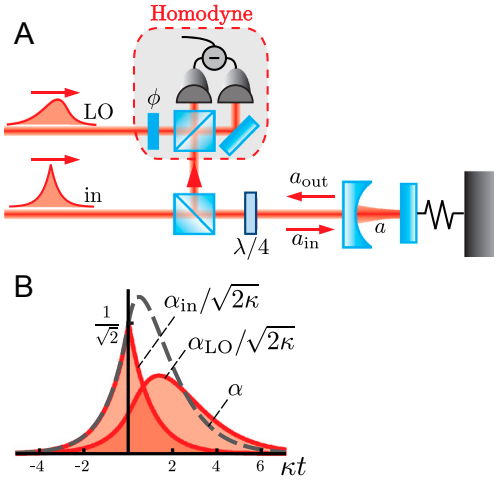

Figure 4.15: Schematic of a setup for pulsed optomechanics from [169]. An incident pulse (in) drives an optomechanical cavity, where the intracavity field a accumulates phase in proportion to the position quadrature of a mechanical oscillator. The pulse leaves the cavity (out) and balanced homodyne detection is used to measure the optical phase with a local oscillator pulse (LO). (B) Scaled envelopes of the optimal input pulse, its corresponding intracavity field and the optimal local oscillator pulse to maximize the measurement of the mechanical position. Figure adapted from [169].

modulate the intracavity field at a rate τ much faster than the oscillation frequency ω_{m} of the oscillator. In the following, experimental schemes that can be implemented under these conditions will be discussed.

In 2011, the group of M. Aspelmeyer in collaboration with Hammerer and Milburn proposed a scheme for quantum state tomography, squeezing and state purification of a mechanical oscillator using short optical pulses [169]. In the light of the fact that the majority of all optomechanical schemes rely on (dynamical) passive or active cooling mechanisms, the authors claim to provide a third method for quantum optomechanics, which can generate high purity mechanical quantum states. The proposed experimental setup is shown in Figure 4.15. A pulse of duration much shorter than the mechanical period is coupled into a single-sided optomechanical system and accumulates phase in proportion to the current displacement of the mechanical oscillator. The reflected pulse is then superimposed with a local oscillator pulse and time domain homodyne detection is used to determine the phase of the field emerging from the cavity. Since the temporal evolution of the oscillator during the pulse is negligible, the pulsed measurement allows for back-action evading QND measurements of the position quadrature. If the pulsed measurement is synchronized to the mechanical oscillation, many of these weak measurements can be used for a quantum state tomography to reconstruct the mechanical quantum state.

For a large measurement strength, however, the pulsed QND measurement leads to strong conditional squeezing of the position quadrature. The authors show that a single pulse can be used for squeezing well below the variance of the ground state, independent of the initial thermal occupation of the oscillator. Furthermore, the uncertainty of the momentum quadrature remains unchanged, which leads to a reduction of the phase space envelope and a lower effective thermal occupation of the oscillator. With a second pulse the thermal occupation can be reduced even further: after a free temporal evolution of duration $T/4 = \frac{\pi}{2}\,\omega_{\text{m}}^{-1}$ the position-squeezed state has evolved into a momentum-squeezed state with large position uncertainty. A second pulse then reduces the remaining position uncertainty below the ground state value, in the same manner as the initial pulse. In this way, the effective thermal occupation can be reduced to arbitrarily small values in the deep ground state regime, only limited by the measurement

strength. The optimal pulse shape for a maximal measurement strength was calculated to have a Lorentzian spectrum in frequency space and a duration on the order of the inverse cavity linewidth κ^{-1} (see Figure 4.15 B). This cooling-by-measurement was experimentally realized in a simplified setup without a cavity and a small measurement strength. Nevertheless, significant cooling and full mechanical state tomography was achieved in the classical regime [170]. The pulses were created using a fiber EOM and the mechanical oscillator was a cantilever at room temperature with a fundamental mode of $\omega_\mathrm{m}/2\pi = 984\,\mathrm{Hz}$.

The protocol presented above works independent from the initial thermal occupation of the oscillator. Nevertheless, it requires small thermal decoherence during the free temporal evolution of the oscillator. The requirement for the oscillator state to remain coherent during a full mechanical period is that the mechanical Q-factor is larger than its thermal occupation at temperature T_bath. This can be expressed through the Qf product [73, 83]: $Q \times f_\mathrm{m} > k_\mathrm{B} T_\mathrm{bath}/h$ (see equation 3.16). Recently, a scheme for ground state cooling and state preparation similar to [169] was proposed, which does not rely on this *quantum coherent oscillation* (QCO) regime [171]. It is based on a single pulse that interacts twice with the mechanical oscillator. In this way, the necessary time delay $T/4$ in the protocol above can be reduced to arbitrarily small values. Hence, the thermal decoherence during the time of the protocol can be neglected.

In 2012, another pulsed experimental protocol for ground state cooling was proposed [172]. The protocol is based on a sequence of pulses much shorter than the mechanical oscillation frequency, which lead to an interaction that approximates the Hamiltonian for resolved-sideband cooling. In this way, cooling in the resolved-sideband regime much faster than conventional resolved-sideband cooling is possible. The protocol also works in the unresolved-sideband regime and its performance can be further improved using optimal control theory to find the best pulse sequence for maximal cooling.

In 2013, the cooling-by-measurement scheme reviewed above was proposed as the starting point in a protocol of four pulsed optomechanical interactions which are capable of preparing non-classical states of motion in a mechanical oscillator [173]. The pulses are created by a single pulse that is recycled four times in an auxiliary ring cavity and interacts with an optomechanical device in each round trip. After each interaction, the pulse is displaced in optical phase space, finally performing a closed loop. In this way, the mechanical oscillator obtains a phase proportional to the area enclosed within the loop, a geometrical phase also called *Berry phase*. This phase generates an effective nonlinear potential for the oscillator which leads to squeezing of mechanical motion.

Recently, a bidirectional optomechanical interface was proposed which can perform an optical-to-mechanical state swap in the unresolved-sideband regime [174]. The deterministic interface is based on three pulsed QND interactions and classical open-loop feedback. Since a coherent optical pulse carries only vacuum noise and has zero temperature, a state swap allows for ground state cooling of the mechanical oscillator (in case the optomechanical cooperativity is larger than its thermal occupation).

Summarizing the applications of pulsed optomechanics for our experiment one can say that the creation of non-classical mechanical states is a realistic prospect. Feedback could be used for deterministic generation of unconditional states. Since $Q \times f_\mathrm{m} \approx 30 \times k_\mathrm{B} T_\mathrm{bath}/h$, our system operates in the QCO regime. Hence, in our MiM system non-classical states could survive for $\tau = \hbar Q/k_\mathrm{B} T_\mathrm{bath} \approx 20\,\mu\mathrm{s}$ (see equation 3.16).

Chapter 5

Sympathetic cooling

This chapter presents the sympathetic cooling measurements we have performed in our hybrid system. They allow for a characterization of the coupling mechanism and the hybrid cooperativity. Finally, we demonstrate the combination of feedback cooling with sympathetic cooling, which represents an important step towards a hybrid atomic-mechanical quantum system.

Specifically, the dependency of the sympathetic cooling performance on essential parameters was investigated. This includes measurements on the number of involved atoms or atomic laser cooling parameters like the intensity, detuning and magnetic field gradients. We observe optimal cooling rates of $\Gamma_{\mathrm{sym}} = 23.3(14)\,\mathrm{Hz}$, minimum mode temperatures of $T_{\mathrm{min}} \approx 20\,\mathrm{mK}$ and a hybrid cooperativity of $C_{\mathrm{hybrid}} = 151 \pm 9$ for sympathetic cooling with an optical molasses using coupling lattice beam powers P_{lat} around $0.5 - 1\mathrm{mW}$ with red detunings of $\Delta_{2,1} \approx -2\pi \times 2\,\mathrm{GHz}$. Similar cooling results were achieved for sympathetic cooling with a MOT using blue lattice detunings of $\Delta_{2,3} \approx 2\pi \times 1\,\mathrm{GHz}$. Furthermore, the resonance condition of the hybrid coupling mechanism was investigated by sweeping the atomic trapping frequency ω_{a} in the coupling lattice, which allows for the determination of the number of resonantly coupled atoms N_{res} and the atomic cooling rate Γ_{a}.

The realization of a hybrid quantum system consisting of ultra-cold atoms and a micromechanical oscillator offers exciting prospects for fundamental research and novel quantum technologies. A wide variety of possible applications has been proposed, ranging from ground state cooling of mechanical motion [27, 29, 31, 33–35, 57], coherent quantum state transfer, teleportation and entanglement [24, 25, 29] to quantum state preparation and protocols for quantum information processing [24, 33, 35], as well as quantum enhanced sensing [36]. Recently, quantum back-action evading measurements of mechanical motion have been realized in a hybrid system consisting of an atomic spin ensemble and an optomechanical MiM device [59].
We have realized a hybrid system consisting of cold ^{87}Rb atoms in an optical lattice and a mechanical membrane oscillator in a cryogenic MiM system (see chapter 2). In order to characterize the hybrid coupling scheme, we performed sympathetic cooling measurements where the mechanical oscillator was cooled far below its thermal equilibrium

temperature ($T_{\mathrm{min}} \approx 20\,\mathrm{mK}$) through coupling to laser cooled ^{87}Rb atoms. Recently, this sympathetic cooling scheme has been demonstrated for the first time by the group of P. Treutlein in an experiment similar to our setup [57].
Besides the possibility of characterizing the hybrid coupling mechanism through sympathetic cooling, this cooling mechanism has its own significance in many fields of research. For the field of optomechanics, it represents a cooling mechanism which is in principle capable of ground state cooling far in the bad cavity regime ($\kappa \gg \omega_{\mathrm{m}}$) [31, 34, 57], although we observe that it would require further improvements in our system. Furthermore, using mechanical oscillators and atomic ensembles radically extends the mass ratio of sympathetic cooling to a factor of 10^{10} [57], as compared to approximately 100 in all previous experiments. Specifically, in all previous applications microscopic particles were sympathetically cooled by other microscopic particles. For example, sympathetic cooling was first demonstrated in the 1980s with different atomic species bound in an ion trap [175, 176]. In the field of ultra-cold quantum gases, sympathetic cooling is a widely used tool for cooling atomic species that are not well suited for laser cooling or evaporative cooling. For this, these atoms are cooled sympathetically through direct interactions with another atomic species that can be cooled using standard techniques [177–180]. Sympathetic cooling is also used for cooling molecules with atoms [181–183] or even antiprotons in particle accelerators [184].
After a brief review of the theoretical principles of sympathetic cooling, the experimental results will be presented in the following. Finally, the combination of feedback cooling with sympathetic cooling will be discussed. Through this coupling of cold atoms to a feedback cooled mechanical oscillator, the potential of our system to become a true hybrid quantum system consisting of ultra-cold atoms and a ground state mechanical oscillator is demonstrated.

5.1 Principles of sympathetic cooling

In this section, the hybrid coupling mechanism between the atomic motion in the optical lattice and the motion of the mechanical oscillator will be described. A fully quantized model of this coupling scheme has been published in [31]. After a brief review of the classical equations of motion and the resulting quantities like the sympathetic cooling rate, this quantized model and the quantum limits of sympathetic cooling will be outlined. Subsequently, modifications of this model including the atomic back-action on the coupling light will be discussed. The section concludes with a classical treatment of combined sympathetic and feedback cooling.

5.1.1 Classical description of the hybrid coupling mechanism

The hybrid coupling scheme for long-distance coupling of a mechanical oscillator in a MiM system to the motion of atoms in an optical lattice is depicted in Figure 5.1. Both the atoms and the mechanical oscillator can be treated as two harmonic oscillators that are coupled by a spring, which is given by the coupling light field. This bi-directional coupling can be understood as follows. A displacement of the mechanical oscillator changes the resonance frequency ω_{cav} of the MiM cavity (see section 3.1) and correspondingly the phase of the reflected light that creates the optical lattice.

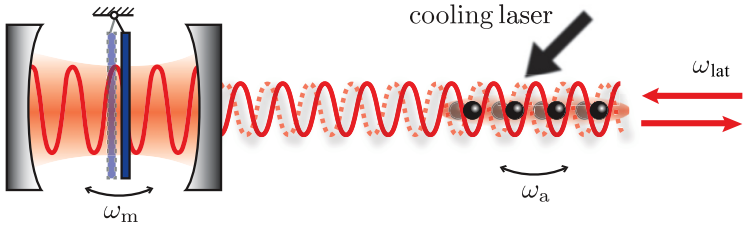

Figure 5.1: Scheme for long-distance coupling of a MiM system to the atomic motion in an optical lattice. The mechanical oscillator in the MiM system (see section 2.3) is coupled to ^{87}Rb atoms in an optical lattice with frequency ω_{lat} (see 2.4.1), which is created by the reflected light from the MiM cavity. The motion of the oscillator with frequency ω_{m} periodically shifts the optical lattice potential of the atoms, while the motion of the atoms with frequency ω_{a} modulates the radiation pressure on the oscillator. Figure taken from [31].

Hence, the position of the lattice potential wells for the atoms is shifted by δx_{lat} and the ensemble of N atoms experience a force $F_{\mathrm{a}} = N m_{\mathrm{a}} \omega_{\mathrm{a}}^2 \delta x_{\mathrm{lat}}$. Conversely, an atom displaced by x_{a} from the center of a potential well experiences a restoring force which is given by the optical dipole force $F_{\mathrm{d}} = -m_{\mathrm{a}} \omega_{\mathrm{a}}^2 x_{\mathrm{a}}$. Microscopically, this force can be understood as a momentum transfer from photons of the optical lattice through absorption and stimulated emission. This leads to a redistribution of photons between the right- and left-propagating lattice beams [31] and changes the radiation pressure on the mechanical oscillator in the MiM system, which experiences a force δF_{rad}.
In order to obtain the classical coupled equations of motion for the hybrid system, the two forces F_{a} and δF_{rad} need to be calculated. Following [118], the force acting on the atomic ensemble F_{a} can be calculated by assuming a phase shift $\delta\phi \approx (4/\kappa) g_{\mathrm{m}} x_{\mathrm{m}}$, which induces a displacement $\delta x_{\mathrm{lat}} = -\delta\phi/(2k_{\mathrm{lat}}) = -2g_{\mathrm{m}} x_{\mathrm{m}}/(\kappa k_{\mathrm{lat}})$ of the lattice potential wells. This yields the interaction force on the center-of-mass of the atomic ensemble of N atoms

$$F_{\mathrm{a}} = N m_{\mathrm{a}} \omega_{\mathrm{a}}^2 \delta x_{\mathrm{lat}} = -\frac{2g_{\mathrm{m}}}{k_{\mathrm{lat}} \kappa} N m_{\mathrm{a}} \omega_{\mathrm{a}}^2 x_{\mathrm{m}} = -K x_{\mathrm{m}}\,, \tag{5.1}$$

with the coupling spring constant K.
The radiation pressure force δF_{rad} on the oscillator induced by a displacement x_{a} of the atomic ensemble can be calculated using the photon redistribution rate $\dot{n}_{\mathrm{p}} = N F_{\mathrm{d}}/(2\hbar k_{\mathrm{lat}})$ [118]. This leads to a variation of the power of the lattice incident beam $\delta P_{\mathrm{lat}} = \dot{n}_{\mathrm{p}} \hbar \omega_{\mathrm{lat}}$ which generates a variation of the intra-cavity photon number $\delta \bar{n}_{\mathrm{cav}} \approx \beta t^2 (4/\kappa) \delta P_{\mathrm{lat}}/\hbar\omega_{\mathrm{cav}}$. The quantity β accounts for the incoupling power efficiency of the cavity due to imperfect mode match and t^2 is the power transmittance of the optical path from the atoms to the cavity (one way). Assuming $F_{\mathrm{rad}} = \hbar g_{\mathrm{m}} \bar{n}_{\mathrm{cav}}$, the radiation pressure variation on the oscillator through a displacement of the atomic ensemble can be expressed as:

$$\delta F_{\mathrm{rad}} = -\beta t^2 \frac{2g_{\mathrm{m}}}{k_{\mathrm{lat}} \kappa} N m_{\mathrm{a}} \omega_{\mathrm{a}}^2 x_{\mathrm{a}} = -\beta t^2 K x_{\mathrm{a}}\,. \tag{5.2}$$

Hence, the force on the mechanical oscillator δF_{rad} has an effectively reduced spring constant, which is smaller by a factor of βt^2. This asymmetry in the coupling complicates the description of the effective Hamiltonian in the quantized model [27, 34].

Furthermore, the optical losses lead to a power imbalance of the counterpropagating lattice beams which can cause collective atomic oscillations [103] which lead to instabilities in the hybrid system [104], as discussed later in section 5.1.3. In our current system the incoupling efficiency β of the fiber MiM cavity can be estimated to be $\beta > 0.95$[1] and the transmittance of the optical path between the atoms and the MiM system is $t^2 = 0.72$ (see appendix A.1).

Coupled equations of motion in the hybrid system

Using equations 5.1 and 5.2, the coupled equations of motion for the mechanical oscillator and the laser cooled, oscillating atomic ensemble can be written as [34, 118]:

$$\begin{aligned} N m_\mathrm{a} \ddot{x}_\mathrm{a} &= -\Gamma_\mathrm{a} N m_\mathrm{a} \dot{x}_\mathrm{a} - N m_\mathrm{a} \omega_\mathrm{a}^2 x_\mathrm{a} - K x_\mathrm{m} \\ m \ddot{x}_\mathrm{m} &= -\Gamma_\mathrm{m} m \dot{x}_\mathrm{m} - m \omega_\mathrm{m}^2 x_\mathrm{m} - \beta t^2 K x_\mathrm{a} + F_\mathrm{th}\,, \end{aligned} \tag{5.3}$$

where the term $-\Gamma_\mathrm{a} N m \dot{x}_\mathrm{a}$ accounts for the damped atomic motion in the harmonic potential of the lattice through laser cooling at rate Γ_a. The atomic bath is assumed to be at zero temperature and the corresponding noise term is omitted, as well as the optical back-action force acting on the mechanical oscillator. A calculation including these quantities is given in [34].
The sympathetic cooling rate Γ_sym corresponds to the new effective damping rate of the mechanical oscillator and can be calculated by solving the equations of motion. This can be done by Fourier transforming the equations, which results in

$$x_\mathrm{a}(\omega)\, \chi_\mathrm{a}^{-1}(\omega) = -K x_\mathrm{m}(\omega) \tag{5.4}$$

$$x_\mathrm{m}(\omega)\, \chi_\mathrm{m}^{-1}(\omega) = F_\mathrm{th} - \beta t^2 K x_\mathrm{a}(\omega)\,, \tag{5.5}$$

with the mechanical susceptibilities

$$\begin{aligned} \chi_\mathrm{a}^{-1}(\omega) &= N m_\mathrm{a} \left(\omega_\mathrm{a}^2 - \omega^2 - i\omega\Gamma_\mathrm{a}\right) \approx 2 N m_\mathrm{a} \omega_\mathrm{a} \left(\omega_\mathrm{a} - \omega - i\Gamma_\mathrm{a}/2\right) \\ \chi_\mathrm{m}^{-1}(\omega) &= m \left(\omega_\mathrm{m}^2 - \omega^2 - i\omega\Gamma_\mathrm{m}\right) \approx 2 m \omega_\mathrm{m} \left(\omega_\mathrm{m} - \omega - i\Gamma_\mathrm{m}/2\right)\,, \end{aligned} \tag{5.6}$$

using the Taylor approximation $\omega_\mathrm{m}^2 - \omega^2 \approx 2\omega_\mathrm{m}(\omega_\mathrm{m} - \omega)$ around ω_m. Inserting equation 5.4 into equation 5.5 yields

$$x_\mathrm{m}(\omega) \Big[\chi_\mathrm{m}^{-1}(\omega) \underbrace{- \beta t^2 K^2 \chi_\mathrm{a}(\omega)}_{\chi_\mathrm{sym}^{-1}(\omega)}\Big] \equiv x_\mathrm{m}(\omega)\, \chi_\mathrm{eff,s}^{-1}(\omega) = F_\mathrm{th} \tag{5.7}$$

[1] The measured finesse is $\mathcal{F}_0 = 60$ (see Table 3.1) and the upper bound on the mirror reflectivity on resonance is $\rho < 0.92$, corresponding to the limited reflectivity $R_2 < 0.998$ of our in-house coating machine (see Figure 2.8). Due to the steepness of $\sigma_\mathrm{ref}(\beta)$ (see Figure 2.10), this indicates that $\beta > 0.95$, since the measured reflectivity on resonance is $\sigma_\mathrm{ref} = 0.73$ (see Figure 2.15).

with the new effective susceptibility $\chi_{\mathrm{eff,s}}$ of the mechanical oscillator. Similar to the formalism of active feedback cooling (see section 4.1.1), the sympathetic cooling mechanism leads to cold damping due to the effectively increased damping rate of the mechanical oscillator. This process is equivalent to the velocity dependent feedback cooling and originates from the imaginary part of χ_{sym}^{-1} (compare equation 4.8). In fact, the sympathetic cooling scheme can be regarded as a coherent feedback process [34].
The real part and imaginary part of χ_{sym}^{-1} are given by

$$\chi_{\mathrm{sym}}^{-1}(\omega) \;=\; -\beta t^2 K^2 \chi_{\mathrm{a}}(\omega) \;=\; -\beta t^2 K^2 \frac{(\omega_{\mathrm{a}}-\omega)+i\Gamma_{\mathrm{a}}/2}{2N m_{\mathrm{a}}\omega_{\mathrm{a}}\left[(\omega_{\mathrm{a}}-\omega)^2+(\Gamma_{\mathrm{a}}/2)^2\right]}\,. \tag{5.8}$$

Using this equation and assuming $\omega \approx \omega_{\mathrm{m}}$ [118], the new effective susceptibility $\chi_{\mathrm{eff,s}}$ of the sympathetically cooled mechanical oscillator can be written as

$$\chi_{\mathrm{eff,s}}^{-1}(\omega) \;=\; 2m\omega_{\mathrm{m}}\left(\omega'_{\mathrm{m}}-\omega-i\Gamma'_{\mathrm{m}}/2\right) \tag{5.9}$$

$$\text{with} \qquad \omega'_{\mathrm{m}} \;=\; \omega_{\mathrm{m}} + (\omega_{\mathrm{m}}-\omega_{\mathrm{a}})\frac{\Gamma_{\mathrm{sym}}}{\Gamma_{\mathrm{a}}} \tag{5.10}$$

$$\text{and} \qquad \Gamma'_{\mathrm{m}} \;=\; \Gamma_{\mathrm{m}}\left(1+\frac{\Gamma_{\mathrm{sym}}}{\Gamma_{\mathrm{m}}}\right) \;\equiv\; \Gamma_{\mathrm{m}}\left(1+g_{\mathrm{sym}}\right)\,, \tag{5.11}$$

where the sympathetic cooling rate Γ_{sym} was introduced. It is often expressed through the single-phonon coupling constant g_{N} [34, 57]:

$$g_{\mathrm{N}} \;=\; K x_{\mathrm{zp}}^{\mathrm{m}} x_{\mathrm{zp}}^{\mathrm{a}}/\hbar \;=\; |r_{\mathrm{m}}|\omega_{\mathrm{a}}\sqrt{\frac{N m_{\mathrm{a}}\omega_{\mathrm{a}}}{m\omega_{\mathrm{m}}}}\,\frac{2\mathcal{F}}{\pi}\,, \tag{5.12}$$

with the quantum zero-point fluctuations $x_{\mathrm{zp}}^{\mathrm{m}} = \sqrt{\hbar/2m\omega_{\mathrm{m}}}$ and $x_{\mathrm{zp}}^{\mathrm{a}} = \sqrt{\hbar/2m_{\mathrm{a}}\omega_{\mathrm{a}}}$ and the field reflectivity r_{m} of the membrane oscillator (see Table 3.1). Using this relation 5.12 and equation 5.8, the sympathetic cooling rate for N atoms can be written as:

$$\Gamma_{\mathrm{sym}}\left[N,\omega_{\mathrm{a}}\right] \;=\; \frac{g_{\mathrm{N}}^2\beta t^2\,\Gamma_{\mathrm{a}}}{\left(\omega_{\mathrm{a}}-\omega_{\mathrm{m}}\right)^2+\left(\Gamma_{\mathrm{a}}/2\right)^2}\,. \tag{5.13}$$

Equation 5.10 shows that the sympathetic cooling leads to shifted frequency ω'_{m} of the mechanical oscillator, which is equivalent to displacement-dependent feedback. However, this effect is negligible in our experiment since $\Gamma_{\mathrm{a}} \gg \Gamma_{\mathrm{sym}}$. The cold damping is generated by the effectively increased damping rate Γ'_{m} of the oscillator, which can be described by the gain g_{sym} similar to velocity-dependent feedback (see equation 4.7). Also similar to active feedback cooling this leads to a reduced mode temperature T_{mode} of the mechanical oscillator [57]:

$$T_{\mathrm{mode}} \;=\; T_{\mathrm{bath}}\frac{1}{1+g_{\mathrm{sym}}} \;=\; T_{\mathrm{bath}}\frac{\Gamma_{\mathrm{m}}}{\Gamma_{\mathrm{sym}}+\Gamma_{\mathrm{m}}}\,. \tag{5.14}$$

Ensemble-integrated sympathetic cooling rate

In the experiment the cold atomic cloud used for sympathetic cooling has a radius R_{a} which is much larger than the waist w_{lat} of the coupling lattice. Hence, it is reasonable

to assume a constant atomic number density n_a in the lattice volume (neglecting the attractive or repulsive potential of the near-resonant lattice beam). However, the Gaussian intensity distribution of the beam leads to a radial dependency of the atomic trapping frequency $\omega_\mathrm{a}(r) = \omega_{\mathrm{a},0}\, e^{-r^2/w_\mathrm{lat}^2}$ (note that outside this context, $\omega_{\mathrm{a},0}$ will simply be denoted by ω_a). Therefore, Γ_sym in equation 5.13 must be integrated over the radial beam profile in order to describe the experimental conditions. The axial dependency $\omega_\mathrm{a}(z)$ of the atomic trapping frequency is omitted, since the Rayleigh range $z_\mathrm{r} \approx 2.5\,\mathrm{cm} \gg R_\mathrm{a}$ in our experiment. Following [118], the integral over the radial coordinate

$$\Gamma_\mathrm{sym}^\mathrm{int} \;=\; 2R_\mathrm{a} n_\mathrm{a} \int_0^{R_\mathrm{a}} \Gamma_\mathrm{sym}\left[N=1, \omega_\mathrm{a}(r)\right] 2\pi r \,\mathrm{d}r \tag{5.15}$$

can be converted into an integral over the frequency

$$\begin{aligned}\Gamma_\mathrm{sym}^\mathrm{int}(\omega_{\mathrm{a},0}) \;&=\; N_\mathrm{lat} \int_{\omega_\mathrm{a}(R_\mathrm{a})}^{\omega_{\mathrm{a},0}} \frac{\Gamma_\mathrm{sym}\left[N=1,\omega_\mathrm{a}\right]}{\omega_\mathrm{a}} \,\mathrm{d}\omega_\mathrm{a} \\ &=\; \frac{m_\mathrm{a} N_\mathrm{lat}}{m} |r_\mathrm{m}|^2 \beta t^2 \,\frac{\Gamma_\mathrm{a}}{\omega_\mathrm{m}} \left(\frac{2\mathcal{F}}{\pi}\right)^2 \int_{\omega_\mathrm{a}(R_\mathrm{a})}^{\omega_{\mathrm{a},0}} \frac{\omega_\mathrm{a}^2}{\left(\omega_\mathrm{a}-\omega_\mathrm{m}\right)^2 + \left(\Gamma_\mathrm{a}/2\right)^2} \,\mathrm{d}\,\omega_\mathrm{a}\,,\end{aligned}$$

where $N_\mathrm{lat} = 2R_\mathrm{a}\pi w_\mathrm{lat}^2 n_\mathrm{a}$ is the number of atoms in the lattice volume. Solving this integral yields:

$$\Gamma_\mathrm{sym}^\mathrm{int}(\omega_{\mathrm{a},0}) \;=\; 2\frac{m_\mathrm{a} N_\mathrm{lat}}{m} |r_\mathrm{m}|^2 \beta t^2 \left(\frac{2\mathcal{F}}{\pi}\right)^2 \omega_\mathrm{m} \cdot S_\mathrm{res}\left(\omega_{\mathrm{a},0}\right)\,, \tag{5.16}$$

with the step-like function $S_\mathrm{res}(\omega_{\mathrm{a},0})$, which describes the transient behavior of the sympathetic cooling rate as a function of the maximal atomic trapping frequency $\omega_{\mathrm{a},0}$ in the center of the coupling beam:

$$\begin{aligned}S_\mathrm{res}(\omega_{\mathrm{a},0}) \;:=\; &\left(1-\frac{\Gamma_\mathrm{a}^2}{4\omega_\mathrm{m}^2}\right)\left(\arctan\left[\frac{2\omega_\mathrm{m}}{\Gamma_\mathrm{a}}\right] + \arctan\left[\frac{2\left(\omega_{\mathrm{a},0}-\omega_\mathrm{m}\right)}{\Gamma_\mathrm{a}}\right]\right) \\ &+ \frac{\Gamma_\mathrm{a}}{2\omega_\mathrm{m}^2}\left(\omega_{\mathrm{a},0} + \omega_\mathrm{m} \ln\left[\frac{\Gamma_\mathrm{a}^2 + 4\left(\omega_{\mathrm{a},0}-\omega_\mathrm{m}\right)^2}{\Gamma_\mathrm{a}^2 + 4\omega_\mathrm{m}^2}\right]\right)\,.\end{aligned} \tag{5.17}$$

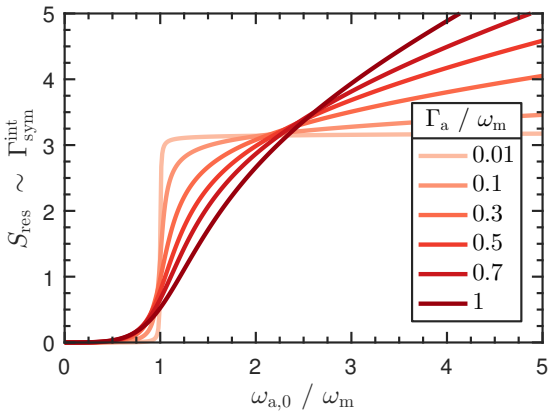

Figure 5.2: Ensemble-integrated sympathetic cooling rate $\Gamma_\mathrm{sym}^\mathrm{int}$ for different Γ_a. $\Gamma_\mathrm{sym}^\mathrm{int}$ is proportional to the function S_res (see equation 5.17), which is plotted here for different atomic cooling rates Γ_a as a function of the atomic trapping frequency $\omega_{\mathrm{a},0}$ on the beam axis of the coupling lattice. Both Γ_a and $\omega_{\mathrm{a},0}$ are in units of the oscillator frequency ω_m. Note that the model assumes a constant atomic density in the lattice volume.

Figure 5.2 shows the behavior of the function $S_{\mathrm{res}}(\omega_{\mathrm{a},0})$. For a small atomic cooling rate $\Gamma_{\mathrm{a}} \ll \omega_{\mathrm{m}}$, the width S_{res} becomes smaller and the diverging part becomes negligible (second line in equation 5.17). In this case, the sympathetic cooling rate can be regarded as a step function with width Γ_{a}. However, this is not a good approximation in our system, as shown later.
The function S_{res} can be absorbed into the effective atom number N_{res}, which account for the number of atoms that participates in the cooling process. Using equation 5.16 this yields:

$$N_{\mathrm{res}} := N_{\mathrm{lat}} S_{\mathrm{res}}\left(\omega_{\mathrm{a},0}\right) = \frac{m\,\Gamma_{\mathrm{sym}}^{\mathrm{int}}\left(\omega_{\mathrm{a},0}\right)}{2\beta t^2 \omega_{\mathrm{m}} m_{\mathrm{a}} |r_{\mathrm{m}}|^2 \left(\frac{2\mathcal{F}}{\pi}\right)^2}\,. \tag{5.18}$$

5.1.2 Quantum description and hybrid cooperativity

In a fully quantized model of the hybrid coupling mechanism depicted in Figure 5.1, the light field can be eliminated in the effective dynamics assuming the bad cavity regime $\kappa_{\mathrm{cav}} \gg \omega_{\mathrm{m}}$ [31]. This yields the effective interaction Hamiltonian [31, 57]:

$$H_{\mathrm{int}} = \hbar g_{\mathrm{N}} \left(\hat{b}_{\mathrm{m}} + \hat{b}_{\mathrm{m}}^{\dagger}\right)\left(\hat{b}_{\mathrm{a}} + \hat{b}_{\mathrm{a}}^{\dagger}\right)\,, \tag{5.19}$$

where $\hat{b}_{\mathrm{m}}$ ($\hat{b}_{\mathrm{a}}$) and $\hat{b}_{\mathrm{m}}^{\dagger}$ ($\hat{b}_{\mathrm{a}}^{\dagger}$) are the annihilation and creation operators of the mechanical mode (atomic mode) and g_{N} is the single-phonon coupling constant (see equation 5.12) which generates coherent exchange of mechanical and atomic quanta.
In the classical model described in the previous subsection, sympathetic cooling can lead to arbitrarily small mode temperatures of the mechanical oscillator (see equation 5.14). However, in a fully quantized model [31] the minimal temperature of the mechanical oscillator is limited by different decoherence mechanisms. This can be expressed through the steady state phonon occupation $\bar{n}_{\mathrm{ss}}$ of the mechanical oscillator:

$$\begin{aligned}\bar{n}_{\mathrm{ss}} &= \frac{\Gamma_{\mathrm{m}}\bar{n}\mathrm{th}}{\Gamma_{\mathrm{m}}+\Gamma_{\mathrm{sym}}} + \frac{\Gamma_{\mathrm{m}}^{\mathrm{diff}}}{\Gamma_{\mathrm{m}}+\Gamma_{\mathrm{sym}}} + \left(\frac{\Gamma_{\mathrm{a}}}{4\omega_{\mathrm{a}}}\right)^2 + \frac{\Gamma_{\mathrm{a}}^{\mathrm{diff}}}{\Gamma_{\mathrm{a}}} \\ &= \bar{n}_1 + \bar{n}_2 + \bar{n}_3 + \bar{n}_4\,.\end{aligned} \tag{5.20}$$

The first term originates from the coupling to the thermal bath with the mode occupation $\bar{n}_{\mathrm{th}} \approx k_{\mathrm{B}} T_{\mathrm{bath}}/\hbar\omega_{\mathrm{m}}$ (see equation 3.14), similar to equation 5.14. The second term describes the radiation pressure noise of the coupling beam in the MiM cavity, which generates a momentum diffusion rate $\Gamma_{\mathrm{m}}^{\mathrm{diff}}$ of the mechanical oscillator. The third term plays a role for strong atomic damping and a correspondingly large cooling rate Γ_{a} where the counter-rotating terms in the rotating wave approximation in the Hamiltonian start to become important. The fourth term describes the atomic momentum diffusion due to photon scattering.
The first two terms in equation 5.20 can be summarized to

$$\bar{n}_1 + \bar{n}_2 = \frac{\Gamma_{\mathrm{m}}\bar{n}_{\mathrm{th}} + \Gamma_{\mathrm{m}}^{\mathrm{diff}}}{\Gamma_{\mathrm{m}}+\Gamma_{\mathrm{sym}}} \equiv \frac{\Gamma_{\mathrm{m}}^{\mathrm{dec}}}{\Gamma_{\mathrm{m}}+\Gamma_{\mathrm{sym}}} \overset{\Gamma_{\mathrm{sym}} \gg \Gamma_{\mathrm{m}}}{\approx} \frac{\Gamma_{\mathrm{m}}^{\mathrm{dec}}}{\Gamma_{\mathrm{sym}}} = \frac{\bar{n}_{\mathrm{th}}}{C_{\mathrm{hybrid}}}\,, \tag{5.21}$$

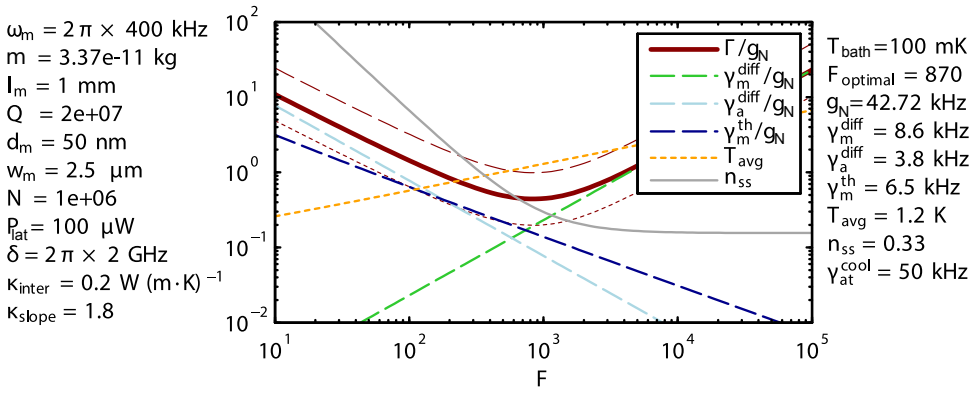

Figure 5.3: Calculation of the strong coupling condition in the hybrid system. According to the model in [31], the total decoherence rate $\Gamma = \Gamma_\mathrm{m}\bar{n}_\mathrm{th} + \Gamma_\mathrm{m}^\mathrm{diff} + \Gamma_\mathrm{a}^\mathrm{diff}$ relative to the coupling rate g_N was calculated as a function of the cavity finesse $\mathcal{F}$. The laser-induced heating of the membrane was modeled by a Gaussian temperature distribution with average temperature T_avg around the cavity mode with waist w_m for a temperature dependent thermal conductivity κ. The strong coupling condition $\Gamma/g_\mathrm{N} < 1$ is fulfilled for an optimal finesse $\mathcal{F}_\mathrm{opt} = 870$ and the steady state phonon occupation is $\bar{n}_\mathrm{ss} < 1$. Figure taken from [86].

introducing the total mechanical decoherence rate $\Gamma_\mathrm{m}^\mathrm{dec} = \Gamma_\mathrm{m}\bar{n}_\mathrm{th} + \Gamma_\mathrm{m}^\mathrm{diff}$ which is the sum of the thermal decoherence rate $\Gamma_\mathrm{m}\bar{n}_\mathrm{th}$ (see equation 3.15) and the momentum diffusion rate $\Gamma_\mathrm{m}^\mathrm{diff}$ due to radiation pressure noise in the cavity. Furthermore, equation 5.21 introduces the cooperativity of the hybrid system C_hybrid. Using equation 5.13 and assuming resonant coupling $\omega_\mathrm{a} \approx \omega_\mathrm{m}$ (and $\Gamma_\mathrm{m}\bar{n}_\mathrm{th} \gg \Gamma_\mathrm{m}^\mathrm{diff}$), the hybrid cooperativity can be written as [34, 102]:

$$C_\mathrm{hybrid} \approx \frac{4\beta t^2 g_\mathrm{N}^2}{\Gamma_\mathrm{a}\Gamma_\mathrm{m}}. \tag{5.22}$$

Regarding equations 5.20 and 5.21 the hybrid cooperativity must be large ($C_\mathrm{hybrid} \gg \bar{n}_\mathrm{th}$) in order to cool the mechanical oscillator into the ground state ($\bar{n}_\mathrm{ss} < 1$).
A large hybrid cooperativity is closely related to the *strong coupling condition* $g_\mathrm{N} \gg \Gamma_\mathrm{a}^\mathrm{diff}, \Gamma_\mathrm{m}^\mathrm{dec}$, which means that the hybrid coupling rate has to exceed all relevant decoherence rates in the system [31]. In the PhD thesis of A. Bick [86] a simulation of this strong coupling condition according to the model in [31] was performed for parameters that are experimentally accessible with our current setup. The calculation shown in Figure 5.3 yields an optimal cavity finesse of $\mathcal{F} = 870$, where the strong coupling condition is fulfilled and ground state cooling is achieved. As long as both parts of the hybrid system are in a quantum state, the hybrid system would evolve coherently when the laser cooling at rate Γ_a is switched off. Furthermore, if the coupling constant exceeds a certain critical value, N. Mann *et al* theoretically predicted a quantum phase transition between the initial phase of the ground state of the atom-membrane system and states of collective quantum many-body motion [185].
However, in our current setup the cryogenic bath temperature $T_\mathrm{bath} \approx 3\,\mathrm{K}$ is much larger than assumed in the simulation, the finesse is about five times smaller and the Q-factor is smaller by a factor of two (see Table 3.1). Furthermore, the simulation assumes an optimal lattice alignment and neglects optical losses (see section 2.4.2). As shown

later, the lattice power for optimal sympathetic cooling in our current setup should be at least a factor of two larger, since otherwise the near-resonant lattice detuning (which is necessary to fulfill the resonance condition $\omega_a = \omega_m$) leads to additional parasitic effects that lower the coupling constant.

5.1.3 Instability in the hybrid system

The hybrid coupling experiments in the group of P. Treulein have shown that the sympathetic cooling can turn into heating and limit-cycle oscillations of the mechanical oscillator, which occurs for small lattice detunings and large atom numbers. This behavior was investigated in detail by A. Vochezer *et al* (neé Faber) [104] and was also observed in our experiment, as presented later. This subsection briefly outlines the mechanism of this hybrid instability.

The underlying mechanism of the hybrid instability is light-mediated collective atomic motion in the optical lattice, generated by back-action of the atoms onto the light field. This phenomenon was predicted theoretically by J.K. Asbóth *et al* [103, 186] and is related to a pump-asymmetry of the optical lattice, which naturally occurs in our system as the back reflected lattice beam from the MiM system has only 35% of the incident lattice beam power P_{lat} (see section 2.4.1).

In order to describe the back-action of the atoms onto the light field, the disk-shaped clouds of atoms can be modeled as beam splitters with certain reflection and transmission coefficients. This explains why the instabilities only occur for large atomic densities. If these atomic beam splitters are included as individual atomic oscillators into the equations of motion of the hybrid system, the instability of the hybrid system can be understood in a feedback picture [104]. If the sympathetic cooling turns into heating and limit-cycle oscillations, there must be some kind of phase delay between the atoms and the mechanical oscillator which exceeds a critical value. If the atomic ensemble is modeled as only one beam splitter, its phase delay to the membrane is too small to explain the instability. However, as soon as two or more beam splitters are taken into account, the model quickly converges to a regime where the delay can become more than 180° [104]. In this way, the collective motion of the atoms gets amplified by positive feedback and drives the system into limit-cycle oscillations.

We only observe this instability for red lattice detuning, which can be explained by the fact that the effect of the lattice pump-asymmetry gets worse for red lattice detuning compared to blue detuning [186]. Furthermore, the red detuned lattice attracts more atoms from the MOT or molasses cloud used for sympathetic cooling which leads to larger atomic densities in the lattice which also increases the instability.

5.1.4 Combined sympathetic and feedback cooling

In this subsection, a classical model for the combination of feedback cooling with sympathetic cooling will be presented. This model neglects the back-action noise on the mechanical oscillator from the cavity light field, as well as the noise induced by a finite temperature of the atomic ensemble. A semi-classical model including these additional noise terms was published in [34].

In order to calculate the effective susceptibility $\chi_{eff,sf}$ of the mechanical oscillator for

combined sympathetic and feedback cooling, the sympathetic cooling force F_{sym} must be added in equation 4.2:

$$x \;=\; \chi_{\mathrm{m}}\left[F_{\mathrm{th}} + F_{\mathrm{fb}} + F_{\mathrm{sym}}\right]. \tag{5.23}$$

Note that the oscillator displacement refers to the coordinate $x(\omega)$ in frequency space and the frequency dependency is omitted for clarity. Substituting $F_{\mathrm{fb}} = -\chi_{\mathrm{fb}}^{-1}(x + x_{\mathrm{n}})$ from equation 4.1 and $F_{\mathrm{sym}} = -\chi_{\mathrm{sym}}^{-1}x$ from equation 5.7 into equation 5.23 yields:

$$\left(\chi_{\mathrm{m}}^{-1} + \chi_{\mathrm{fb}}^{-1} + \chi_{\mathrm{sym}}^{-1}\right) x \;\equiv\; \chi_{\mathrm{eff,sf}}^{-1}\, x \;=\; F_{\mathrm{th}} - \chi_{\mathrm{fb}}^{-1}\, x_{\mathrm{n}} \tag{5.24}$$

$$\Leftrightarrow \quad \left(\chi_{\mathrm{m}}^{-1} + \chi_{\mathrm{fb}}^{-1} + \chi_{\mathrm{sym}}^{-1}\right)(x + x_{\mathrm{n}}) \;\equiv\; \chi_{\mathrm{eff,sf}}^{-1}\, y \;=\; F_{\mathrm{th}} + \underbrace{\left(\chi_{\mathrm{m}}^{-1} + \chi_{\mathrm{sym}}^{-1}\right)}_{\chi_{\mathrm{eff,s}}^{-1}(\omega)} x_{\mathrm{n}}\,, \tag{5.25}$$

with the effective susceptibility $\chi_{\mathrm{eff,s}}^{-1}(\omega)$ from equation 5.7. Equation 5.24 will be used in the following to calculate the displacement PSD $S_{\mathrm{x}}^{\mathrm{sf}}(\omega)$ and the mode temperature $T_{\mathrm{mode}}^{\mathrm{sf}}$ of the oscillator for combined feedback and sympathetic cooling. Nevertheless, the measured PSD in the experiment is the in-loop PSD $S_{\mathrm{y}}^{\mathrm{sf}}(\omega)$ which corresponds to the measured signal $y = x + x_{\mathrm{n}}$. This in-loop PSD can be calculated from equation 5.25.

Similar to the calculation of $S_{\mathrm{x}}(\omega)$ (see equation 4.9), the displacement PSDs $S_{\mathrm{x}}^{\mathrm{sf}}(\omega)$ and $S_{\mathrm{y}}^{\mathrm{sf}}(\omega)$ can be calculated using equations 5.24 and 5.25 under the assumption that the feedback detector noise x_{n} and the thermal noise force F_{th} are uncorrelated:

$$S_{\mathrm{x}}^{\mathrm{sf}}(\omega) \;=\; \langle\,|x(\omega)|^2\rangle \;=\; |\chi_{\mathrm{eff,sf}}|^2\left[S_{F_{\mathrm{th}}}(\omega) + |\chi_{\mathrm{fb}}|^{-2} S_{x_{\mathrm{n}}}(\omega)\right] \tag{5.26}$$

$$S_{\mathrm{y}}^{\mathrm{sf}}(\omega) \;=\; \langle\,|y(\omega)|^2\rangle \;=\; |\chi_{\mathrm{eff,sf}}|^2\left[S_{F_{\mathrm{th}}}(\omega) + |\chi_{\mathrm{eff,s}}|^{-2} S_{x_{\mathrm{n}}}(\omega)\right]. \tag{5.27}$$

In order to obtain the mode temperature from the displacement PSD $S_{\mathrm{x}}^{\mathrm{sf}}(\omega)$, the effective susceptibility $\chi_{\mathrm{eff,sf}}$ needs to be calculated. For this, we treat the sympathetic cooling as purely velocity-dependent, which corresponds to a purely imaginary χ_{sym}. This is a very good approximation as long as $\Gamma_{\mathrm{sym}} \ll \Gamma_{\mathrm{a}}$ (see equation 5.10), as in our case. Assuming also purely velocity-dependent feedback cooling ($g_{\mathrm{d}} = 0$), the purely imaginary functions χ_{fb}^{-1} and χ_{sym}^{-1} can both be absorbed into the effective mechanical damping rate $\Gamma_{\mathrm{m}}' = \Gamma_{\mathrm{m}}(1 + g_{\mathrm{v}} + g_{\mathrm{sym}})$:

$$\chi_{\mathrm{eff,sf}}^{-1} \;=\; \left(\chi_{\mathrm{m}}^{-1} + \chi_{\mathrm{fb}}^{-1} + \chi_{\mathrm{sym}}^{-1}\right) \;=\; 2m\omega_{\mathrm{m}}\left[\omega_{\mathrm{m}} - \omega - i\frac{\Gamma_{\mathrm{m}}}{2}\left(1 + g_{\mathrm{v}} + g_{\mathrm{sym}}\right)\right], \tag{5.28}$$

With this result, the mode temperature of the mechanical oscillator for combined feedback and sympathetic cooling can be obtained by integrating the displacement PSD $S_{\mathrm{x}}^{\mathrm{sf}}(\omega)$. A similar calculation as shown in equation 4.17 yields:

$$T_{\mathrm{mode}}^{\mathrm{sf}} \;=\; \frac{T_{\mathrm{bath}}}{(1 + g_{\mathrm{v}} + g_{\mathrm{sym}})} + \frac{k_{\mathrm{m}}\omega_{\mathrm{m}}}{4k_{\mathrm{B}}Q}\,\frac{g_{\mathrm{v}}^2}{(1 + g_{\mathrm{v}} + g_{\mathrm{sym}})}\,S_{x_{\mathrm{n}}}. \tag{5.29}$$

5.2 Experimental realization of sympathetic cooling

In this section, the performed sympathetic cooling experiments will be presented, which can be used to characterize the sympathetic cooling performance and its dependency on important experimental parameters. Furthermore, the demonstration of combined feedback cooling and sympathetic cooling represents an important milestone towards a hybrid quantum system consisting of ultra-cold atoms and a quantum mechanical oscillator.
The measurements were prepared and performed by the following people: the optical coupling lattice was set up and aligned by the author together with T. Wagner. The software for triggered data acquisition of the homodyne signal in cycled experiments was programmed by H. Zhong. The experiments and data analysis were performed by the author together with T. Wagner.

5.2.1 Parameter optimization and experimental sequences

As shown in section 5.1.1, the sympathetic cooling rate Γ_{sym} (see equation 5.16) depends on parameters of the atomic ensemble (Γ_{a}, N_{lat}), the coupling lattice (ω_{a}) and the MiM system (m, ω_{m}, r_{m}, $\mathcal{F}$). For a given experimental realization of the MiM system, the main parameters that can be changed in a systematic manner are the the atomic cooling rate Γ_{a}, the atom number N_{lat} in the lattice volume and the trapping frequency ω_{a} of the coupling lattice.
Finding the optimal parameter set of values for Γ_{a}, N_{lat} and ω_{a} is complicated for several reasons, which will be listed in the following:

Large parameter space
The three parameters Γ_{a}, N_{lat} and ω_{a} also depend on many other parameters that increase the dimension of the parameter space. For example, the atomic trapping frequency ω_{a} can be generated by different combinations of the lattice power P_{lat} and the lattice detuning Δ. Also Γ_{a} depends on many other parameters of the used laser cooling method for the atomic cloud (like the laser detuning, laser power or the magnetic field gradient).

Complex interplay of parameters
Changing laser cooling parameters also changes the atomic density and overall atom number of the cloud. Hence, the quantities Γ_{a} and N_{lat} are directly connected, which makes the parameter optimization a highly iterative process.

Parameters difficult to measure
The quantity Γ_{a} and the atom number N_{lat} are difficult to measure independently. For example, even though a lot of effort was spent measuring N_{lat} with an additional detection beam, the indirect measurement of the atom number through measuring Γ_{sym} still remains the most reliable method we have found.

Dynamical processes
The method for generating very dense MOTs, as well as generating an optical molasses used for sympathetic cooling are dynamical processes. This allows for a large variety of possible timing configurations as an extra parameter.

The sympathetic cooling measurements were performed with three different laser cooling configurations of the atomic cloud. All three configurations were optimized for a maximum sympathetic cooling rate of the mechanical oscillator. Due to the difficulties listed above, each optimization was performed with an individual strategy. The laser cooling configurations are:

- Steady state sympathetic cooling with a continuously loaded MOT
- Pulsed sympathetic cooling with an optical molasses
- Pulsed sympathetic cooling with a MOT

In the following, these experimental configurations and the specific optimization for a maximum sympathetic cooling rate Γ_{sym} will be discussed in more detail.

Steady state sympathetic cooling: MOT configuration A

If the coupling lattice is guided through a continuously loaded MOT and the lattice trapping frequency is $\omega_{\mathrm{a}} \approx \omega_{\mathrm{m}}$, the mechanical oscillator is sympathetically cooled and quickly reaches a steady state with a mode temperature $T_{\mathrm{mode}} < T_{\mathrm{bath}}$. In this steady state, the floating average peak PSD of the oscillator was monitored using a spectrum analyzer connected to the homodyne detector. In this way, the MOT parameters could be changed iteratively, until the lowest mode temperature of the oscillator was reached. Our measurements show that the optimal cooling could be achieved for a large magnetic field gradient of 25 G/cm using a current of 50 A and the maximum available laser intensity of $I_{\mathrm{max}} = 75\,\mathrm{mW/cm^2} = 45\,I_{\mathrm{sat}}$ with a detuning of $\delta_{\mathrm{MOT}} = -6.2\,\Gamma_{\mathrm{D_2}} = -2\pi \times 37.8\,\mathrm{MHz}$.[2] The optimization procedure yields a relatively dense MOT as compared to the normal MOT used in our BEC cycle. This makes sense, as a large atom number in the lattice volume is beneficial for the sympathetic cooling. The dense MOT has a temperature of $T = 170(15)\,\mu\mathrm{K}$, which was determined by ballistic expansion measurements (see appendix C.1). The optimization was performed with a blue lattice detuning of $\Delta_{2,3} = 2\pi \times 224\,\mathrm{MHz}$,[3] which results in a (calibrated) trapping frequency of $\omega_{\mathrm{a}} \approx 2.5\,\omega_{\mathrm{m}}$ for the used lattice power of $P_{\mathrm{lat}} = 250\,\mu\mathrm{W}$.
As shown later in Figure 5.16, these parameters (called *MOT configuration A*) allow for steady state sympathetic cooling with $\Gamma_{\mathrm{sym}} \approx 8\,\mathrm{Hz}$ down to mode temperatures of $T_{\mathrm{mode}} \approx 25\,\mathrm{mK}$ for the corresponding $T_{\mathrm{bath}} \approx 1\,\mathrm{K}$.

Pulsed sympathetic cooling with an optical molasses

As the atoms in an optical molasses are not spatially confined, they have a finite lifetime on the order of 1 s. Therefore, the sympathetic cooling with an optical molasses must be performed in a cycled experiment in order to average the mode temperature during the cooldown over many experimental runs. For this, the homodyne signal from the

[2] I define the maximum intensity I_{max} for the MOT and the optical molasses as the summed intensity of all six beam, which was measured with a power meter

[3] The Ti:sapph frequency was locked at $n_{\mathrm{FSR}} = 0$ FSR with the transfer lock (see equation 2.8)

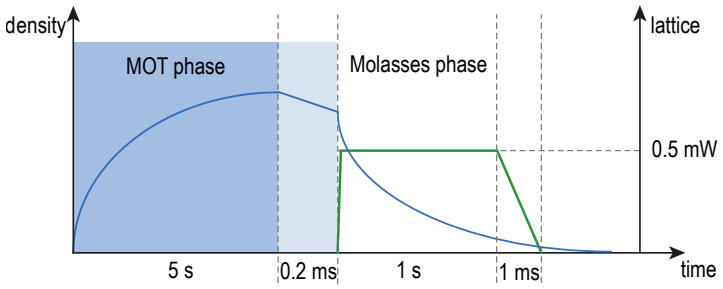

Figure 5.4: Experimental sequence for sympathetic cooling with an optical molasses. After loading the 3D MOT for 5 s (dark blue shading), the current through the magnetic coils and the 3D MOT light are switched off for a short period of 200 µs (light blue shading). After this, the magnetic fields have decayed and allow creating an optical molasses by switching on the cooling lasers again. Simultaneously, the coupling lattice is switched on with the intensity control (bandwidth ≈ 50 kHz) until it is ramped down again after a coupling period of 1 s. Blue line: atomic density, green line: lattice power, shaded blue area: MOT phase. Time axis not to scale.

mechanical oscillator was measured using zero-span traces from the lock-in amplifier[4] (see Figure 4.8), as described in section 4.4.1.
In order to find the optimal molasses parameters for sympathetic cooling, the detuning δ_{Mol} and the intensity I_0 of the molasses light were varied systematically. Figure 5.5 exemplarily shows the time traces of the oscillator temperature for one specific I_0 and ten different detunings. After the cooldown during $0 < t < 0.5\,\mathrm{s}$, the mode temperature starts to increase again due to the finite lifetime of the atoms in the molasses. The

[4]The data acquisition and storage of the zero-span traces is triggered by the experimental control, which allows for extracting the parameters of each cycle from the experimental protocol files.

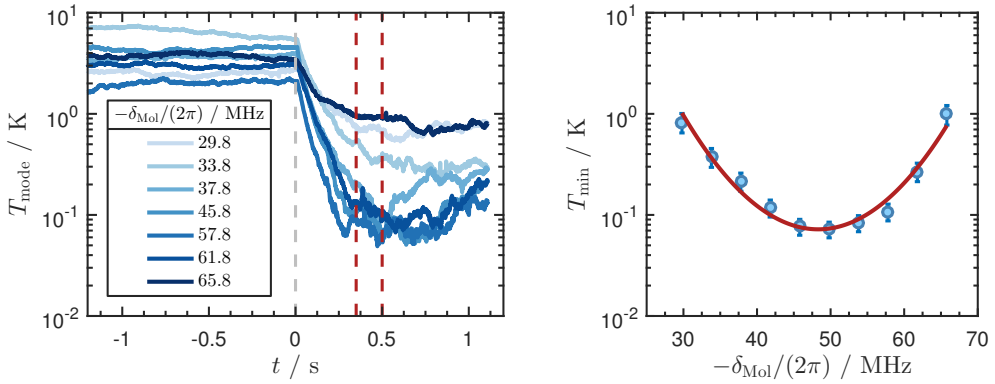

Figure 5.5: Sympathetic cooling for different molasses detunings. Left: time traces of the oscillator temperature T_{mode} during sympathetic cooling with an optical molasses for a fixed molasses intensity $I = 0.43 \cdot I_{\mathrm{max}} = 32.3\,\mathrm{mW/cm^2}$ and different molasses detunings. The molasses phase starts at $t = 0$, where the coupling lattice is also quickly switched on ($\tau_{\mathrm{rise}} < 1\,\mathrm{ms}$). Right: minimum temperature in the time interval indicated by the red dashed lines in the left figure and a parabolic fit to the data. Parameters: lattice power $P_{\mathrm{lat}} = 0.5\,\mathrm{mW}$, blue lattice detuning $\Delta_{2,3} = 2\pi \times 224\,\mathrm{MHz}$ ($n_{\mathrm{FSR}} = 0$) $\Rightarrow \omega_{\mathrm{a}} = 3.5\,\omega_{\mathrm{m}}$ (calibrated), optomechanical parameters summarized in Table 3.1, each zero-span trace averaged 20 times, demodulator bandwidth $B_{\mathrm{d}} = 300\,\mathrm{Hz}$, total cycle time 13 s.

lowest mode temperature T_{min} for each parameter set was extracted by averaging within a meaningful time interval before this increase occurs at $t \approx 0.75\,\mathrm{s}$. We found that for large data sets this method is more reliable and robust than individual fits to the cooldown curves, as presented later in subsection 5.2.2.
For each I_0 we find a clear minimum of the achieved minimum temperatures T_{min} at one specific optimal molasses detuning $\delta_{\mathrm{Mol}}^{\mathrm{opt}}$, which can be extracted by a fit to the T_{min} (see Figure 5.5 at right). The minimum achievable temperature at these optimal detunings are shown in Figure 5.6 (a) and the corresponding sympathetic cooling rates Γ_{sym} according to equation 5.14 are shown in Figure 5.6 (b). The measurements were performed for two different coupling lattice configurations with red and blue detuning. One can see that for the blue lattice detuning $\Delta_{2,3} = 2\pi \times 224\,\mathrm{MHz}$ with the large atomic trapping frequency $\omega_{\mathrm{a}} = 3.5\,\omega_{\mathrm{m}}$, the sympathetic cooling rate slightly increases for larger I_0. In contrast, the red lattice detuning with $\omega_{\mathrm{a}} = 1.65\,\omega_{\mathrm{m}}$ leads to a rather constant Γ_{sym} for a large range of molasses light intensities I_0 and the corresponding

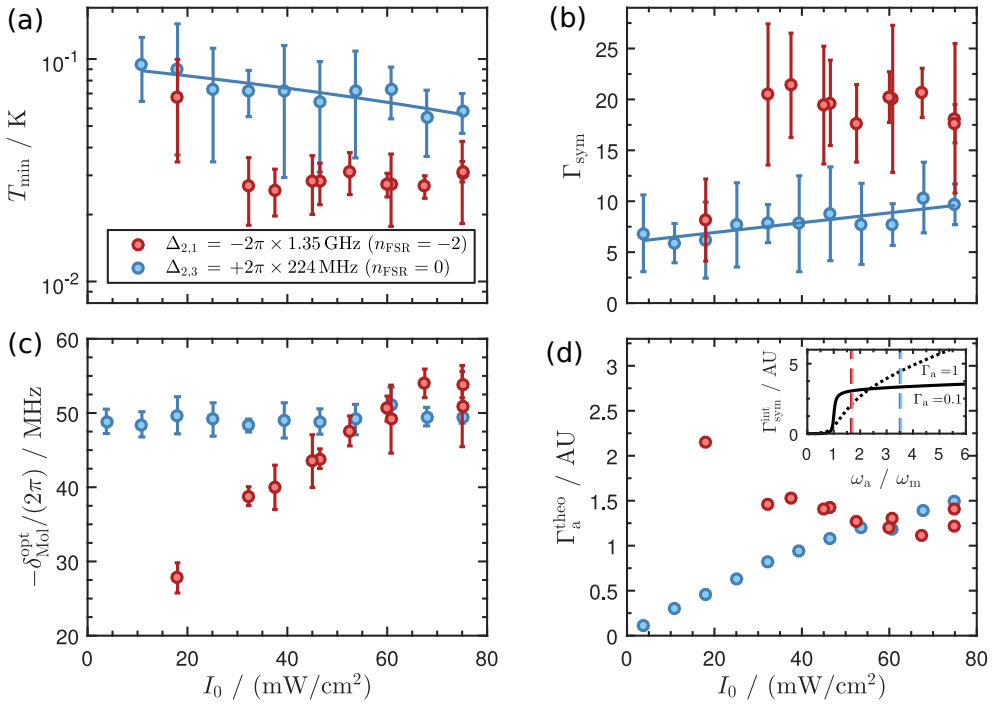

Figure 5.6: Parameter optimization for sympathetic cooling with an optical molasses. (a): Minimum mode temperature during sympathetic cooling with an optical molasses for different molasses light intensities I_0. Each data point corresponds to the optimal molasses detuning $\delta_{\mathrm{Mol}}^{\mathrm{opt}}$ obtained by a molasses detuning sweep shown in Figure 5.5. (b): Corresponding sympathetic cooling rate according to equation 5.14 with T_{bath} extracted by averaging the time traces for $t < 0$ (see Figure 5.5). (c): Combinations of I_0 and $\delta_{\mathrm{Mol}}^{\mathrm{opt}}$ that corresponds to the optimal cooling points in Figure (a). (d): Theoretically expected $\Gamma_{\mathrm{a}}^{\mathrm{theo}}$ for the combinations of I_0 and $\delta_{\mathrm{Mol}}^{\mathrm{opt}}$ from Figure (c) (see equation 5.30). Inset figure: model for $\Gamma_{\mathrm{sym}}^{\mathrm{int}}$ (see equation 5.16) for $\Gamma_{\mathrm{a}} = 0.1\,\omega_{\mathrm{m}}$ (black solid line) and $\Gamma_{\mathrm{a}} = \omega_{\mathrm{m}}$ (black dashed line). The blue and red dashed lines indicate the (calibrated) trapping frequencies $\omega_{\mathrm{a}} = 1.65\,\omega_{\mathrm{m}}$ for the red detuned lattice and $\omega_{\mathrm{a}} = 3.5\,\omega_{\mathrm{m}}$ for the blue detuned lattice. Parameters as described in the caption of Figure 5.5 and $P_{\mathrm{lat}} = 0.7\,\mathrm{mW}$ for the red detuned lattice.

optimal molasses detunings $\delta_{\mathrm{Mol}}^{\mathrm{opt}}$. The fact that Γ_{sym} is always smaller than for the red lattice detuning could be explained by the fact that the repulsive potential of the blue lattice beam leads to a smaller atom number N_{lat} in the lattice volume.
The combinations of I_0 and $\delta_{\mathrm{Mol}}^{\mathrm{opt}}$ at the points of optimal cooling are shown in Figure 5.6 (c). Interestingly, $\delta_{\mathrm{Mol}}^{\mathrm{opt}}$ for the blue lattice detuning is constant at $\delta_{\mathrm{Mol}}^{\mathrm{opt}} \approx -2\pi \times 50\,\mathrm{MHz} = -8.2\,\Gamma_{\mathrm{D}_2}$, while for the red lattice detuning the optimal molasses detuning $\delta_{\mathrm{Mol}}^{\mathrm{opt}}$ changes with I_0. It is unclear what leads to these combinations of I_0 and $\delta_{\mathrm{Mol}}^{\mathrm{opt}}$. However, the measurement shows that for a wide parameter range the maximum available intensity $I_0 = I_{\mathrm{max}} = 75\,\mathrm{mW/cm^2} = 45\,I_{\mathrm{sat}}$ and a molasses detuning around $-2\pi \times 50\,\mathrm{MHz} = 8.2\,\Gamma_{\mathrm{D}_2}$ leads to a large sympathetic cooling rate. Hence, we performed all our sympathetic cooling measurements presented in the following with these parameters.
Nevertheless, even though the origin of the optimal combinations of I_0 and $\delta_{\mathrm{Mol}}^{\mathrm{opt}}$ remains unclear, one can try to compare them with the theoretical prediction of the sympathetic cooling rate $\Gamma_{\mathrm{sym}}^{\mathrm{int}}$ in equation 5.16. For this, the atomic damping rate $\Gamma_{\mathrm{a}}^{\mathrm{theo}}$ can be calculated from the measured I_0 and $\delta_{\mathrm{Mol}}^{\mathrm{opt}}$, which allows for comparing the measured Γ_{sym} with the theoretical prediction of $\Gamma_{\mathrm{sym}}^{\mathrm{int}}[\Gamma_{\mathrm{a}}^{\mathrm{theo}}, \omega_{\mathrm{a}}]$, using the well-known expression for the atomic damping rate in an optical molasses [187]

$$\Gamma_{\mathrm{a}}^{\mathrm{theo}} = -\frac{\hbar k^2}{m_{\mathrm{a}}} \frac{4 s_0 \left(\delta_{\mathrm{Mol}}/\Gamma_{\mathrm{D}_2}\right)}{\left(1 + s_0 + \left(2\delta_{\mathrm{Mol}}/\Gamma_{\mathrm{D}_2}\right)^2\right)^2}\,, \quad s_0 \equiv I_0/I_{\mathrm{sat}}\,. \tag{5.30}$$

As shown Figure 5.6 (d), the calculated $\Gamma_{\mathrm{a}}^{\mathrm{theo}}$ for the blue lattice detuning with $\omega_{\mathrm{a}} = 3.5\,\omega_{\mathrm{m}}$ is constantly increasing. This corresponds very well with the slight increase of the measured Γ_{sym}, as the model of $\Gamma_{\mathrm{sym}}^{\mathrm{int}}$ predicts an increasing sympathetic cooling rate at $\omega_{\mathrm{a}} = 3.5\,\omega_{\mathrm{m}}$. The calculated $\Gamma_{\mathrm{a}}^{\mathrm{theo}}$ for the red lattice detuning are rather constant, which also agrees well with the measured Γ_{sym}, which is also constant within error bars. Even the one data point with a significantly larger calculated $\Gamma_{\mathrm{a}}^{\mathrm{theo}}$ fits well to the theory, as the measured Γ_{sym} is significantly smaller, which is expected for the lattice depth $\omega_{\mathrm{a}} = 1.65\,\omega_{\mathrm{m}}$.

Pulsed sympathetic cooling: MOT configuration B

Compared to the steady state sympathetic cooling with a MOT, a cycled experiment with pulsed sympathetic cooling allows for much larger densities in the MOT and assumingly larger sympathetic cooling rates. This can be achieved by dynamical processes in the MOT which generate a collapse of the atomic cloud into a very dense state. For example, the group of P. Treutlein reports the use of a *dark MOT* for sympathetic cooling, which is generated by reducing the repumping laser power until the MOT collapses into a very dense cloud. These experiments were discussed in detail in the PhD thesis of A. Vochezer *et al* (neé Faber) [102].
Since the collapse of the MOT is a very time critical process, the density can not be measured with TOF absorption images and must be measured time resolved. For this, an additional detection beam, mode matched with the coupling lattice was installed. It passes the atomic cloud and allows for measuring its optical density (OD). For several reasons, this OD measurement is technically extremely challenging:

- **Dynamic range**: In order to achieve a reasonable dynamic range and a large SNR of the OD measurement, the detection beam should be not too far-detuned from the atomic resonance. Hence, the detection beam power P_{det} must be very small to keep the intensity $I_{\mathrm{det}} \ll I_{\mathrm{sat}}$, which is necessary for the measurement (see appendix C.2). For example, we typically work at detunings of $\delta_{\mathrm{det}} \approx 2\pi \times 30\,\mathrm{MHz} = 5\,\Gamma_{\mathrm{D_2}}$ and powers of $P_{\mathrm{det}} \approx 100\,\mathrm{nW}$[5]. To resolve a large dynamic range of a beam with maximum power of 100 nW, a photo detector with very low noise at DC frequencies is required. Furthermore, the fluorescence light of the atomic cloud creates a typically much larger signal than the small signal from the detection beam. We solve these two problems by a lock-in measurement of the detection beam, which enables a very large SNR around the modulation frequency and which filters out the DC signal from the fluorescence.

- **Parasitic quantum optical effects**: Since the OD must be measured during the MOT or molasses phase, the atomic transitions are continuously driven by the cooling lasers. Hence, the additional near-resonant driving of the detection beam can lead to quantum interference caused by the interplay of the detection light with the cooling light. For example, we observe clear indications for electromagnetically induced transparency (EIT) in the MOT and in the molasses, as discussed in appendix C.2. This leads to an effectively broadened linewidth of the atomic transition and a sensitive dependence of the measured OD on the relative detunings of cooling and detection light.

- **Parasitic effects caused by the coupling lattice**: Due to the fact that the near-resonant coupling lattice creates an attractive or repulsive potential for the atoms, it is important to measure the OD inside the lattice volume with a detection beam that is mode-matched with the lattice. An additional complication is that the coupling beam could in principle be involved into the EIT effect.

  Furthermore, the periodic atomic density pattern of the atoms in the lattice can lead to a photonic band gap for the detection light [188]. This leads to a reduced transmission of the detection light and an apparently larger OD.

The mentioned parasitic effects and the performance of the lock-in based OD measurements were investigated in detail. However, this topic is of very technical nature and will therefore only be discussed in appendix C.2. As shown there, the absolute value of the OD measurements has a systematic error between 200% and 300%. Yet, the parasitic effects described above can be regarded as constant in time for one specific experimental run and the relative behavior of the OD can be determined quite accurately. Nevertheless, the OD inside the lattice beam also behaves predictable according to the repulsive and attractive potential of the lattice beam. Hence, OD measurements inside the lattice volume also give reliable qualitative information on the atom number in the coupling lattice.
Using the OD detection beam (see appendix C.2), we could perform sweeps of the MOT parameters in order to generate a collapse of the atomic cloud into a very dense state. Although some effort was spent, we could not reproduce the generation of a *dark MOT*

[5] The small saturation power originates from the small detection beam waist $w_{\mathrm{det}} = w_{\mathrm{lat}} = 78\,\mu\mathrm{m}$.

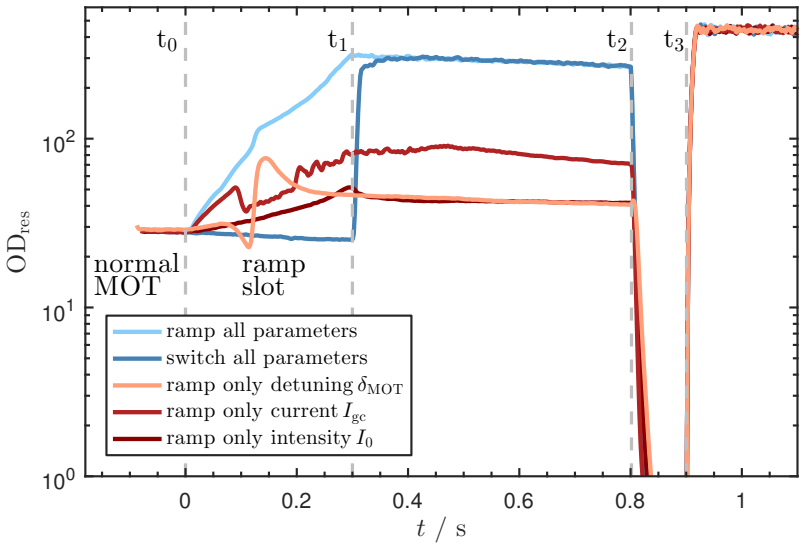

Figure 5.7: Generation of a MOT with very high OD for pulsed sympathetic cooling. Zero-span lock-in measurement of the OD during the collapse of the normal MOT into a high-density MOT state. $\mathrm{OD}_{\mathrm{res}}$ was calculated as described in appendix C.2 using the reference signal without atoms at $t_2 < t < t_3$, which corresponds to $\mathrm{OD} = \mathrm{OD}_{\mathrm{res}} = 0$. At $t = t_0$ the normal MOT parameters are ramped linearly to the optimized values (intensity $I_0 = 0.7 I_{\mathrm{max}} = 52.2\,\mathrm{mW/cm^2} \Rightarrow 0.05 I_{\mathrm{max}}$, gradient $5\,\mathrm{G/cm} \Rightarrow 45\,\mathrm{G/cm}$ with current $I_{\mathrm{gc}} = 10\,\mathrm{A} \Rightarrow 90\,\mathrm{A}$, detuning $\delta_{\mathrm{MOT}} = -2\pi \times 17.8\,\mathrm{MHz}(2.9\,\Gamma_{\mathrm{D_2}}) \Rightarrow -2\pi \times 37.8\,\mathrm{MHz}(6.2\,\Gamma_{\mathrm{D_2}})$). As described in the legend, either all or only one parameter is changed. The dark blue curve corresponds to a hard switching to the final parameters at $t = t_1$. At $t > t_3$ the detection light is switched off, which shows the maximum detectable OD. Detection parameters: OD beam modulation at 50 kHz, demodulator bandwidth $B_{\mathrm{d}} = 100\,\mathrm{Hz}$, detection beam power $P_{\mathrm{det}} \approx 100\,\mathrm{nW}$ with red detuning $\delta_{\mathrm{det}} = -2\pi \times 25.8\,\mathrm{MHz} = -4.3\,\Gamma_{\mathrm{D_2}}$, each zero-span trace averaged ten times.

by sweeping the repumping laser power as described in [102]. However, we have found an optimized parameter set which allows for a collapse of the MOT without changing the repumping power. For this, the MOT light intensity I_0, the detuning δ_{MOT} and the current I_{gc} for the magnetic field gradient are rapidly switched to a new parameter set, which is quoted in the caption of Figure 5.7. Interestingly, this rapid switching leads to the same final OD as a linear ramp of all three parameters. Hence, we only used the linear ramps for finding the optimal parameters with the largest final OD, while in the experiment we just perform a hard switching of the parameters. It is worth noting that the linear sweep of δ_{MOT} (see the orange curve in Figure 5.7) leads to a measured $\mathrm{OD}_{\mathrm{res}}$ with a dispersive feature which is centered exactly at $t \approx 0.1\,\mathrm{s}$ where the MOT frequency equals the detection beam frequency. This is another indication of EIT, as discussed further in appendix C.2. The high-density MOT state is an emergent phenomenon which can only be generated by changing all three parameters together: changing only one parameter at a time leads to final ODs that do not add up to the final value obtained by changing all three parameters. Furthermore, the final state can only be generated dynamically: if the final MOT parameters are adjusted from the beginning of the MOT loading cycle, no atoms can be trapped at all.

MOT configuration B. The high-density MOT, called *MOT configuration B* in the following, has a ten times larger OD than the normal MOT and a lifetime on the

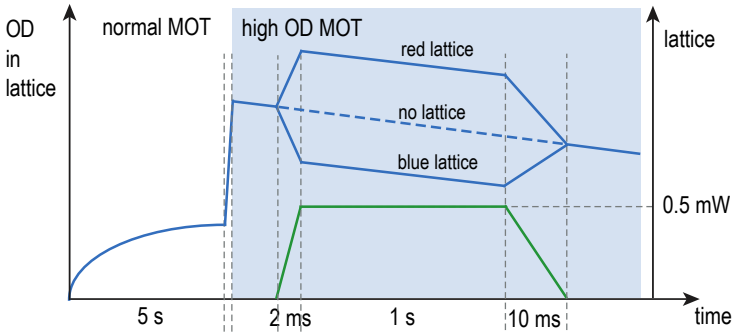

Figure 5.8: Experimental sequence for pulsed sympathetic cooling with a MOT. After loading the 3D MOT for about 5 s, the MOT parameters are switched to the optimized values for a high OD MOT, as described in Figure 5.7. After this, the MOT (MOT configuration B) is slowly decaying and the coupling lattice is quickly ramped up. Depending on the lattice detuning, the measured OD in the lattice volume is increased or decreased by the lattice potential. Ramping down the lattice after a sympathetic cooling period on the order of 1 s leads to the same OD that would be measured without the coupling lattice, as long as the lattice is sufficiently far-detuned so that the atom loss due to the lattice can be neglected.

order of 10 s (which reduces if a near-resonant coupling beam is switched on). The temperature of this MOT is $T_{\mathrm{MOT}} = 390(46)\,\mu\mathrm{K}$, which is about two times larger than in a normal MOT (see appendix C.1). Even though we do not fully understand the nature of the high-density MOT state, we find that it is an emergent, dynamical state which possesses a larger OD and larger sympathetic cooling rates, which are about two times larger than with a normal MOT in steady state sympathetic cooling.
A typical experimental sequence for pulsed sympathetic cooling with this MOT configuration B is shown in Figure 5.8. Due to the long lifetime of the MOT, the process is not as time critical as for the cooling with an optical molasses. The lattice is ramped up in 2 ms, which is also not very critical. We observe the same sympathetic cooling effect for faster switching or much slower ramping of the lattice power (as discussed more detailed in the next subsection). During the sympathetic cooling slot with a duration on the order of 1 s, the measured OD in the lattice volume is altered by the lattice beam, depending on the lattice detuning (further details in appendix C.2).

The influence of timing and experimental sequences

In contrast to the results published in [102], we do not observe any significant dependency of the sympathetic cooling performance on timing-related issues in the experimental sequences. For example, the compression of the atomic cloud before sympathetic cooling with an optical molasses did not improve Γ_{sym} (contrary to the results in [102]). Also for sympathetic cooling with a MOT, the state of the atomic cloud before the coupling slot does not seem to play a role. Furthermore, many different time sequences for the coupling lattice were tried without any improvement of Γ_{sym}. An overview of the tried sequences is shown in Figure 5.9.
As compared to [102], our maximum sympathetic cooling rate Γ_{sym} is about 15 times smaller [57]. This means that in our case, any effect of compressing the atomic cloud before the sympathetic cooling has already completely vanished before the coldest quasi

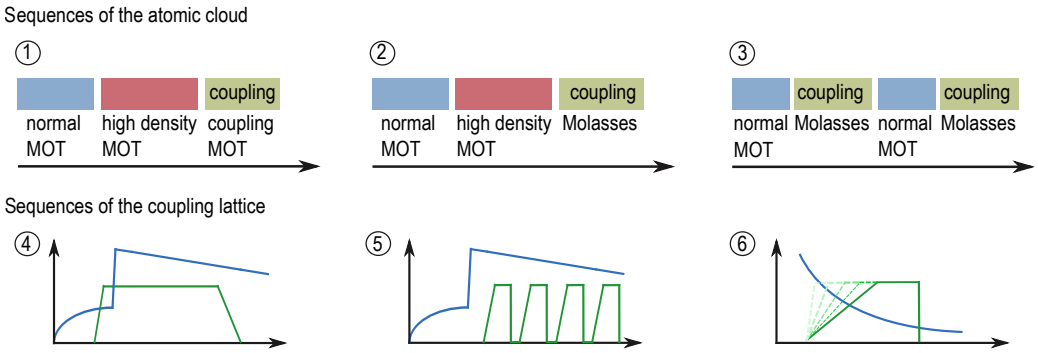

Figure 5.9: Different experimental sequences for sympathetic cooling. Sketch of the different experimental sequences that were tried for improving the performance of sympathetic cooling. None of them resulted in a significant increase of Γ_{sym}. **1**: three-step MOT sequence where the parameters of the second and third slot were changed systematically. **2**: MOT configuration B with subsequent sympathetic cooling with a molasses. **3**: quick cycle time $T_{\mathrm{cycle}} < 4\,\mathrm{s}$, which is much faster than the rethermalization time of the oscillator. **4**: ramping up the lattice before the MOT density is increased in MOT configuration B. **5**: pulsed ramping of the lattice in MOT configuration B. **6**: different ramping speed of the lattice during molasses. All axes are not to scale. The blue line indicates the atomic density and the green line indicates the coupling lattice power.

steady state temperature is reached. Therefore, even though a compression might be relevant for the very beginning of the cooldown process, it has no influence on the final temperature.

5.2.2 Sympathetic cooling in time domain

As described in section 5.1.1, the sympathetic cooling process can be treated as velocity-dependent feedback cooling. Hence, the time-dependent model in equation 4.24 can also be used for sympathetic cooling, by replacing the velocity-dependent feedback gain g_{v} with the sympathetic cooling gain g_{s} (see equation 5.11). Due to the fact that in our current system $g_s \ll g_{\mathrm{v,opt}}$, the sympathetic cooldown process happens on a much longer time scale than the optimal feedback cooling. Therefore, our typical zero-span demodulator bandwidth $B_{\mathrm{d}} \approx 200\,\mathrm{Hz}$ is sufficient to resolve the time evolution during sympathetic cooling without bandwidth limitations.

MOT cooling in time domain

The time evolution of the oscillator temperature $T_{\mathrm{mode}}(t)$ for pulsed sympathetic cooling with the MOT configuration B (see subsection 5.2.1) was compared to the time dependent model in equation 4.24. Figure 5.10 shows the fit result for the cooldown process and the rethermalization after the sympathetic cooling is switched off at $t = 1\,\mathrm{s}$ (by switching off the repumping laser for the atoms). All fits were performed with a simple least-square algorithm to the logarithmic data. At $t = 0$ the coupling lattice is quickly ramped up within 1 ms. The cooldown process for $t > 0$ can be fitted very well, which results in a sympathetic cooling gain of $g_{\mathrm{s}} = 75.7 \pm 0.5$ and a corresponding sympathetic cooling rate of $\Gamma_{\mathrm{sym}} = 11.6(2)\,\mathrm{Hz}$ (see equation 5.11). The final steady state temperature of the fit yields $T_{\mathrm{min}} = 24\,\mathrm{mK}$.

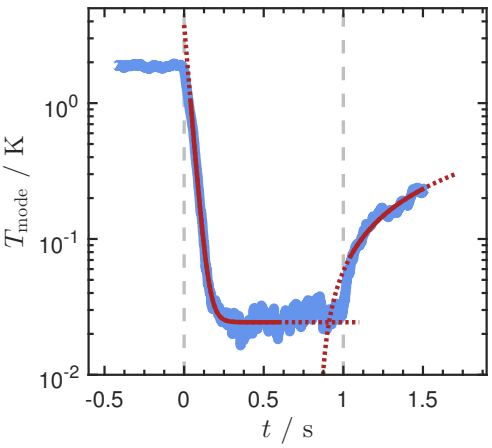

Figure 5.10: Sympathetic MOT cooling in time domain. Oscillator mode temperature T_{mode} during sympathetic cooling with MOT configuration B. The cooldown was fitted with equation 4.24, which yields $\Gamma_{\mathrm{sym}} = 11.6(2)\,\mathrm{Hz}$ and $T_{\mathrm{min}} = 24\,\mathrm{mK}$. The rethermalization was fitted using equation 4.25, which yields $\Gamma_{\mathrm{m}}^{\mathrm{heat}} = 0.204(2)\,\mathrm{Hz}$. The solid lines indicate the fitted intervals, the dashed lines indicate the extension of the fit function. Parameters: blue lattice detuning $\Delta_{2,3} = 2\pi \times 0.507\,\mathrm{GHz}$, $P_{\mathrm{lat}} = 0.5\,\mathrm{mW}$, $\omega_{\mathrm{a}} \approx 2.5\,\omega_{\mathrm{m}}$ (calibrated), optomechanical parameters shown in Table 3.1, each zero-span trace averaged 30 times, demodulator bandwidth $B_{\mathrm{d}} = 200\,\mathrm{Hz}$, total cycle time 8 s.

After the cooldown, the oscillator temperature is approximately constant, which shows that the MOT has a lifetime which is much longer than the time scale of the cooldown process. The rethermalization can also be fitted very well starting approximately 40 ms after the sympathetic cooling ends at $t = 1.04\,\mathrm{s}$. The faster increase of T_{mode} during these 40 ms could be explained by the fact that the coupling lattice was ramped down over 10 ms within this time interval. The fitted oscillator damping rate $\Gamma_{\mathrm{m}}^{\mathrm{heat}} = 0.204(2)\,\mathrm{Hz}$ is slightly larger than the value $\Gamma_{\mathrm{m}} = 0.154\,13(9)\,\mathrm{Hz}$ measured with ringdown measurements (see Table 3.1) and also as the value obtained by the rethermalization after feedback cooling (see Figure 4.10). The reason for this could be that the rethermalization in this experimental sequence was distorted by additional noise. For example, if the cavity was slightly blue detuned, which can be caused by a thermal drift induced by the lattice beam, there might have been a small optomechanical heating rate $\Gamma_{\mathrm{opt}} < 0$ and a slightly increased rethermalization rate with a larger effective Γ_{m} (see Figure 3.5).

Molasses cooling in time domain

Contrary to the sympathetic cooling with a MOT, the atomic density in a molasses can not be regarded as constant during the sympathetic cooldown process. However, we observe that the atom number that participates in the sympathetic cooling changes only by a factor of 20% until the coldest temperature is reached, as discussed in the following.

Figure 5.11 shows the cooldown process during sympathetic cooling with an optical molasses. All fits were performed with a simple least-square algorithm to the logarithmic data. The initial cooldown slope can be fitted well with the model in equation 4.24, which yields $g_{\mathrm{s}} = 167 \pm 3$ and $\Gamma_{\mathrm{sym}} = 25.6(4)\,\mathrm{Hz}$. Shortly before this fit function reaches its coldest temperature, the temperature starts to increase again, which can be well modeled by assuming a time dependent sympathetic cooling rate $\Gamma_{\mathrm{sym}}(t)$ and the corresponding temperature evolution according to the steady state equation 5.14. Even though the temperature changes during this interval $0.15\,\mathrm{s} < t < 1\,\mathrm{s}$ is not constant,

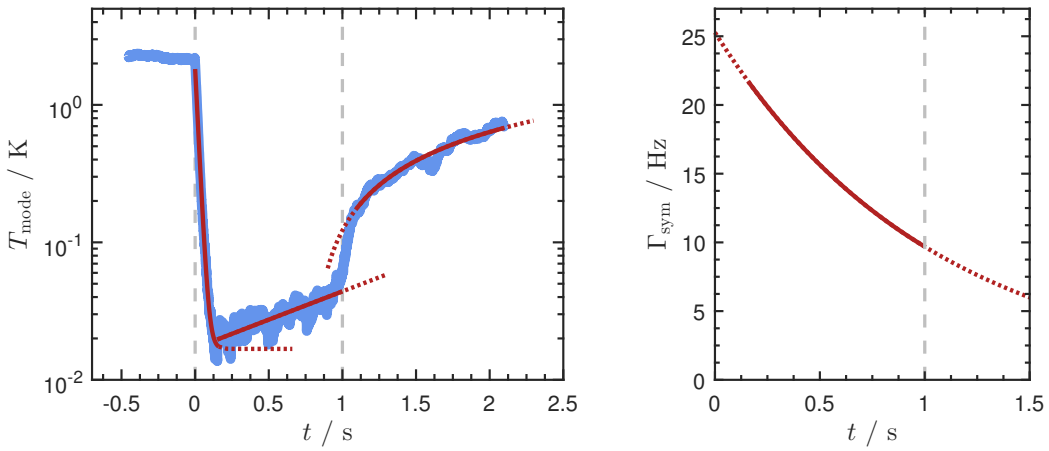

Figure 5.11: Sympathetic molasses cooling in time domain. Left: oscillator mode temperature T_{mode} during sympathetic cooling with an optical molasses. At $t = 0$ the coupling lattice is ramped up within 200 µs before the molasses starts (unlike shown in Figure 5.4), at $t = 1\,\mathrm{s}$ the molasses light is quickly switched off and the lattice is kept on. Cooldown and rethermalization fits as described in Figure 5.10 yield $g_{\mathrm{s}} = 167 \pm 3$ and $\Gamma_{\mathrm{sym}} = 25.6(4)\,\mathrm{Hz}$. The interval $0.15\,\mathrm{s} < t < 1\,\mathrm{s}$ was fitted assuming a time dependent $\Gamma_{\mathrm{sym}}(t)$ in equation 5.14. The minimum temperature is $T_{\mathrm{min}} = 20\,\mathrm{mK}$. Right: fitted exponential decay of $\Gamma_{\mathrm{sym}}(t)$ in the interval $0.15\,\mathrm{s} < t < 1\,\mathrm{s}$ with a time constant $\tau_{\mathrm{sym}} = 1.04(2)\,\mathrm{s}$. Parameters: red lattice detuning $\Delta_{2,1} = -2\pi \times 1.35\,\mathrm{GHz}$ (locked at $n_{\mathrm{FSR}} = -2$), $P_{\mathrm{lat}} = 0.56\,\mathrm{mW}$, $\omega_{\mathrm{a}} = 1.48\,\omega_{\mathrm{m}}$ (calibrated), optomechanical parameters shown in Table 3.1, each zero-span trace averaged 25 times, demodulator bandwidth $B_{\mathrm{d}} = 300\,\mathrm{Hz}$, total cycle time 8.8 s.

this steady state model is a good approximation, since the time scale of the temperature change is much slower than the ringdown time Γ_{m}^{-1}. Assuming that the change of $\Gamma_{\mathrm{sym}}(t)$ is related to atom loss in the coupling lattice due to the decay of the molasses, this change can be approximated as $\Gamma_{\mathrm{sym}}(t) \sim N_{\mathrm{lat}}(t) \sim e^{-t/\tau_{\mathrm{sym}}}$ (see equation 5.16). The fit with this model yields a time constant $\tau_{\mathrm{sym}} = 1.04(2)\,\mathrm{s}$, which agrees well to the typical life time of the optical molasses.

The rethermalization of the oscillator temperature can also be fitted very well starting approximately 100 ms after the sympathetic cooling ends at $t = 1.1\,\mathrm{s}$. Similar to the MOT measurement presented above, the fitted oscillator damping rate $\Gamma_{\mathrm{m}}^{\mathrm{heat}} = 0.211(2)\,\mathrm{Hz}$ is slightly larger than the value measured with ringdown measurements (see Table 3.1) and also as the value obtained by the rethermalization after feedback cooling (see Figure 4.10). The reason for this could be that the rethermalization in this experimental sequence was distorted by the additional noise of the coupling laser or optomechanical heating as described above.

5.2.3 Resonant hybrid coupling

As described in section 5.1.1, the sympathetic cooling mechanism is based on the resonance between the atomic oscillations in the coupling lattice with frequency ω_{a} and the oscillations of the mechanical oscillator with frequency ω_{m}. Due to the fact that the atomic cloud has a diameter much larger than the size of the coupling beam and $\omega_{\mathrm{a}}(r)$ depends on the radial distance r from the beam axis, the predicted sympathetic cooling rate $\Gamma_{\mathrm{sym}}^{\mathrm{int}}(\omega_{\mathrm{a}})$ has a specific resonance behavior depending on the maximum

trapping frequency ω_a[6] on the beam axis (see Figure 5.2). This resonance behavior of $\Gamma_{sym}(\omega_a)$ was investigated in detail by sweeping the atomic trapping frequency ω_a. The measurements were performed by sweeping either the lattice power P_{lat} or the lattice detuning Δ. Both methods are equivalent for the coupling mechanism, but they lead to different parasitic effects. For example, a large P_{lat} leads to heating of the MiM system and thermal drifts of the cavity length which can distort the measurement. On the other hand, sweeping Δ leads to large atomic scattering for small detunings, which

[6]Note that in the calculation of Γ_{sym}^{int}, ω_a is denoted by $\omega_{a,0}$. Furthermore, the expression Γ_{sym}^{int} for the sympathetic cooling rate will only be used for an explicit reference to this theoretical prediction.

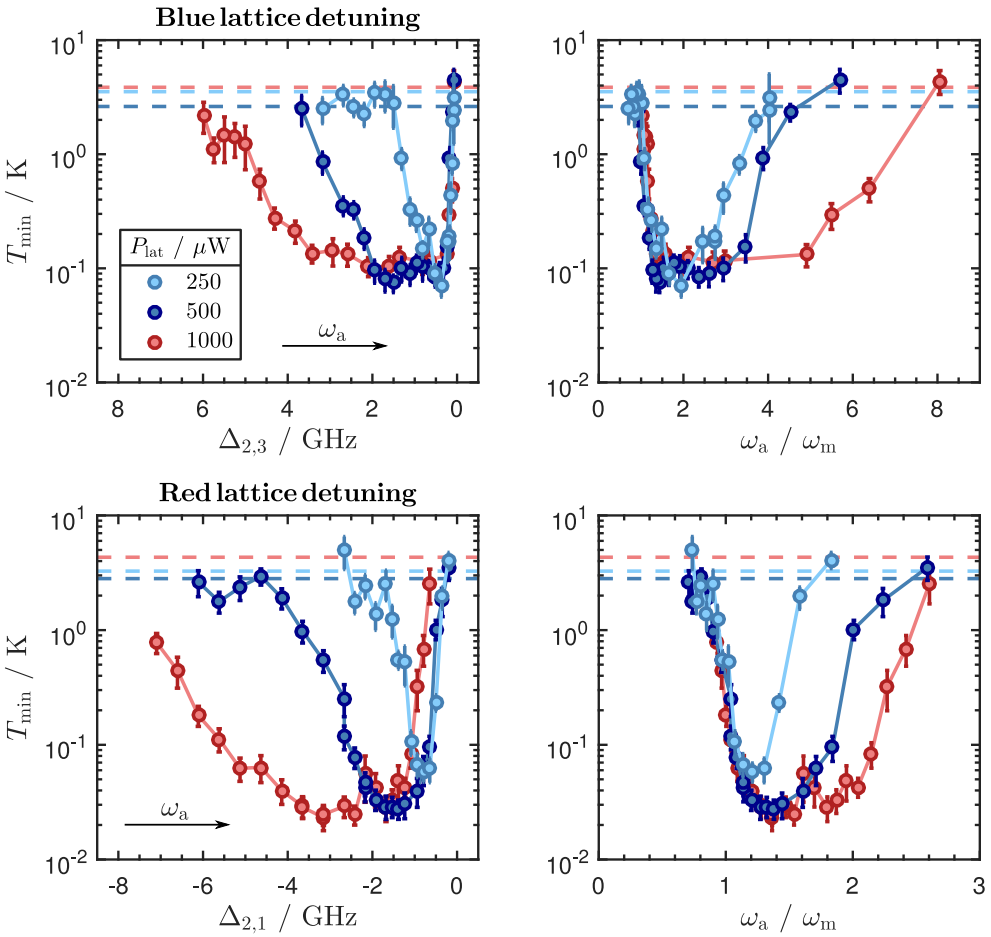

Figure 5.12: Resonance behavior of sympathetic molasses cooling. Minimum oscillator mode temperature T_{min} during sympathetic cooling with an optical molasses for different blue (top line) and red (bottom line) lattice detunings and for different lattice powers P_{lat}. The right column shows T_{min} as a function of the corresponding (calibrated) atomic trapping frequency ω_a in units of the oscillator frequency ω_m. Note that in all four figures ω_a increases from left to right. The dashed lines indicate the measured bath temperatures T_{bath}, determined by averaging $T_{mode}(t)$ before the cooldown. The blue detunings $\Delta_{2,3}$ are with respect to the $F = 3$ level of the D_2 line, red detunings $\Delta_{2,1}$ with respect to $F = 1$. However, ω_a was calculated including all hyperfine levels. Molasses parameters: see subsection 5.2.1. Optomechanical system parameters summarized in Table 3.1. Sequence parameters, data acquisition and determination of T_{min} similar as described in Figure 5.5.

can drastically reduce Γ_{sym}. Furthermore, some optical elements in the beam path of the lattice are strongly frequency dependent and must be adjusted for different lattice frequencies (for example the thermal polarization control described in appendix A.1). In order to minimize these parasitic effects in the specific experiment configuration, the sweeps of the trapping frequency ω_{a} presented in this subsection were performed either by sweeping Δ or by sweeping P_{lat}.

Resonance behavior of molasses cooling

In order to measure the sympathetic cooling rate Γ_{sym} as a function of the atomic trapping frequency ω_{a} for cooling with an optical molasses, different lattice detunings were adjusted within a range of several gigahertz around the atomic transition[7]. For each lattice detuning the oscillator mode temperature $T_{\mathrm{mode}}(t)$ was measured in zero-span mode (as described in section 4.4.1) and the minimum temperature T_{min} during the sympathetic cooldown was determined as shown in Figure 5.5. This measurement was performed for three different lattice powers P_{lat} for each value of the detuning. Figure 5.12 shows the minimum temperatures during sympathetic molasses cooling for red and blue lattice detunings. It shows that the coldest temperatures are reached for red lattice detunings. This is most likely related to the attractive lattice potential for red detunings, which leads to larger atom numbers and accordingly a larger sympathetic

[7]The lattice frequencies were adjusted manually with a precision of $\approx 10\,\mathrm{MHz}$ relative to a start frequency f_0, which was known with an absolute accuracy of 3 MHz, as described in section 2.4.1.

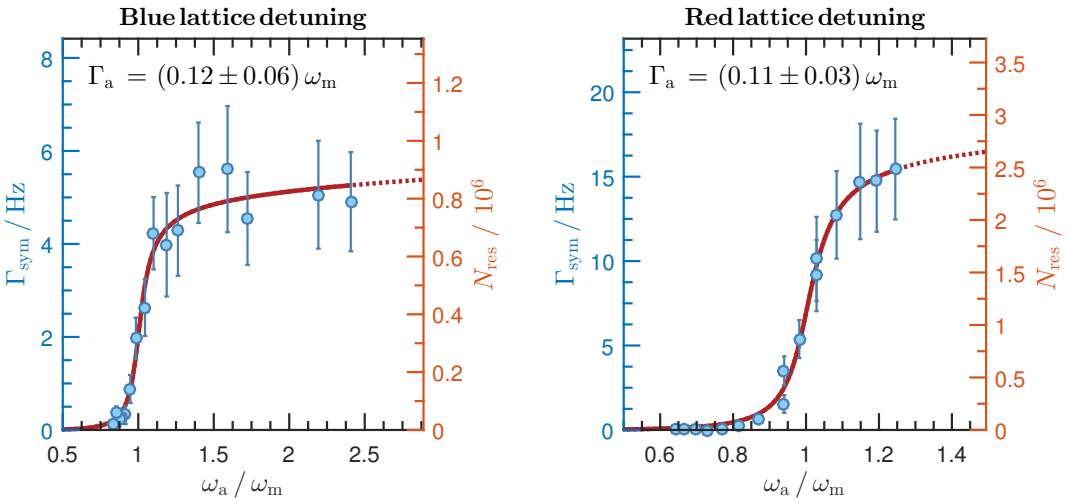

Figure 5.13: Resonance behavior of Γ_{sym} for molasses cooling. Sympathetic cooling rate Γ_{sym} calculated with equation 5.14 using the temperatures T_{min} and T_{bath} from Figure 5.12 (using the data for $P_{\mathrm{lat}} = 1\,\mathrm{mW}$ from the blue detunings and the data from $P_{\mathrm{lat}} = 0.5\,\mathrm{mW}$ from the red detunings). The data points for large ω_{a} with decreasing Γ_{sym} were omitted because the effect of light scattering is not included into the model. The resonant atom number N_{res} was calculated from Γ_{sym} according to equation 5.18. The fits according to equation 5.16 (red lines) yield an atomic cooling rate Γ_{a}, which is displayed above. The x axis was rescaled using the fit function, yielding the correction factors 0.81 ± 0.02 (left) and 0.903 ± 0.007 (right), which represents the deviation from the lattice calibration (see section 2.4.2). Parameters as described in Figure 5.12.

cooling rate. This dependency of the atom number in the lattice volume on the lattice detuning was also confirmed by OD measurements, as discussed in appendix C.2.

Figure 5.12 also shows that for each lattice power P_{lat}, there exists an optimal detuning Δ where the lowest temperatures T_{min} are achieved. This means that unlike expected by the theoretical prediction of $\Gamma_{\mathrm{sym}}^{\mathrm{int}}$ (see Figure 5.2), the sympathetic cooling rate decreases again for small detunings and large atomic trapping frequencies ω_{a}. This effect clearly gets worse for small lattice powers, as can be seen in the right column of Figure 5.12. This indicates that increased light scattering is causing the increase of T_{min} for large ω_{a}, because it is proportional to Δ^2 and a small P_{lat} corresponds to a small detuning Δ, as described in section 2.4.1. Most likely, the small detunings lead to an increased atomic light scattering, which causes atom loss in the coupling beam and a reduced sympathetic cooling rate. However, this assumption could not be proven independently, especially not by a corresponding OD measurement of the atom number.

Nevertheless, the measurement in Figure 5.12 also allows for the verification of the resonance behavior of the sympathetic cooling rate Γ_{sym}, as shown in Figure 5.13. It shows that the measured data can be fitted very well with the theoretical prediction of the ensemble-integrated sympathetic cooling rate $\Gamma_{\mathrm{sym}}^{\mathrm{int}}$ in equation 5.16. The fit allows for a determination of the atomic cooling rate Γ_{a}, which yields the same result for blue and red lattice detuning, as it is expected since it should only depend on the molasses parameters, which were the same for both measurements. In contrast to the results published in [102], Γ_{sym} can not be regarded as a step function, as it is diverging for large ω_{a}. This is because in our case Γ_{a} is not much smaller than ω_{m}.

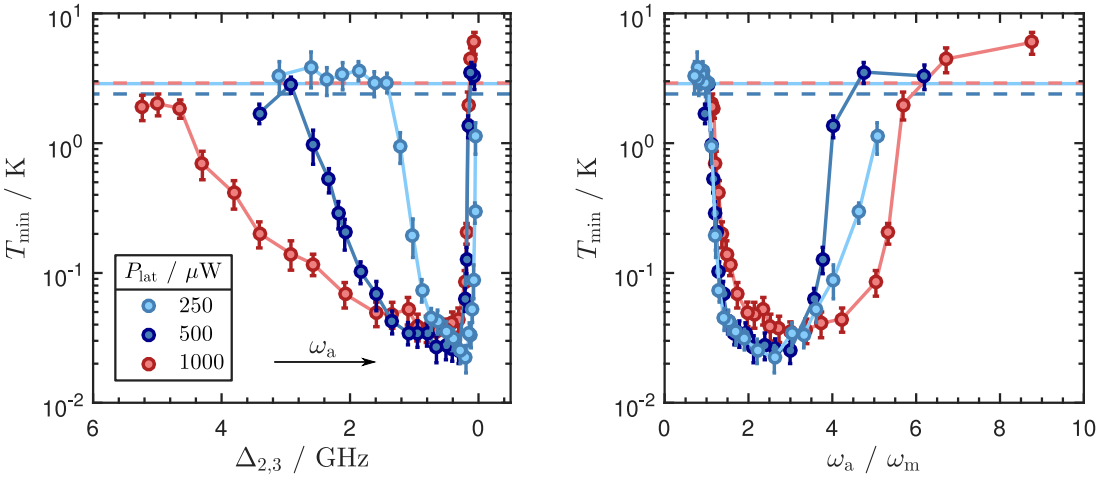

Figure 5.14: Resonance behavior of sympathetic MOT cooling for a blue detuned lattice. Minimum oscillator mode temperature T_{min} during sympathetic cooling with MOT configuration B for different blue lattice detunings and for different lattice powers P_{lat}. The right figure shows T_{min} as a function of the corresponding (calibrated) atomic trapping frequency ω_{a} in units of the oscillator frequency ω_{m}. Note that in both figures ω_{a} increases from left to right. The dashed lines indicate the measured bath temperatures T_{bath}, determined by averaging $T_{\mathrm{mode}}(t)$ before the cooldown. The blue detunings $\Delta_{2,3}$ are with respect to the $F = 3$ level of the D_2 line. However, ω_{a} was calculated including all hyperfine levels. MOT sequence parameters: see subsection 5.2.1. Optomechanical system parameters summarized in Table 3.1. Data acquisition and determination of T_{min} similar as described in Figure 5.5.

Resonance behavior of MOT cooling

The same measurement as described above was performed for sympathetic cooling with MOT configuration B (see subsection 5.2.1). In contrast to sympathetic cooling with a molasses, cooling with this MOT configuration only works with blue lattice detunings, because for red lattice detunings we observe heating instead of cooling. As discussed in subsection 5.1.3, this heating effect for red lattice detunings and large atomic densities is predicted by the theoretical model of atomic back-action and the resulting phase lag of the coupling laser light [103, 104, 186]. For MOT configuration A, which has a smaller atomic density, this heating effect could be investigated more systematically, as presented at the end of this subsection.

Nevertheless, the sympathetic MOT cooling with blue lattice detunings yields similar results as the molasses cooling, as shown in Figure 5.14. Similar to molasses cooling with a red detuned lattice, the lowest achievable oscillator temperature here is also $T_{\mathrm{min}} \approx 20\,\mathrm{mK}$. As discussed above, the vanishing sympathetic cooling for large ω_{a} is most likely related to atomic light scattering, which could not be proven by a separate measurement.

The main difference between this measurement and sympathetic molasses cooling is a significant difference in the lowest achievable temperature for different lattice powers P_{lat} in the regime of $\omega_{\mathrm{m}} < \omega_{\mathrm{a}} < 3\,\omega_{\mathrm{m}}$. Fits to the theoretical model of $\Gamma_{\mathrm{sym}}^{\mathrm{int}}$ (see equation 5.16) suggest that the extracted atomic cooling rates Γ_{a} differ for the different lattice depths, as shown in Figure 5.15. However, the confidence interval of the fit for Γ_{a} is very large, so that this assumption remains unproven. Furthermore, it is unclear which mechanism should lead to a deviation of the atomic cooling rate depending on the lat-

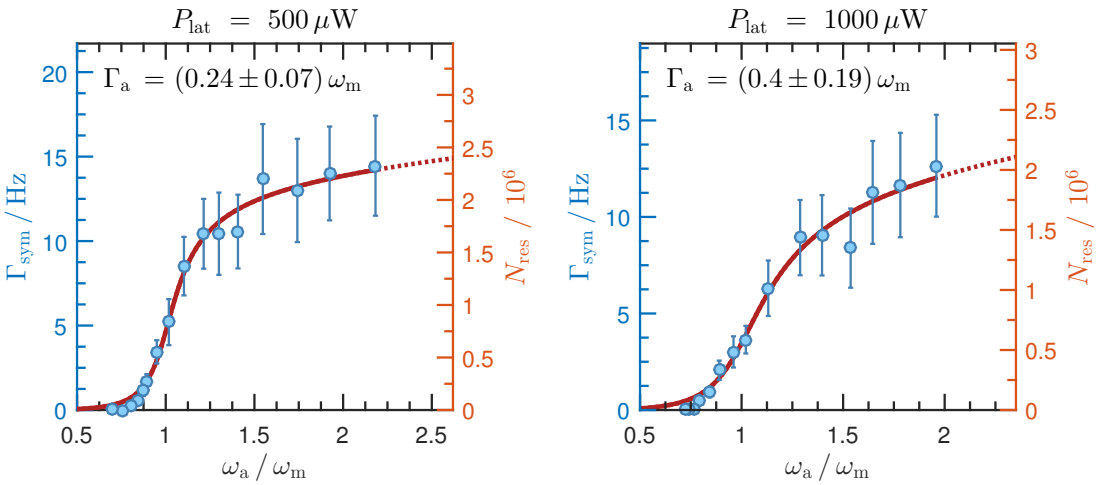

Figure 5.15: Resonance behavior of Γ_{sym} for MOT cooling. Sympathetic cooling rate Γ_{sym} calculated with equation 5.14 using the temperatures T_{min} and T_{bath} from Figure 5.14 for $P_{\mathrm{lat}} = 0.5\,\mathrm{mW}$ (left) and for $P_{\mathrm{lat}} = 1\,\mathrm{mW}$ (right). The data points for large ω_{a} with decreasing Γ_{sym} were omitted. The resonant atom number N_{res} was calculated from Γ_{sym} according to equation 5.18. The fits according to equation 5.16 (red lines) yield an atomic cooling rate Γ_{a}, which is displayed above. The x axis was rescaled using the fit function, yielding the correction factors 0.73 ± 0.02 (left) and 0.65 ± 0.04 (right), which represents the deviation from the lattice calibration (see section 2.4.2). Parameters as described in Figure 5.14.

tice power. Another possibility is that the particular measurement for $P_{\mathrm{lat}} = 1000\,\mu\mathrm{W}$, which differs from the measurements for the two smaller powers, was somehow corrupted. An indication for this assumption is that the lattice alignment was significantly worse for the measurement with $P_{\mathrm{lat}} = 1000\,\mu\mathrm{W}$ (see caption of Figure 5.15). This could lead to a larger beam imbalance between the two lattice beams, which causes an instability in the hybrid system, as discussed in subsection 5.1.3.
The most remarkable result from this measurement is that the sympathetic cooling rates Γ_{sym} and the calculated number of resonantly coupled atoms $N_{\mathrm{res}} \sim N_{\mathrm{lat}}$ (see equation 5.18) are only about three times larger than the values obtained for sympathetic molasses cooling for blue lattice detunings (see Figure 5.13). However, the atom number N_{lat} in MOT configuration B, which was optimized for a maximal atomic density, should be much larger than in an optical molasses. Since Γ_{sym} is expected to be proportional to N_{lat} (see equations 5.17) and should therefore be much larger in a MOT, these measurements indicate that additional effects in the coupling lattice play a role that were not included into the model. As presented later in subsection 5.2.4, further measurements have proven that this is not related to a non-linear dependency of Γ_{sym} on the atom number N_{lat}, which would be the case for the hybrid instability discussed in subsection 5.1.3.
A possible explanation for the mentioned discrepancy could be that Γ_{sym} for MOT configuration B is somehow limited by additional parasitic effects that counteract the cooling mechanism. This could mean that without these parasitic effects, Γ_{sym} would be much larger for MOT cooling than for molasses cooling, as it would be expected by the model. For example, the classical model for Γ_{sym} assumes that the atomic ensemble is at zero temperature and neglects the noise on the coupling beam which is related to a finite temperature of the atoms. The optical molasses is about 40 times colder than the cloud in MOT configuration B (see section 2.2 and appendix C.1), which could possibly explain why molasses cooling leads to comparable sympathetic cooling rates as achieved by MOT cooling with much larger atomic densities.

Heating and instability of MOT cooling

For sympathetic cooling with a MOT, we observe that the cooling can turn into heating if the lattice is red detuned. As described above, the MOT configuration B with a large atomic density always shows this behavior for red lattice detunings, which agrees well with the theoretical model of atomic back-action discussed in subsection 5.1.3. However, for steady state sympathetic cooling with MOT configuration A (see subsection 5.2.1) the heating only occurs above a critical value of ω_{a}, which allows for a more systematic investigation of the hybrid instability.
As shown in Figure 5.16, the oscillator mode temperature $T_{\mathrm{mode}}(\omega_{\mathrm{a}})$ behaves similar for the red and blue lattice detunings, until the system is abruptly driven into limit-cycle oscillations above a critical value of $\omega_{\mathrm{a}} \approx 1.25\,\omega_{\mathrm{m}}$ for the red detuning. By contrast, sympathetic cooling for the blue detuning is also possible for much larger values of ω_{a}. This could be explained by the smaller effects of atomic back-action as compared to red lattice detunings, which are the origin of the hybrid instability [103, 104, 186].
The resonance behavior of Γ_{sym} for the blue lattice detuning is similar to the measurements presented above and can be evaluated in the same manner as described above.

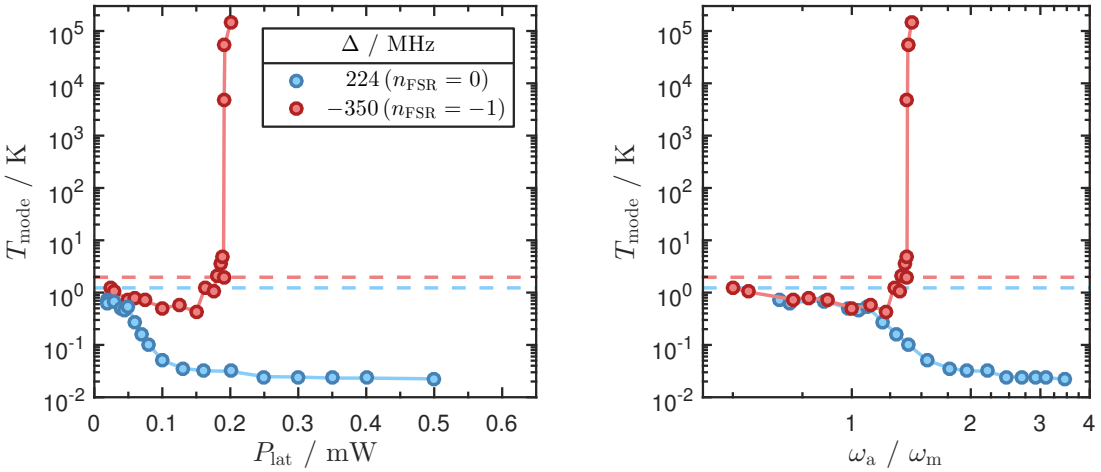

Figure 5.16: Instability in the hybrid coupling mechanism. Oscillator mode temperature T_{mode} for coupling to the continuously loaded MOT configuration A (see subsection 5.2.1) using different coupling lattice powers P_{lat} and two different lattice detunings Δ. The blue detuning refers to the $F = 3$ level of the D_2 line, the red detuning to the $F = 1$ level. The right figure shows T_{min} as a function of the corresponding (calibrated) atomic trapping frequency ω_{a} in units of the oscillator frequency ω_{m}, which was calculated including all hyperfine levels and the lattice calibration (see Table 2.4.2). For both detunings sympathetic cooling is visible, until the cooling with the red lattice detuning abruptly turns into heating at $\omega_{\mathrm{a}} \approx 1.25\,\omega_{\mathrm{m}}$. The dashed lines indicate the measured bath temperatures $T_{\mathrm{bath}} = T_{\mathrm{mode}}(P_{\mathrm{lat}} = 0)$. Note that in the case of heating, the oscillator performs limit-cycle oscillations and T_{mode} is not well defined. MOT parameters and data acquisition as described in subsection 5.2.1. Optomechanical system parameters summarized in Table 3.1.

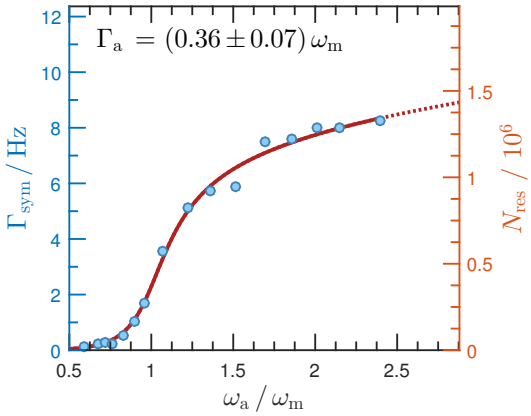

Figure 5.17: Resonance behavior of Γ_{sym} for steady state MOT cooling. Sympathetic cooling rate Γ_{sym} calculated with equation 5.14 using the temperatures T_{min} and T_{bath} from Figure 5.16 for the blue lattice detuning. The resonant atom number N_{res} was calculated from Γ_{sym} according to equation 5.18. The fit according to equation 5.16 (red line) yields the atomic cooling rate Γ_{a} displayed in the figure. The x axis was rescaled using the fit function, yielding the correction factor 0.69±0.02, which represents deviation from the optimal lattice alignment for this particular measurement (see section 2.4.2). Parameters as described in Figure 5.16.

The result is shown in Figure 5.17. One can see that the maximal sympathetic cooling rate Γ_{sym} is about a factor of two times smaller than the maximum value for MOT configuration B, which is most likely related to the different atomic densities of the two MOT configurations. Furthermore, the atomic cooling rate Γ_{a} obtained by the fit to Γ_{sym} lies within error bounds of the values obtained for MOT configuration B, which is about two times larger than Γ_{a} for molasses cooling (see Figure 5.13).

5.2.4 Influence of the atom number

In order to investigate the dependency of the sympathetic cooling rate Γ_{sym} on the number of atoms that participate in the sympathetic cooling process, the size of the atomic cloud was varied by systematical changes of the MOT loading time. Furthermore, the OD detection beam described in appendix C.2 was used to obtain quantitative results for the atom number N_{lat} in the lattice volume. Since this beam is mode matched with the coupling lattice, the effect of the repulsive or attractive potential for the atoms generated by the near-resonant lattice can be taken into account. Moreover, the detection beam allows for evaluating the OD at different times during the sympathetic cooling process. These measurements were performed for sympathetic MOT cooling and molasses cooling, which will be discussed in the following.

OD measurement for sympathetic MOT cooling

The MOT loading time t_{MOT} in the sequence for MOT configuration B (see Figure 5.8) was systematically altered in a cycled sympathetic cooling experiment. Figure 5.18

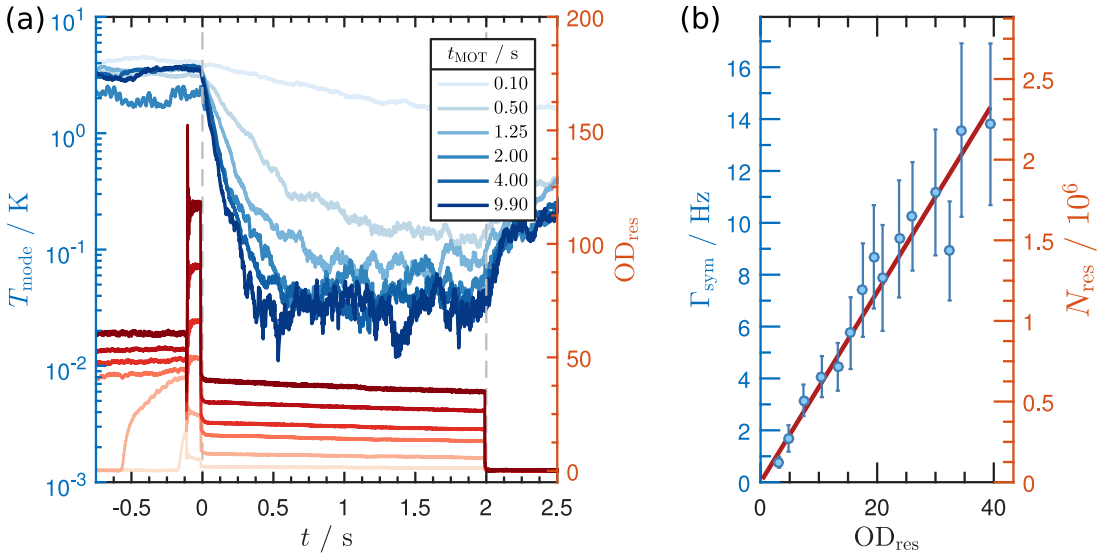

Figure 5.18: Sympathetic MOT cooling for different MOT lading times. Left: oscillator mode temperature $T_{\mathrm{mode}}(t)$ for sympathetic cooling with MOT configuration B and different loading times t_{MOT} in the beginning of the sequence (see Figure 5.8). Also shown is the optical density $\mathrm{OD}_{\mathrm{res}}$ in the lattice volume, measured with a mode matched detection beam (see appendix C.2). At $t = -0.1\,\mathrm{s}$ the initial MOT parameters are quickly changed to the high density MOT parameters and at $t = 0$ the lattice is ramped up within 2 ms. At $t = 2\,\mathrm{s}$ the repumping laser for the atoms and the lattice are quickly switched off. **Right:** Sympathetic cooling rate Γ_{sym} as a function of $\mathrm{OD}_{\mathrm{res}}$, which was averaged during the sympathetic cooling phase $0 < t < 2\,\mathrm{s}$. The red solid line is a linear fit to Γ_{sym}, which was calculated with equation 5.14 using the temperatures T_{min} and T_{bath} that were obtained as described in Figure 5.5. The resonant atom number N_{res} was calculated from Γ_{sym} according to equation 5.18. Parameters: blue lattice detuning $\Delta_{2,3} = 2\pi \times 0.48\,\mathrm{GHz}$, $P_{\mathrm{lat}} = 0.35\,\mathrm{mW}$, $\omega_{\mathrm{a}} = 2.1\,\omega_{\mathrm{m}}$ (calibrated), optomechanical parameters shown in Table 3.1, each zero-span trace averaged 20 times, demodulator bandwidths $B_{\mathrm{d,T}} = 300\,\mathrm{Hz}$ (temperature) and $B_{\mathrm{d,O}} = 3\,\mathrm{kHz}$ (OD), OD beam blue detuned at $\delta_{\mathrm{det}} = 2\pi \times 24.2\,\mathrm{MHz} = 4\,\Gamma_{\mathrm{D_2}}$ with $P_{\mathrm{det}} \approx 350\,\mathrm{nW}$, total cycle time 21.5 s.

(a) shows the mode temperature of the oscillator $T_{\mathrm{mode}}(t)$ and the OD in the lattice volume during sympathetic cooling, which were acquired simultaneously.[8]
The measurement shows that when the MOT parameters are changed for creating the high density MOT at $t = -0.1\,\mathrm{s}$, the desired compression only works for large loading times t_{MOT}. By contrast, for a small t_{MOT} the OD actually gets smaller when the MOT parameters are changed. This non-linear dependency of the final OD on the initial OD in the normal MOT is related to the complex behavior of this MOT configuration B, as discussed in subsection 5.2.1.
When the coupling lattice is quickly ramped up at $t = 0$, the OD in the lattice volume is reduced by a factor of three, which holds for all initial ODs and is related to the repulsive potential of the blue detuned lattice beam, as shown in appendix C.2. After this, the lattice power P_{lat} is kept constant for 2 s and the mechanical oscillator is sympathetically cooled with a constant cooling rate Γ_{sym}, as the measured OD indicates a quite constant atom number in this time interval.
Figure 5.18 (b) shows that Γ_{sym} depends linearly on the OD, which is proportional to the atom number N_{lat} in the lattice volume. Hence, Γ_{sym} is proportional to N_{lat} as predicted by the model in equation 5.16. As already mentioned above, this agreement with the model indicates that non-linear effects in the sympathetic cooling process like the hybrid instability discussed in subsection 5.1.3 do not play a role in this parameter regime. If the atom number in the lattice volume is calculated from the measured OD (see equation C.2), the result is in good qualitative agreement with the resonant atom number N_{res}, which was calculated from Γ_{sym} (see equation 5.18).

OD measurement for sympathetic molasses cooling

A similar measurement as described above was performed for sympathetic cooling with an optical molasses. However, in this measurement the atom number in the molasses was altered by a combination of MOT loading time and power of the resonant beam which transfers the atoms from the 2D MOT into the 3D MOT (see Figure 2.3). Therefore, no single parameter can be used as a legend for the time traces in Figure 5.19. However, the increasing MOT size is indicated by the color code, which depicts large MOT samples in dark colors and small samples in light colors.
We observe that within the first 100 ms of the molasses phase, the measured OD decays much faster than Γ_{sym}, which can be seen in a comparable measurement in Figure 5.11. This is an indication for a distorted OD measurement during the change of the laser cooling parameters from the MOT to the molasses at $t = 0$, where also the coupling lattice is switched on. Details on the various parasitic effects of this parameter change on the OD measurement can be found in appendix C.2.
Nevertheless, the OD before the molasses phase is measured with constant laser cooling parameters and without the coupling lattice. Hence, this OD value is a good qualitative measure of the number of atoms that participate in the sympathetic cooling process and was therefore used in the analysis, similar as in [102]. Plotting these OD values against the measured sympathetic cooling rate yields the same linearity $\Gamma_{\mathrm{sym}} \sim \mathrm{OD} \sim N_{\mathrm{lat}}$ as for MOT cooling, which is shown on the right side of Figure 5.19.

[8] Our lock-in amplifier has six demodulators for simultaneous data acquisition, see Figure 4.8.

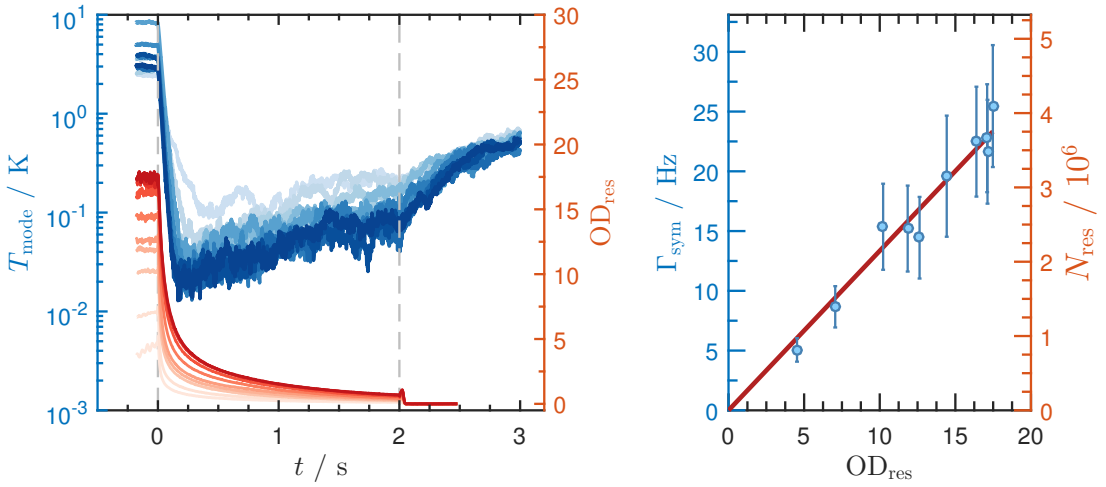

Figure 5.19: Sympathetic molasses cooling for different MOT lading times. Left: oscillator mode temperature $T_{\mathrm{mode}}(t)$ for sympathetic cooling with an optical molasses and different loading times t_{MOT} in the beginning of the sequence (see Figure 5.4). Also shown is the optical density $\mathrm{OD}_{\mathrm{res}}$ in the lattice volume, measured with a mode matched detection beam (see appendix C.2). At $t = 0$ the lattice is ramped up within 200 µs before the molasses starts (unlike depicted in Figure 5.4). At $t = 2\,\mathrm{s}$ the repumping laser for the atoms and the lattice are quickly switched off. **Right:** Sympathetic cooling rate Γ_{sym} as a function of $\mathrm{OD}_{\mathrm{res}}$, which was averaged within a short interval $t_0 < t < 0$ before the molasses phase. The red solid line is a linear fit to Γ_{sym}, which was calculated with equation 5.14 using the temperatures T_{min} and T_{bath} that were obtained as described in Figure 5.5. The resonant atom number N_{res} was calculated from Γ_{sym} according to equation 5.18. **Parameters**: red lattice detuning $\Delta_{2,1} = -2\pi \times 1.56\,\mathrm{GHz}$, $P_{\mathrm{lat}} = 0.5\,\mathrm{mW}$, $\omega_{\mathrm{a}} = 1.3\,\omega_{\mathrm{m}}$ (calibrated), optomechanical parameters shown in Table 3.1, each zero-span trace averaged 25 times, demodulator bandwidths $B_{\mathrm{d,T}} = 200\,\mathrm{Hz}$ (temperature) and $B_{\mathrm{d,O}} \approx 200\,\mathrm{Hz}$ (OD), OD beam red detuned at $\delta_{\mathrm{det}} = -2\pi \times 5.8\,\mathrm{MHz} = 0.95\,\Gamma_{\mathrm{D_2}}$, total cycle time 20.9 s.

In this measurement our maximum value of the sympathetic cooling rate $\Gamma_{\mathrm{sym}} = 23.3(14)\,\mathrm{Hz}$ was achieved, which was obtained by the linear fit to the measured Γ_{sym}. The corresponding hybrid cooperativity according to equation 5.21 is $C_{\mathrm{hybrid}} = 151 \pm 9$. The minimum mode temperature of the mechanical oscillator is $T_{\mathrm{min}} = 21(4)\,\mathrm{mK}$ (the statistical error is quoted, not the systematic error of the homodyne calibration).

5.2.5 Feedback-assisted sympathetic cooling

The experimental results in the previous subsections can be regarded as a characterization of the hybrid coupling mechanism, which shows that for our system $1 \ll C_{\mathrm{hybrid}} \ll \bar{n}_{\mathrm{th}}$. This means that we operate far outside the strong coupling regime and ground state cooling of the mechanical oscillator by sympathetic cooling or coherent dynamics of the hybrid system are not possible [31]. However, the combination of feedback cooling with sympathetic cooling may relax the conditions for quantum mechanical state swaps between the two parts of the hybrid system [34]. In this way, it might be possible to create an atomic-mechanical quantum hybrid system through feedback cooling of the mechanical oscillator.
In view of these exciting prospects, we tested the experimental feasibility of combining

the hybrid coupling mechanism with feedback cooling of the mechanical oscillator. For this, the oscillator was first feedback cooled into a steady state with a reduced mode temperature, as described in section 4.4. Subsequently, sympathetic cooling with a MOT was additionally switched on.

The main difficulty of the experimental sequence for combined feedback cooling is the data acquisition of the oscillator mode temperature T_{mode}. This is because zero-span measurements are not suitable to resolve very low mode temperatures, as described in subsection 4.4.1. Therefore, the zero-span function was only used for monitoring the time evolution $T_{\mathrm{mode}}(t)$ during the experimental sequence, while the final minimum temperatures were calculated from the displacement PSD spectra $S_{\mathrm{y}}(\omega)$, which were acquired with the Zoom-FFT function of the used lock-in amplifier (as described in subsection 4.4.3). During the acquisition of the spectra, the oscillator needs to be in a steady state, which is easy to achieve with feedback cooling. By contrast, reaching a quasi steady state with sympathetic cooling is only possible with a MOT instead of an optical molasses, as shown in subsection 5.2.2.

Figure 5.20 shows the time evolution of $T_{\mathrm{mode}}(t)$ during the experimental sequence for combined cooling of the oscillator for different feedback gains P (set in the feedback loop, see Figure 4.8). The time trace for $P = 0$ (dark blue) corresponds to pure sympathetic MOT cooling. One can see that $T_{\mathrm{mode}}(t)$ reaches a steady state of 20 mK after a cooldown time $t_{\mathrm{cool}} \approx 250\,\mathrm{ms}$. If a finite feedback gain $P > 0$ is adjusted, the oscillator gets feedback cooled in the first cooling interval $0 < t < 3\,\mathrm{s}$. This leads to a reduced mode temperature $T_{\mathrm{mode}} < 20\,\mathrm{mK}$ in the combined cooling interval for $t > 3\,\mathrm{s}$. One can

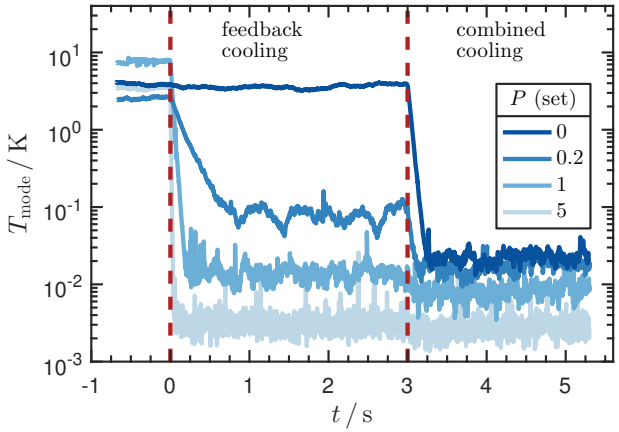

Figure 5.20: Time evolution of the oscillator temperature during the combined cooling sequence. Oscillator mode temperature $T_{\mathrm{mode}}(t)$ for different feedback gains P (gain set in the feedback loop, see Figure 4.8) and constant sympathetic MOT cooling parameters. At $t = 0$ the feedback cooling is started by opening the feedback beam shutter. At $t = 3\,\mathrm{s}$ the sympathetic cooling is switched on by quickly changing the MOT parameters to MOT configuration B (see subsection 5.2.1) and simultaneously ramping up the coupling lattice within 1 ms. For $P = 0$ the cooling is purely sympathetic, which allows for calculating the sympathetic cooling gain $g_{\mathrm{s}} = 170$, according to equations 5.11 and 5.14 using $T_{\mathrm{bath}} = 3.8(12)\,\mathrm{K}$ obtained by averaging $T_{\mathrm{mode}}(t < 0)$. Parameters: feedback light power $P_{0.5} = 425\,\mu\mathrm{W}$ in front of cavity fiber at 50% working point of EOM, blue lattice detuning $\Delta_{2,3} = 2\pi \times 160\,\mathrm{MHz}$, $P_{\mathrm{lat}} = 150\,\mu\mathrm{W}$, $\omega_{\mathrm{a}} = 2.2\,\omega_{\mathrm{m}}$ (calibrated), zero-span traces averaged 30 times, demodulator BW $B_{\mathrm{d}} = 400\,\mathrm{Hz}$, sequence cycle time 20.0 s, optomechanical system and detection parameters: see Table 3.1.

clearly see that the temperature during the combined cooling gets smaller with increasing feedback gain. Nevertheless, the additional cooling effect from sympathetic cooling also gets smaller with increasing feedback gain. For the gain $P = 5$ the temperature

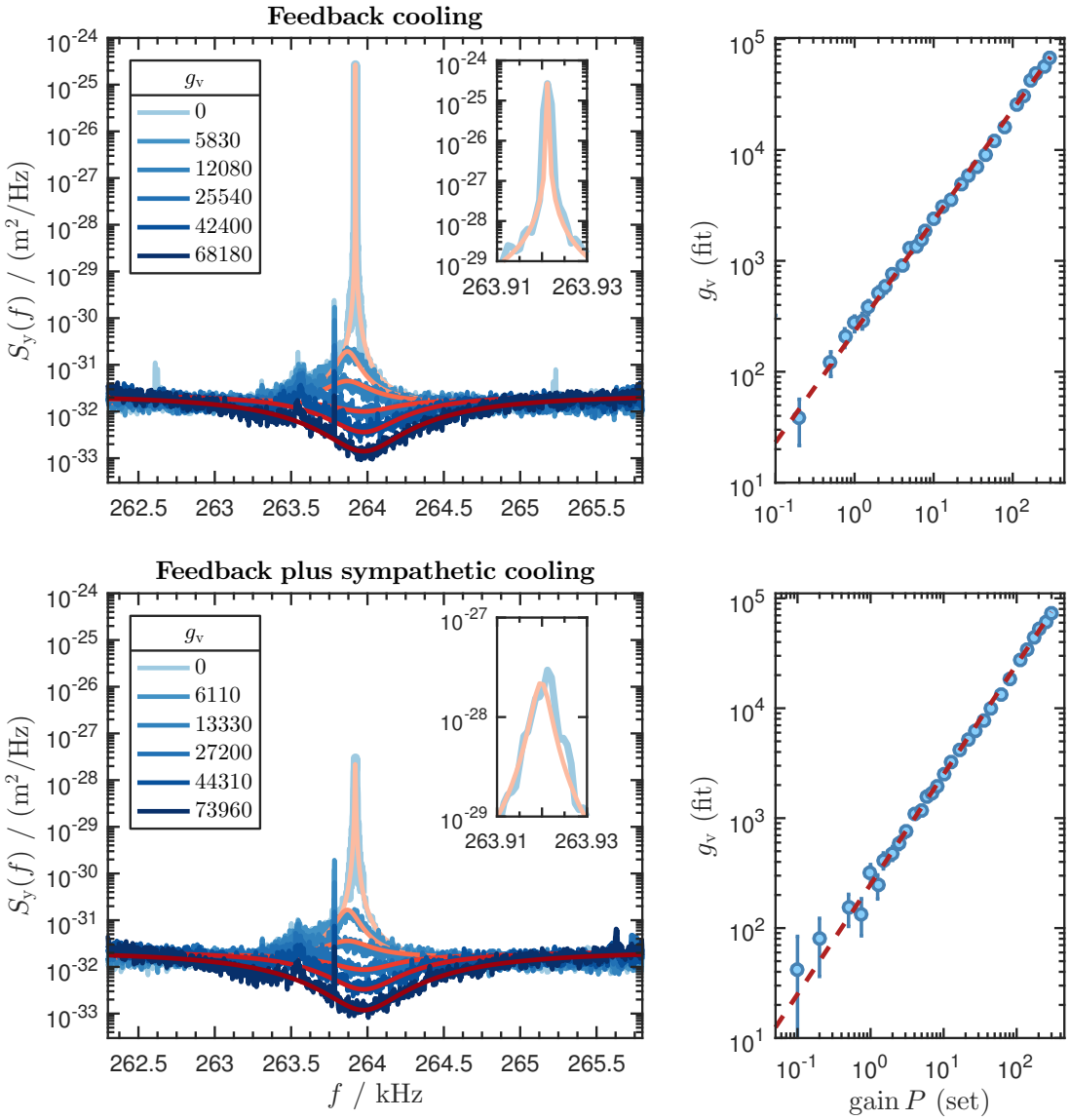

Figure 5.21: Spectral analysis of combined sympathetic and feedback cooling. Left column: In-loop displacement PSD $S_y(f)$ for different feedback gains g_v (blue) and fits to the spectra (red). The fits are simple least-square fits to the logarithmic data. Both cooling configurations were fitted with expression 5.27 using g_v as the only free fit parameter and the fixed value $T_{bath} = 3.8(12)$ K. For this, g_{sym} was set to zero for pure feedback cooling and set to $g_{sym} = 170$ for combined cooling (T_{bath} and g_{sym} taken from the traces in Figure 5.20). Inset figure: zoom into the peak area. Right column: feedback gains g_v obtained by the fits in the left column as a function of the adjusted amplification gains P in the feedback loop (see Figure 4.8). Data acquisition: Zoom-FFT spectra from the lock-in amplifier, demodulator bandwidth $B_d = 1.5$ kHz, sampling rate 7.2 kSa/s, resolution 880 mHz, each spectrum averaged over ten cycles. Sequence parameters: see Figure 5.20.

reduction during combined cooling is barely visible. However, when T_{mode} approaches 1 mK, the result from the zero-span traces can not be trusted anymore.
In order to determine T_{mode} also for large feedback gains, the in-loop displacement PSD $S_{\mathrm{y}}(\omega)$ (see section 4.1) was acquired using Zoom-FFT spectra. These spectra were precisely triggered by the experimental control and in both cooling intervals a PSD spectrum of the oscillator was acquired within a time interval of 2 s. The measured spectra are shown in Figure 5.21. Contrary to the measurement presented in subsection 4.4.3, the bath temperature T_{bath} in this measurement was simply obtained by averaging the data for $T_{\mathrm{mode}}(t < 0)$ from the zero-span measurement (see Figure 5.20). In this way, the spectra $S_{\mathrm{y}}(\omega)$ for pure feedback cooling (see equation 4.10) in the first cooling time slot can be fitted using the feedback gain g_{v} as the only free fit parameter, as described in subsection 4.4.3. However, the equation for the PSD $S_{\mathrm{x}}^{\mathrm{sf}}(\omega)$ during combined cooling also includes the sympathetic cooling gain g_{sym} (see equation 5.27). Therefore, g_{sym} was calculated from the pure sympathetic cooling process for $P = 0$, as described in Figure 5.20. Using this value for g_{sym} in the expression for $S_{\mathrm{x}}^{\mathrm{sf}}(\omega)$, the spectra for combined cooling can also be fitted with g_{v} as the only free fit parameter, which is shown in Figure 5.21 (bottom left).
The right column in Figure 5.21 shows the fitted feedback gains g_{v} as a function of the adjusted gain P in the feedback loop (see Figure 4.8). A linear fit shows that $g_{\mathrm{v}} \sim P$, which means that the feedback cooling is performed in the linear regime of all involved

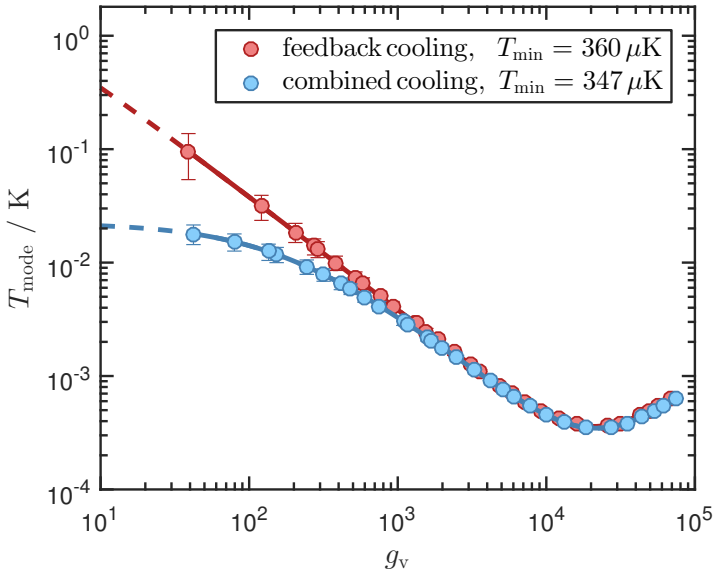

Figure 5.22: Cooling limit of feedback-assisted sympathetic cooling. Mode temperatures of the oscillator T_{mode} as a function of the feedback gain g_{v} and a least-square fit to the data using expression 5.29. For this, g_{sym} was set to zero for pure feedback cooling and set to $g_{\mathrm{sym}} = 170$ for combined cooling (see Figure 5.20). The mode temperatures were obtained by fits to the spectra in Figure 5.21. The error bars include the statistical error of g_{v}. The minimum temperatures T_{min} displayed above have a very small statistical error and the difference between them is significant. Note that both values still have the same systematic error from the error of $T_{\mathrm{bath}} = 3.8(12)\,\mathrm{K}$ used for the calculation of T_{mode} and the usual systematic error of 18% from the homodyne calibration (see equation 3.20).

parts in the feedback loop. Furthermore, the fact that this linearity also holds for the combined cooling is a validation of the model for the combined cooling displacement PSD $S_x^{sf}(\omega)$.
Moreover, the fitted feedback gains g_v allow for calculating the mode temperatures T_{mode} of the oscillator for pure feedback cooling and for combined cooling. Both temperatures can be calculated from equation 5.29 by setting $g_{sym} = 0$ for pure feedback cooling. The resulting temperatures are shown in Figure 5.22 together with a fit using the same expression 5.29. In this way, the minimum achievable mode temperature T_{min} can be determined very precisely, which shows that the combined cooling leads to a slightly lower minimum temperature. The fact that the additional cooling effect is so small originates from the small sympathetic cooling gain g_{sym} compared to the much larger feedback cooling gain $g_{v,opt} \gg g_{sym}$ at the point of optimal cooling. However, in the regime where both gains are comparable the combined cooling leads to significantly lower mode temperatures of the oscillator.
Nevertheless, the very small temperature reduction of less than 5% for combined cooling is completely compensated by the additional heating effects of the experimental sequence. In fact, pure feedback cooling in the steady state leads to a significantly lower temperature of $T_{min} = 234\,\mu K$, as described in subsection 4.4.3. Further measurements revealed that the larger temperature in the combined cooling experiment can be explained by heating of the coupling lattice beam, as discussed in appendix C.3.
Finally it can be said that the combined cooling process in our parameter regime can be described very well with the classical model described in subsection 5.1.4. The measurements demonstrate the technical feasibility of creating and detecting a quasi steady state of a feedback cooled mechanical oscillator coupled to a laser cooled atomic cloud. Possible improvements and future prospects of this experimental configuration will be discussed in the following section.

5.3 Conclusion

We have demonstrated sympathetic cooling of a membrane oscillator in a cryogenic MiM system through coupling to a laser cooled atomic cloud. The setup allows for a robust operation in cycled experiments, which exhibit very small cycle-to-cycle parameter fluctuations and long-term stability. This proves the robustness of the cavity-enhanced long-distance coupling mechanism based on an optical 1D lattice, which couples the atomic motion to the mechanical oscillator [31].
Sympathetic cooling in our parameter regime can be regarded as a robust phenomenon that works in a wide parameter range of the coupling lattice and the laser cooling of the atomic cloud. We observe the largest sympathetic cooling rates for cooling with an optical molasses with a large number of atoms. Starting from cryogenic bath temperatures around $T_{bath} \approx 3\,K$ of the mechanical oscillator, this enables sympathetic cooling down to minimum temperatures of $T_{min} \approx 20\,mK$, which corresponds to a measured cooling rate of $\Gamma_{sym} = 23.3(14)\,Hz$ and a hybrid cooperativity of $C_{hybrid} = 151 \pm 9$. Sympathetic cooling with a MOT leads to comparable cooling rates, but also allows for reaching a quasi steady state of the oscillator, as the atom number of the used MOT configuration can be regarded as being constant on the timescale of 1 s. More-

over, the sympathetic cooling mechanism also works in a real steady sate, by coupling the mechanical oscillator to a continuously loaded MOT, which leads to slightly smaller cooling rates in our setup.
As the hybrid coupling mechanism can become instable for very large atom numbers in the coupling lattice [104], the maximum sympathetic cooling rate is limited on the atomic side. However, we only observe this effect for red coupling lattice detunings, which shows that for blue lattice detunings the hybrid coupling mechanism might be stable even for larger atom numbers than in our setup. This asymmetry is also predicted by the theory [103, 104, 186]. Moreover, the sympathetic cooling rate Γ_{sym} can also be enhanced without changing the atomic side of the hybrid system. For example, the mass of the mechanical oscillator could be reduced and the Q-factor could be further increased, which both contribute linearly to Γ_{sym} (see equations 5.12, 5.13). Nevertheless, the MiM system could be further optimized in terms of the cavity finesse $\mathcal{F}$, which has on optimal value that follows from the quantum mechanical noise contributions (see Figure 5.3). Assuming the mechanical oscillator in our system would be replaced by a trampoline oscillator [73, 74], which has a ten times lower mass and a ten times larger Q-factor, this would increase C_{hybrid} by a factor of 100. Choosing the optimal value $\mathcal{F} \approx 850$ for the finesse in our system (see Figure 5.3) would increase the hybrid cooperativity by another factor of 30, as $C_{\mathrm{hybrid}} \sim \Gamma_{\mathrm{sym}} \sim \mathcal{F}^2$ (the current value is $\mathcal{F} \approx 160$). With these technical improvements we would already enter the strong coupling regime $C_{\mathrm{hybrid}} > \bar{n}_{\mathrm{th}}$, even for our current thermal phonon occupation $\bar{n}_{\mathrm{th}} \approx k_{\mathrm{B}}T/\hbar\omega_{\mathrm{m}} \approx 2.4 \times 10^5$. We are also confident that the thermal occupation of the oscillator $\bar{n}$ can be significantly reduced by improvements of the cryogenic MiM system. This would even relax the conditions for the strong coupling regime.
Hence, our hybrid system offers exciting prospects for reaching the strong coupling condition, which may enable ground state cooling of the mechanical oscillator even in the bad cavity regime [31, 34, 57] which has not been demonstrated to date. Furthermore, reaching the strong coupling regime in the hybrid system offers the possibilities for coherent quantum state transfer, teleportation and entanglement [24, 25, 29].
In addition to the hybrid coupling experiments, we have demonstrated for the first time the combination of feedback cooling with sympathetic cooling. Through this combined cooling, ground state cooling is facilitated in our system [34]. Another important result of these measurements is that we can couple a feedback cooled mechanical oscillator to a cold atomic ensemble that is not laser cooled. Hence, our system enables coupling a BEC to a feedback cooled mechanical oscillator. As described in subsection 4.4.3, feedback cooling into the quantum ground state is technically feasible in our setup if trampoline oscillators are used. In this way, the creation of a true hybrid quantum system consisting of two quantum systems of a very different nature might be achieved in the near future.

Appendix A

Details of the coupling lattice

A.1 Optical losses

In the following, the most relevant optical loss mechanisms in the coupling lattice will be listed, which are also sketched in Figure A.1 for clarity. The transmittance of the glass cell $T_{\mathrm{gc}} = 0.9$ was measured with the lattice beam (same polarization, same angle), which leads to $\sqrt{T_{\mathrm{gc}}} \approx 0.95$ for the passage of only one glass plate. The losses for the first passage of the lattice telescope are given by the transmittance $T_{\mathrm{T},1} = 0.965$ of the lens and the PBS, as well as the fiber coupling with transmittance $T_{\mathrm{FC}} = 0.85$ (the loss at the PBS due to impure polarization is only 0.33%). The losses of the fiber MiM device can be divided into losses in the fiber itself and the finite reflectivity on resonance $\sigma_{\mathrm{ref}} = 0.61$ of the MiM system (see equation 2.6), which is slightly lower than the empty

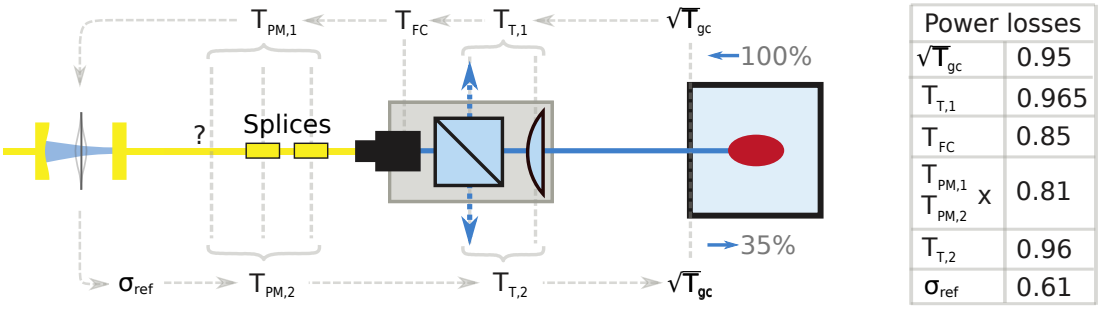

Figure A.1: Optical losses of the lattice beam. Sketch of the most relevant optical losses measured in the lattice beam setup depicted in Figure 2.22, showing also the two fiber splices in the MiM fiber. From the lattice incident beam power of 100% at the position of the atoms, 35% comes back to the atoms from the MiM device (cavity on resonance). The measured power transmittances for the incident beam (upper line, right to left) are: $\sqrt{T_{\mathrm{gc}}}$ (single wall of glass cell), $T_{\mathrm{T},1}$ (cube and lens of telescope, first passage), T_{FC} (fiber coupling into PM fiber) and $T_{\mathrm{PM},1}$ (losses of two splices and unknown losses in PM fiber). The lower line describes the losses of the back reflected light: σ_{ref} (reflectivity on resonance of the MiM device), $T_{\mathrm{PM},2}$ (losses of two splices and unknown losses in PM fiber), $T_{\mathrm{T},2}$ (cube and lens of telescope, second passage) and T_{gc} of the second passage through the glass cell. The dashed blue arrows at the PBS indicate reflected light due to impure polarization. The transmittance of the two splices (and possible additional losses) in the fiber could only be measured in sum for light that passed the fiber two times.

cavity value of 0.73 (see Figure 2.15). The reason might by a small tilt between the fibers and the membrane or the fact that the wave vectors of the intra-cavity field are not perfectly perpendicular to the membrane, due to the planar-concave cavity geometry. The fiber losses (including two splices) were measured by tuning the cavity off resonance and measuring the reflected power of the fiber MiM system relative to the incoupling power (assuming $T_{\mathrm{FC}} = 0.85$, $\sigma_{\mathrm{ref}} = 1$). The measured total transmittance of the light that travels to the MiM device and back is $T_{\mathrm{PM},1} \times T_{\mathrm{PM},2} = 0.81$ (we assume two different transmittances for the two directions because the losses might also be polarization dependent). This was confirmed in two different ways (reflection and transmission of PBS in telescope). Since this would correspond to a transmittance of only $(0.81)^{1/4} \approx 0.95$ of a single splice, the transmittance of the first splice was measured separately by breaking the fiber after this splice. In this way, the transmittance of the first splice was measured to be larger than 0.95, whereas the second splicing was repeated four times, each time leading to the same result of the total fiber loss. The large total loss indicates that the used PM fiber has additional losses apart from the splices. However, these losses could not be determined separately. They might be related to the fact that the used PM fiber (planar cavity fiber) does not properly maintain the polarization. Possible explanations could be the Swagelock fiber feedthrough into the cryostat or the asymmetric pressure on the cavity fibers in the MiM ferrules (two 125 µm fibers were glued into a 250 µm ferrule). It should be noted that the loss can not be explained by losses at the PBS in the telescope due to impure polarization. We control the polarization of the back reflected light via a $\approx$ 5 cm large piece of fiber which is temperature controlled. In this way, we achieve a 99% transmittance of the back reflected light at the PBS in the telescope. This slightly larger polarization dependent loss on the way back is the reason why $T_{\mathrm{T},2} = 0.96$ is slightly smaller than $T_{\mathrm{T},1} = 0.965$. The thermal polarization control is not active and must be adjusted by hand a few times a day.

Future enhancements of the optical setup could be a larger reflectivity on resonance of the fiber cavity ($\sigma_{\mathrm{ref}} \approx 0.9$) and the usage of a normal single mode fiber with only one splice (total round trip fiber transmittance ≈ 0.95). We measured that two perpendicular polarizations can be coupled into the cryogenic non-PM fiber in the cryostat and then be perfectly separated again in the reflected beam using mechanical polarization controllers [91]. The usage of such a fiber and the enhanced MiM device would lead to a total reflected power of 60% instead of 35% at the position of the atoms.

A.2 Theory of Kapitza-Dirac diffraction

If the optical lattice is switched on abruptly at $t = 0$, the wave function $|\Psi(t = 0)\rangle = |\phi_q\rangle$ of the BEC can be written as a superposition of Bloch states $|n, q\rangle = \psi_{n,q}(x)$. Following [189] and [190] this can be expanded into:

$$|\Psi(t = 0)\rangle = \sum_{n=0}^{\infty} |\Psi_n(t = 0)\rangle = \sum_{n=0}^{\infty} |n, q\rangle \langle n, q|\phi_q\rangle . \tag{A.1}$$

Using equation 2.10 one can find

$$\langle n,q|\phi_q\rangle \;=\; \sum_{l=-\infty}^{\infty} c^*_{l,n,q}\,\langle \phi_{2l\hbar k+q}|\phi_q\rangle \;=\; c^*_{0,n,q}\,. \tag{A.2}$$

With this one can write down the time evolution of the BEC-wavepacket in the nth band:

$$|\Psi_n(t)\rangle = |\Psi_n(t=0)\rangle\, e^{-i(E_{n,q}\cdot E_\mathrm{r}/\hbar)t} = c^*_{0,n,q}\,|n,q\rangle\, e^{-i(E_{n,q}\cdot E_\mathrm{r}/\hbar)t}\,. \tag{A.3}$$

If the lattice is kept on for a time Δt and then abruptly turned off again, we project the wave function onto the plane wave basis $|\phi_{2l\hbar k+q}\rangle$. Using equation 2.10 this can be written as:

$$|\Psi_n(\Delta t)\rangle = \sum_{l=-\infty}^{\infty} b_{l,n,q}\,|\Phi_{2l\hbar k+q}\rangle\;, \tag{A.4}$$

where the coefficients $b_{l,n,q}$ are given by

$$b_{l,n,q} = c^*_{0,n,q} c_{l,n,q} e^{-i(E_{n,q}\cdot E_\mathrm{r}/\hbar)\Delta t}\,. \tag{A.5}$$

In the lattice calibration based on Kapitza-Dirac diffraction we measure the population N_l/N_tot of different momentum orders l as a function of lattice pulse time Δt. This quantity corresponds to the sum over all bands of the $b_{l,n,q}$ coefficients:

$$\frac{N_l(\Delta t)}{N_\mathrm{tot}} \;=\; |\sum_{n=0}^{\infty} b_{l,n,q}|^2\,. \tag{A.6}$$

The $b_{l,n,q}$ coefficients oscillate in time, each with a different frequency depending on the different bands. Hence, the temporal behavior of the different momentum orders N_l gets more complicated the more bands are involved. The functions N_l/N_tot are the entries of our solution vector $|\psi(t)\rangle$ in the time dependent Schrödinger equation (SDG). The fit is a simple least-square algorithm which minimizes the residual between the numerical parametric solution of the SDG and the measured data points $N_l(t_i)/N_\mathrm{tot}$ for the individual order l.

Appendix B

Details of the feedback setup

B.1 Experimental setup for feedback cooling

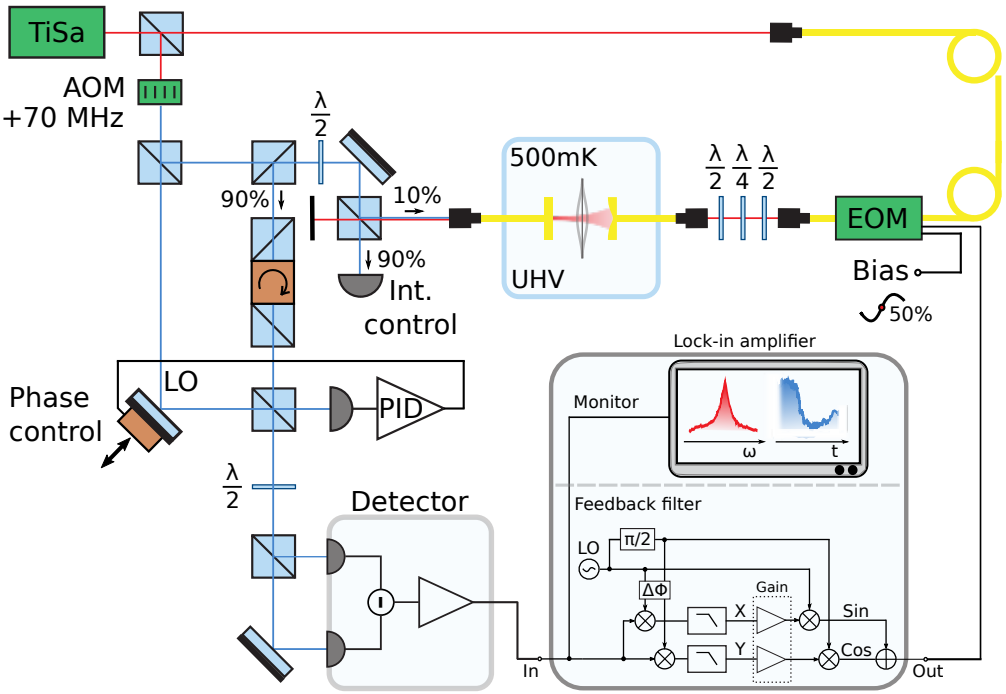

Figure B.1: Experimentally realized setup for feedback cooling. Figure 4.8 in section 4.3 shows schematically the planned setup for feedback cooling. A detailed description of the setup can be found in the caption of Figure 4.8. This figure shows the slightly different setup that was realized in the experiment. The detection beam is guided into the cryostat without using a Faraday rotator and is *reflected* by the last PBS in front of the cryostat. Still, it is possible to separate the back reflected light: A $\lambda/2$ wave plate in front of the last PBS is adjusted such that 90% of the detection light is transmitted and used for intensity control of the detection beam. 10% of the light gets reflected into the cryostat. On its way back all the light gets reflected by the PBS (adjusted by a temperature polarization controller, not shown) and passes the wave plate again. Now 90% of the light gets reflected at the next cube (10% loss) that can be used for homodyning. The following Faraday rotator is only used as an optical isolator, since any parasitic back reflected light from the homodyning setup can drive the membrane. The reason for this realization is of purely technical nature: A Faraday rotator close to the last PBS in front of the cryostat is located too close to the BEC chamber (large magnetic fields).

B.2 Data sheet of homodyne photodetector

Datasheet **HCA-S** **Ser.Nr.: 02-99-406**

Low Noise Balanced Photoreceiver with Integrated Si PIN Photodiodes
(Customized Version)

Features

- **Two Si PIN Photodiodes with 0.8 mm Active Diameter**
- **Bandwidth DC ... 1 MHz**
- **Amplifier Transimpedance (Gain) 50 x 10^3 V/A**
- **Conversion-Gain 28.5 x 10^3 V/W (@ 800 nm)**
- **Spectral Range 320 ... 1000 nm**

Applications

- **Spectroscopy**
- **Fast Pulse and Transient Measurements**
- **Optical Triggering**
- **Optical Front-End for Oscilloscopes, A/D Converters and Fast Lock-In Amplifiers**

Specifications

	Test Conditions	*Vs = ± 15 V, Ta = 25°C*	
Gain	Transimpedance	20 x 10^3 V/A	(@ > 10 kΩ load)
	Conversion Gain	28.5 x 10^3 V/W	(@ 800 nm, > 10 kΩ load)
	Common Mode Rejection	> 90 dB typ.	(f < 1 kHz)
		> 79 dB typ.	(f < 10 kHz)
		> 61 dB typ.	(f < 100 kHz)
		> 50 dB typ.	(f < 1 MHz)
Frequency Response	Lower Cut-Off Frequency	DC	
	Upper Cut-Off Frequency (-3 dB)	1 MHz	(± 10%)
	Rise- / Fall-Time	350 ns	(10% - 90%)
Detectors	Detector Material	Two Si PIN photodiodes	
	Active Diameter	0.8 mm	
	Spectral Response	320 ... 1000 nm	
	Peak Sensitivity	0.57 A/W	(@ 800 nm)
Input	Max. Optical Input Power	350 µW	(differential, for linear amplification, @ 800 nm)
Noise	NEP	1.1 pW/√Hz	(@ 800 nm, 100 kHz, > 10 kΩ load)
		1.4 pW/√Hz	(@ 800 nm, 1 MHz, > 10 kΩ load)
	Equivalent input noise	1.9 nW rms	(@ 800 nm, > 10 kΩ load)
	Equivalent input noise	11.4 µW peak-peak	(@ 800 nm, > 10 kΩ load)
Output	Output Voltage Range	± 10 V	(@ > 10 kΩ load)
	Output Impedance	50 Ω	(terminate with > 10 kΩ load for best performance)
	Output Offset Compensation	± 200 mV	(adjustable by offset trimpot)
	Output Noise	54 µV rms	(@ > 10 kΩ load, no signal on photodiode)
Power Supply	Supply Voltage	± 15 V	
	Supply Current	± 40 mA typ.	(depends on operating conditions, recommended power supply capability minimum ± 150 mA)
Case	Weight	210 g (0.5 lb.)	
	Material	AlMg4.5Mn, nickel-plated	

SOPHISTICATED TOOLS FOR SIGNAL RECOVERY FEMTO

Datasheet **HCA-S** **Ser.Nr.: 02-99-406**

Low Noise Balanced Photoreceiver with Integrated Si PIN Photodiodes
(Customized Version)

Temperature Range	Storage Temperature Operating Temperature	– 40 ... + 100 °C 0 ... + 60 °C
Absolute Maximum Ratings	Optical Input Power Power Supply Voltage	10 mW ± 22 V
Spectral Response		

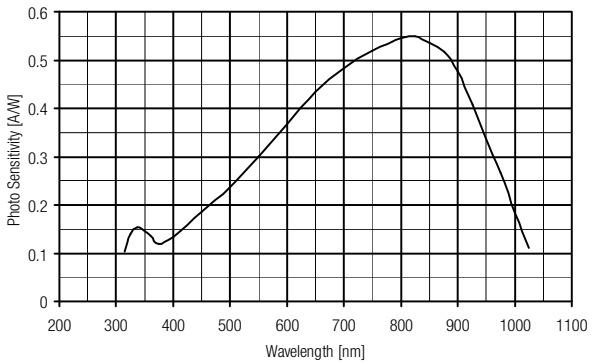

Connectors	Input	optical, 2x Si PIN photodiode in free space flange
	Output	BNC
	Power Supply	LEMO series 1S, 3-pin fixed socket Pin 1: + 15V Pin 2: – 15V Pin 3: GND

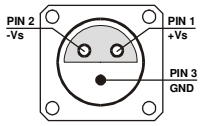

SOPHISTICATED TOOLS FOR SIGNAL RECOVERY F E M T O

B.3 Transfer function of electrical bandpass

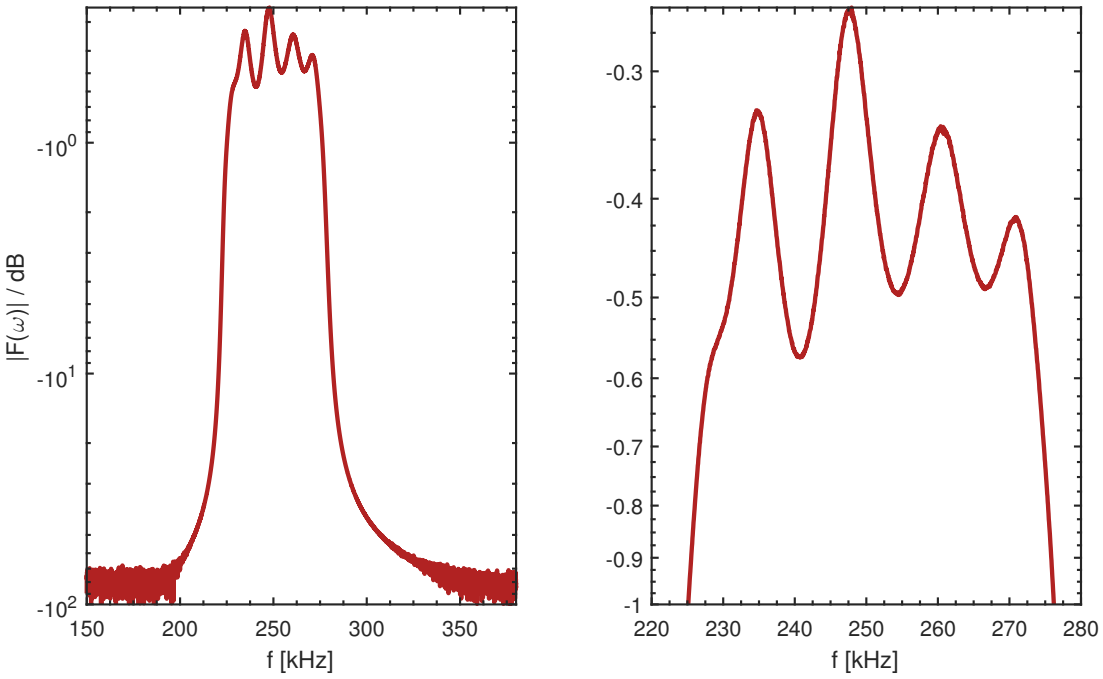

Figure B.2: Measured power transfer function $|\mathbf{F}(\omega)|$ of bandpass in front of lock-in amplifier. The bandpass filter KR 2994 from *KR Electronics* was measured with a spectrum analyzer in network mode. The bandpass has a 3 dB width of the passband of 55 kHz and an extinction outside the passband of 80 dB. The ripples in the passband are below 0.5 dB with a maximum slope of 0.07 dB/kHz (corresponding to maximum voltage transfer function ripples of approximately 5% with a slope of less than 1% per kilohertz). The phase shift between two consecutive ripple peaks was determined separately to be π, which corresponds to a phase change of roughly $\pi/13\,\mathrm{kHz}$. At 247 kHz the transfer loss is practically zero ($|F(\omega)| = 0\,\mathrm{dB}$) and the phase shift is also zero. The membrane oscillator used in this thesis has a resonance frequency of $\omega_\mathrm{m}/2\pi = 263.9\,\mathrm{kHz}$ at 500 mK cryostat temperature, where the bandpass has a power transmission loss of 0.43 dB (field transmission $10^{-0.43/20} = 95\%$) and a phase shift of roughly π.

B.4 Data sheet of fiber EOM

Integrated Optical Amplitude Modulator (AMXXXXb)
Waveguide-based electro-optical light modulator

Specifications

Type		AM 532b	AM 635b	AM 830b	AM 1064b	AM 1550b
Wavelength [nm] Other wavelengths on request (AMXXXXb)		532	635	830	1064	1550
Spectral bandwidth [nm]		± 10	± 20	± 40	± 60	± 100
Insertion loss, typical [dB]		7	7	6	5	5
Extinction, typical		200 : 1	500 : 1	800 : 1	1000 : 1	1000 : 1
Optical connection, input	Standard Fibre connector	Polarisation maintaining single mode fibre Without / FC/PC / FC/APC				
Optical connection, output	Standard Optional Fibre connector	Polarisation maintaining single mode fibre Single mode fibre Without / FC/PC / FC/APC				
Half wave voltage RF / bias [V]		2 / 2	3 / 3	3 / 3	3 / 3	5 / 5
Minimum optical rise time RF 10/90, typical		1 ns	500 ps	500 ps	500 ps	500 ps
Maximum bias modulation frequency (sine) [kHz]		1	1	1	1	1
Maximum optical input power (cw) [mW]		10	20	50	300	300
Dimensions L x W x H [mm] (housing, without fibre feed-through)		96 x 31 x 10				

Dimensions Amplitude Modulator

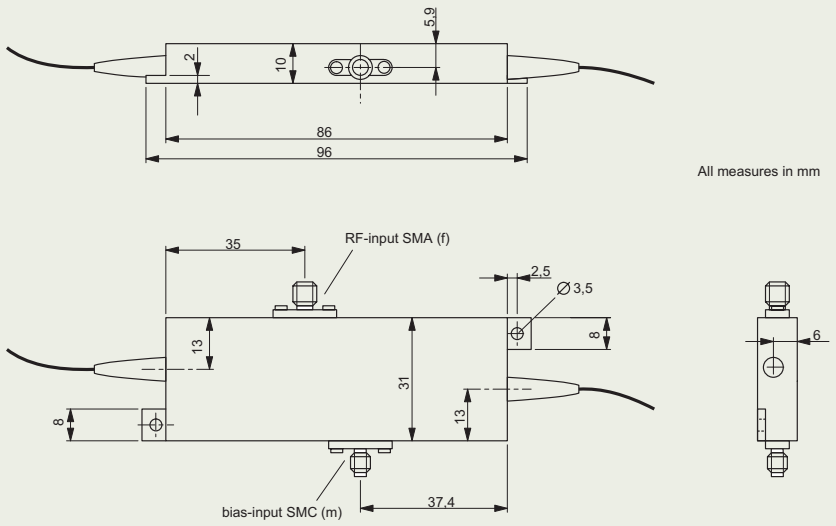

It is our policy to constantly improve the design and specifications. Accordingly, the details represented herein cannot be regarded as final and binding.

JENOPTIK I Healthcare & Industry
Healthcare Business Unit
JENOPTIK Optical Systems GmbH
Goeschwitzer Strasse 25 I 07745 Jena I Germany
Phone +49 3641 65-4530 I Fax -3807
lightmodulators@jenoptik.com I www.jenoptik.com/light-modulators

60054333-004-99-14-0116-en

Appendix C

Details of the sympathetic cooling measurements

C.1 Measurement of the MOT temperature

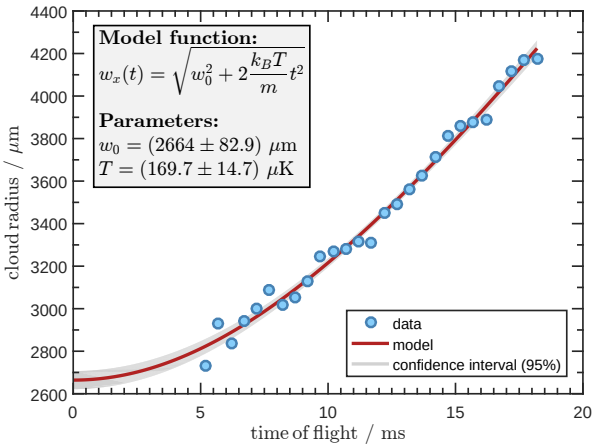

Figure C.1: Determination of the temperature in MOT configuration A. The ballistic expansion of the MOT that was optimized for steady state sympathetic cooling (see section 5.2.1) was analyzed with TOF absorption images and 2D Gaussian fits to the cloud images.

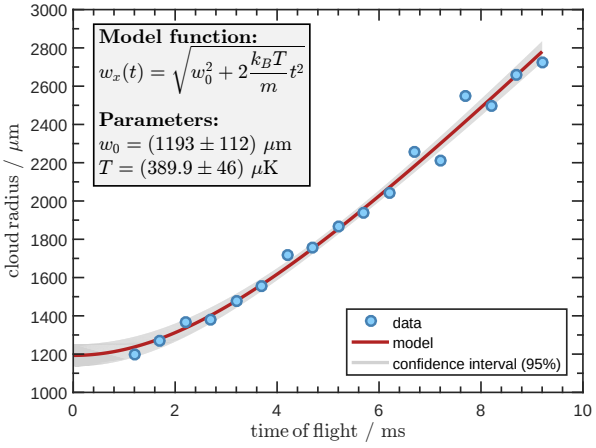

Figure C.2: Determination of the temperature in MOT configuration B. The ballistic expansion of the MOT that was optimized for pulsed sympathetic cooling was analyzed with TOF absorption images and 2D Gaussian fits to the cloud images.

C.2 OD measurements of the atom number

We measure the atom number in the coupling lattice volume during sympathetic cooling with an OD detection setup with a beam that is very well mode matched with the coupling lattice. This section outlines the principles of OD measurements, the technical details of the setup and the technical difficulties that occur.

Principles of OD measurements

In the low saturation regime with $s_0 \equiv I_{\mathrm{det}}/I_{\mathrm{sat}} \ll 1$ the intensity of the detection laser beam which has passed the atomic cloud is given by:

$$I_{\mathrm{abs}} \;=\; I_{\mathrm{det}}\, e^{-\mathrm{OD}}\,. \tag{C.1}$$

OD denotes the optical depth

$$\mathrm{OD} \;=\; \frac{\mathrm{OD}_{\mathrm{res}}}{1+(2\delta_{\mathrm{det}}/\Gamma)^2} \text{ with } \mathrm{OD}_{\mathrm{res}} \;=\; \sigma_0 \int \rho\, \mathrm{d}x\,, \tag{C.2}$$

which depends on the detuning δ_{det} of the beam with respect to the FWHM linewidth Γ of the atomic transition. The quantity $\mathrm{OD}_{\mathrm{res}}$ denotes the resonant optical depth (for zero detuning) and represents the scattering cross-section of the atomic transition, integrated over the atomic density ρ along the beam propagation axis x.
Hence, for every atomic sample the detuning δ_{det} can in principle be adjusted such that the optical density is $\mathrm{OD} = 1$, which corresponds to an attenuation of the beam that is easy to measure. The resonant optical density $\mathrm{OD}_{\mathrm{res}}$ and accordingly the atom number can then be calculated according to equation C.2.

Technical setup

To achieve a very good mode match with the coupling lattice, a similar fiber collimator as in telescope T1 is used for the detection beam (see Figure 2.22). The beam is superimposed with the lattice in the PBS cube of T1 and has linear polarization, perpendicular to the lattice. Hence, after passing the atoms, it gets reflected at the cube in T2 and can be picked up with a photodiode. A measurement of the detection beam showed that its waist size differs only by 5% from the lattice waist. The axial alignment of both beams at the waist position is checked on a daily basis before each OD measurement using a flip mirror and a beam view (accuracy better than 10 µm).
In order to ensure a large SNR and to suppress the background from the fluorescence of the laser cooled atomic cloud, we modulate the detection beam at 50 kHz and measure its signal with the same lock-in amplifier which is used for the measurement of the oscillator temperature. The advantage is that the zero-span traces from the OD measurement can be acquired and saved simultaneously with the oscillator temperature. For small bandwidths $B_{\mathrm{d}} \approx 100\,\mathrm{Hz}$ of the demodulator we achieve a very large SNR for accurate OD measurements. For time-critical OD measurements the bandwidth can be increased up to $B_{\mathrm{d}} \approx 10\,\mathrm{kHz}$, at the cost of a smaller SNR. The modulation of the detection beam is applied using a Bias-Tee at a mixer which is inserted into the RF signal path of the BEC detection AOM. With the DC port of the Bias-Tee we can

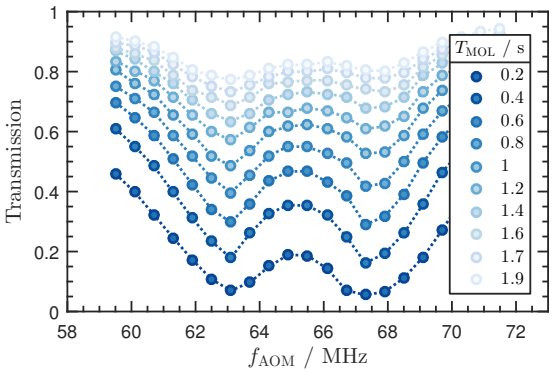

Figure C.3: EIT-like feature of the detection beam in the optical molasses. The transmission of the OD detection beam trough the optical molasses was measured for different detunings of the detection beam, indicated by the frequency of the double-pass AOM in the detection beam. The different curves correspond to the same OD measurement, evaluated at different times after the molasses has started. The dashed lines are a guide to the eye. The atomic resonance is at $f_{\mathrm{AOM}} = 67.1\,\mathrm{MHz}$ (see Figure 2.2).

ensure that the mixer passes the RF signal for constant light power after the AOM and with the RF port of the Bias-Tee the modulation is applied. The OD detection light is then split off from the BEC detection light.

The saturation intensity of the D_2 line of Rb for π light is $I_{\mathrm{sat}} = 2.5\,\mathrm{mW/cm^2}$ (see [97]). Hence, the saturation power for a beam waist of $w_{\mathrm{lat}} \approx 80\,\mu\mathrm{m}$ is only $P_{\mathrm{sat}} = \frac{1}{2}\pi w_{\mathrm{lat}}^2 I_{\mathrm{sat}} \approx 250\,\mathrm{nW}$, which would require at least $P_{\mathrm{det}} < 50\,\mathrm{nW}$ in order to ensure a meaningful OD measurement. Since we work off-resonant, the saturation power gets larger (similar to $\mathrm{OD}/\mathrm{OD}_{\mathrm{res}}$, see equation C.2) and $P_{\mathrm{det}} \approx 100\,\mathrm{nW}$ is still acceptable.

In the OD measurement, the reference signal which corresponds to I_{det} is obtained by switching off the laser cooling for the atoms, which quickly removes all the atoms in the beam path. The OD is then calculated according to equation C.1 and the resonant OD follows from equation C.2.

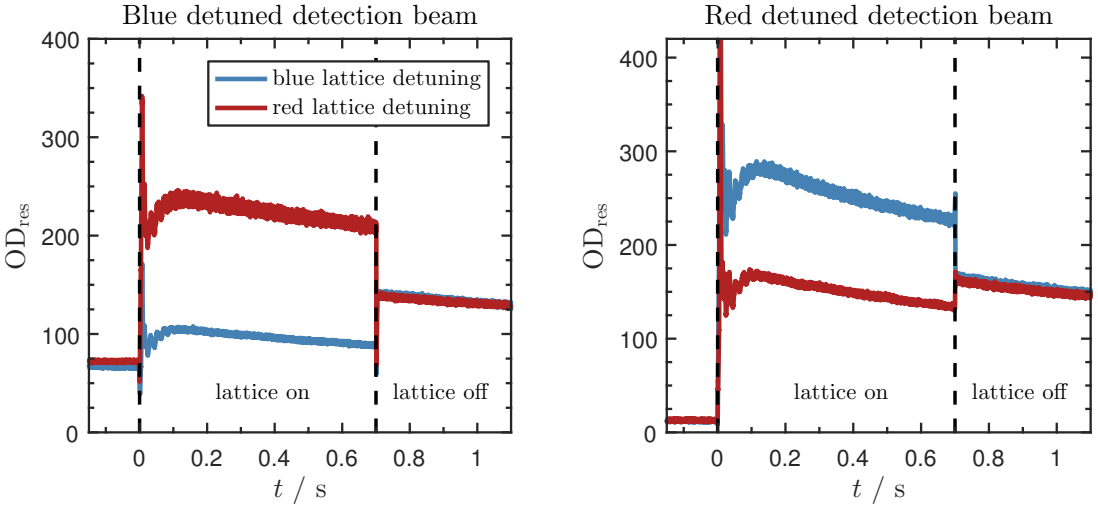

Figure C.4: Measured OD for red and blue detuned detection beam. The OD in the lattice volume was measured with the OD detection beam (mode matched with coupling lattice) for MOT configuration B (see section 5.2.1). Left: detection beam blue detuned ($\delta_{\mathrm{det}} = 2\pi\times 30.2\,\mathrm{MHz} = 5\,\Gamma_{\mathrm{D_2}}$), right: detection beam red detuned ($\delta_{\mathrm{det}} = -2\pi\times 41.8\,\mathrm{MHz} = -6.9\,\Gamma_{\mathrm{D_2}}$). At $t = 0$ the coupling lattice is switched on and simultaneously the normal BEC MOT is quickly switched to the sympathetic cooling MOT. At $t = 0.7\,\mathrm{s}$ the coupling lattice is switched off again. Parameters: $P_{\mathrm{det}} = 100\,\mathrm{nW}$, lattice power 441 μW, OD demodulator BW 3 kHz.

Technical difficulties

Calculating OD_{res} from the off-resonant optical density OD requires that equation C.2 holds, which is based on the assumption of a Lorentzian line shape of the atomic transition. However, the atomic resonance can get effectively broadened by effects like electromagnetically induced transparency (EIT). This means that the calculated OD_{res} is larger than the real value and the OD measurement is distorted.

Linewidth broadening: EIT. We observe such a broadening of the atomic transition, which corresponds to the EIT-like resonance curve shown in Figure C.3. The feature is present over a large period of 2 s during the expansion of the optical molasses. Even though it would in principle be possible to include this measured broadening into the calculation of OD_{res}, this would hold only for one specific combination of molasses parameters and detection beam detuning δ_{det}. However, in the experimental cycle the laser cooling parameters are not always constant. For example, the MOT is changed to the optical molasses or into the high density MOT for sympathetic cooling (MOT configuration B, see section 5.2.1). Furthermore, we observe that the measured broadening of the atomic transition in a MOT is much less defined than the clear feature for the molasses. If the EIT effect involves different m_F states, this could be explained by the presence of large magnetic field gradients in a MOT. Furthermore, the EIT effect is a coherent process and the decoherence effects in a MOT are certainly stronger than in a molasses.

Lattice effects. In addition to the distortions due to linewidth broadening effects, the coupling lattice can also distort the OD measurement, as discussed in the following.

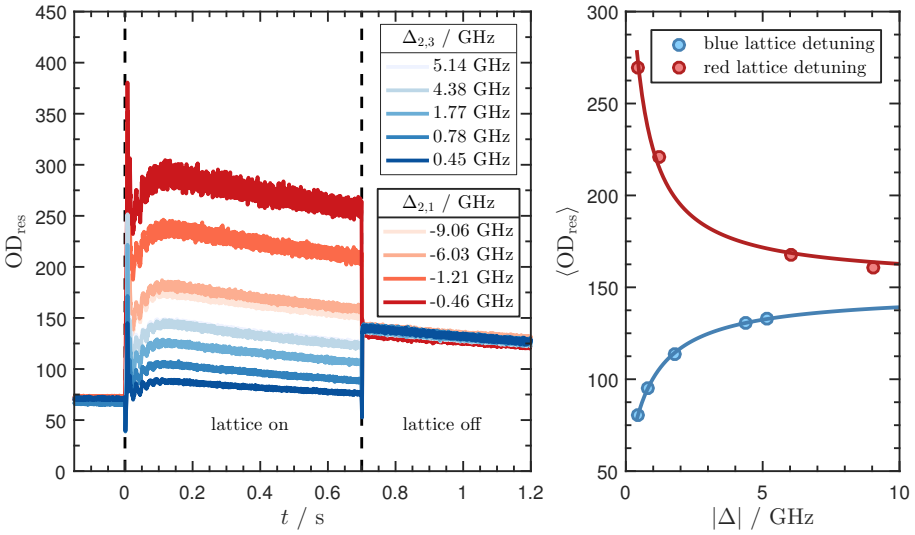

Figure C.5: Change of the OD by the lattice potential. The OD in the lattice volume was measured with a blue detuned OD detection beam (mode matched with coupling lattice) for different lattice detunings in MOT configuration B (see section 5.2.1). Left: OD time traces for the same configuration like in Figure C.4 (left) and for more red and blue lattice detunings. Right: Mean OD during the MOT phase ($0 < t < 0.7$ s) for the different lattice detunings and fits to the data using a simple model which reflects the lattice beam potential. Parameters: detection beam power $P_{det} = 100$ nW, detection beam blue detuned ($\delta_{det} = 2\pi \times 30.2$ MHz $= 5\,\Gamma_{D_2}$), lattice power $P_{lat} = 441\,\mu$W, OD demodulator BW $B_d = 3$ kHz.

Firstly, the near-resonant lattice beam can also be involved in processes like EIT. Secondly, we observe indications of a photonic band gap for the detection light. This effect was predicted in [188] and is based on Bragg scattering of the detection beam by the periodical density distribution of the atoms in the lattice. It depends on the sign of the detection beam detuning and theoretically only occurs for a red detuned detection beam. This different behavior for blue and red detection beam detuning δ_{det} is shown in Figure C.4 for the MOT configuration B used for sympathetic cooling (see section 5.2.1). Firstly, one can see that the sign of δ_{det} changes the result $\mathrm{OD}_{\mathrm{res}}$ of the OD measurement in the normal MOT for $t < 0$. This effect is less pronounced in the final MOT (without lattice) for $t > 0.7\,\mathrm{s}$. Secondly, one can see that the coupling lattice in the period $0 < t < 0.7\,\mathrm{s}$ also changes the calculated $\mathrm{OD}_{\mathrm{res}}$. For blue detection beam detuning $\delta_{\mathrm{det}} > 0$ this effect is consistent with the predicted behavior, that the blue detuned lattice pushes atoms out of the lattice, while the red detuned lattice attracts atoms. This effect was confirmed by a systematic measurement and is shown in Figure C.5. However, for the red detuned detection beam the change of $\mathrm{OD}_{\mathrm{res}}$ is reversed and can not be explained by this model. We tried to confirm that this effect is connected to a photonic band gap by measuring the reflection of the detection beam from the atomic cloud. This measurement is shown in Figure C.6 and can be regarded as a strong indication for the presence of Bragg scattering and a photonic band gap in the coupling lattice for $\delta_{\mathrm{det}} > 0$. Specifically, we observe a detection beam signal on the lattice reflection photodiode (see Figure 2.22) which is only present if the lattice is switched on and which is larger than the signal from the lattice itself. The only possibility which could explain this fact without the existence of Bragg scattering is that the beat signal of the lattice light and some detection beam stray light has AC components in the demodulator bandwidth around the demodulator frequency 50 kHz. This could not be ruled out in this measurement.

Validation of the OD measurements. In order to estimate the accuracy of our OD measurements in a MOT, we tried to exclude all effects like EIT or the lattice effects on the OD measurement. For this, the OD was measured without the lattice beam and the laser cooling was quickly switched off at different times during the high-OD phase of MOT configuration B. Hence, the atoms then experience a TOF phase and are only illuminated by the OD detection beam, just like in the normal TOF absorption imaging

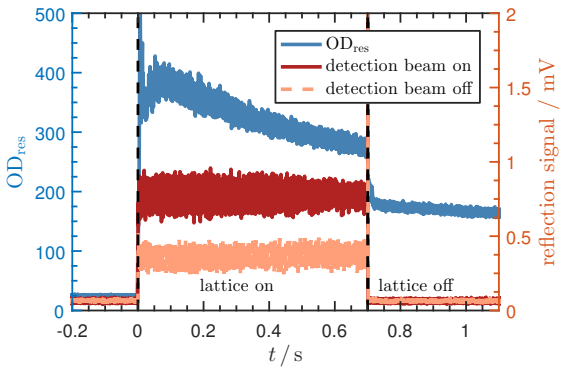

Figure C.6: Evidence of a photonic band gap in the coupling lattice. The OD in the lattice volume was measured with a red detuned OD detection beam (mode matched with coupling lattice) in a similar configuration like in Figure C.4 (right). Additionally, the signal of the lattice back reflection photodiode (see Figure 2.22) was measured with another demodulator. Parameters: detection beam power $P_{\mathrm{det}} = 100\,\mathrm{nW}$, detection beam red detuned ($\delta_{\mathrm{det}} = -2\pi \times 37.8\,\mathrm{MHz} = -6.2\,\Gamma_{\mathrm{D_2}}$), lattice power $P_{\mathrm{lat}} = 221\,\mu\mathrm{W}$, OD demodulator BW $B_{\mathrm{d}} = 3\,\mathrm{kHz}$.

of a BEC. This measurement is shown in Figure C.7 and it shows that the lock-in OD measurement can be trusted after a TOF of approximately 6 ms for a demodulator bandwidth $B_\mathrm{d} = 3\,\mathrm{kHz}$ (before there are some strange bumps in the zero-span traces, which are most likely related to the demodulator).
Assuming that the radius $w(t)$ of the atomic cloud during ballistic expansion evolves according to

$$w(t) \;=\; \sqrt{w_0^2 + 2\frac{k_\mathrm{B}T}{m_\mathrm{a}}t^2}\,, \tag{C.3}$$

the atomic density ρ will evolve according to $\rho \sim w^{-3}(t)$ and the integrated density along the axis of the detection beam can be modeled as $\rho_\mathrm{int} \sim \mathrm{OD}_\mathrm{res} \sim w^{-2}(t) = 1/\left(w_0^2 + 2(k_\mathrm{B}T/m_\mathrm{a})t^2\right)$. Even though the temperature T of MOT configuration B was measured in a separate measurement (see Figure C.2), it must be regarded as a free fit parameter. This is because the fit function must be assumed as $OD_\mathrm{fit} = c_1/(c_2 + 2k_\mathrm{B}T/m_\mathrm{a}t^2) \equiv 1/\left(c_1' + c_2' t^2\right)$. The fit to the zero-span OD traces in Figure C.7 shows that the measured OD_res before the TOF phase corresponds to the fitted values from the TOF measurements up to a factor of two to three (except for one outlier). The fit results for the initial cloud radius $w_{0,\mathrm{fit}}$ are all consistent with the value $w_{0,\mathrm{2D}} \approx 1.2(1)\,\mathrm{mm}$ obtained by the 2D fit results of the TOF temperature measurement in Figure C.2. Due to the fact that a more precise estimation of the initial cloud radius w_0 is very

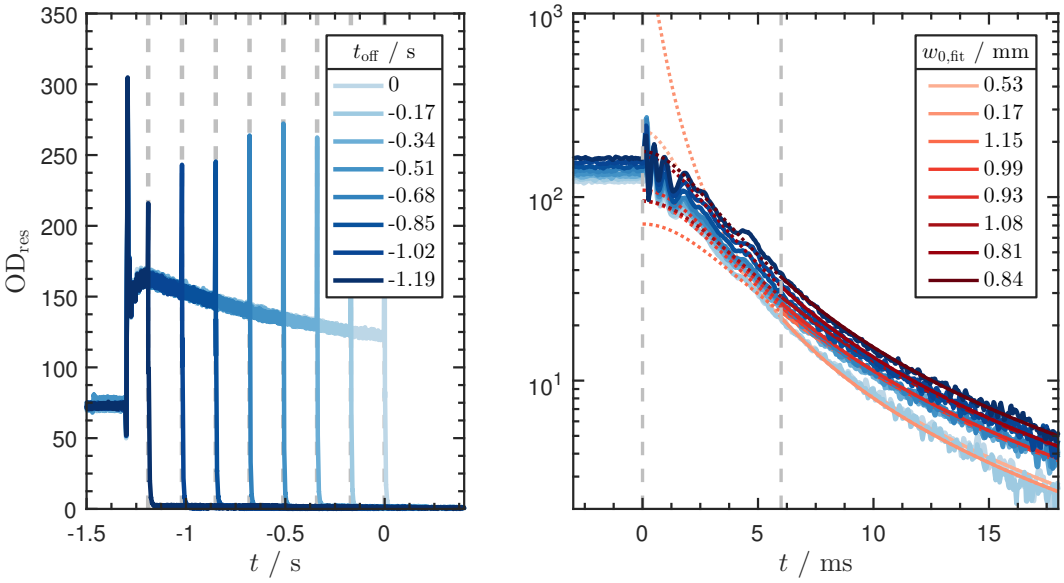

Figure C.7: OD measurement via TOF samples. The OD of the MOT configuration B (see section 5.2.1) without the coupling lattice was measured for different switch-off times t_off of the MOT. Left: Overview of all OD time traces. The switch-off times are indicated by the gray dashed lines. Right: All MOT switch-off events shifted to $t = 0$ and a zoom into the first 15 ms of the OD during TOF. The fits to the OD traces were performed for $t > 6\,\mathrm{ms}$, which is indicated by the right dashed line and a red solid lines for the fits. The fit functions are extended to $t = 0$, which is indicated by the red dotted lines. The fit results for the initial cloud radius $w_{0,\mathrm{fit}}$ are shown in the legend. Parameters: detection beam power 100 nW, detection beam blue detuned ($\delta = 2\pi \times 30.2\,\mathrm{MHz} = 5\,\Gamma_{\mathrm{D}_2}$), OD demodulator BW 3 kHz.

difficult, this uncertainty represents a limit for the accuracy of the fitted $\mathrm{OD}_{\mathrm{res}}$.
In summary it can be said that the OD measurements without coupling lattice can be trusted up to a factor of two to three. Using a blue detuned detection beam, also the OD measurements with the lattice beam can be trusted qualitatively, as Bragg scattering does not play a role and the change of the OD behaves very predictable as expected by the attractive and repulsive lattice potential for the atoms. However, a more precise and reliable measure of the atom number in the lattice during the sympathetic cooling process remains a technically very challenging issue.

C.3 Parasitic heating in combined cooling

In the same experimental run as the measurement of steady state feedback cooling (see subsection 4.4.3), the coupling lattice was additionally switched on without atoms in the beam path. In this way, the parasitic effects of the coupling lattice on the feedback cooling performance could directly be observed. For this, the coupling lattice was switched on with a constant power $P_{\mathrm{lat}} = 1\,\mathrm{mW}$ and it was waited until the new thermal steady state was reached. Especially the length drift of the fiber cavity in the MiM system needs to be compensated. In this configuration, the same measurement as described in subsection 4.4.3 was performed.

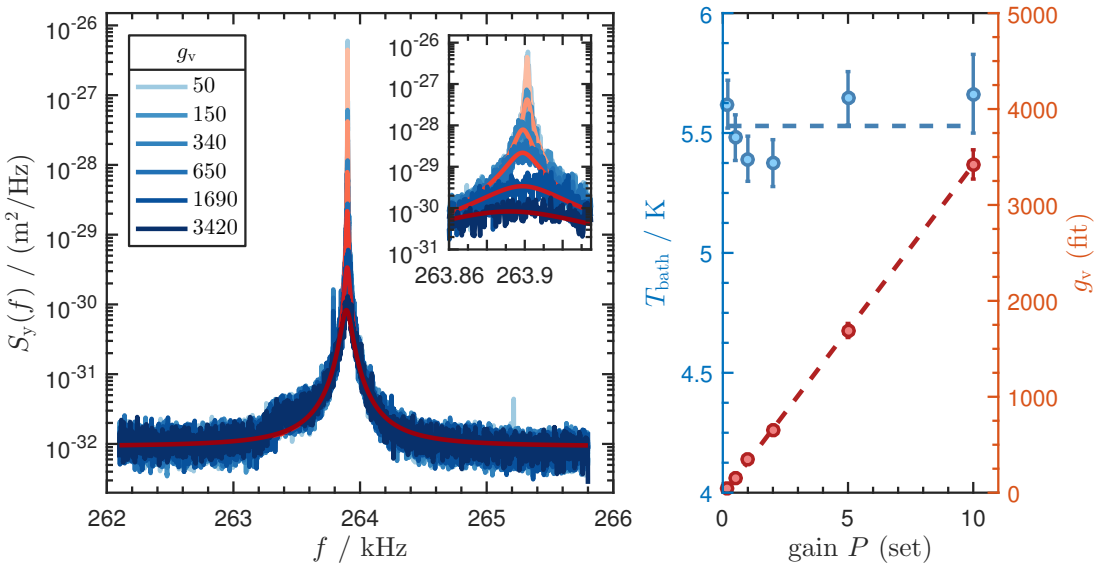

Figure C.8: Spectral determination of the bath temperature T_{bath} with coupling lattice switched on. The measurement in Figure 4.12 was repeated in the same experimental run with the coupling lattice switched on at a power of $P_{\mathrm{lat}} = 1\,\mathrm{mW}$. Left panel: In-loop displacement PSD $S_y(f)$ for different feedback gains g_v (blue) and fits to the spectra (red) using expression 4.10 with g_v and T_{bath} as free fit parameters. Inset figure: zoom into the peak area. Right panel: bath temperatures and feedback gains obtained by the fits in the left panel for the different adjusted gains P (gain of the feedback loop, see Figure 4.8). Mean of bath temperatures is $T_{\mathrm{bath}} = 5.53(13)\,\mathrm{K}$ (blue dashed line). Data acquisition: Zoom-FFT spectra from lock-in amplifier, resolution 220 mHz, each spectrum averaged ten times. Parameters: feedback light power $P_{0.5} = 462\,\mu\mathrm{W}$ in front of cavity fiber at 50% working point of EOM, optomechanical system and detection parameters summarized in table 3.1.

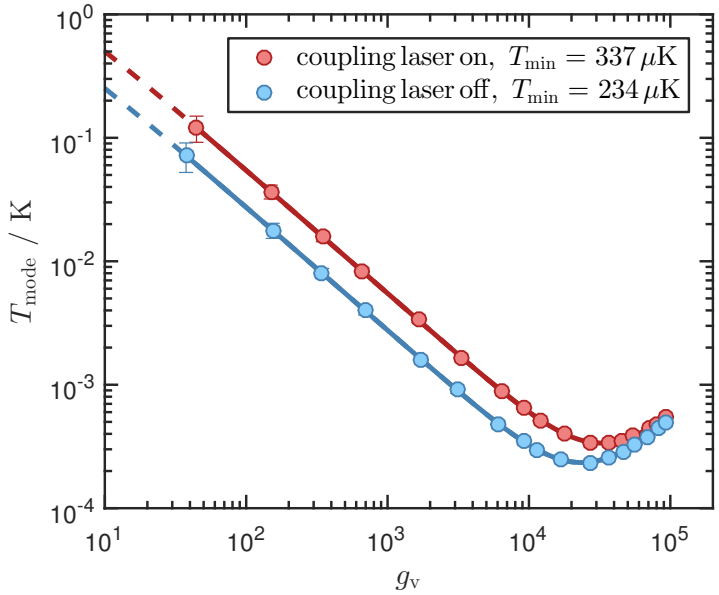

Figure C.9: Parasitic effects of the coupling lattice during feedback cooling. Mode temperatures of the oscillator T_{mode} as a function of the feedback gain g_{v} and a least-square fit to the data using expression 4.19 (with $g_{\mathrm{d}} = 0$). The data without the coupling laser is the same data as in Figure 4.14, the data with the coupling laser switched on was obtained by fits to the measured spectra using $T_{\mathrm{bath}} = 5.53(13)\,\mathrm{K}$, similar as shown in Figure 4.13. The error bars include the statistical error of g_{v}.

Figure C.8 shows the spectra that were obtained for feedback cooling with intermediate gains that can be used to determine the bath temperature T_{bath}. In contrast to the measurement without coupling lattice, the obtained bath temperature $T_{\mathrm{bath}} = 5.53(13)\,\mathrm{K}$ is significantly larger than without the coupling beam (see Figure 4.12). Using this value of T_{bath}, the spectra can be fitted with g_{v} as the only free fitting parameter similar as shown in Figure 4.13. Finally, the obtained values for g_{v} can be used to calculated the mode temperatures T_{mode}.
Figure C.9 shows that the minimum achievable mode temperature T_{min} with the coupling beam on is significantly larger than T_{min} without the coupling beam. This temperature temperature difference is in good agreement with the larger bath temperature for the measurement with coupling beam on, according to equation 4.22.

Bibliography

[1] M. D. Eisaman, J. Fan, A. Migdall and S. V. Polyakov: "Invited Review Article: Single-photon sources and detectors", Review of Scientific Instruments **82** (7), 071101 (2011), ISSN 0034-6748. 2

[2] I. Bloch, J. Dalibard and S. Nascimbène: "Quantum simulations with ultracold quantum gases", Nature Physics **8** (4), 267–276 (2012), ISSN 1745-2473. 2

[3] M. Johanning, A. F. Varón and C. Wunderlich: "Quantum simulations with cold trapped ions", Journal of Physics B: Atomic, Molecular and Optical Physics **42** (15), 154009 (2009). 2

[4] J. J. Morton and B. W. Lovett: "Hybrid Solid-State Qubits: The Powerful Role of Electron Spins", Annual Review of Condensed Matter Physics **2** (1), 189–212 (2011), ISSN 1947-5454. 2

[5] C. R. Kagan, E. Lifshitz, E. H. Sargent and D. V. Talapin: "Building devices from colloidal quantum dots", Science **353** (6302) (2016). 2

[6] J. Clarke and F. Wilhelm: "Superconducting quantum bits", Nature **453** (7198), 1031–1042 (2008), ISSN 0028-0836. 2

[7] M. Poot and H. S. J. van der Zant: "Mechanical systems in the quantum regime", Physics Reports **511** (5), 273–336 (2012). 2, 16, 53, 54, 55, 56, 67, 69, 70, 72, 78, 79, 90

[8] M. Aspelmeyer, T. J. Kippenberg and F. Marquardt: "Cavity optomechanics", Reviews of Modern Physics **86** (4), 1391–1452 (2014). 2, 3, 4, 44, 50, 51, 53, 54, 56, 57, 58, 73, 94

[9] M. H. Anderson, J. R. Ensher, M. R. Matthews, C. E. Wieman and E. A. Cornell: "Observation of Bose-Einstein Condensation in a Dilute Atomic Vapor", Science **269** (5221), 198–201 (1995), ISSN 0036-8075. 2

[10] K. B. Davis, M. O. Mewes, M. R. Andrews, N. J. van Druten, D. S. Durfee, D. M. Kurn and W. Ketterle: "Bose-Einstein condensation in a gas of sodium atoms", Physical Review Letters **75** (22), 3969–3973 (1995), ISSN 00319007. 2

[11] LIGO Scientific Collaboration and Virgo Collaboration: "Observation of gravitational waves from a binary black hole merger", Physical Review Letters **116** (6), 1–16 (2016), ISSN 10797114. 2

[12] M. A. Nielsen and I. L. Chuang: *Quantum computation and quantum information*, Cambridge University Press (2000), ISBN 0521635039. 2

[13] N. Gisin, G. Ribordy, W. Tittel and H. Zbinden: "Quantum cryptography", Reviews of Modern Physics **74** (1), 145–195 (2002), ISSN 00346861. 2

[14] V. Giovannetti, S. Lloyd and L. Maccone: "Advances in quantum metrology", Nature Photonics **5** (4), 222–229 (2011), ISSN 1749-4885. 2

[15] M. Wallquist, K. Hammerer, P. Rabl, M. Lukin and P. Zoller: "Hybrid quantum devices and quantum engineering", Phys. Scr **137**, 14001–7 (2009). 3

[16] P. Treutlein, C. Genes, K. Hammerer, M. Poggio and P. Rabl: "Hybrid Mechanical Systems", in M. Aspelmeyer, T. J. Kippenberg and F. Marquardt (editors), "Cavity Optomechanics", chapter 14, pages 327–351, Springer-Verlag Berlin Heidelberg (2014), ISBN 978-3-642-55311-0.

[17] G. Kurizki, P. Bertet, Y. Kubo, K. Mølmer, D. Petrosyan, P. Rabl and J. Schmiedmayer: "Quantum technologies with hybrid systems", Proceedings of the National Academy of Sciences of the United States of America **112** (13), 3866–73 (2015), ISSN 1091-6490.

[18] B. Rogers, N. L. Gullo, G. De Chiara, G. M. Palma and M. Paternostro: "Hybrid optomechanics for Quantum Technologies", Quantum Meas. Quantum Metrol **2**, 11–43 (2014).

[19] Z.-L. Xiang, S. Ashhab, J. Q. You and F. Nori: "Hybrid quantum circuits: Superconducting circuits interacting with other quantum systems", Reviews of Modern Physics **85** (2), 623–653 (2013), ISSN 0034-6861. 3

[20] A. D. Armour, M. P. Blencowe and K. C. Schwab: "Entanglement and Decoherence of a Micromechanical Resonator via Coupling to a Cooper-Pair Box", Physical Review Letters **88** (14), 148301 (2002), ISSN 0031-9007. 3

[21] A. S. Sørensen, C. H. van der Wal, L. I. Childress and M. D. Lukin: "Capacitive Coupling of Atomic Systems to Mesoscopic Conductors", Physical Review Letters **92** (6), 063601 (2004), ISSN 0031-9007.

[22] J. Verdú, H. Zoubi, C. Koller, J. Majer, H. Ritsch and J. Schmiedmayer: "Strong magnetic coupling of an ultracold gas to a superconducting waveguide cavity", Physical Review Letters **103** (4), 1–4 (2009), ISSN 00319007.

[23] D. Petrosyan, G. Bensky, G. Kurizki, I. Mazets, J. Majer and J. Schmiedmayer: "Reversible state transfer between superconducting qubits and atomic ensembles", Physical Review A - Atomic, Molecular, and Optical Physics **79** (4), 1–4 (2009), ISSN 10502947.

[24] K. Hammerer, M. Wallquist, C. Genes, M. Ludwig, F. Marquardt, P. Treutlein, P. Zoller, J. Ye and H. J. Kimble: "Strong coupling of a mechanical oscillator and a single atom", Physical Review Letters **103** (6), 2–5 (2009), ISSN 00319007. 99, 133

[25] K. Hammerer, M. Aspelmeyer, E. S. Polzik and P. Zoller: "Establishing Einstein-Poldosky-Rosen Channels between Nanomechanics and Atomic Ensembles", Physical Review Letters **102** (2), 020501 (2009), ISSN 0031-9007. 3, 4, 99, 133

[26] P. Rabl, P. Cappellaro, M. V. G. Dutt, L. Jiang, J. R. Maze and M. D. Lukin: "Strong magnetic coupling between an electronic spin qubit and a mechanical resonator", Physical Review B **79** (4), 041302 (2009), ISSN 1098-0121.

[27] K. Hammerer, K. Stannigel, C. Genes, P. Zoller, P. Treutlein, S. Camerer, D. Hunger and T. W. Hänsch: "Optical lattices with micromechanical mirrors", Physical Review A **82** (2), 021803 (2010), ISSN 1050-2947. 4, 99, 101

[28] M. Paternostro, G. De Chiara and G. M. Palma: "Cold-Atom-Induced Control of an Optomechanical Device", Physical Review Letters **104** (24), 243602 (2010), ISSN 0031-9007.

[29] C. Genes, H. Ritsch, M. Drewsen and A. Dantan: "Atom-membrane cooling and entanglement using cavity electromagnetically induced transparency", Physical Review A **84** (5), 051801 (2011), ISSN 1050-2947. 99, 133

[30] M. Gao, Y. X. Liu and X. B. Wang: "Coupling Rydberg atoms to superconducting qubits via nanomechanical resonator", Physical Review A - Atomic, Molecular, and Optical Physics **83** (2), 2–6 (2011), ISSN 10502947.

[31] B. Vogell, K. Stannigel, P. Zoller, K. Hammerer, M. T. Rakher, M. Korppi, A. Jöckel and P. Treutlein: "Cavity-enhanced long-distance coupling of an atomic ensemble to a micromechanical membrane", Physical Review A - Atomic, Molecular, and Optical Physics **87** (2), 1–12 (2013), ISSN 10502947. 4, 18, 34, 99, 100, 101, 105, 106, 128, 132, 133

[32] A. Dantan, B. Nair, G. Pupillo and C. Genes: "Hybrid cavity mechanics with doped systems", Physical Review A - Atomic, Molecular, and Optical Physics **90** (3), 1–9 (2014), ISSN 10941622.

[33] F. Bariani, J. Otterbach, H. Tan and P. Meystre: "Single-atom quantum control of macroscopic mechanical oscillators", Physical Review A - Atomic, Molecular, and Optical Physics **89** (1), 1–5 (2014), ISSN 10502947. 99

[34] J. S. Bennett, L. S. Madsen, M. Baker, H. Rubinsztein-Dunlop and W. P. Bowen: "Coherent control and feedback cooling in a remotely coupled hybrid atom–optomechanical system", New Journal of Physics **16** (8), 083036 (2014), ISSN 1367-2630. 4, 7, 79, 100, 101, 102, 103, 106, 107, 128, 133

[35] F. Bariani, S. Singh, L. F. Buchmann, M. Vengalattore and P. Meystre: "Hybrid optomechanical cooling by atomic Λ systems", Physical Review A - Atomic, Molecular, and Optical Physics **90** (3), 1–13 (2014), ISSN 10941622. 4, 99

[36] F. Bariani, H. Seok, S. Singh, M. Vengalattore and P. Meystre: "Atom-based coherent quantum-noise cancellation in optomechanics", Physical Review A - Atomic, Molecular, and Optical Physics **92** (4), 1–6 (2015), ISSN 10941622. 3, 4, 99

[37] A. D. O'Connell, M. Hofheinz, M. Ansmann, R. C. Bialczak, M. Lenander, E. Lucero, M. Neeley, D. Sank, H. Wang, M. Weides, J. Wenner, J. M. Martinis and A. N. Cleland: "Quantum ground state and single-phonon control of a mechanical resonator", Nature **464** (7289), 697–703 (2010), ISSN 0028-0836. 3

[38] J. Chan, T. P. M. Alegre, A. H. Safavi-Naeini, J. T. Hill, A. Krause, S. Gröblacher, M. Aspelmeyer and O. Painter: "Laser cooling of a nanomechanical oscillator into its quantum ground state", Nature **478** (7367), 89–92 (2011), ISSN 1476-4687. 65, 80

[39] J. D. Teufel, T. Donner, D. Li, J. W. Harlow, M. S. Allman, K. Cicak, A. J. Sirois, J. D. Whittaker, K. W. Lehnert and R. W. Simmonds: "Sideband cooling of micromechanical motion to the quantum ground state", Nature **475** (7356), 359–63 (2011), ISSN 1476-4687.

[40] R. Peterson, T. Purdy, N. Kampel, R. Andrews, P.-L. Yu, K. Lehnert and C. Regal: "Laser Cooling of a Micromechanical Membrane to the Quantum Backaction Limit", Physical Review Letters **116** (6), 063601 (2016), ISSN 0031-9007. 45

[41] J. B. Clark, F. Lecocq, W. Raymond, J. Aumentado and J. D. Teufel: "Sideband cooling beyond the quantum backaction limit with squeezed light", Nature Publishing Group **541** (7636), 191–195 (2017), ISSN 0028-0836.

[42] E. E. Wollman, C. U. Lei, A. J. Weinstein, J. Suh, A. Kronwald, F. Marquardt, A. A. Clerk and K. C. Schwab: "Quantum squeezing of motion in a mechanical resonator", Science **349** (6251), 952–955 (2015), ISSN 0036-8075. 80, 81

[43] J. M. Pirkkalainen, E. Damskägg, M. Brandt, F. Massel and M. A. Sillanpää: "Squeezing of Quantum Noise of Motion in a Micromechanical Resonator", Physical Review Letters **115** (24), 1–5 (2015), ISSN 10797114. 80, 81

[44] J. M. Fink, M. Kalaee, A. Pitanti, R. Norte, L. Heinzle, M. Davanço, K. Srinivasan and O. Painter: "Quantum electromechanics on silicon nitride nanomembranes", Nature Communications **7**, 12396 (2016), ISSN 2041-1723. 3, 65

[45] C. L. Degen, M. Poggio, H. J. Mamin, C. T. Rettner and D. Rugar: "Nanoscale magnetic resonance imaging", Proceedings of the National Academy of Sciences of the United States of America **106** (5), 1313–7 (2009), ISSN 1091-6490. 3

[46] O. Arcizet, V. Jacques, A. Siria, P. Poncharal, P. Vincent and S. Seidelin: "A single NV defect coupled to a nanomechanical oscillator", Nature Physics **7** (11), 879–883 (2011), ISSN 1745-2473.

[47] S. Kolkowitz, A. C. Bleszynski Jayich, Q. P. Unterreithmeier, S. D. Bennett, P. Rabl, J. G. E. Harris and M. D. Lukin: "Coherent Sensing of a Mechanical Resonator with a Single-Spin Qubit", Science **335** (6076), 1603–1606 (2012), ISSN 0036-8075.

[48] J. Teissier, A. Barfuss, P. Appel, E. Neu and P. Maletinsky: "Strain Coupling of a Nitrogen-Vacancy Center Spin to a Diamond Mechanical Oscillator", Physical Review Letters **113** (2), 020503 (2014), ISSN 0031-9007.

[49] P. Ovartchaiyapong, K. W. Lee, B. A. Myers and A. C. B. Jayich: "Dynamic strain-mediated coupling of a single diamond spin to a mechanical resonator", Nature Communications **5**, 1–6 (2014), ISSN 2041-1723. 3

[50] I. Yeo, P.-L. de Assis, A. Gloppe, E. Dupont-Ferrier, P. Verlot, N. S. Malik, E. Dupuy, J. Claudon, J.-M. Gérard, A. Auffèves, G. Nogues, S. Seidelin, J.-P. Poizat, O. Arcizet and M. Richard: "Strain-mediated coupling in a quantum dot–mechanical oscillator hybrid system", Nature Nanotechnology **9** (2), 106–110 (2013), ISSN 1748-3387. 3

[51] M. Montinaro, G. Wüst, M. Munsch, Y. Fontana, E. Russo-Averchi, M. Heiss, A. Fontcuberta I Morral, R. J. Warburton and M. Poggio: "Quantum dot opto-mechanics in a fully self-assembled nanowire", Nano Letters **14** (8), 4454–4460 (2014), ISSN 15306992. 3

[52] T. A. Palomaki, J. W. Harlow, J. D. Teufel, R. W. Simmonds and K. W. Lehnert: "Coherent state transfer between itinerant microwave fields and a mechanical oscillator", Nature **495** (7440), 210–214 (2013), ISSN 0028-0836. 3

[53] J.-M. Pirkkalainen, S. U. Cho, J. Li, G. S. Paraoanu, P. J. Hakonen and M. A. Sillanpää: "Hybrid circuit cavity quantum electrodynamics with a micromechanical resonator", Nature **494** (7436), 211–215 (2013), ISSN 0028-0836. 3

[54] Y.-J. Wang, M. Eardley, S. Knappe, J. Moreland, L. Hollberg and J. Kitching: "Magnetic Resonance in an Atomic Vapor Excited by a Mechanical Resonator", Physical Review Letters **97** (22), 227602 (2006), ISSN 0031-9007. 3

[55] D. Hunger, S. Camerer, T. W. Hänsch, D. König, J. P. Kotthaus, J. Reichel and P. Treutlein: "Resonant coupling of a bose-einstein condensate to a micromechanical oscillator", Physical Review Letters **104** (14), 1–4 (2010), ISSN 00319007.

[56] S. Camerer, M. Korppi, A. Jöckel, D. Hunger, T. W. Hänsch and P. Treutlein: "Realization of an optomechanical interface between ultracold atoms and a membrane", Physical Review Letters **107** (22), 1–5 (2011), ISSN 00319007. 4

[57] A. Jöckel, A. Faber, T. Kampschulte, M. Korppi, M. T. Rakher and P. Treutlein: "Sympathetic cooling of a membrane oscillator in a hybrid mechanical-atomic system", Nature Nanotechnology **10**, 55–59 (2015). 4, 45, 52, 99, 100, 103, 105, 116, 133

[58] C. Montoya, J. Valencia, A. A. Geraci, M. Eardley, J. Moreland, L. Hollberg and J. Kitching: "Resonant interaction of trapped cold atoms with a magnetic cantilever tip", Physical Review A - Atomic, Molecular, and Optical Physics **91** (6), 1–5 (2015), ISSN 10941622.

[59] C. B. Møller, R. A. Thomas, G. Vasilakis, E. Zeuthen, Y. Tsaturyan, M. Balabas, K. Jensen, A. Schliesser, K. Hammerer and E. S. Polzik: "Quantum back-Action-evading measurement of motion in a negative mass reference frame", Nature **547** (7662), 191–195 (2017), ISSN 14764687. 3, 4, 45, 99

[60] S. Chu: "Cold atoms and quantum control", Nature **416** (6877), 206–210 (2002), ISSN 0028-0836. 3

[61] K. Hammerer, A. S. Sørensen and E. S. Polzik: "Quantum interface between light and atomic ensembles", Reviews of Modern Physics **82** (2), 1041–1093 (2010), ISSN 0034-6861. 3

[62] B. Vogell, T. Kampschulte, M. T. Rakher, A. Faber, P. Treutlein, K. Hammerer and P. Zoller: "Long distance coupling of a quantum mechanical oscillator to the internal states of an atomic ensemble", New Journal of Physics **17** (4), 043044 (2015), ISSN 1367-2630. 4

[63] D. Hunger, S. Camerer, M. Korppi, A. Jöckel, T. W. Hänsch and P. Treutlein: "Coupling ultracold atoms to mechanical oscillators", Comptes Rendus Physique **12** (9-10), 871–887 (2011), ISSN 1631-0705. 4

[64] D. J. Wilson, C. A. Regal, S. B. Papp and H. J. Kimble: "Cavity Optomechanics with Stoichiometric SiN Films", Physical Review Letters **103** (20), 207204 (2009), ISSN 0031-9007. 4, 8, 45, 49

[65] A. M. Jayich, J. C. Sankey, B. M. Zwickl, C. Yang, J. D. Thompson, S. M. Girvin, A. A. Clerk, F. Marquardt and J. G. Harris: "Dispersive optomechanics: A membrane inside a cavity", New Journal of Physics **10** (2008), ISSN 13672630. 4, 8, 45, 49, 50

[66] D. Hunger, T. Steinmetz, Y. Colombe, C. Deutsch, T. W. Hänsch and J. Reichel: "A fiber Fabry–Perot cavity with high finesse", New Journal of Physics **12** (6), 065038 (2010), ISSN 1367-2630. 4, 8, 16, 23

[67] A. Bick, C. Staarmann, P. Christoph, O. Hellmig, J. Heinze, K. Sengstock and C. Becker: "The role of mode match in fiber cavities", Review of Scientific Instruments **87** (2016). 4, 8, 14, 16, 17, 18, 19, 20, 21, 22, 33

[68] P. Cohadon, A. Heidmann and M. Pinard: "Cooling of a Mirror by Radiation Pressure", Physical Review Letters **83** (16), 3174–3177 (1999), ISSN 0031-9007. 4, 33, 66

[69] D. J. Wilson, V. Sudhir, N. Piro, R. Schilling, A. Ghadimi and T. J. Kippenberg: "Measurement and control of a mechanical oscillator at its thermal decoherence rate", Nature **524** (7565) (2014), ISSN 0028-0836. 4, 33, 66, 69, 70, 77, 78, 81

[70] S. Riedl, M. Lettner, C. Vo, S. Baur, G. Rempe and S. Dürr: "Bose-Einstein condensate as a quantum memory for a photonic polarization qubit", Physical Review A **85** (2012). 6

[71] M. Lettner, M. Mücke, S. Riedl, C. Vo, C. Hahn, S. Baur, J. Bochmann, S. Ritter, S. Dürr and G. Rempe: "Remote Entanglement between a Single Atom and a Bose-Einstein Condensate", Physical Review Letters **106** (21), 210503 (2011), ISSN 0031-9007. 6

[72] S. van Frank, A. Negretti, T. Berrada, R. Bücker, S. Montangero, J.-F. Schaff, T. Schumm, T. Calarco and J. Schmiedmayer: "Interferometry with non-classical motional states of a Bose-Einstein condensate", Nature Communications **5**, 4009 (2014). 6

[73] R. Norte, J. Moura and S. Gröblacher: "Mechanical Resonators for Quantum Optomechanics Experiments at Room Temperature", Physical Review Letters **116** (14), 147202 (2016), ISSN 0031-9007. 6, 8, 16, 56, 96, 98, 133

[74] C. Reinhardt, T. Müller, A. Bourassa and J. C. Sankey: "Ultralow-Noise SiN Trampoline Resonators for Sensing and Optomechanics", Physical Review X **6** (2), 021001 (2016), ISSN 2160-3308. 8, 16, 96, 133

[75] T. P. Purdy, K. E. Grutter, K. Srinivasan and J. M. Taylor: "Observation of Optomechanical Quantum Correlations at Room Temperature", ArXiv e-prints (2016). 6

[76] S. L. Adler and A. Bassi: "Is Quantum Theory Exact?", Science **325** (5938) (2009). 6

[77] O. Romero-Isart: "Quantum superposition of massive objects and collapse models", Physical Review A **84** (5), 052121 (2011), ISSN 1050-2947. 6

[78] R. Penrose: "On Gravity's role in Quantum State Reduction", General Relativity and Gravitation **28** (5), 581–600 (1996), ISSN 1572-9532. 6

[79] D. Kleckner, I. Pikovski, E. Jeffrey, L. Ament, E. Eliel, J. van den Brink and D. Bouwmeester: "Creating and verifying a quantum superposition in a micro-optomechanical system", New Journal of Physics **10** (9), 095020 (2008), ISSN 1367-2630. 6

[80] I. Pikovski, M. R. Vanner, M. Aspelmeyer, M. S. Kim and Č. Brukner: "Probing Planck-scale physics with quantum optics", Nature Physics **8** (5), 393–397 (2012), ISSN 1745-2473. 6

[81] K. Dieckmann, R. J. C. Spreeuw, M. Weidemüller and J. T. M. Walraven: "Two-dimensional magneto-optical trap as a source of slow atoms", Physical Review A **58** (5), 3891–3895 (1998), ISSN 1050-2947. 7

[82] M. Korppi: "Optomechanical Coupling between Ultracold Atoms and a Membrane Oscillator", Phd thesis, Universität Basel, Switzerland (2014). 8

[83] Y. Tsaturyan, A. Barg, E. S. Polzik and A. Schliesser: "Ultracoherent nanomechanical resonators via soft clamping and dissipation dilution", Nature Nanotechnology **12** (8), 776–783 (2017), ISSN 1748-3387. 8, 56, 98

[84] J. D. Thompson, B. M. Zwickl, A. M. Jayich, F. Marquardt, S. M. Girvin and J. G. E. Harris: "Strong dispersive coupling of a high-finesse cavity to a micromechanical membrane", Nature **452** (7183), 72–75 (2008), ISSN 0028-0836. 8, 45

[85] H. Zhong, G. Fläschner, A. Schwarz, R. Wiesendanger, P. Christoph, T. Wagner, A. Bick, C. Staarmann, B. Abeln, K. Sengstock and C. Becker: "A millikelvin all-fiber cavity optomechanical apparatus for merging with ultra-cold atoms in a hybrid quantum system", Review of Scientific Instruments **88** (2), 023115 (2017), ISSN 0034-6748. 9, 14, 15, 16, 25, 26, 49, 59, 63

[86] A. Bick: "Interfacing Ultracold Atoms and a Cryogenic Micromechanical Oscillator", Phd thesis, Universität Hamburg, Germany (2015). 10, 11, 14, 16, 17, 21, 24, 32, 35, 106

[87] C. Staarmann: "Towards a Hybrid Quantum System", Phd thesis, Universität Hamburg, Germany (2016). 10, 11, 12, 13, 16, 23, 24, 25, 32, 34

[88] S. H. Pan, E. W. Hudson and J. C. Davis: "^{3}He refrigerator based very low temperature scanning tunneling microscope", Review of Scientific Instruments **70** (1999). 15

[89] H. Zhong, A. Schwarz and R. Wiesendanger: "Miniaturized high-precision piezo driven two axes stepper goniometer", Review of Scientific Instruments **85** (4), 045006 (2014), ISSN 0034-6748. 15, 16

[90] P. Christoph: "Fiber Cavities for Quantum Optomechanics: Concepts, Manufacturing and Characterization", Masters thesis, Universität Hamburg, Germany (2013). 16, 24

[91] J. Petermann: "Simulations and Fabrication of Optical Fiber Cavities for a Quantum Hybrid Experiment", Masters thesis, Universität Hamburg, Germany. 16, 18, 24, 135

[92] O. Svelto: *Principles of Lasers*, Springer US, Boston, MA (2010), ISBN 978-1-4419-1301-2. 19

[93] J. Gallego, S. Ghosh, S. K. Alavi, W. Alt, M. Martinez-Dorantes, D. Meschede and L. Ratschbacher: "High-finesse fiber Fabry–Perot cavities: stabilization and mode matching analysis", Applied Physics B **122** (3), 47 (2016), ISSN 0946-2171. 19, 26

[94] D. Hunger, C. Deutsch, R. J. Barbour, R. J. Warburton and J. Reichel: "Laser micro-fabrication of concave, low-roughness features in silica", AIP Advances **2** (1), 012119 (2012), ISSN 2158-3226. 23

[95] D. Malacara, M. Servín and Z. Malacara: *Interferogram Analysis For Optical Testing, Second Edition*, CRC Press (2005), ISBN 978-1-57444-682-1. 24

[96] Y. Jiang: "High-resolution interrogation technique for fiber optic extrinsic Fabry-Perot interferometric sensors by the peak-to-peak method", Applied Optics **47** (7), 925 (2008), ISSN 0003-6935. 25, 29, 31

[97] D. A. Steck: "Rubidium 87 D Line Data", (2015). 31, 33, 34, 144

[98] E. D. Black: "An introduction to Pound–Drever–Hall laser frequency stabilization", American Journal of Physics **69** (1), 79–87 (2001), ISSN 0002-9505. 33

[99] H. P. Yuen and V. W. S. Chan: "Noise in homodyne and heterodyne detection", Optics Letters **8** (3), 177 (1983), ISSN 0146-9592. 33, 56, 57

[100] M. S. Stefszky, C. M. Mow-Lowry, S. S. Y. Chua, D. A. Shaddock, B. C. Buchler, H. Vahlbruch, A. Khalaidovski, R. Schnabel, P. K. Lam and D. E. McClelland:

"Balanced homodyne detection of optical quantum states at audio-band frequencies and below", Classical and Quantum Gravity **29** (14), 145015 (2012), ISSN 0264-9381. 33, 56

[101] O. Morsch and M. Oberthaler: "Dynamics of Bose-Einstein condensates in optical lattices", Reviews of Modern Physics **78** (1), 179–215 (2006), ISSN 00346861. 34, 38

[102] A. Faber: "Sympathetic cooling and self-oscillations in a hybrid atom-membrane system", Phd thesis, Universität Basel, Switzerland (2016). 38, 45, 46, 47, 106, 113, 115, 116, 122, 127

[103] J. K. Asbóth, H. Ritsch and P. Domokos: "Collective Excitations and Instability of an Optical Lattice due to Unbalanced Pumping", Physical Review Letters **98** (20), 203008 (2007), ISSN 0031-9007. 38, 102, 107, 123, 124, 133

[104] A. Vochezer, T. Kampschulte, K. Hammerer and P. Treutlein: "Light-mediated collective atomic motion in a hybrid atom-optomechanical system", ArXiv e-prints (2017). 38, 102, 107, 123, 124, 133

[105] T. A. Savard, K. M. O'Hara and J. E. Thomas: "Laser-noise-induced heating in far-off resonance optical traps", Physical Review A **56** (2), R1095–R1098 (1997), ISSN 1050-2947. 39, 41, 42

[106] S. Friebel, C. D'Andrea, J. Walz, M. Weitz and T. W. Hänsch: "CO2-laser optical lattice with cold rubidium atoms", Physical Review A **57** (1), R20–R23 (1998), ISSN 1050-2947. 39, 41, 42

[107] P. L. Kapitza and P. A. M. Dirac: "The reflection of electrons from standing light waves", Mathematical Proceedings of the Cambridge Philosophical Society **29** (02), 297 (1933), ISSN 0305-0041. 39

[108] Y. B. Ovchinnikov, J. H. Müller, M. R. Doery, E. J. D. Vredenbregt, K. Helmerson, S. L. Rolston and W. D. Phillips: "Diffraction of a Released Bose-Einstein Condensate by a Pulsed Standing Light Wave", Physical Review Letters **83** (2), 284–287 (1999), ISSN 0031-9007. 39

[109] M. Greiner: "Ultracold quantum gases in three-dimensional optical lattice potentials", Phd thesis, Ludwig-Maximilians-Universität München, Germany (2003). 40

[110] B. Gadway, D. Pertot, R. Reimann, M. G. Cohen and D. Schneble: "Analysis of Kapitza-Dirac diffraction patterns beyond the Raman-Nath regime", Optics Express **17** (21), 19173 (2009), ISSN 1094-4087. 40

[111] M. Aspelmeyer, S. Groeblacher, K. Hammerer and N. Kiesel: "Quantum Optomechanics - throwing a glance", Journal of the Optical Society of America B **27** (6), A189 (2010), ISSN 0740-3224. 44

[112] M. Aspelmeyer, T. J. Kippenberg and F. Marquardt: *Cavity Optomechanics*, Springer-Verlag Berlin Heidelberg (2014), ISBN 978-3-642-55311-0. 44, 45, 50

[113] J. C. Sankey, C. Yang, B. M. Zwickl, A. M. Jayich and J. G. E. Harris: "Strong and tunable nonlinear optomechanical coupling in a low-loss system", Nature Physics **6** (9), 707–712 (2010), ISSN 1745-2473. 45

[114] T. P. Purdy, R. W. Peterson and C. A. Regal: "Observation of radiation pressure shot noise on a macroscopic object", Science (New York, N.Y.) **339** (6121), 801–4 (2013), ISSN 1095-9203. 45

[115] D. J. Wilson: "Cavity Optomechanics with High-Stress Silicon Nitride Films", Phd thesis, California Institute of Technology, USA (2012). 45, 47, 48, 50, 53, 63, 64

[116] T. Wagner: "Homodyne Detection of a Nanomechanical Oscillator for Thermometry and Active Feedback Cooling", Masters thesis, Universität Hamburg, Germany (2016). 48, 49, 58, 60, 63

[117] A. A. Clerk, M. H. Devoret, S. M. Girvin, F. Marquardt and R. J. Schoelkopf: "Introduction to quantum noise, measurement, and amplification", Reviews of Modern Physics **82** (2), 1155–1208 (2010), ISSN 00346861. 55, 56, 57, 58, 79

[118] A. Jöckel: "Sympathetic cooling of a membrane oscillator in a hybrid mechanical-atomic system", Phd thesis, Universität Basel, Switzerland (2014). 55, 101, 102, 103, 104

[119] N. S. Kampel, R. W. Peterson, R. Fischer, P.-L. Yu, K. Cicak, R. W. Simmonds, K. W. Lehnert and C. A. Regal: "Improving Broadband Displacement Detection with Quantum Correlations", Physical Review X **7** (2), 021008 (2017), ISSN 2160-3308. 58

[120] S. S. Verbridge, J. M. Parpia, R. B. Reichenbach, L. M. Bellan and H. G. Craighead: "High quality factor resonance at room temperature with nanostrings under high tensile stress", Journal of Applied Physics **99** (2006). 64

[121] J. M. Courty, A. Heidmaim and M. Pinard: "Quantum limits of cold damping with optomechanical coupling", European Physical Journal D **17** (3), 399–408 (2001), ISSN 14346060. 65, 77

[122] C. Genes, D. Vitali, P. Tombesi, S. Gigan and M. Aspelmeyer: "Ground-state cooling of a micromechanical oscillator: Comparing cold damping and cavity-assisted cooling schemes", Physical Review A - Atomic, Molecular, and Optical Physics **77** (3), 1–10 (2008), ISSN 10502947. 65, 66, 77

[123] S. Mancini, D. Vitali, P. Tombesi, U. Camerino and I. Camerino: "Optomechanical Cooling of a Macroscopic Oscillator by Homodyne Feedback", Physical Review Letters **80** (4), 2–5 (1998). 66

[124] D. Kleckner and D. Bouwmeester: "Sub-kelvin optical cooling of a micromechanical resonator", Nature **444** (7115), 75–78 (2006). 66

[125] O. Arcizet, P.-F. Cohadon, T. Briant, M. Pinard, A. Heidmann, J.-M. Mackowski, C. Michel, L. Pinard, O. Français and L. Rousseau: "High-Sensitivity Optical

Monitoring of a Micromechanical Resonator with a Quantum-Limited Optomechanical Sensor", Physical Review Letters **97** (13), 1–4 (2006), ISSN 0031-9007. 66

[126] M. Poggio, C. Degen, H. Mamin and D. Rugar: "Feedback Cooling of a Cantilever's Fundamental Mode below 5 mK", Physical Review Letters **99** (1), 1–4 (2007), ISSN 0031-9007. 66, 72

[127] A. Vinante, M. Bignotto, M. Bonaldi, M. Cerdonio, L. Conti, P. Falferi, N. Liguori, S. Longo, R. Mezzena, A. Ortolan, G. A. Prodi, F. Salemi, L. Taffarello, G. Vedovato, S. Vitale and J.-P. Zendri: "Feedback Cooling of the Normal Modes of a Massive Electromechanical System to Submillikelvin Temperature", Physical Review Letters **101** (3), 033601 (2008), ISSN 0031-9007. 66, 70

[128] LIGO Scientific Collaboration: "Observation of a kilogram-scale oscillator near its quantum ground state", New Journal of Physics **11**, 073032 (2009), ISSN 1367-2630. 66, 74

[129] C. Schäfermeier, H. Kerdoncuff, U. B. Hoff, H. Fu, A. Huck, J. Bilek, G. I. Harris, W. P. Bowen, T. Gehring and U. L. Andersen: "Quantum enhanced feedback cooling of a mechanical oscillator using nonclassical light", Nature Communications **7**, 13628 (2016), ISSN 2041-1723. 66, 70, 96

[130] J. C. Maxwell: "On governors", Proceedings of the Royal Society of London **16**, 270–283 (1867), ISSN 03701662. 66

[131] K. J. Bruland, J. L. Garbini, W. M. Dougherty and J. A. Sidles: "Optimal control of force microscope cantilevers. I. Controller design", Journal of Applied Physics **80** (1996), 1951–1958 (1996), ISSN 00218979. 69

[132] A. C. Doherty, A. Szorkovszky, G. I. Harris and W. P. Bowen: "The quantum trajectory approach to quantum feedback control of an oscillator revisited", Philosophical Transactions of the Royal Society A: Mathematical, Physical and Engineering Sciences **370** (1979), 5338–5353 (2012), ISSN 1364-503X. 69

[133] K. H. Lee, T. G. McRae, G. I. Harris, J. Knittel and W. P. Bowen: "Cooling and control of a cavity optoelectromechanical system", Physical Review Letters **104** (12), 1–4 (2010), ISSN 00319007. 70

[134] M. Montinaro, A. Mehlin, H. S. Solanki, P. Peddibhotla, S. MacK, D. D. Awschalom and M. Poggio: "Feedback cooling of cantilever motion using a quantum point contact transducer", Applied Physics Letters **101** (13), 1–5 (2012), ISSN 00036951. 70

[135] M. Pinard, P. F. Cohadon, T. Briant and A. Heidmann: "Full mechanical characterization of a cold damped mirror", Physical Review A - Atomic, Molecular, and Optical Physics **63** (1), 1–12 (2001), ISSN 10502947. 76

[136] K. Jacobs, H. I. Nurdin, F. W. Strauch and M. James: "Comparing resolved-sideband cooling and measurement-based feedback cooling on an equal footing: Analytical results in the regime of ground-state cooling", Physical Review A - Atomic, Molecular, and Optical Physics **91** (4), 1–15 (2015), ISSN 10941622. 77

[137] H. Habibi, E. Zeuthen, M. Ghanaatshoar and K. Hammerer: "Quantum Feedback Cooling of a Mechanical Oscillator Using Variational Measurements: Tweaking Heisenberg's Microscope", Journal of Optics **18 (8)** (2016). 77, 81

[138] A. A. Clerk: "Quantum-limited position detection and amplification: A linear response perspective", Physical Review B - Condensed Matter and Materials Physics **70** (24), 1–9 (2004), ISSN 10980121. 79

[139] H. M. Wiseman and G. J. Milburn: *Quantum measurement and control*, Cambridge University Press (2010), ISBN 9780521804424. 79

[140] J. Zhang, Y.-x. Liu, R.-B. Wu, K. Jacobs and F. Nori: "Quantum feedback: Theory, experiments, and applications", Physics Reports **679**, 1–60 (2017), ISSN 03701573. 79, 80

[141] S. Lloyd: "Coherent quantum feedback", Physical Review A **62** (2), 1–12 (2000), ISSN 1050-2947. 79

[142] T. J. Kippenberg and K. J. Vahala: "Cavity Optomechanics: Back-Action at the Mesoscale", Science **321** (5893) (2008). 80

[143] H. Mabuchi: "Coherent-feedback quantum control with a dynamic compensator", Physical Review A - Atomic, Molecular, and Optical Physics **78** (3), 1–5 (2008), ISSN 10502947. 80

[144] R. Hamerly and H. Mabuchi: "Coherent controllers for optical-feedback cooling of quantum oscillators", Physical Review A - Atomic, Molecular, and Optical Physics **87** (1) (2013), ISSN 10502947. 80

[145] A. Kronwald, F. Marquardt and A. A. Clerk: "Arbitrarily large steady-state bosonic squeezing via dissipation", Physical Review A - Atomic, Molecular, and Optical Physics **88** (6), 1–10 (2013), ISSN 10502947. 80

[146] F. Lecocq, J. B. Clark, R. W. Simmonds, J. Aumentado and J. D. Teufel: "Quantum Nondemolition Measurement of a Nonclassical State of a Massive Object", Physical Review X **5** (4), 041037 (2015), ISSN 2160-3308. 80, 81

[147] J. Kerckhoff, H. I. Nurdin, D. S. Pavlichin and H. Mabuchi: "Designing Quantum Memories with Embedded Control: Photonic Circuits for Autonomous Quantum Error Correction", Physical Review Letters **105** (4), 040502 (2010), ISSN 0031-9007. 80

[148] J. Kerckhoff, D. S. Pavlichin, H. Chalabi and H. Mabuchi: "Design of nanophotonic circuits for autonomous subsystem quantum error correction", New Journal of Physics **13** (2011), ISSN 13672630. 80

[149] S. Shankar, M. Hatridge, Z. Leghtas, K. M. Sliwa, A. Narla, U. Vool, S. M. Girvin, L. Frunzio, M. Mirrahimi and M. H. Devoret: "Autonomously stabilized entanglement between two superconducting quantum bits", Nature **504** (7480), 419–422 (2013), ISSN 0028-0836. 80

[150] H. M. Wiseman: "Adaptive Phase Measurements of Optical Modes: Going Beyond the Marginal Q Distribution", Physical Review Letters **75** (25), 4587–4590 (1995), ISSN 0031-9007. 80

[151] M. A. Armen, J. K. Au, J. K. Stockton, A. C. Doherty and H. Mabuchi: "Adaptive Homodyne Measurement of Optical Phase", Physical Review Letters **89** (13), 133602 (2002), ISSN 0031-9007. 81

[152] W. P. Smith, J. E. Reiner, L. A. Orozco, S. Kuhr and H. M. Wiseman: "Capture and Release of a Conditional State of a Cavity QED System by Quantum Feedback", Physical Review Letters **89** (13), 133601 (2002), ISSN 0031-9007. 81

[153] C. Sayrin, I. Dotsenko, X. Zhou, B. Peaudecerf, T. Rybarczyk, S. Gleyzes, P. Rouchon, M. Mirrahimi, H. Amini, M. Brune, J.-M. Raimond and S. Haroche: "Real-time quantum feedback prepares and stabilizes photon number states", Nature **477** (7362), 73–7 (2011), ISSN 1476-4687. 81

[154] D. Ristè, M. Dukalski, C. A. Watson, G. de Lange, M. J. Tiggelman, Y. M. Blanter, K. W. Lehnert, R. N. Schouten and L. DiCarlo: "Deterministic entanglement of superconducting qubits by parity measurement and feedback", Nature **502** (7471), 350–354 (2013), ISSN 0028-0836. 81

[155] S. S. Szigeti, M. R. Hush, A. R. R. Carvalho and J. J. Hope: "Continuous measurement feedback control of a Bose-Einstein condensate using phase-contrast imaging", Physical Review A - Atomic, Molecular, and Optical Physics **80** (1) (2009), ISSN 10502947. 81

[156] S. S. Szigeti, M. R. Hush, a. R. R. Carvalho and J. J. Hope: "Feedback control of an interacting Bose-Einstein condensate using phase-contrast imaging", Physical Review A - Atomic, Molecular, and Optical Physics **82** (4), 1–10 (2010), ISSN 10502947. 81

[157] P. Bushev, D. Rotter, A. Wilson, F. Dubin, C. Becher, J. Eschner, R. Blatt, V. Steixner, P. Rabl and P. Zoller: "Feedback cooling of a single trapped ion", Physical Review Letters **96** (4), 1–5 (2006), ISSN 10797114. 81

[158] D. Rugar and P. Grütter: "Mechanical parametric amplification and thermomechanical noise squeezing", Physical Review Letters **67** (6), 699–702 (1991), ISSN 00319007. 81

[159] R. Ruskov, K. Schwab and A. N. Korotkov: "Squeezing of a nanomechanical resonator by quantum nondemolition measurement and feedback", Physical Review B - Condensed Matter and Materials Physics **71** (23), 1–19 (2005), ISSN 10980121. 81, 82

[160] A. Szorkovszky, A. C. Doherty, G. I. Harris and W. P. Bowen: "Mechanical squeezing via parametric amplification and weak measurement", Physical Review Letters **107** (21), 1–5 (2011), ISSN 00319007. 81

[161] A. Szorkovszky, G. A. Brawley, A. C. Doherty and W. P. Bowen: "Strong thermomechanical squeezing via weak measurement", Physical Review Letters **110** (18), 1–5 (2013), ISSN 00319007. 81

[162] G. Vasilakis, H. Shen, K. Jensen, M. Balabas, D. Salart, B. Chen and E. S. Polzik: "Generation of a squeezed state of an oscillator by stroboscopic back-action-evading measurement", Nature Physics **11** (5), 389–392 (2015), ISSN 1745-2473. 81

[163] V. B. Braginsky, Y. I. Vorontsov and K. S. Thorne: "Quantum Nondemolition Measurements", Science **209** (4456) (1980). 81

[164] A. A. Clerk, F. Marquardt and K. Jacobs: "Back-action evasion and squeezing of a mechanical resonator using a cavity detector", New Journal of Physics **10** (2008), ISSN 13672630. 82

[165] M. J. Woolley and A. A. Clerk: "Two-mode back-action-evading measurements in cavity optomechanics", Physical Review A - Atomic, Molecular, and Optical Physics **87** (6), 1–24 (2013), ISSN 10502947. 82

[166] M. Rossi, N. Kralj, S. Zippilli, R. Natali, A. Borrielli, G. Pandraud, E. Serra, G. Di Giuseppe and D. Vitali: "Enhancing Sideband Cooling by Feedback-Controlled Light", Physical Review Letters **119** (12), 123603 (2017), ISSN 0031-9007. 82

[167] M. Grimm, C. Bruder, N. Lörch, J. S. Bennett, L. S. Madsen and M. Baker: "Enhancement of three-mode optomechanical interaction by feedback-controlled light", Quantum Science and Technology **2 (3)** (2017). 82

[168] V. Sudhir, D. Wilson, R. Schilling, H. Schütz, S. Fedorov, A. Ghadimi, A. Nunnenkamp and T. Kippenberg: "Appearance and Disappearance of Quantum Correlations in Measurement-Based Feedback Control of a Mechanical Oscillator", Physical Review X **7** (1), 011001 (2017), ISSN 2160-3308. 82

[169] M. R. Vanner, I. Pikovski, G. D. Cole, M. S. Kim, C. Brukner, K. Hammerer, G. J. Milburn and M. Aspelmeyer: "Pulsed quantum optomechanics", Proceedings of the National Academy of Sciences **108** (39), 16182–16187 (2011), ISSN 0027-8424. 97, 98

[170] M. R. Vanner, J. Hofer, G. D. Cole and M. Aspelmeyer: "Cooling-by-measurement and mechanical state tomography via pulsed optomechanics", Nature Communications **4** (May), 1–8 (2012), ISSN 2041-1723. 98

[171] K. Khosla, G. A. Brawley, M. R. Vanner and W. P. Bowen: "Quantum optomechanics beyond the quantum coherent oscillation regime", pages 1–6. 98

[172] S. Machnes, J. Cerrillo, M. Aspelmeyer, W. Wieczorek, M. B. Plenio and A. Retzker: "Pulsed laser cooling for cavity optomechanical resonators", Physical Review Letters **108** (15), 1–5 (2012), ISSN 00319007. 98

[173] K. E. Khosla, M. R. Vanner, W. P. Bowen and G. J. Milburn: "Quantum state preparation of a mechanical resonator using an optomechanical geometric phase", New Journal of Physics **15** (2013), ISSN 13672630. 98

[174] J. S. Bennett, K. Khosla, L. S. Madsen, M. R. Vanner, H. Rubinsztein-Dunlop and W. P. Bowen: "A quantum optomechanical interface beyond the resolved sideband limit", New Journal of Physics **18** (5), 053030 (2016), ISSN 1367-2630. 98

[175] R. E. Drullinger, D. J. Wineland and J. C. Bergquist: "High-resolution optical spectra of laser cooled ions", Applied Physics **22** (4), 365–368 (1980), ISSN 0340-3793. 100

[176] D. J. Larson, J. C. Bergquist, J. J. Bollinger, W. M. Itano and D. J. Wineland: "Sympathetic cooling of trapped ions: A laser-cooled two-species nonneutral ion plasma", Physical Review Letters **57** (1), 70–73 (1986), ISSN 0031-9007. 100

[177] G. Modugno, G. Ferrari, G. Roati, R. J. Brecha, A. Simoni and M. Inguscio: "Bose-Einstein condensation of potassium atoms by sympathetic cooling", Science (New York) **294** (5545), 1320–2 (2001), ISSN 0036-8075. 100

[178] I. Bloch, M. Greiner, O. Mandel, T. W. Hänsch and T. Esslinger: "Sympathetic cooling of ^{85}Rb and ^{87}Rb", Physical Review A **64** (2), 021402 (2001), ISSN 1050-2947.

[179] C. J. Myatt, E. A. Burt, R. W. Ghrist, E. A. Cornell and C. E. Wieman: "Production of Two Overlapping Bose-Einstein Condensates by Sympathetic Cooling", Physical Review Letters **78** (4), 586–589 (1997), ISSN 0031-9007.

[180] F. Schreck, G. Ferrari, K. L. Corwin, J. Cubizolles, L. Khaykovich, M.-O. Mewes and C. Salomon: "Sympathetic cooling of bosonic and fermionic lithium gases towards quantum degeneracy", Physical Review A **64** (1), 011402 (2001), ISSN 1050-2947. 100

[181] D. Offenberg, C. B. Zhang, C. Wellers, B. Roth and S. Schiller: "Translational cooling and storage of protonated proteins in an ion trap at subkelvin temperatures", Physical Review A - Atomic, Molecular, and Optical Physics **78** (6), 1–4 (2008), ISSN 10502947. 100

[182] E. R. Hudson: "Sympathetic cooling of molecular ions with ultracold atoms", EPJ Techniques and Instrumentation **3** (1), 8 (2016), ISSN 2195-7045.

[183] X. Tong, A. H. Winney and S. Willitsch: "Sympathetic cooling of molecular ions in selected rotational and vibrational states produced by threshold photoionization", Physical Review Letters **105** (14), 1–4 (2010), ISSN 00319007. 100

[184] G. Gabrielse, X. Fei, L. A. Orozco, R. L. Tjoelker, J. Haas, H. Kalinowsky, T. A. Trainor and W. Kells: "Cooling and slowing of trapped antiprotons below 100 meV", Physical Review Letters **63** (13), 1360–1363 (1989), ISSN 0031-9007. 100

[185] N. Mann, M. R. Bakhtiari, A. Pelster and M. Thorwart: "Nonequilibrium Quantum Phase Transition in a Hybrid Atom-Optomechanical System", ArXiv e-prints (2017). 106

[186] J. K. Asbóth, H. Ritsch and P. Domokos: "Optomechanical coupling in a one-dimensional optical lattice", Physical Review A **77** (6), 063424 (2008), ISSN 1050-2947. 107, 123, 124, 133

[187] H. J. Metcalf and P. van der Straten: *Laser cooling and trapping*, Graduate Texts in Contemporary Physics, Springer, New York (1999). 113

[188] I. H. Deutsch, R. J. C. Spreeuw, S. L. Rolston and W. D. Phillips: "Photonic band gaps in optical lattices", Physical Review A **52** (2), 1394–1410 (1995), ISSN 1050-2947. 114, 146

[189] J. H. Denschlag, J. E. Simsarian, H. Häffner, C. McKenzie, A. Browaeys, D. Cho, K. Helmerson, S. L. Rolston and W. D. Phillips: "A Bose-Einstein condensate in an optical lattice", Journal of Physics B: Atomic, Molecular and Optical Physics **35** (14), 307 (2002), ISSN 09534075. 135

[190] H. K. Andersen: "Bose-Einstein condensates in optical lattices", Phd thesis, University of Aarhus, Denmark (2008). 135

Danksagung

An dieser Stelle würde ich gerne allen danken, die mich bei meiner Doktorarbeit unterstützt haben. Die präsentierten Ergebnisse sind im Team entstanden und wären alleine nicht möglich gewesen. Dafür wurden uns exzellente Rahmenbedingungen geschaffen und ich möchte mich ganz besonders bei meinem Doktorvater Klaus Sengstock bedanken, der dafür sorgt, dass diese Forschungsgruppe so erfolgreich sein kann und ein so tolles Arbeitsklima herrscht. Du hast mir in meiner Arbeit sehr große Freiheiten gelassen und ein großes Vertrauen entgegengebracht, unserer physikalischen Intuition und unseren Visionen zu folgen. Das weiß ich sehr zu schätzen und dafür bin ich dir sehr dankbar. Mein Dank gilt auch Herrn Prof. Wiesendanger, der so freundlich war, das Zweitgutachten meiner Dissertation zu übernehmen. Vielen Dank dafür, dass Sie uns hier in der Jungiusstraße so gute Forschungsbedingungen geschaffen haben, was insbesondere bei unserem Projekt sehr schwierig war. Ich möchte mich auch bei den weiteren Mitgliedern der Prüfungskomission bedanken, bei Herrn Prof. Thorwart und Herrn Prof. Hemmerich, sowie insbesondere bei Herrn Prof. Schnabel, der freundlicherweise den Vorsitz der Prüfungskomission übernommen hat.
Ein besonderer Dank gilt auch unserem Teamleiter Christoph Becker, der sich außerordentlich für unser Projekt engagiert hat. Ohne dein Fachwissen und deine permanente Unterstützung wären wir im Labor unzählige Male aufgeschmissen gewesen und hätten vermutlich aufgegeben. Außerdem schaffst du es immer wieder, dem Team mit deiner positiven Art neuen Mut zu geben, wenn die unvermeidbare Laborfrustration Überhand zu nehmen droht. Jeder der schon einmal monatelang im Labor an einer bestimmten Aufgabe verzweifelt ist, weiß was so eine Hilfe wert ist.
Ich habe mich in unserem Projekt immer sehr wohl gefühlt und möchte dem gesamten Team Nano-BEC, sowie allen ehemaligen Teammitgliedern dafür meinen Dank aussprechen. An erster Stelle möchte ich dabei Andreas Bick und Christina Staarmann nennen, die mich schon während meiner Masterarbeit so nett ins Team aufgenommen haben und mit denen ich eine schöne Zeit im Labor verbracht habe, an die ich gerne zurückdenke. Außerdem habe ich sehr viel von euch gelernt. Ganz besonders möchte ich auch Tobias Wagner danken. Du hast uns mit deinen klugen Ideen immer sehr vorangebracht und wir waren in den letzten anderthalb Jahren ein super Laborteam. Auch möchte ich mich sehr bei Hai Zhong bedanken. Es hat viel Spaß gemacht mit dir zu arbeiten und du hast dich mit besonderer Kraft für unser Projekt eingesetzt. Vielen Dank auch an Alexander Schwarz, der stets neue Ideen in den Projektmeetings eingebracht hat.
Ganz besonderer Dank gilt auch Ortwin Hellmig, der uns im Bereich Fasertechnologie immens geholfen hat und immer Zeit für uns hatte. Außerdem hat es immer besonders Spaß gemacht mit dir zu arbeiten. Einen großen Dank auch an Reinhard Mielck für die Unterstützung während des Experimentumzugs und an Horst Biedermann, der uns sehr in der Elektronikentwicklung geholfen hat. Auch möchte ich Tim Erke und Dieter Barlösius, sowie dem gesamten Verwaltungspersonal danken, das wesentlich zu der guten Arbeitsatmosphäre beigetragen hat.
Zu guter Letzt möchte ich meiner Familie und Freunden meinen besonderen Dank aussprechen: Meinen Eltern, die mich immer unglaublich toll unterstützt haben. Meinen Freunden, die viel Verständnis dafür hatten, dass ich die letzten Jahre wenig Zeit für sie hatte. Ganz besonders meiner Freundin Sinje bin ich auch großen Dank schuldig, denn sie hat sicher am meisten darunter gelitten und hat mich trotzdem immer unterstützt. Ein großer Dank auch an Alex Rohse für das Korrekturlesen.